Petrology and geochemistry of pyroxenites from the Cabo Ortegal Complex, Spain

Romain Tilhac

Université Fédérale
Toulouse Midi-Pyrénées

THÈSE

En vue de l'obtention du

DOCTORAT DE L'UNIVERSITÉ DE TOULOUSE

Délivré par :

l'Université Toulouse III Paul Sabatier
en Cotutelle internationale avec Macquarie University (Sydney)

Présentée et soutenue par :

Romain TILHAC

le 22 août 2017

Titre :

Pétrologie et géochimie des pyroxénites
du Complexe de Cabo Ortegal, Espagne

École doctorale et discipline ou spécialité :
ED SDU2E : Sciences de la Terre et des Planètes Solides

Unité de recherche :
Géosciences Environnement Toulouse (GET)

Directeur/trice(s) de thèse :
Michel GREGOIRE & Damien GUILLAUME (Université Toulouse III Paul Sabatier)
Suzanne Y' O'REILLY & William L. GRIFFIN (Macquarie University)

Jury :
Stéphanie DUCHENE, Professeur à l'Université Paul Sabatier (Toulouse), Présidente
Costanza BONADIMAN, Professeur associée à l'Université de Ferrara, Examinatrice
Jean-Louis BODINIER, Directeur de recherche CNRS à Géosciences Montpellier, Rapporteur
José Ignacio GIL IBARGUCHI, Professeur à l'Université du Pays Basque (Bilbao), Rapporteur
Michel GREGOIRE, Directeur de recherche CNRS au GET (Toulouse), Directeur de thèse
Suzanne Y. O'REILLY, Professeur à Macquarie University (Sydney), Directrice de thèse
Damien GUILLAUME, Professeur à l'Université Jean Monnet (Saint Etienne), Co-directeur de thèse
William L. GRIFFIN, Professeur à Macquarie University (Sydney), Co-directeur de thèse
Georges CEULENEER, Directeur de recherche CNRS au GET (Toulouse), Invité
Jacques GIRARDEAU, Professeur à l'Université de Nantes, Invité

"Where the sea is seen, but not heard..."

For Garazi

Table of Contents

Abstract

Mafic lithologies such as pyroxenites play a major role in the development of chemical heterogeneity in the upper mantle and in the recycling of elements between the deep Earth and its external envelopes. Pyroxenites are notably involved in the differentiation of primitive arc magmas whose genesis has had a major impact on continent formation in post-Archean times, but the rarity of exposures of deep arc sections limits our understanding of the details of melt migration and melt-rock interaction. In the Variscan suture of north-western Iberia, the Herbeira massif of the Cabo Ortegal Complex represents a unique km-scale section of sub-arc mantle harzburgites exposing abundant pyroxenites associated with dunites and chromitites. However, the processes responsible for their abundance and geochemical characteristics are not well established, notably due to a particularly complex tectonothermal history.

This work combines new field and petrographic observations with the characterization of major-, trace-element and radiogenic-isotope (Sr, Nd, Hf and Os) compositions of these pyroxenites. After constraining the effects of secondary processes by studying small-scale heterogeneities, it is shown that the low-Al content of pyroxenes, the high abundance of compatible elements and the absence of plagioclase are related to primitive hydrous parental melts. Olivine websterites and clinopyroxenites preserving dunite lenses (*type 1*, and their foliated *type-3* products) record the partial replacement of peridotites at decreasing melt/rock ratios, following intrusion of picritic melts at relatively low pressure (< 1.2 GPa), potentially within an arc root. Massive websterites (*type 2*) represent the final products of this reaction at higher melt/rock ratios, potentially as veins and dykes crystallized from boninitic melts differentiated from the initial picritic melts. Interaction between these Si-rich melts and dunites produced rare opx-rich websterites (*type 4*) with Cr-rich spinels. Chromatographic reequilibration accompanied the late-magmatic crystallization of amphibole from migrating or trapped residual melts, producing a range of REE patterns from spoon-shaped to strongly LREE-enriched, consistent with increasingly unradiogenic Nd compositions. Particularly high CaO/Al_2O_3 and the selective enrichment of LILE/HFSE in Cabo Ortegal pyroxenites suggest the generation of their Ca-rich parental melts via low-degree, second-stage melting of a refractory lherzolite at < 2 GPa, following percolation of slab-derived fluids and/or carbonatite melts. Radiogenic-isotope systematics indicate the involvement of an old metasomatized mantle domain, suggesting the reworking of a continental margin during this arc magmatism, and of recycled sediments. Their geochronology suggests that Cabo Ortegal pyroxenites formed at around

500 Ma, which implies that previously reported ages around 390 Ma probably correspond to a metamorphic event.

Pyroxenites and their host peridotites then recorded the development of sheath folds and mylonites following high-temperature deformation. We suggest that this episode corresponds to the delamination of the arc root associated with prograde metamorphism peaking at 1.6-1.8 GPa and 780-800°C, as recorded by undeformed garnet coronas around spinel. Exhumation of the arc root after its intrusion into a subduction zone was accompanied by hydration, as suggested by abundant post-kinematic amphibole, and by addition of S and mobilization of Re, as suggested by Os-isotope systematics and the association of amphibole and abundant base-metal sulfides. The Cabo Ortegal Complex may thus preserve a unique example of delaminated arc root, bearing evidence of the role of melt-peridotite interaction during the differentiation of primitive arc magmas at depth.

RÉSUMÉ

Les roches mafiques telles que les pyroxénites jouent un rôle majeur dans le développement des hétérogénéités du manteau supérieur et le recyclage des éléments entre la Terre interne et ses enveloppes externes. Les pyroxénites sont notamment impliquées dans la différenciation des magmas d'arc primitifs dont la genèse a eu un impact important sur la formation des continents depuis l'Archéen. La rareté des affleurements de sections profondes d'arc limite cependant notre compréhension des modalités de la migration des liquides magmatiques et de leur interaction avec les roches encaissantes. Dans la suture Varisque du nord-ouest de l'Ibérie, le massif de Herbeira du complexe de Cabo Ortegal représente un affleurement unique d'harzburgites et d'abondantes pyroxenites, associées à des dunites et chromitites issues du manteau sub-arc. Cependant, les processus responsables de leur abondance et de leurs caractéristiques géochimiques ne sont pas bien contraints, en particulier en raison d'une histoire tectono-métamorphique polyphasée.

Cette étude présente de nouvelles observations pétrographiques et de terrain, combinées avec la caractérisation de la composition en éléments majeurs et traces, et en isotopes radiogéniques (Sr, Nd, Hf et Os) de ces pyroxénites. Après avoir contraint les effets des processus secondaires en étudiant les hétérogénéités à petite échelle, il est démontré que la faible teneur en Al des pyroxènes, la forte abondance des éléments compatibles et l'absence de plagioclase sont liées au caractère hydraté et primitif des magmas parents. Les webstérites et clinopyroxénites à olivine (de *type 1*) qui préservent des lentilles de dunite, et leurs dérivés foliés (de *type 3*), ont enregistré le remplacement partiel de péridotites à rapports magma/roche décroissants, suite à l'intrusion de magmas picritiques à relativement faible profondeur (< 1,2 GPa), potentiellement au sein d'une racine d'arc. Les webstérites massives (de *type 2*) représentent le produit final de cette réaction à des rapports magma/roche plus élevés, potentiellement sous forme de veines et filons cristallisés à partir de magmas boninitiques différenciés des magmas initialement picritiques. L'interaction entre ces magmas enrichis en Si et les dunites a produit de rares webstérites à opx (de *type 4*). La rééquilibration chromatographique a accompagné la cristallisation d'amphibole à partir de liquides magmatiques résiduels, percolant ou piégés, ce qui a produit une large gamme de profils de terres rares, en accord avec la composition du Nd progressivement non-radiogénique. Les forts rapports CaO/Al_2O_3 et l'enrichissement spécifique des LILE par rapport aux HFSE suggèrent la génération de magmas parents riches en Ca par des faibles degrés de fusion d'une lherzolite réfractaire à < 2 GPa, suite à la percola-

tion de fluides issus du slab et/ou de carbonatites. La systématique des isotopes radiogéniques indique l'implication d'un manteau ancien et métasomatisé, suggérant la remobilisation d'une marge continentale par ce magmatisme d'arc, et de sediments recyclés. La géochronologie de ces mêmes isotopes suggère que les pyroxénites de Cabo Ortegal se sont formées autours de 500 Ma, impliquant que les âges précédemment reportés à ~ 390 Ma correspondent probablement à un épisode métamorphique.

Les pyroxénites et leurs péridotites hôtes ont enregistré le développement de plis en fourreaux et de mylonites faisant eux-mêmes suite à un épisode de déformation à haute température. Nous proposons que cette transition correspond à la délamination de la racine d'arc, associée à du métamorphisme prograde jusqu'à 1,6-1,8 GPa et 780-800°C, comme en témoignent les couronnes de grenat autours du spinelle. L'exhumation dans une zone de subduction a ensuite été accompagnée par de l'hydratation, comme le suggère l'abondance d'amphiboles automorphes, et par l'addition de S et la mobilisation du Re, comme en témoignent la composition isotopique de l'Os et l'association systématique entre l'amphibole et les sulfures de métaux de base. Le complexe de Cabo Ortegal préserve donc un exemple unique de racine d'arc délaminée qui illustre le rôle de l'interaction magma-roche pendant la différentiation des magmas d'arc primitifs en profondeur.

DECLARATION

This thesis is based on work carried out in the ARC Centre of Excellence for CCFS and GEMOC National Key Centre, Department of Earth and Planetary Sciences at Macquarie University, Australia and in the Géosciences Environnement Toulouse at Paul Sabatier University, France, over the period of February 2013 to August 2016. I hereby declare that all the data and interpreations presented in this thesis are from my own work, except for information cited from published or unpublished sources, which has been explicitely indicated and acknowledged.

No part of this thesis has ever been submitted for any other degree in any university or education institute. This thesis is submitted to both Macquarie University, Australia and Paul Sabatier University, France, under the conditions of a co-tutelle agreement between these two universities for this PhD program.

Sydney, August 15th 2016

Romain Tilhac

ACKNOWLEDGEMENTS

I first would like to thank my French and Australian supervisors Sue O'Reilly, Bill Griffin and Norm Pearson at Macquarie University, and Michel Grégoire, Georges Ceuleneer and Damien Guillaume at Paul Sabatier University. Their very complementary supervision and expertise have been highly valued and the freedom they have allowed me has been very gratifying and rewarding.

Having spent most of my PhD time in Australia, I have had the great opportunity to use the amazing set of analytical tools available at GEMOC/CCFS, owing entirely to the continuing and innovative work of Sue, Bill and Norm, over many years. You have made me feel like I joined a family who shares the same passion and I have earned more than a degree in the process. To these acknowledgements, I would like to add some more contrasted feelings and say that I have very much missed the highly skilled and cautious contribution to the writing of this manuscript that Norm would have provided. Witnessing how unfair the last few months have been for such a kind person has been for me the most pitiable introduction to some aspects of the world of science...

I am deeply grateful for the constant and enthusiastic support I have received from Michel and Georges during the few months I have spent in Toulouse, and before and during my entire candidature over (too) many emails. I especially thank Georges, and his family Elisabeth, Camille and Tom, for spending their summer holidays on the field in Galicia with Hadrien, Laure and me. I shall say that I owe you my entire, although very modest, experience on the field of mantle rocks. To Michel, I would like to say thank you very much for having always believed in me and giving me the opportunity to start a whole chapter of my life in Australia, and thank you Damien, along with Francis Odonne, for making this project possible in bringing me to Michel's attention. I am also grateful to Jacques Girardeau for the samples, field notes and advices he kindly gave in preparation of our fieldtrips.

I wish to thank those who helped me with my analytical work and have always provided their technical assistance: Manal Bebbington, Dave Adams, Will Powell, Peter Wieland, Steve Craven, Bruce Schaeffer, Rosanna Murphy and Sarah Gain at Macquarie University, and Mathieu Benoit, Philippe de Parceval and Sophie Gouy at Paul Sabatier University. Thanks especially to Peter, Mathieu and Bruce for introducing me to the pleasures of lab chemistry. I would like to thank Olivier Gaul, Sally-Ann Hodgekiss, the late Carol McMahon and all

GEMOC/CCFS admin staff for their availability in always finding solutions to the most unexpected requests. I am also grateful to Jean-Louis Bodinier, Lukáš Ackerman and Giulio Borghini, and to José Ignacio Gil Ibarguchi, Sun-Lin Chung and Greg Yaxley, for providing very constructive comments in the review of the paper published in the Journal of Petrology and of this thesis, respectively. The ideas and interpretations developed in this thesis have benefited from it.

This work was supported by the Australian Research Council grant for the ARC Centre of Excellence for Core to Crust Fluid Systems (CCFS), a Macquarie University International Postgraduate Scholarship (iMQRES), Macquarie postgraduate funds, and CNRS funds (UMR 5563, Géosciences Environnement Toulouse). The project used instrumentation funded by ARC LIEF and DEST Systemic Infrastructure Grants, Macquarie University, NCRIS AuScope and industry partners. I would also like to thank everyone from both universities who made this co-tutelle program possible.

My PhD experience would have been completely different without the great, friendly working environment brought together by the people of the department of Earth and Planetary Sciences and GEMOC/CCFS at Macquarie University: Beñat Oliveira Bravo, Bruno Colas, Yoann Gréau, Mathieu Chassé, Yu Wang, Cait Stuart, Louise Goode, Olivier Alard, Alexis Geisler, José María González-Jiménez, Qing Xiong, Jason Jiang, and of the Géosciences Environnement Toulouse at Paul Sabatier University: Paul Antonio, Alexandre Boutin, Léandre Ponthus, Mathieu Rospabé, and all the people that I have left out here, mainly PhD students, whom I shared offices, flats, lunches or parties with. I have especially enjoyed interacting with you in such a stimulating and casually serious way. Some of you will certainly remain life-long friends and I should also apologize to Hadrien Henry, who has already been one of them for many years, for having dragged him to the joy of mantle petrology. I must say however that I have enjoyed sharing most of my short career with you.

Before adding some words for my family and friends in French, I would like to use my little Basque repertoire for a very special person.

Garazi Gil Azpitarte, eskerrik asko zure maitasunagatik!

Une pensée d'abord à tous mes amis français, géologues et non géologues. Je pense en particulier à quelques personnages uniques, Thibaud Candeleda, Florian Bérail, François Guyader, les Bretons, et tous ceux que j'oublie. Un clin d'œil aussi aux spéléologues du Groupe Spéléologique Haut-Pyrénéen (GSHP) de Tarbes et à tous les Amalgamés et amoureux de la Pierre Saint-Martin, pour leur passion communicative des grottes, des Pyrénées et du monde minéral, et pour avoir largement contribué à mon goût pour l'exploration. Je pense à Alain Bressan, Joël Danflous, Michel Douat, Bruno Nurisso, Madeleine Cabidoche, Dominique Prébende, et tant d'autres.

Je voudrais maintenant dire toute ma reconnaissance et ma gratitude à ma famille et leur témoigner l'amour que je n'ai pas l'habitude de montrer. Merci pour avoir toujours été des parents et grands-parents exceptionnels. Vous m'avez donné mes racines pyrénéennes, bigourdanes, et plus loin encore, vous êtes et resterez dans mon cœur.

Merci à mon père, Jean Marc Tilhac, et à ma mère, Sabine Sanchez, pour avoir toujours su me donner tout ce que j'avais besoin intellectuellement et matériellement. Maman, j'aimerais te dire merci pour ton soutien inconditionnel et ton ouverture d'esprit, pour m'avoir permis de développer mon esprit critique et pour toutes nos longues discussions. Tu m'as toujours permis de m'épanouir, et ce avec tellement de modestie, que jamais je n'ai ressenti de difficulté à y parvenir. Papa, j'aimerais te dire merci pour m'avoir transmis ta passion contagieuse et la curiosité de voir l'Afrique et le reste du monde, d'escalader des montagnes et explorer les gouffres de la Pierre Saint-Martin et d'ailleurs. Tu m'as tellement appris et inspiré, je ne serais jamais, sans toi, devenu géologue. Je voudrais te dire toute mon admiration.

Je tiens également à remercier mes grands-parents, René et Raymonde Tilhac et Raymond Sanchez et Martine Demanche, pour leur amour, leur complicité, et pour être toujours restés jeunes. Vous m'avez appris les choses simples, celles qui n'ont pas de prix. J'ai la chance énorme de partager et d'avoir partagé tant de temps, d'expérience et de savoir avec vous. Je ne serais jamais, sans chacun de vous, devenu ce que je suis. Papé, mami, vous êtes partis tous les deux, je vous garderai à jamais au fond de mon cœur.

Enfin, je voudrais surtout remercier Laure Basterreix, celle qui a partagé ma vie pendant dix ans. Merci pour m'avoir toujours aimé et soutenu quelques soient mes choix, et même quand ceux-là signifiaient d'aller vivre à l'autre bout du monde. Nos vies ont pris des chemins différents, mais je garderai toujours dans mon cœur chaque moment que nous avons partagé. Nous avons tout appris ensemble et je te dois une grande partie de cette thèse. Je ne serais jamais devenu qui je suis sans t'avoir connue, sans ta curiosité, ta générosité et ton courage.

Merci Laure.

Chapter I.

General Introduction

A. WHY STUDY (CABO ORTEGAL) PYROXENITES?

Pyroxenites and eclogites play a major role in the development of chemical heterogeneity in the upper mantle and in the recycling of elements between the deep Earth and its external envelopes. It is not only increasingly apparent that their signature may be recognisable in the source region of mid-ocean ridge and intra-plate basalts (*e.g.* Sobolev *et al.*, 2005, Lambart *et al.*, 2012, Lambart *et al.*, 2013) but they may also contribute to the generation and evolution of primary arc melts. Since arc magmatism has been of a great interest for petrologists and geochemists for several decades, two main scientific questions underpin the reasons why to study pyroxenites and more particularly arc-related pyroxenites such those exposed in the Cabo Ortegal Complex.

- What is the nature of the source region of arc magmas?

When compared to any other lavas, whether they be mid-ocean ridge basalts (MORB) or ocean island basalts (OIB), lavas produced along subduction zones such island arc basalts (IAB) are selectively enriched in certain incompatible trace elements, the large ion lithophile elements (LILE), the light rare earth elements (LREE), U and Th, over others, the high field strength elements (HFSE). Igneous rocks formed along volcanic arcs also contain significant amounts of volatiles. These fingerprints are, at present, best explained by the contribution of slab-derived components to mantle-wedge melts (Kelemen, 1990, Kostopoulos & Murton, 1992, Hawkesworth *et al.*, 1993, Schiano *et al.*, 2000, Bénard & Ionov, 2013). Metamorphic reactions occurring in the subducting slab upon increasing pressure and temperature indeed release water and volatiles, thus lowering the solidus temperature of mantle-wedge peridotites and generating primary arc melts. This constitutes one of the most important paradigms of modern plate tectonics. However, the nature and compositions of these slab-derived components (sediment-derived and/or basalts-derived fluids and/or melts), and the quantification of their respective contribution with respect to mantle-wedge melts has been a matter of debate.

- What processes are involved in the differentiation of arc magmas?

Experimental petrology predicts that abundant pyroxenites are left after fractionation of primitive, mantle-derived arc melts (Kay & Kay, 1985, DeBari *et al.*, 1987, Müntener & Ulmer, 2006). However, in the exposed sections of arc crust and sub-arc mantle, these are either much less abundant than expected from mass-balance calculations - this is the case in the Talkeetna

arc, Alaska (DeBari & Sleep, 1991, Miller & Christensen, 1994, Greene *et al.*, 2006, Kelemen *et al.*, 2014) - or their origin as crustal cumulates is debated due to the lack of crystal-fractionation linkage - this is the case in the Kohistan arc, Pakistan (Khan *et al.*, 1993, Burg *et al.*, 1998, Garrido *et al.*, 2007). Important implications of this contradiction relate to the debated role of arc magmatism (*e.g.* Kay & Kay, 1988, Rudnick, 1995, Holbrook *et al.*, 1999, Garrido *et al.*, 2006, Hawkesworth & Kemp, 2006, Lee *et al.*, 2006, Kelemen *et al.*, 2014) and density-sorting processes (Jagoutz & Behn, 2013, Jagoutz & Kelemen, 2015) during the generation and refinement of the continental crust. A better understanding of the genesis, migration and differentiation of arc magmas is thus required, but this is limited by the rarity of exposures of deep arc sections.

This work is dedicated to the characterization of one of the rare worldwide occurrences of arc-related pyroxenites, reported as a kilometre-sized body with individual pyroxenite layers reaching up to 3 m-thick in the Herbeira massif of the Cabo Ortegal Complex, north-western Spain (Girardeau *et al.*, 1989, Girardeau & Gil Ibarguchi, 1991). These pyroxenites have previously been studied and reported in 3 PhD thesis (Ben Jamaa, 1988, Gravestock, 1992, Laribi-Halimi, 1992) and only one recent publication (Santos *et al.*, 2002). These have pointed out the complexity of their petrological and geochemical features relating to a subduction- and/or arc-related environments and a comprehensive understanding of their origin has remained elusive. This work is original in combining detailed structural and textural observations, whole-rock and *in-situ* major- and trace-element compositions and Sr-, Nd-, Hf- and Os-isotope geochemistry, benefiting from the high spatial resolution and high sensitivity of modern analytical techniques. It aims to:

- characterize the different subtypes of pyroxenites;
- evaluate the overprint of sub-solidus reequilibration and fluid-/melt-rock interaction;
- determine a magmatic sequence and the composition of the fluids/melts involved;
- speculate on the nature of their source region;
- add timing constraints to the corresponding processes;
- discuss them within the frame of regional tectonics and global arc magmatism.

For that purpose, this thesis will be articulated as follows:

- **Chapter 1** constitutes a literature review encapsulating some of the scientific contribution from the study of peridotites and pyroxenites, from both the oceanic and continental

lithosphere, with succinct insights from xenoliths and remote geophysical methods. An additional background is provided related to the problematics stated above from the studies of modern and ancient volcanic arcs.

- **Chapter 2** is an introduction to the geodynamics associated with the origin and convergence of the exotic terranes exposed in north-western Iberian complexes. It is mainly related to the opening and closure of peri-Gondwanan oceanic domains, notably the Rheic Ocean, followed by the Variscan orogeny. A more detailed structural and geological description of the Cabo Ortegal complex follows with a particular emphasis on the deformation and metamorphism recorded by its high-pressure units.

- **Chapter 3** reports new detailed field observations from the Herbeira massif of the Cabo Ortegal Complex, where the pyroxenites are exposed. This includes an updated map of the massif, with modest, but significant changes in the main field relationships. The sample collection is also presented and the main lithological types texturally described and illustrated.

- **Chapter 4** reports major- and trace-element compositions for Cabo Ortegal pyroxenites and their main forming minerals, clinopyroxene (cpx), orthopyroxene (opx), olivine, amphibole (amph), spinel (spl) and garnet (grt), also including some peridotites and other subordinate rock types. This section also contains two detailed major- and trace-element profile of heterogeneous pyroxenite samples, reconstructions of bulk-rock compositions, trace-element distribution between the major phases and thermobarometric calculations.

- **Chapter 5** follows on the radiogenic-isotope compositions of a subset of samples selected for being representative of the different lithological subtypes and covering the range of major- and trace-element compositions. Sr, Nd and Hf systematics have been applied to leached and unleached mineral separates of cpx and amphibole, and to whole rocks. A selection of whole-rock samples has also been analysed for Os-isotope compositions along with some chromitites sampled in the Herbeira massif.

- **Chapter 6** discusses the impact of secondary processes such as serpentinization and fluid/melt percolation, and most importantly debates the metasomatic *vs* metamorphic origin of amphibole. Nature and composition of the parental melts of Cabo Ortegal pyroxenites are then discussed along with the extent of melt-peridotite interaction and inferences of these on the nature of their source region and its tectonic implications are envisaged.

- **Chapter 7** is a conclusive chapter where a schematic tectonic model is proposed for the petrogenesis of Cabo Ortegal pyroxenites, along with potential implications of this work.

B. LITERATURE REVIEW

Ophiolites, abyssal and orogenic (alpine[1]) peridotites (massifs), such as those exposed in the Cabo Ortegal Complex, are, with xenoliths, the only sources of rock samples from the lithospheric mantle (**Fig. I. 1**), while remote geophysical methods record physical properties of large mantle domains. These materials have been instrumental in understanding mantle structure and composition since the idea of their mantle origin emerged in the late fifties (*e.g.* Hess, 1962, Thayer, 1969, for orogenic and oceanic peridotites, respectively). Compared with xenoliths, ophiolites and orogenic massifs have the advantage of providing large outcrops that preserve structural features and relationships between igneous ultramafic and mafic rocks. However, most of these massifs represent only the shallowest part of the mantle and are often affected by metamorphism and deformation related to their emplacement (Bodinier & Godard, 2014), or by strong hydrothermal alteration in the case of oceanic peridotites (Baker & Beckett, 1999). On the other hand, xenoliths are only moderately impacted by their travel toward the surface and may provide information on deeper subcontinental mantle sources, but they are sparse and small samples, often fist-sized, and can thus reveal only small-scale features (mineralogy, microstructure, inclusions, etc.) or very large compositional variations between lithospheric provinces (*e.g.* O'Reilly *et al.*, 2001), with poor geometrical information. Both peridotite massifs and xenoliths are also restricted in time: magmas hosting xenoliths in Europe are for instance dominantly Cenozoic whereas ophiolites and ultramafic massifs mostly record Mesozoic events (*e.g.* Coltorti *et al.*, 2010).

Pyroxenites occur in variable amounts in the crustal section of ophiolites (*e.g.* Ceuleneer & Le Sueur, 2008, Clénet *et al.*, 2010) and frequently in greater proportion in orogenic peridotite massifs (*e.g.* Kornprobst, 1969, Conquéré, 1977, Fabries *et al.*, 1991, Pearson *et al.*, 1993, Hirschmann & Stolper, 1996, Garrido & Bodinier, 1999, Downes, 2007, Gysi *et al.*, 2011, Borghini *et al.*, 2013, Bodinier & Godard, 2014, Borghini *et al.*, 2016). They have been interpreted as crystallized melts produced by partial melting of host peridotites (Dickey, 1969, Van Calsteren, 1978) or elongated slices of subducted oceanic crust recycled through mantle convection (Polvé & Allègre, 1980, Hamelin & Allègre, 1985, Allègre & Turcotte, 1986, Kornprobst *et al.*, 1990) but they are commonly believed to represent minerals segregated from upwelling melts in magmatic conduits (O'Hara & Yoder, 1967, Kornprobst, 1969, Frey & Prinz, 1978, Irving,

1 Since the early classification of orogenic peridotites is no longer used (Den Tex, 1969), references are made to Menzies and Dupuy (1991) and Bodinier and Godard (2014), for their peridotite terminology, and to Dilek (2003) and Dilek and Furnes (2011), for their classification of ophiolites.

1980, Loubet & Allègre, 1982, Griffin *et al.*, 1984, Bodinier *et al.*, 1987). The study of orogenic and ophiolitic peridotite massifs has also increasingly highlighted the contribution of other pyroxenite-forming processes and notably melt-peridotite interaction (Kelemen & Ghiorso, 1986, Bodinier *et al.*, 1990, Kumar *et al.*, 1996, Downes, 2001, Downes, 2007, Garrido *et al.*, 2007, Bodinier *et al.*, 2008, Ackerman *et al.*, 2009, Lambart *et al.*, 2012, Borghini *et al.*, 2016).

The next sections aim to provide a brief historical review of what is known about the lithospheric mantle since the discovery of ophiolites and their first modern interpretations. This is

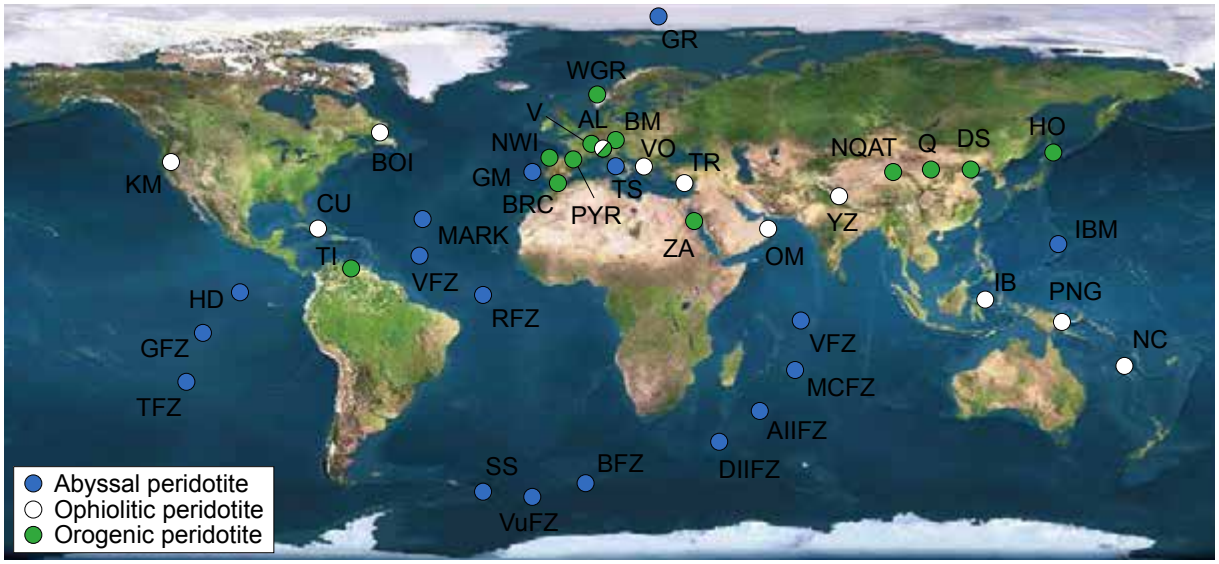

Fig. I. 1. Location of major occurrences of abyssal, ophiolitic and orogenic peridotites (compiled from Bodinier & Godard, 2014). Fast-spreading ridges have been sampled along the East Pacific Rise: Hess Deep (HD), Garret fracture zone (GFZ), Terevaka fracture zone (TFZ). Slow-spreading ridges have been sampled along the Mid-Atlantic Ridge: Kane and Atlantis fracture zones (MARK), Verna and 15°20'N fracture zones (VFZ), Romanche fracture zone (RFZ), and along the Central Indian Ridge: Marie Celeste fracture zone and Green Rock Hill (MCFZ), Verna fracture zone (VFZ). Ultra-slow spreading ridges have been sampled along the American-Antarctic Ridge: Vulcan fracture zone (VuFZ), Bullard fracture zone (BFZ), along the Southwest Indian Ridge: Discovery II fracture zone (DIIFZ), Atlantis II fracture zone (AIIFZ) and in the Arctic Ocean: Gakkel Ridge (GR). Arc basins have been sampled off the South Sandwich Islands (SS), in the Izu-Bonin-Mariana system and in the Tyrrhenian Sea (TS). Continental margins have been sampled in the Galicia margin and Gorringe Bank (GM). Ophiolites occur along the Circum-Pacific Phanerozoic belt (450–0 Ma): in the Klamath Mountains (KM), California, with Trinity and Josephine, in New Caledonia (NC), Papua New Guinea (PNG) and the Indonesian back arc (IB). Occurrences along the Himalaya–Alps–Caribbean Mesozoic belt (150–80 Ma) are Cuba (CU), Semail (OM), Oman and the United Arab Emirates, Troodos (TR), Greece, Vourinos and Pindos (VO), Cyprus, in the Western Alps (WA) with the Internal Ligurides and Lanzo, in Cuba (CU) and the Yarlung Zangbo (YZ) suture zone, China. Ophiolites also occur along the Appalachian–Caledonian belt (450 Ma) as in the Bay of Islands (BOI), Newfoundland and along the Pan-African belt (750 Ma). Orogenic peridotites occur in Europe: in the Bohemian Massif (BM), Czech Republic, Germany, Austria, and Poland; Western Gneiss Region (WGR), Norway, in the Vosges (V) and the Pyrenees (PYR), France, along the Betico-Rifean cordillera (BRC), Spain and Morocco, with Ronda and Beni Bousera, in north-western Iberia (NWI) with Cabo Ortegal and Órdenes, Spain and Bragança, Portugal, and along the Alps (Alpe Arami, Switzerland, Val Malenco, Lanzo and the Ivrea zone, Italy, with Finero, Balmuccia, and Baldissero) and in Liguria (Internal and External Ligurides) – grouped under AL (Alps & Liguria) for clarity. Outside Europe, major occurrences are: Tinaquillo (TI), Venezuela, Horoman (HO), Japan, Dabie–Sulu (DS), Qinling (Q) and North Qaidam-Altyn-Tagh (ANQ), China and Zabargad (ZA) in the Rea Sea, Egypt.

illustrated by geodynamic interpretations of some of the major occurrences of ophiolitic and orogenic peridotite massifs, along with some examples of oceanic peridotites available from core drilling and dredging of the seafloor.

1. Oceanic lithosphere: the concept of ophiolites and its (r)evolution

Ophiolites are exposed remnants of oceanic lithosphere that have been incorporated into continental margins or orogenic belts (Coleman, 1977, Nicolas, 1989). The term "ophiolite", was firstly used in 1813 for describing a suite of igneous rocks in the Apennines (Brongniart, 1821) as an "assemblage of consanguineous igneous rocks in the axial part of geosynclines" (Steinmann, 1927). Hess (1955), then de Roever (1957) and Vuagnat (1964) induced a significant shift in this cogenetic paradigm, leading to the Penrose's definition of the ophiolite model for the oceanic crust, which involves a distinctive and restricted assemblage of mafic to ultramafic rocks and sedimentary cover (Anonymous, 1972). The study of ophiolites has played a major role in the understanding of mid-ocean spreading ridges, and particularly of their magmatic activities (MacLeod & Yaouancq, 2000, and references therein). Studies of modern ocean samples have confirmed strong controls of the rate of magmatic supply and of the thermal structure of the mantle on the architecture of ridges (Dick *et al.*, 2006). This ranges from a Penrose-type oceanic crust in fast-spreading centres to a faulted structure in which the serpentinized mantle is exhumed in the slowest ones. A significant contribution to the model of magmatic chambers in fast-spreading ridges has notably resulted from the study of the Oman ophiolite (*e.g.* Nicolas, 1986), which is considered to have formed in an ancient analogue of the East Pacific Rise (Sinton & Detrick, 1992), whose deep parts are exposed in the Hess Deep (Gillis *et al.*, 2013, Lissenberg *et al.*, 2013).

The implementation by Miyashiro (1973) of trace-element geochemistry to the traditional field and petrographic study of ophiolites questioned the paradigm of new crust being only produced at mid-ocean ridges, raising a long-lasting debate (*e.g.* Gass *et al.*, 1975, Cann, 2003, for a review). Initially based on the calc-alkaline trend of a volcanic suite of the Troodos ophiolite, which turned out to be biased by the FeO*/MgO *vs* SiO_2 representation of those high-SiO_2 lavas, their subduction-related origin is still supported by the association of boninitic and tholeiitic affinities (Pearce & Robinson, 2010). However, the genesis of such magmas at mid-ocean ridges is not excluded (Nonnotte *et al.*, 2005). Since the Troodos ophiolite was one of the best studied of that time and considered as a typical ophiolitic complex (*e.g.* Moores & Vine, 1971), this debate was of major geodynamic significance and eventually led to the definition

of supra-subduction zone (SSZ) ophiolites (Pearce *et al.*, 1984). This evolution of the ophiolite concept is also well illustrated by the studies of the Hellenic ophiolites, as summarized by Rassios and Smith (2000).

Based on this broadened classification of ophiolites (Dilek, 2003), a wide range of tectonic contexts, including various stages of development of magmatic arcs is covered by the definition of SSZ ophiolites (*e.g.* Robertson, 2002, for Mediterranean-type ophiolites). They range from continental back-arc settings, as in the Chilean-type Rocas Verdes ophiolites, Chile associated with early-Cretaceous trench roll-back (Stern & De Wit, 2003), to subduction initiation in the Siluro-Devonian Trinity ophiolite, California (Wallin & Metcalf, 1998), although the tectonic setting associated with the latter remains poorly constrained (Ceuleneer & Le Sueur, 2008, and references therein). In addition, based on the existence of thick portions of arc crust and on tectonic settings implying prolonged subduction that has not resulted in continental collision, volcanic arc Sierran-type ophiolites have been distinguished from other subduction-related ones. Among notable occurrences of these ophiolites in the Pacific Rim, ophiolites of the Philippines archipelago have provided a meaningful timeframe to palaeogeographical reconstruction of the evolution of the Philippines island-arc (Yumul, 2007, and references therein). However, studies of other ophiolites such as Jarbo Gab, in the Smartville arc sequence, Sierra Nevada show that these ophiolites could simply be described as old and heterogeneous portions of oceanic crust that provided a basement for the building of an island arc (Dilek *et al.*, 1990), instead of a distinct type of ophiolite.

Although such classification is debated (Nicolas & Boudier, 2003), it provides a convenient systematic approach of the variety and intricacy of mechanisms involved. The differences between previous petrological and geochemical classifications (Ishiwatari, 1985) and structural classifications (Boudier & Nicolas, 1985) outline the need for combined approaches (Karson, 1998), including associated sediments when available (*e.g.* Pessagno *et al.*, 2000). Moreover, the comprehensive understanding of local igneous processes, and notably the timing of magmatic and volcanic intrusions is critical (*e.g.* Nicolas *et al.*, 1988, Manning *et al.*, 2000). This is illustrated by the case study of the Oman ophiolite, which has been classified as a SSZ ophiolite (Dilek & Furnes, 2011) on the basis of an arc-related generation of seamount-type lavas, as mentioned above, although these might be related to the separation of the ophiolite from its igneous settings (*e.g.* Hacker *et al.*, 1996). Possible fluid contaminations, for instance related to hydrothermal activity near the ridge axis (*e.g.* Benoit *et al.*, 1999, Abily *et al.*, 2011), are summarized by Nicolas and Boudier (2003) as alternative explanations for the arc signature of those lavas.

Nonetheless, MacLeod *et al.* (2013) recently modelled high water concentrations for the Oman Geotimes lavas (*i.e.* significantly higher than that of the East Pacific Rise basalts), which have been so far considered as of the most normal-mid-ocean-ridge-basalt (N-MORB)-like composition. These new results would be consistent with the formation of the whole ophiolite in a hydrous system such as a spreading centre above a subduction zone.

The distinction between mid-ocean ridges and plume-related ophiolites represents another classification issue. Dilek and Furnes (2011) discriminated these based on their distance to the trench and plume (*e.g.* plume-proximal, such as Iceland, or -distal, such as Macquarie Island) and on the basis of trace-element proxies. For instance, on a Th/Yb *vs* Nb/Yb projection, oceanic basalts plotting near the primitive mantle (PM) array (and/or exhibiting garnet signature) are interpreted as related to plume, Caribbean-type ophiolites (Pearce, 2008). However, similarly to volcanic-arc ophiolites, these highly heterogeneous crustal assemblages could be more simply regarded as a portion of oceanic lithosphere, formerly originated in a mid-ocean ridge that has, in this case, evolved into a plateau structure, being thickened by repeated intrusions and eruptions of magmas of plume-head origin (Saunders *et al.*, 1996). Accordingly, Hauff *et al.* (1997) reasonably used "oceanic igneous terranes" instead of ophiolites for describing similar Costa Rican occurrences, although they could fit the Penrose's definition of incomplete ophiolites (Anonymous, 1972).

Finally, another chapter of the (r)evolution of the ophiolite concept may have been taking place for about 30 years with the potential recognition of a mantle process in which shallow sub-oceanic rocks are buried down to the transition zone (> 410 km) and exhumed back to the surface (Yoshikawa *et al.*, 2010, Arai, 2013, McGowan *et al.*, 2015, Griffin *et al.*, 2016). This has been suggested by the increasingly reported occurrence of diamond-bearing chromitites and peridotites in Tibetan (and other) ophiolites, and notably in the Luobosa massif (*e.g.* Bai *et al.*, 1993). Their resemblance to synthetic diamonds has been obscuring their potential significance but the recent discovery of exceptional assemblages of minerals and native elements, associated with genuine natural diamonds, seems to indicate the existence of extremely reducing conditions in deep mantle domains (Dobrzhinetskaya *et al.*, 2009, Howell *et al.*, 2015, Satsukawa *et al.*, 2015, Xu *et al.*, 2015, Griffin *et al.*, 2016).

2. Subcontinental lithosphere: passive margins, subduction zones and orogenesis

While ophiolites are obducted portions of the oceanic lithosphere, orogenic peridotites are classically regarded as remnants of the subcontinental lithospheric mantle (SCLM). Due to its

buoyancy and rigidity, the SCLM has a strong control on the formation, evolution and recycling of the lithosphere and is thus a key for understanding global geodynamics (*e.g.* Griffin *et al.*, 2009). Variation of seismic velocities revealed by tomography have indicated geothermal and compositional variations within the SCLM (Griffin *et al.*, 1999), as well as variations in thickness (O'Reilly & Griffin, 2006). In addition, studies of xenoliths/xenocrysts have evidenced the role played by metasomatic processes in refertilizing the depleted SCLM during the Proterozoic evolution of Archean cratons (*e.g.* Griffin *et al.*, 2003, Simon *et al.*, 2007, O'Reilly & Griffin, 2013).

Emplacement of orogenic peridotites varies with the different orogenic stages, resulting in varying degrees of preservation (Manatschal & Müntener, 2009). They are commonly classified on the basis of their petrological features and on their pressure-temperature trajectory, from their initial environment to their incorporation into continental margins and sutures. However, some occurrences, such as the symplectite-bearing Horoman peridotites (Malaviarachchi *et al.*, 2010), have experienced multiphase evolutions and, again, challenge the classification systematics. Other issues include Ronda and Beni Bousera massifs. These massifs of the Betico-Rifean cordillera bear graphitized diamonds as an evidence of ultra-high pressure conditions (Pearson *et al.*, 1995), but they are dominated by spinel peridotites that were affected by a shallow high-temperature event (Lenoir *et al.*, 2001).

a. Mantle refertilization and exhumation

For clarity, and because they share fairly similar geodynamic significance, ophiolitic and orogenic peridotite bodies are grouped here, although some of them are considered (or debated) as ophiolites, as discussed below.

The actual ophiolites of the Alpine-Apennine orogenic system (the Internal Ligurides) represent exposed remnants of magma-poor margins of the Western Tethys, which is considered as an analogue of the present-day Iberia-Newfoundland rifted margins (Whitmarsh & Wallace, 2001, Robertson, 2007). These so-called ocean-continent transition ophiolites, formerly interpreted as dismembered Penrose-type ophiolites (Manatschal, 2004, Manatschal & Müntener, 2009), are similar to modern slow-spreading ridges such the Mid-Atlantic Ridge (MAR), Southwest Indian Ridge (SWIR) and Gakkel ridge (*e.g.* Liu *et al.*, 2008). They have exhumed portions of lherzolitic mantle associated with N-MORB-like crustal rocks in a Hess-type faulted structure, and generally lack melt-residue relationships, thus providing natural field laboratories to investigate the isotopic disequilibrium between abyssal peridotites and MORB (Rampone *et al.*, 1998, Rampone & Piccardo, 2000, Rampone & Hofmann, 2012). Potential explanations for

this disequilibrium now include the preferential contribution of enriched lithologies during adiabatic partial melting that generates MORB (Salters & Dick, 2002, Byerly & Lassiter, 2014), or the exhumation of abyssal peridotites that experienced ancient partial melting events, unrelated to their current settings (Cipriani *et al.*, 2004, Bizimis *et al.*, 2007, Warren *et al.*, 2009, Stracke *et al.*, 2011). Similarly, it has been recently suggested that slow-spreading ridges may incorporate subcontinental rocks that recorded ancient crust-forming processes prior to the exhumation (McCarthy & Müntener, 2015). Another example is Zabargad peridotite, where isotopic investigations have revealed that the pre-rifting Red Sea mantle experienced ancient subduction-zone processes related to the Pan-African orogeny (Bonatti *et al.*, 1986, Brueckner *et al.*, 1995, Brooker *et al.*, 2004).

Strictly speaking, low-pressure peridotites are lherzolite bodies representing fertile pieces of mantle that were exhumed on seafloor along passive continental margins. They are very abundant in the Alpine chain, and particularly in the Western Alps (Bodinier & Godard, 2014, for a review). However, some of them, notably at Val Malenco, were part of the subcontinental lithosphere prior to the onset of rifting and are still dominated by spinel peridotite facies (Hermann *et al.*, 1997, Müntener *et al.*, 2000); these are considered to be low-temperature end members (*e.g.* Vissers *et al.*, 1991). Others, such as Lanzo, were intruded by gabbros and MORB-like dikes and extensively reequilibrated in the plagioclase peridotite facies (Bodinier *et al.*, 1988, Bodinier *et al.*, 1991); these are considered as high-temperature end-members, and even sometimes as ophiolites. Between these two end members, other occurrences such as Erro-Tobbio or the External Ligurides are transitional (Vissers *et al.*, 1991). Nonetheless, most studies have focused on the mechanisms involved in their exhumation, notably in the Western Tethys (Bodinier *et al.*, 1988), and a model involving normal detachment faults has been notably proposed (Lemoine *et al.*, 1987, Trommsdorff *et al.*, 1993). Such major shear zones indicate the relatively high-temperature evolution of these domains with respect to a stable SCLM. This is due either to thermo-mechanical erosion during asthenospheric upwelling or to the involvement of asthenospheric slices during mantle exhumation (*e.g.* Vissers *et al.*, 1991, Kaczmarek & Müntener, 2008).

Similar geological processes are addressed from the study of intermediate-pressure peridotites. These massifs are generally in the spinel-peridotite facies of either Ariegite (garnet in mafic layers) or Seiland (mafic layers devoid of garnet) subfacies (O'Hara & Yoder, 1967, Obata, 1980). They are mainly located in Europe and Northern Africa, in the Pyrenees (*e.g.* Lherz), along the Betico-Rifean belt (Ronda and Beni Bousera), and in the Ivrea zone of the Italian

Alps (Baldissero, Balmuccia, and Finero), and have been extensively studied as they are believed to preserve features from subcontinental realm that are little obscured by metamorphic reactions (Bodinier & Godard, 2014). Studies of Ronda peridotite have, for instance, evidenced the heating of lithospheric peridotites by asthenospheric upwelling and pervasive melt-rock processes, resulting in a kilometre-scale recrystallization front (Obata, 1980, Van der Wal & Bodinier, 1996, Van der Wal & Vissers, 1996, Garrido & Bodinier, 1999). More recently, Marchesi *et al.* (2013) documented the interaction between these peridotites and melts generated from crustal-derived garnet pyroxenites. Refertilization of spinel peridotite massifs has been also evidenced in the Lherz massif (*e.g.* Le Roux *et al.*, 2007) and in fact, mantle refertilization has now been reported in many modern supra-subduction, suboceanic and subcontinental environments (Hirschmann & Stolper, 1996, Kogiso *et al.*, 2003, Sobolev *et al.*, 2005).

Among other localities outside Europe and Northern Africa, the Tinaquillo lherzolite is known for having provided source material for partial melting experiments of mantle peridotites (Bodinier & Godard, 2014, and references therein).

b. Subduction and deep-mantle processes

High-pressure/ultra-high pressure (HP/UHP) peridotites potentially bear exceptional, yet debated, information on deep mantle processes and subduction dynamics (Brueckner & Medaris, 2000, and references therein). Studies of the Gföhl nappe in the Bohemian Massif (Medaris *et al.*, 2005, Medaris *et al.*, 2006), or the Dabie-Sulu terrane, China (Zhang *et al.*, 2000, Zhang *et al.*, 2011), illustrate the wide range of mantle environments and complexity of depletion-enrichment events potentially occurring above subduction zones. For instance, Sm-Nd (Jamtveit *et al.*, 1991)and Re-Os ages (Beyer *et al.*, 2004) have for instance suggested that garnet peridotites hosted in depleted harzburgites and dunites in the Western Gneiss Region of the Norwegian Caledonides represent the Proterozoic refertilization of an Archean SCLM (Beyer *et al.*, 2006).

Crustal-derived peridotites representing subducted layered ultramafic cumulates (*e.g.* the Fe-Ti peridotites of the Western Gneiss Region, Norway) are distinguished from mantle-derived peridotites (Bodinier & Godard, 2014, for a review). Their wide distribution, among the European Variscides in particular, provide a great insight into the tectonic processes of high-pressure belts (Matte, 1998). Most Alpine and Variscan occurrences of HP/UHP peridotites were emplaced following oceanic subduction, arc-continent collision or continental collision. They are so-called "prograde", such as in the Massif Central Variscides (Gardien *et al.*, 1990), or "HP-HT", such as Nove Dvory-type peridotites in the Gföhl Nappe of the

Bohemian Massif (Medaris *et al.*, 1995, Brueckner & Medaris, 1998), whether they intruded a slab then acquired garnet-bearing assemblages, or were originally garnet peridotites prior to intrusion. The former are characterized by similar prograde metamorphism and structural fabrics with their host garnet-bearing crustal rocks, and synchronous mineral Sm-Nd ages related to the time of subduction (Brueckner & Medaris, 2000). These subduction-related peridotites contrast with "relict" garnet peridotites, which show no subduction imprint, such as that of the Mg-Cr-type garnet peridotites of the Western Gneiss region, Norway (Brueckner & Medaris, 1998, Brueckner & Medaris, 2000). To account for the emplacement of these peridotites, the development of intracratonic fault away from the suture zone has been suggested. Alternatively, high-temperature conditions recorded by some of these peridotites may indicate mantle diapirism leading to their accretion to the cratonic lithosphere (*e.g.* Drury *et al.*, 2001). In this respect, they are similar to ultra-high temperature garnet peridotites, which were once equilibrated at < 1200°C, under spinel-peridotite facies, before reaching the conditions of the garnet-peridotite facies via subduction. Examples includes Mohelno-type peridotites in the Bohemian Variscides (Medaris *et al.*, 1995), and in some regards (*i.e.* the fact that they once experienced high-temperature conditions), Ronda and Beni Bousera.

From a tectonic perspective, the ultramafic massifs of the Cabo Ortegal Complex, and those of other allochthonous complexes of north-western Iberia, can be regarded as prograde peridotite massifs because they share with associated crustal rocks a common metamorphic and deformational history from their intrusion into a subduction zone to their exhumation (*e.g.* Ábalos *et al.*, 2003). When compared with the Bohemian Massif, it appears that they may both be interpreted as a former piece of oceanic lithosphere modified through Palaeozoic subduction zones (Brueckner & Medaris, 2000). Pyroxenites of the Gföhl nappe are dated ca 360 Ma (Jamtveit *et al.*, 1991), which indeed corresponds to the closure of the ocean between Gondwana and Laurussia. Chapter 6 discusses the involvement of arc magmatism during this event fron the perspective of the Cabo Ortegal Complex.

3. Arc magmatism: geochemical characteristics and geodynamic significance

For the purpose of this review, petrological and geochemical constraints are gathered from the extensive literature related to the study of lavas and batholiths in modern island arcs and continental arcs (**Fig. I. 2**), and complemented with geophysical insights and information provided by xenoliths. Studies of rare exposures of ancient arc basements are also reviewed to provide a modest state of knowledge in order to address, notably from the study of the Cabo

Ortegal Complex, the contribution of primitive pyroxenites in the differentiation of arc magmas.

a. Active (or extinct) continental arcs

The American continent provides exceptional laboratories to study continental arc magmatics and dynamics (Ducea *et al.*, 2015, for a review). Active volcanoes are mainly found in Central and South America (the Andes and the Central American Volcanic Arc) but also in North America (*e.g.* Cascades arc), where numerous batholiths have been exhumed from now-extinct arcs along the North America Cordillera (*e.g.* Sierra Nevada batholiths). Such batholiths are also present in South America (Pampean and Famatinian arcs). In addition, the

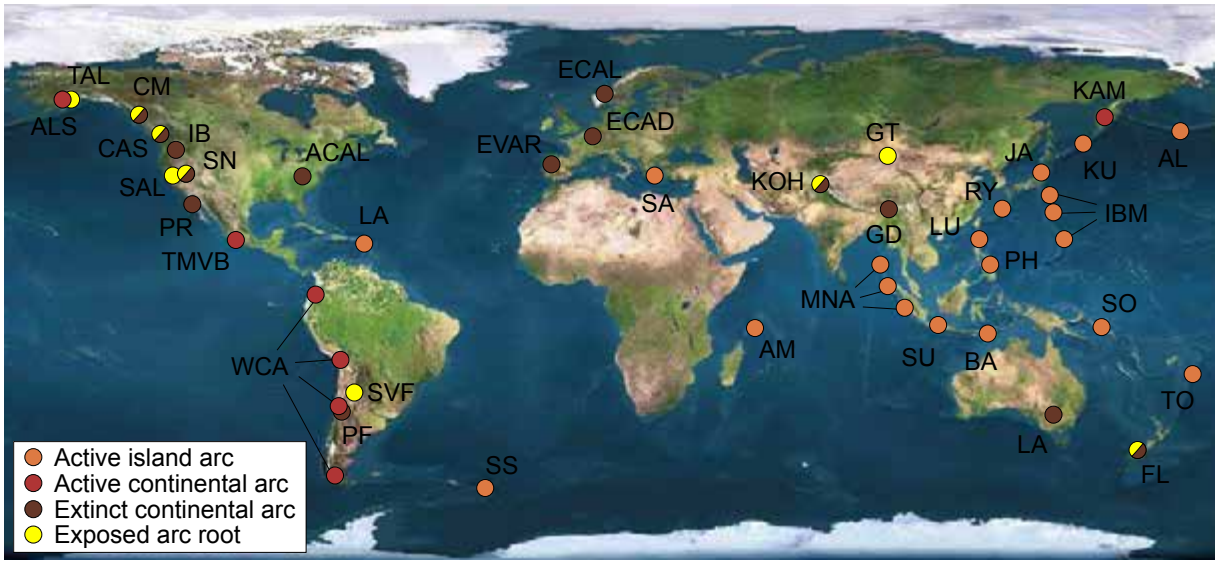

Fig. I. 2. Location of active and extinct continental and (volcanic) island arcs, including the exposures of ancient arc roots (compiled from Ducea *et al.*, 2015, and references therein for continental arcs, and from Leat & Larter, 2003 and McCaffrey, 2009, for island arcs). Active island arcs are mainly in the western Pacific Ocean: the Aleutian Islands (AL), the Kuril Islands (KU), Japan (JA) and Ryukyu Islands (RY), Luzon (LU) and other islands in the Philippines (PH), the Izu-Bonin-Mariana system (IBM), the Solomon Islands (SO) and Tonga (TO) and in the Indian Ocean: Andaman and Nicobar Islands and Mentawai Islands (MNA), and Sunda (SU) and Banda (BA) Islands, Indonesia. Active island arcs exist elsewhere: the South Sandwich Islands, the Lesser Antilles (LA), and the South Aegean (SA). Active continental arcs are mainly in the Americas: the Western Cordillera of the Andes (WCA), the Trans-Mexican Volcanic Belt (TMVB) and the continental extension of the Aleutian Islands on the Alaska Peninsula (ALS). The extension of the Kuril Islands onto the Kamchatka Peninsula (KAM) is the only active continental arc outside the Americas. Remnants of extinct continental arcs are found in the Coast Mountains (CM) from Alaska to British Columbia, in the Cascades (CAS), the Idaho Batholith (IB) and the Sierra Nevada (SN) in western United States of America (USA), the Peninsular Range (PR) in Mexico and along the Pampean-Famatinian belt (PF) from Peru to Argentina. They are found elsewhere in the Himalayan-Karakoram region (Ladhak-Kohistan, LK), in Tibet (Gandese, GD), in eastern Australia (Lachlan), and in Fiordland (FL), New Zealand. In Europe, the Variscan (EVAR), Cadomian (ECAD) and Caledonian belts (ECAL, or ACAL, in the Appalachian) are simplified as discrete symbols for clarity, although they cover large and complex areas. Some of these occurrences also preserve tilted sections of arc root (split symbols). In addition, these are found in the Salinia block (SAL), California, and in the Sierra de Valle Fértil (SVF), Argentina and elsewhere in Talkeetna (TAL), Alaska, Kohistan (LK), Pakistan and India, Gobi-Tianshan (GT), Mongolia, and Fiordland (FL), New Zealand.

Aleutian island arc extends on to the continental Alaska Peninsula. Similarly, the Kuril island arc is prolonged onto the Kamchatka peninsula, which constitutes one of the rare active continental arcs outside the Americas. Many Phanerozoic arcs are also found worlwide such as the Gandese arc, Tibet, the Lachlan arc, Australia and Variscan arcs throughout Europe. The preservation of exposed Precambrian arcs is however very limited due to orogenic reworking.

Continental arcs mainly differ from intra-oceanic (island) arcs in having a thick continental crust acting as a physical, chemical and thermal filter and adding a secondary source of potential crustal geochemical signature, in addition to subducted sediments. While primitive mantle melts are much less frequently found here than in island arcs (*e.g.* Gill, 1981, Grove *et al.*, 2012), primitive high-Mg# andesites are only common in continental arcs suggesting that their genesis may be related to specific intracrustal differentiation (Kelemen *et al.*, 2014, for a review). As detailed above, subduction-derived magmatism is systemically driven by dehydration reactions in the down going slab, whether the upper plate is oceanic, continental, or transitional (Gill, 1981). Wet peridotite melting then produces basaltic melts, or when melt generation occurs under specific conditions (at shallow depths particularly), basaltic andesites or high-Mg#[2] andesites (Kelemen, 1995, Müntener *et al.*, 2001). Following this, the distinction between primitive basalts and andesites could depend on the relative proportion of mantle wedge- *vs* slab-derived melts (Kelemen *et al.*, 2014).

Major-element composition of continental arcs ranges between that of island arcs (particularly for extensional arcs) and that of the upper continental crust (for mature compressional arcs). Their architecture includes a 2-4 km-thick volcanic edifice, 20-30 km-thick, vertically-structured batholiths, and a horizontally-structured arc root. Virtually no compositional difference exists between volcanoes and their batholitic counterparts, indicating no crustal filter fractionating the arc crust (Ducea *et al.*, 2015). The root is composed of mafic magmas differentiated into garnet-, pyroxene-, amphibole-rich cumulate/residue ("arclogites" of Lee *et al.*, 2006) from which more felsic material are derived, and lesser amounts of pre-existing residual crust. The average root composition is less silicic than average mantle peridotites and corresponds to materials that are at least 0.15 g/cm^3 denser than peridotite (Hacker *et al.*, 2003). From both geochemistry and mass balance calculation, it is required that these arclogites are delaminated (*i.e.* convectively removed), and probably so by progressive entrainment of small bodies beneath the arc (Currie *et al.*, 2015). As discussed below, this accounts for the absence of feldspar-free residue in the lower arc crust and balances out the shortening estimates that

2 Molar ratio Mg/(Mg+Fe^{2+})

would otherwise imply a lithosphere thickness exceeding the depth of the slab interface (Ducea & Barton, 2007).

b. Modern island arcs

Active island arcs are numerous in the western Pacific Ocean and the Philippine sea (*e.g.* Japanese archipelago, Izu-Bonin-Mariana system, Solomon Islands, New Hebrides and Tonga arcs), but also around the Indian Ocean, in the Indonesian region (Sunda and Banda arcs) and in the Caribbean (the lesser Antilles). Oceanic crust subducted under island arcs mostly originates at back-arc spreading centres and, for instance in the Pacific Ocean, only the Aleutian Islands override mid-ocean-ridge-derived crust (Leat & Larter, 2003).

Because of the absence of thick crust acting as density filter, island-arc magmas can reach near-surface levels with limited contamination from the overriding crust. Their composition is thus derived from primary mantle melts generated from flux melting of peridotite. As mentioned above, primitive andesites are rare in island arcs, with the notable exception of the Aleutian arc, indicating that they may be locally derived from primary andesitic melts (Kelemen *et al.*, 2014). However, the major-element composition of primary arc melts is debated due to our limited understanding of the ability of primitive melts to reach shallow crustal levels and of the extent of melt differentiation. Assuming high-Mg primary melts (*e.g.* basalt with 12 wt % MgO), an important corollary to the production of low-Mg basalts (*i.e.* < 8 wt % MgO) by fractional crystallization is the existence of significant amounts of mafic and ultramafic cumulates at depth. Lower crustal layers with high P-wave velocities (~ 7 km/s) detected seismically within the Aleutian arc (Holbrook *et al.*, 1999) and the Izu-Bonin-Mariana system (Suyehiro *et al.*, 1996, Takahashi *et al.*, 2007) may indicate the presence of such cumulates.

Island arcs have been geochemically divided in two groups (Hawkesworth *et al.*, 1993). Typical island arcs such as Tonga, Mariana, South Sandwich and Aleutian have homogeneous radiogenic-isotope compositions, relatively similar to MORB. Other arcs such as Banda, Java, Philippines and the lesser Antilles have a more continental signature, similar to continental arcs. They have more radiogenic Sr and Pb, less radiogenic Nd and Hf, greater light (LREE)/heavy-rare-earth elements (HREE) and lesser large-ion lithophile elements (LILE)/high-field-strength elements (HFSE). Understanding the origin of this continental signature is critical to estimating the extent of crustal production and recycling (Davidson & Arculus, 2006). By doing so, two main slab components have been recognized:

- the percolation of aqueous fluids produced from dehydration of serpentinized basalts,

which leads to enrichment of highly fluid-mobile elements and results in high Ba/Th, B/Be and Cs/Rb (Ryan *et al.*, 1995, Elliott *et al.*, 1997, Turner & Hawkesworth, 1997, Peate & Pearce, 1998);

- the contribution of partial melts from sediments carried with the slab, as indicated by high LREE/HREE and LILE/HFSE (*e.g.* Th/Nb) and continental Sr- and Nd-isotope signatures (Turner *et al.*, 1996, Elliott *et al.*, 1997, Class *et al.*, 2000, Macpherson *et al.*, 2003). The contribution of partial melts from subducted basalts (adakites) has also been noted, but only as a minor component (*e.g.* Bédard, 1999).

c. Exhumed arc roots

Several sections of ancient arc roots are exposed, mainly from continental arcs, along the western coast of North America, Argentina and New Zealand (Ducea *et al.*, 2015, for a review). A transitional arc section (Gobi-Tianshan) is also exposed in Mongolia (Economos *et al.*, 2012). Worldwide occurrences of arc-related mid-crustal plutonic complexes have been reviewed by Kelemen and Ghiorso (1986). Potential arc-related mantle fragments have also been reported (*e.g.* Xiong *et al.*, 2014). However, in addition to the incomplete section of the Bonanza arc exposed on Vancouver Island (DeBari & Greene, 2011), only two complete tilted sections preserv-

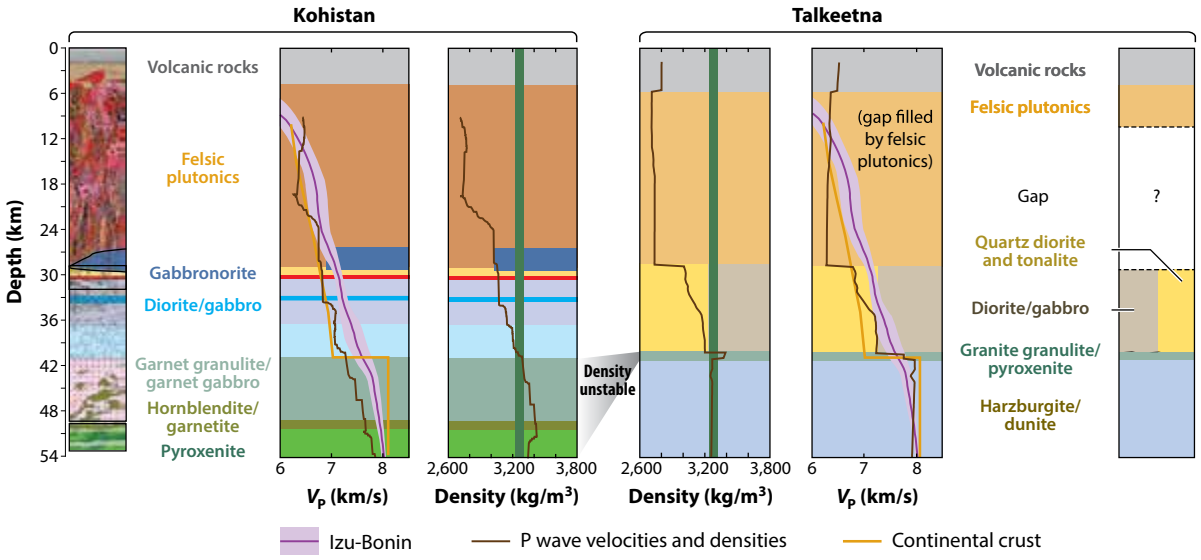

Fig. I. 3. Schematic illustrations of the lithological, seismic, and density properties of the exposed Kohistan and Talkeetna arc sections (modified from Jagoutz & Behn, 2013). Dark brown lines are calculated averages of seismic P wave velocities (Vp) and densities of the main crustal blocks, compared with seismic profiles from continental crust and the Izu-Bonin arc. The dark green vertical bands represent the density of mantle peridotite at 1.5 GPa. The igneous crust-mantle transition is sharply defined in Talkeetna, ressembling continental crust. By contrast, the seismic profile beneath Kohistan resembles that of modern island arcs such as Izu-Bonin. Note the small amount of density-unstable rocks preserved in Talkeetna. Filling of the mid-crustal gap by felsic plutonic corresponds to the model A of Jagoutz & Kelemen (2015).

ing island arc roots have been recognised to date: the Kohistan and Talkeetna arcs (**Fig. I. 3**).

The Jurassic Talkeetna arc is exposed in South Central Alaska, from the Tonsina region along the Kenai and Alaska Peninsulas. Its igneous crust is ~ 40 km-thick (DeBari & Coleman, 1989, Hacker *et al.*, 2008), with 5-9 km of basaltic to rhyolitic volcanics. Their major- and trace-element composition is nearly identical to that of mid-crustal igneous rocks, which probably excludes the cumulate origin of the latter (Jagoutz & Kelemen, 2015). However, gabbros and diorites that are found at deeper crustal level represent the complementary cumulates of the lavas (Greene *et al.*, 2006). Near the base of the igneous crust, a few hundreds of meters of plagioclase-free pyroxenites (websterites, orthopyroxenites, clinopyroxenites and olivine clinopyroxenites) with high Mg# (0.90-0.92) are sandwiched by gabbros and mantle harzburgites. They represent 1 % of the igneous section while > 25 % of cumulates with Mg# between 0.85 and 0.90 are expected from petrologic models (Greene *et al.*, 2006) and mass-balance calculations (Kelemen *et al.*, 2014). Knowing that uncertainty related to missing exposures does not affect the deep part of the section, gravitational instabilities that may follow densification processes, are suggested to account for these missing cumulates (*e.g.* Jull & Kelemen, 2001, Müntener *et al.*, 2001). Besides, old crust representing pre-arc basement is strikingly missing from the exposed section (Rioux *et al.*, 2007, Rioux *et al.*, 2010), potentially due to its extensional removal.

The Cretaceous to Eocene Kohistan arc is exposed in Northern Pakistan. It consists of a 26 km-thick batholith and 4-6 km-thick of basaltic to rhyolitic volcanics with an average composition remarkably similar to the those of the Talkeetna arc (Jagoutz & Schmidt, 2012). Gabbronorites and diorites associated with tabular bodies of dunites, pyroxenites, troctolites are found at mid-crustal level (Jan *et al.*, 1992, Khan *et al.*, 1993). The lowermost crust consists of increasingly mafic rocks down to the Jijal ultramafic complex. Their origin is still debated as potential mantle sequences (*e.g.* Burg *et al.*, 1998) or crustal cumulates (*e.g.* Khan *et al.*, 1993). Formation of these mid- and lower-crustal units probably followed two distinct lines of descent (*i.e.* dry and wet) from primitive basaltic magmas, which has been interpreted as resulting from the multistage evolution of the arc (Dhuime *et al.*, 2007, Garrido *et al.*, 2007, Jagoutz *et al.*, 2011). The absence of old continental basement suggests, in agreement with paleomagnetic data (Khan *et al.*, 2009), that the Kohistan (like the Talkeetna) arc formed within an oceanic domain, in this case intra-Neotethys, during the subduction of the Indian plate under Asia (Bard, 1983). However, it is isotopically more enriched than the Talkeetna arc, perhaps due to the existence of a MORB component and/or recycled sediments in the mantle source, comparable

to what is observed in the Izu-Bonin-Mariana system.

In addition, many ophiolites referred to as SSZ ophiolites have been affected to some extent by arc magmatism, as detailed above. A noteworthy example is the Trinity ophiolite exposed in the Klamath Mountains, which constitutes the largest (3000 km^2) and best preserved mafic-ultramafic body cropping out in California. The tectonic setting associated with this ophiolite is still debated but its association with arc-derived volcano-sedimentary formations has led to a consensus on its arc-related oceanic origin (Lindsey-Griffin, 1977, Coleman, 1986, Lapierre *et al.*, 1986, Wallin & Metcalf, 1998). A recent study notably suggested the evolution of a marginal back-arc basin to account for the association of fertile mantle peridotites and boninitic cumulates (Ceuleneer & Le Sueur, 2008), but once again the cogenecity of mantle and crust remains problematic due to inherent difficulties of dating mantle rocks.

d. Continental crust-making factories?

How continental crust has been produced and recycled through time is a major issue of modern Earth sciences (Roberts *et al.*, 2014, for a review). Assuming that there is presently little crustal growth, it can be reasonably expected that there was a greater production rate in the past, potentially due to higher heat flow and the generation of mantle-derived silicic melts (*e.g.* Rudnick, 1995). It is indeed estimated that at least 50 % of the continental crust was present by the end of the Archean (Taylor & McLennan, 1995) although our limited knowledge of the present composition and structure of continents (*e.g.* underestimated masses of relict Archean lithosphere and ultramafic plutonic rocks) might question the models of crustal growth altogether (Griffin *et al.*, 2009, O'Reilly *et al.*, 2001).

Two main contrasting views exist for continental formation during the Archean: modern-like (horizontal) plate tectonics (*e.g.* Kerrich & Polat, 2006) and (vertical) non-plate tectonics (Bédard, 2006, Hawkesworth *et al.*, 2010, for a review). The latter questions the uniformitarian paradigm although these views are not mutually exclusive (*e.g.* Van Kranendonk *et al.*, 2007). Among them, the petrogenesis of tonalite-trondhjemite-granodiorite (TTG) intrusive suites suggests the growth of Archean continental crust in island arcs (Polat, 2012). Higher degrees of melting may have resulted in thicker island arcs and buoyant oceanic lithosphere and thus allowed for their preservation and accretion (Condie & Kröner, 2013). The contribution of oceanic plateaus is also suggested (Van Kranendonk *et al.*, 2015).

By contrast, post-Archean island arcs have been mostly subducted and thus make up less than 10 % of accretionary orogens whereas continental arcs compose 40–80 % of these orogens

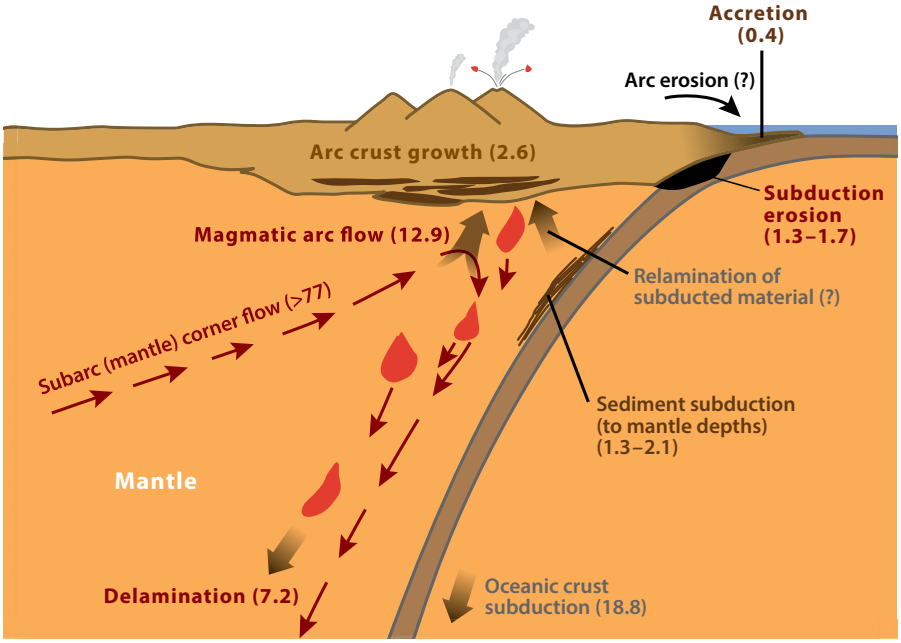

Fig. I. 4. Mass fluxes (km^3/yr) related to arc magmatism and, among others, density-sorting processes (delamination and relamination) in a subduction zone, as constrained by Jagoutz and Schmidt (2013). Modified after Jagoutz and Kelemen (2015).

(Condie & Kröner, 2013). This suggests that continental arcs have probably been the major factory of continents in post-Archean times. Accordingly, the average andesitic to dacitic composition[3] of the continental crust is similar to that of mature continental arcs, which contrasts with the basaltic composition of modern primitive arc magmas. Either of these compositions needs to be revised and/or additional mechanisms should be envisaged to transform basaltic mantle-derived melts into andesitic material (*e.g.* DeBari & Greene, 2011, Jagoutz & Kelemen, 2015).

The main hypothesis for refining a felsic crust from a basaltic input (*i.e.* < 52 wt % SiO_2 with Mg# > 0.65) consists of intracrustal differentiation, followed by convective removal of dense mafic and ultramafic residue (Kay & Mahlburg Kay, 1993). Such foundering has been seismically evidenced in the Sierra Nevada arc root (Boyd *et al.*, 2004, Zandt *et al.*, 2004). It is also supported by the gap in Mg# between less dense gabbronorites and denser pyroxenites and garnet granulites observed in both the Talkeetna and Kohistan arcs. However, Kelemen and Behn (2016) recently noted that the trace-element composition of lower continental crust, as inferred from the average compositions of continental granulites, is very different from that of the lower crust of the Kohistan and Talkeetna arcs, even after correcting for the effect of

3 Estimates range between 0.45 to 0.66 wt % SiO_2 with Mg# between 0.43 and 0.57 (Christensen & Mooney 1995; Kelemen 1995; Rudnick & Fountain 1995; Rudnick & Gao, 2003).

delamination. Relamination of buoyant arc material, either following subduction erosion or arc-arc/continent collision, may therefore be required to explain the composition of the lower continental crust (Hacker *et al.*, 2011, Kelemen & Behn, 2016). The role of these density-sorting processes is summarized in **Fig. I. 4**.

Prior to such root-removal concepts, it was postulated that island arcs were the main factories of continental crust (Taylor & McLennan, 1985), because low Sr/Y, low La/Yb and negative Eu anomalies recorded in continental sediments are absent in young continental arcs but found in island arcs, due to their relatively shallow depth of fractionation (Ducea *et al.*, 2015). In addition, at pressures exceeding 0.8 GPa and high water content prevailing beneath arcs (including island arcs), it is predicted from experiments that significant amounts of plagioclase-free ultramafic cumulates are produced (Müntener *et al.*, 2001, Müntener & Ulmer, 2006). Thus, assuming that it corresponds to the plagioclase-saturation boundary, this implies that the seismic Moho may be significantly shallower than the depth of the igneous crust, which obviously questions the compositional estimates of the igneous arc crust. If temperatures > 700°C are sustained for more than 10 million years, such cumulates, which are denser than residual peridotites due to their higher Fe/Mg, would be unstable. Assuming greater temperatures at Moho depths (*e.g.* Zhao *et al.*, 1992), even cumulates less than 1 km-thick could delaminate in less than 1 Ma as a near steady-state process (Jull & Kelemen, 2001). An important corollary is that the Moho may represent a delamination feature, as developed by Tatsumi *et al.* (2008) and DeBari and Greene (2011) from the study of active arcs and exposed arc sections, respectively.

Chapter II.

Geodynamic and Geological Background

A. GEODYNAMIC CONTEXT OF NORTH-WESTERN IBERIA

Following modern plate-tectonic considerations over 30 years (*e.g.* Matte, 1986, Matte, 1991), relict oceanic domains separating the Palaeozoic continents have been found in the north-western Iberian Peninsula (**Fig. II. 1**). They are regarded as the remnants of a rootless suture located in the hanging wall of a thrust system, which constitutes the hinge of the Ibero-Armorican Arc, an oroclinally folded section of the Variscan (Hercynian[1]) belt (Ries & Shackleton, 1971, Matte, 1986, Martínez Catalán *et al.*, 2009, Díez Fernández *et al.*, 2013). Five allochthonous complexes

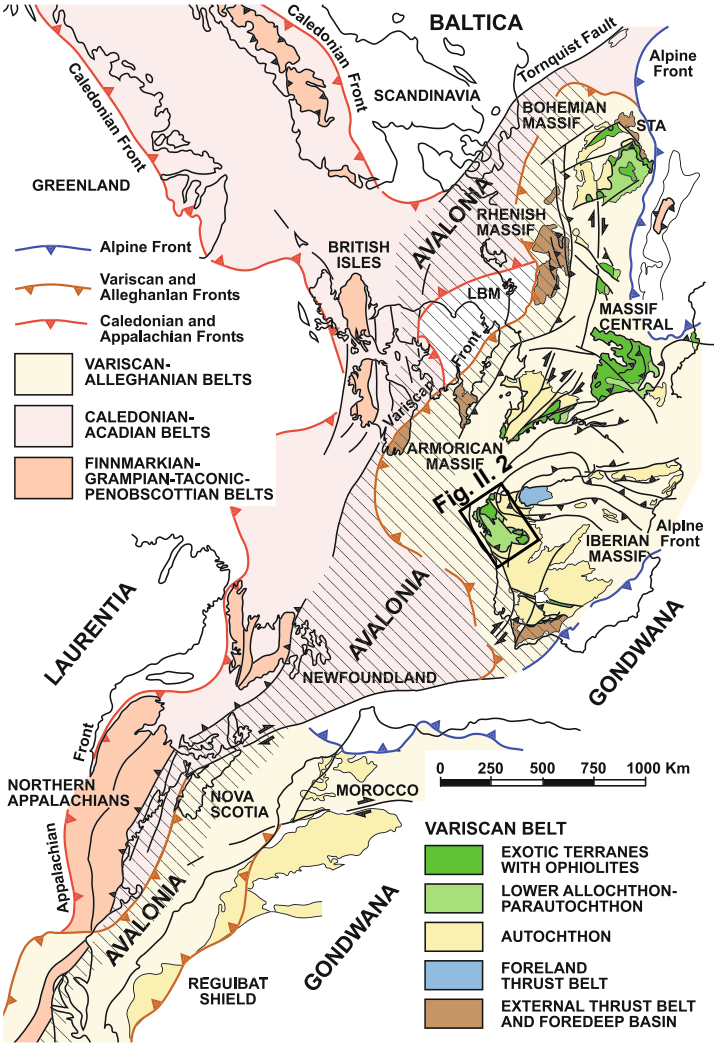

Fig. II. 1. Location of the Iberian Massif and other European Variscides, within the Variscan belt during the Palaeozoic convergence (after Martinez Catalan *et al.*, 2009, and references therein).

1 Hercynian is here used as a synonym of Variscan although it is sometimes specifically used to refer to Variscan orogenies in Europe. Historically, both terms were originally used to describe opposite strike descriptions by German geologists of the 19th century.

are located in the axial zone of this belt: Cabo Ortegal, Malpica-Tuy and Órdenes in Spain, Bragança and Morais in Portugal (**Fig. II. 2**).

The different complexes consist of various nappes of dismembered meta-sedimentary and meta-igneous terranes, whose subdivisions are correlated into three main units (Arenas *et al.*, 1986): (1) the Upper Allochthon, representing fragments of a Cambro-Ordovician ensialic[2] island arc (Santos Zalduegui *et al.*, 1996, Fuenlabrada *et al.*, 2010), (2) an intermediate Ophiolitic

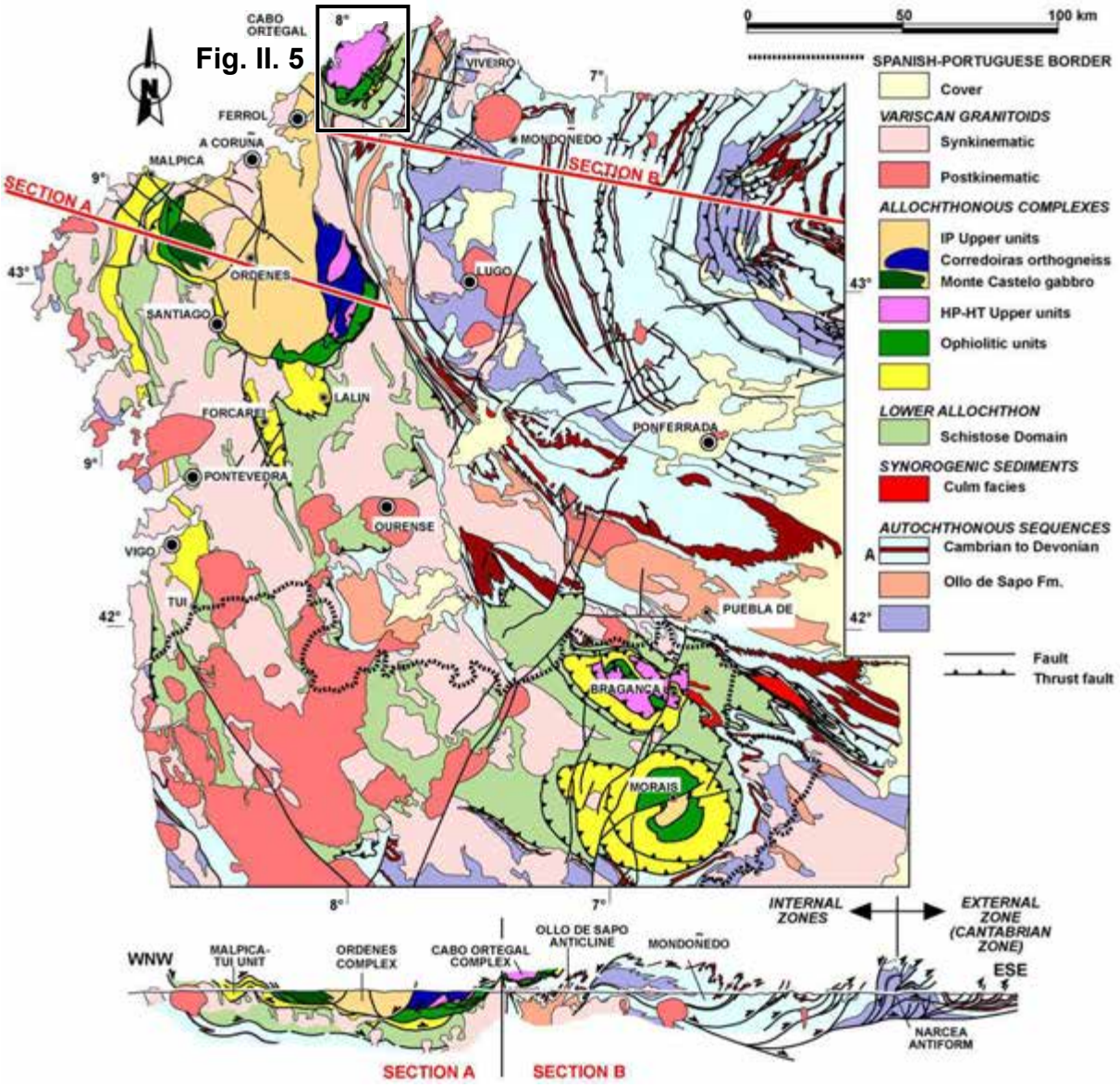

Fig. II. 2. Geological map and cross sections of north-western Iberia (modified after Dallmeyer *et al.*, 1997 by Martinez Catalan *et al.*, 2009) showing the location of the Cabo Ortegal Complex (**Fig. II. 5**).

2 Ensialic indicates an origin or occurrence in or on sialic material, that is derived from the continental upper crust. In the present case, ensialic island arcs are formed on passive continental margin as opposed to ensimatic island arcs formed within oceanic domains (Frisch *et al.*, 2010).

Unit preserving remnants of oceanic domains with various Palaeozoic ages (Díaz García *et al.*, 1999, Pin *et al.*, 2006, Arenas *et al.*, 2007a, Sánchez Martínez *et al.*, 2007, Sánchez Martínez *et al.*, 2011), and (3) the Basal Unit representing part of the distal Gondwanan margin (Santos Zalduegui *et al.*, 1995, Martínez Catalán *et al.*, 1996, Díez Fernández *et al.*, 2011). They overly the parautochthon (or Lower Allochthon), also described as the Schistose Domain of Galicia-Trás-os-Montes and, at the base of the pile, the Iberian Autochthon or Central Iberian Zone (**Fig. II. 2**). This intercalation of thrust sheets of HP metamorphic rocks and ophiolites, also including mélanges (*e.g.* Arenas *et al.*, 1986, Albert *et al.*, 2012), is a characteristic feature of supra-subduction zones, whether (Mediterranean-type ophiolites) or not (Franciscan-type) trench-continent collision led to tectonic emplacement on continental margins as it is the case here (Dilek & Furnes, 2011)

1. Peri-Gondwanan arc magmatism and Gondwanan-Laurussian convergence

The absence of Alpine-related strike-slip faults in north-western Iberia has allowed for a particularly detailed tectonic reconstruction of the Gondwanan-Laurussian convergence. Pre-Variscan and Variscan orogenic events recognized here are also recorded in the Armorican, Massif Central and Bohemian massifs (**Fig. II. 1**). These constitute the European Variscides, which result from the collision of northern Gondwana with eastern Avalonia and Baltica (**Fig. II. 3**).

Cambro-Ordovician arc magmatism on the Gondwanan margin facing the Tornquist (or possibly the Iapetus) Ocean is suggested by detrital zircons derived from the West African craton (Santos Zalduegui *et al.*, 1995, Albert *et al.*, 2014, Roper, 2016). In the Iberian Autochthon, thick sedimentary sequences due to high rates of subsidence and the voluminous volcanics of the Ollo de Sapo formation recorded early-Ordovician extension (**Fig. II. 3**). This reflects continental rifting and the separation of the ensialic arc from the Gondwanan margin (**Fig. II. 4**), as also recorded by terrigenous metasediments and igneous rocks in the Lower Allochthon (Pin *et al.*, 1992).

2. The Rheic Ocean

Among the European Variscides, the existence of the Rheic Ocean suture is best recognized in north-western Iberia (Murphy *et al.*, 2011), and particularly in the Órdenes Complex (Arenas, 2015), where the range of ages of the ophiolitic units is similar to the span of life of the Rheic Ocean (Winchester *et al.*, 2002). However, two main groups can be distinguished: meta-igne-

ous rocks of late-Cambrian ages and gabbroic rocks of middle-Devonian ages, which suggests that their generation may not be explained by the evolution of a single oceanic domain. They thus not only provide information about the Rheic Ocean (Arenas, 2015), but potentially also about pre-Ordovician, peri-Gondwana oceanic domains (**Fig. II. 4**). Bazar ophiolite may for instance represent a relic of the Iapetus-Tornquist Ocean (Sánchez Martínez *et al.*, 2012).

Back-arc birth of the Rheic Ocean was recorded by ophiolites dated back to 497-495 Ma, and including pelitic and siliceous sediments in tectonic contact with serpentinized ultramafic (Arenas *et al.*, 2007b). Early-Devonian remnants of supra-subduction oceanic crust are found

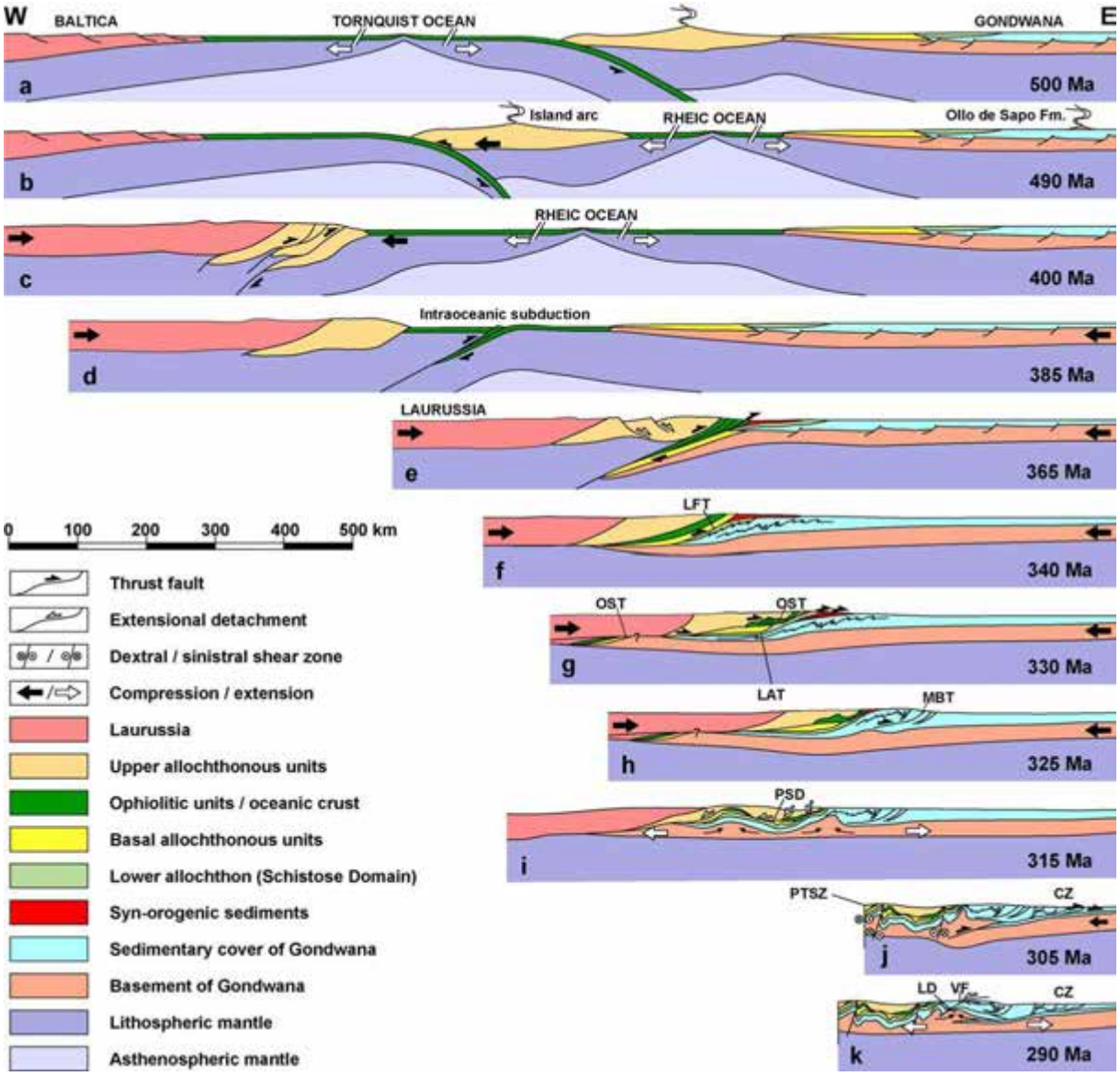

Fig. II. 3. Tectonic evolution of the different structural units exposed in north-western Iberia (modified after Martinez Catalan *et al.*, 2007 by Martinez Catalan *et al.*, 2009). CZ: Cantabrian Zone; LAT: lower Allochthon thrust; LD: Lugodome; LFT: Lalín-Forcarei thrust; MBT: Mondoñedo basal thrust; OST: out-of-sequence thrusts; PSD: Pico Sacro detachment; PTSZ: Porto-Tomar shear zone; VF: Viveiro fault.

in Careón ophiolite of the Órdenes Complex (Díaz García *et al.*, 1999, Sánchez Martínez *et al.*, 2007) and in the Morais-Talhinhas Unit of the Morais Complex (Pin *et al.*, 2006). They indicate intra-oceanic subduction associated with the closure of the Rheic Ocean, in agreement with HP metamorphism recorded in the Lower Allochthon. Final closure was marked by the development of an accretionary wedge resulting in progressive younging of metamorphic ages from

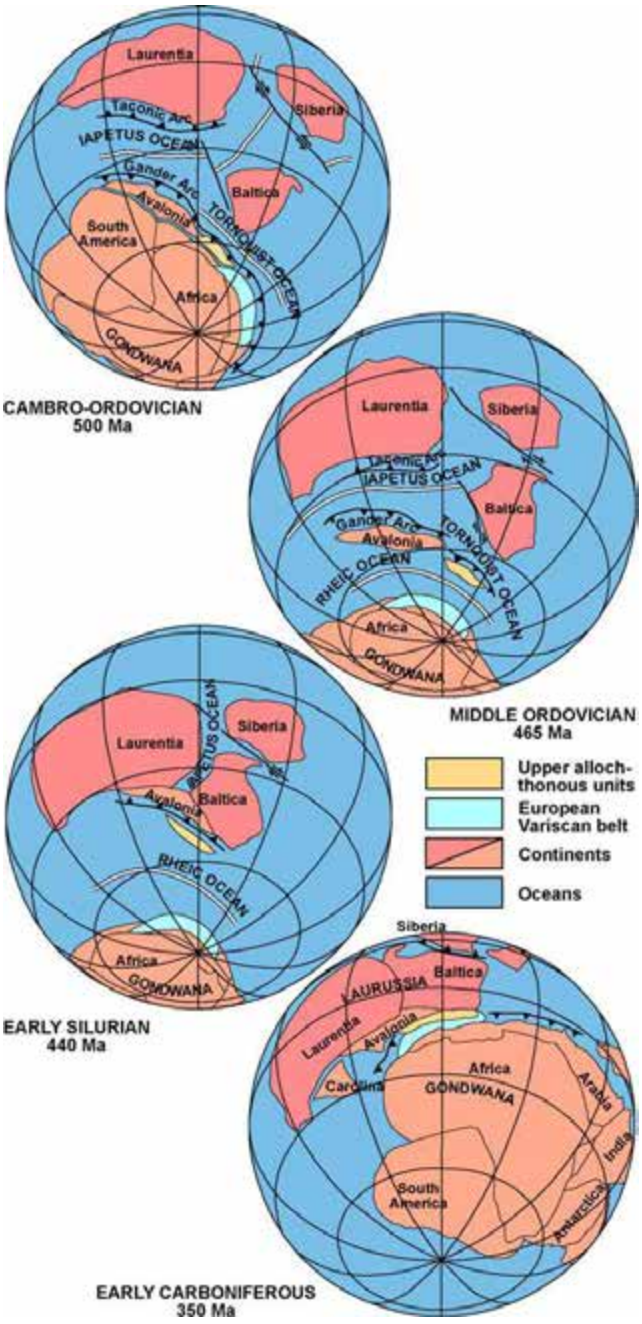

Fig. II. 4. Distribution of the Palaeozoic continents and location of the European Variscides and of the ensialic arc exposed in the upper allochthonous units of the Iberian Massif (modified after Gómez Barreiro *et al.*, 2007 and Winchester *et al.*, 2002 by Martinez Catalan *et al.*, 2009).

the top to the bottom of the allochthonous units (Martínez Catalán *et al.*, 2009, and references therein). This scenario is regarded as a strong evidence for the absence of normal mid-ocean ridge spreading in this part of the Variscan belt (Gómez Barreiro *et al.*, 2007), although the Ize-da-Remondes ophiolite of the Morais complex is still an exception to that rule (Pin *et al.*, 2006). However, new U-Pb and Lu-Hf zircon data from the Purrido (Sánchez Martínez *et al.*, 2011) and Moeche (Arenas *et al.*, 2014b) ophiolites yielded evidence for old continental crust in the source of their mafic rocks, questioning altogether the presence of a true Rheic Ocean suture in north-western Iberia (Nance *et al.*, 2010, for a review).

3. Variscan collision

The first manifestations of the subduction-related Variscan collision are dated at ca. 380 Ma and correspond to the thrusting of hot oceanic lithosphere (Santos Zalduegui *et al.*, 1995, Díaz García *et al.*, 1999) but the Variscan orogeny *sensu stricto* began with the onset of the collisional regime[3] during the Carboniferous (**Fig. II. 3**). Shortening of the orogenic edifice occurred via recumbent folding (D_1) until the continental subduction became locked against Gondwana, propagating recumbent folds inland, then large thrusts (D_2). This episode of crustal thickening dismembered the suture and led to the stacking and emplacement of the allochthonous complexes (Gómez Barreiro *et al.*, 2007). Gravitational extension then led to the loss of orogenic root due to partial melting. Upright folding (D_3) associated with this extensional collapse further contributed to the rootless character of the suture (Martínez Catalán *et al.*, 2009).

3 Deformation episodes D_1, D_2 and D_3 are here defined regionally from the onset of the Variscan collision and with respect of the Gondwanan margin. They are therefore not directly related to the deformation episodes (D_{1-4}) defined below for the subduction and exhumation of the allochthonous units of the Cabo Ortegal Complex.

B. GEOLOGY OF THE CABO ORTEGAL COMPLEX

This section introduces the different structural units of the Cabo Ortegal Complex and describes their main geological features with respect to regional geodynamics. For the sake of this study, it mainly focusses on the allochthonous units, where the ultramafic massifs belong. Their subdivisions are described structurally from the bottom to the top.

Parts of the two uppermost units constitute most of the Cabo Ortegal Complex (Vogel, 1967, Bastida *et al.*, 1984, Marcos *et al.*, 1984, Arenas *et al.*, 1986, Sánchez Martínez *et al.*, 2011): the Upper Allochthon and the Ophiolitic Unit (**Fig. II. 5**). At the base of the pile, the Basal Unit is poorly exposed, associated with a frontal serpentinized mélange. They overly the thick meta-sedimentary and volcanic series of the Lower Allochthon, which is not included in the allochthonous complexes because of its resemblance to the autochthonous sequences of the Central-Iberian Zone, and for not being exotic in nature.

1. Basal units and tectonic mélange

The Somozas Mélange, firstly described as a fragmented ophiolite (Arenas, 1985), is to date the only tectonic mélange of the Iberian Massif (Marcos *et al.*, 2002). It is a typical serpentinites mélange where a mantle wedge was involved in a mixing unit, structurally located at the base of the exotic terranes (here cutting the contact between the Basal Unit and the Ophiolitic Unit at high angle). It consists of igneous rocks mixed with serpentinites, of meta-phyllites and -phyllonites with scarce conglomerates, marbles and quartzites and of HT metamorphic rocks, with various types of amphibolites and orthogneisses. These three rock assemblages represent former pieces of the subducted Gondwanan margin, including peri-Gondwanan volcanic arcs and ultramafic rocks involved in the closure of the Rheic Ocean and final accretion (Arenas *et al.*, 2009, Novo-Fernández *et al.*, 2016).

The Espesante unit represents the Basal Units in the Cabo Ortegal Complex (**Fig. II. 5**). It consists of felsic orthogneisses, amphibolites and retro-eclogites, and is interpreted as a fragment of the most external Gondwanan margin, subducted below the orogenic wedge. This unit thus records the latest Variscan deformation of the Gondwanan margin in Europe, associated to the final stages of the Pangea assembly (Arenas *et al.*, 1995, Martínez Catalán *et al.*, 1996, Arenas *et al.*, 1997).

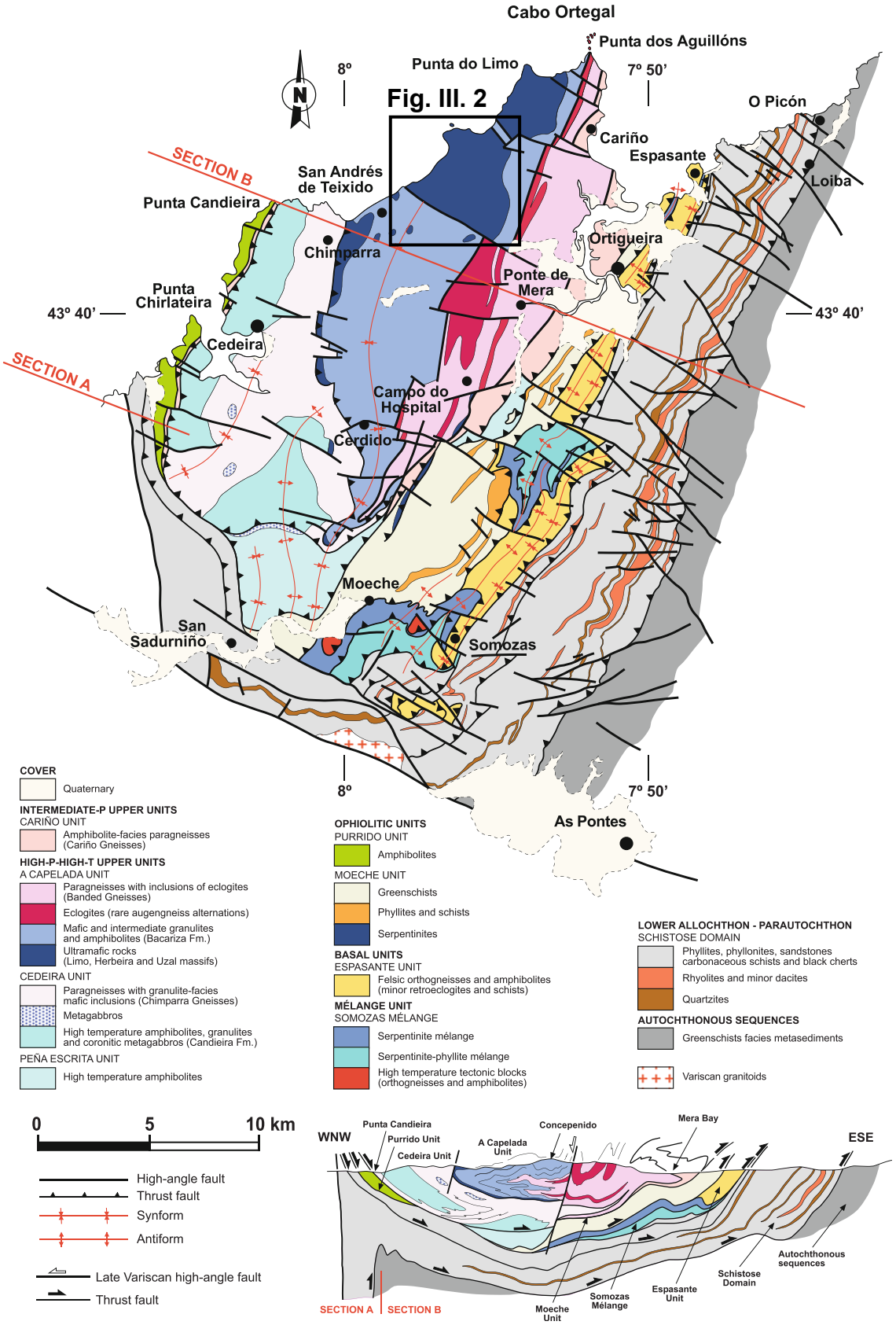

Fig. II. 5. Geological map and cross section of the Cabo Ortegal Complex (modified after Vogel, 1967, Marcos *et al.*, 1984, Arenas *et al.*, 1986 and 2009 by Arenas *et al.*, 2014) showing the location of the Herbeira massif (**Fig. III. 2**).

2. The Ophiolitic Unit

The Ophiolitic Unit of the Cabo Ortegal Complex includes Purrido (Sánchez Martínez *et al.*, 2011) and Moeche (Arenas *et al.*, 2014b) ophiolites (**Fig. II. 5**). They have unclear structural relationships although Moeche Ophiolite seems to locally appear in a lower structural position. This ophiolite was formerly described as a sheet of mylonitic–ultramylonitic greenschists (Arenas *et al.*, 1986) and its internal structure remains poorly constrained (Arenas, 2015). Purrido ophiolite consists of monotonous amphibolites and garnet-bearing amphibolites of meta-gabbroic origin. Although its igneous features are poorly preserved, this ophiolite is compositionally and mineralogically similar to Careón ophiolite, in the Órdenes Complex. However, the regional significance of Cabo Ortegal ophiolites is far more limited than that of the better-preserved ophiolites of the Órdenes Complex, as mentioned above and reviewed by Arenas (2015).

3. The Upper Allochthon

This unit is described in details in the present section as it is the main focus of this work. The primary structure of the Upper Allochthon is related to the earliest tectonic events, associated with the highest pressure and temperature. It is a 10-12 km-thick pile (Albert *et al.*, 2014), divided in a structurally lower ensemble of various HP-HT paragneisses, mafic and ultramafic rocks and an upper unit of IP amphibolitic gneisses, the uppermost of the Cabo Ortegal Complex (**Fig. II. 5**).

a. High-temperature-high-pressure (HP-HT) unit

The HP-HT unit is divided into an upper member (Concepenido-La Capelada unit), an intermediate member (Cedeira unit) and a lower member (Peña Escrita unit). In the following section, we focus on the HP gneisses, eclogites, granulites and ultramafics of the Concepenido-La Capelada unit, most related to the present work, after briefly describing the lower members.

Peña Escrita unit

This small amphibolitic unit is in the structural continuity of Purrido ophiolite; they were formerly recognized together as the Ophiolitic Complex (*e.g.* Gil Ibarguchi *et al.*, 1990).

Cedeira unit

This unit includes paragneisses, and granulites as mafic inclusions, in the Chimparra

gneisses formation (Fernandez, 1994) and a heterogeneous nappe of amphibolite, metagabbros and scarce greenschists in the Candelaria formation (Gil Ibarguchi *et al.*, 1999). The latter is separated from Purrido ophiolite by the Carreiro Zone of Tectonic Movement (Vogel, 1967, Maaskant, 1970, Azcárraga *et al.*, 2002). Outcrops of ultramafic rocks occur along the contact between the Candelaria and Chimparra formations (Azcárraga *et al.*, 2002). Mylonitic garnet harzburgites and olivine orthopyroxenites have been distinguished. From their microstructural and textural relationships, they were interpreted as deep mantle fragments and buried serpentinite, respectively, and both subsequently incorporated into a subduction zone (Gil Ibarguchi *et al.*, 1999).

Concepenido-La Capelada unit

We here described only granulites, eclogites and associated HP gneisses. Mantle-derived ultramafic and mafic rocks of this unit are fully described in the next section.

Massive and deformed eclogites are exposed among the eclogite-facies Banded gneisses (Bernard-Griffiths *et al.*, 1985) and constitute one of the longest and most continuous outcrops of eclogite in the world (Ábalos, 1997), 20 km-long and 500-700 m-thick. They are metasedimentary gneisses with abundant mafic and rare ultramafic inclusions (Vogel, 1967, Gil Ibarguchi *et al.*, 1990), representing a former pelitic and greywacke volcano-sedimentary sequence, intruded by N-MORB-like diabasic dykes and gabbros (now eclogites) and minor granites and tonalities (now orthogneisses). The gabbroic melts were variously differentiated from homogeneous tholeiitic parental melts (Bernard-Griffiths *et al.*, 1985, Peucat *et al.*, 1990). This formation is interpreted as a metamorphosed piece of oceanic crust, potentially affected by significant continental contamination (Gravestock, 1992), but the existence of felsic rocks generated during decompressive partial melting complicates the distinction of former lithologies and compositions (Albert *et al.*, 2012).

Granulites are exposed in the Bacariza formation as a heterogeneous unit dominated by garnet- and plagioclase-rich types (Galán & Marcos, 1998). Potential protoliths include deep anatectic residues (Drury, 1980), a stratiform gabbroic complex at the base of the continental crust (Galán & Marcos, 1997) or the upper crust of a volcanic arc (Peucat *et al.*, 1990), probably derived from a primitive-mantle source (Gravestock, 1992) and metamorphosed during the eo-Variscan subduction (Puelles *et al.*, 2005). Alternatively, they have been interpreted as the retrogressed products of the early exhumation of eclogites (Galán & Marcos, 2000), notably due to the presence of relict kyanite and the restricted occurrence of plagioclase in symplectites

(Galán & Marcos, 1998). These interpretations are not mutually exclusive considering the lithological diversity of the granulites, ranging from mainly mafic and ultramafic, to intermediate and gneissic, and even including granitic, carbonate-rich and mineralogically more exotic varieties (Vogel, 1967, Gil Ibarguchi *et al.*, 1990, Galán & Marcos, 1997).

b. Intermediate-pressure (IP) unit

In the Cabo Ortegal Complex (**Fig. II. 5**), the IP unit is only exposed in the Cariño gneisses formation (Castiñeiras, 2005, Albert *et al.*, 2014). It consists of an amphibolite-facies metaturbiditic sequence whose metamorphic grade decreases upward, from granulite to greenschist facies. A characteristic counter-clockwise P-T path has been evidenced and ascribed to the underplating of a volcanic arc (Abati *et al.*, 1999).

C. DEFORMATION AND METAMORPHISM OF THE ULTRAMAFIC MASSIFS

Ultramafic and mafic rocks are mainly exposed in the Herbeira (~ 12.5 km^2), Limo (~ 6.6 km^2) and Uzal (3.6 km^2) massifs, but also in ~40 sparse outcrops within Bacariza granulites (Fig. 5). In the Limo and Uzal massifs, they are dominated by strongly serpentinized amphibole-bearing harzburgites (with variable amount of spinel), minor amounts of dunites and layered pyroxenites, and subordinate garnet-rich pyroxenites and mafic rocks (Girardeau and Gil Ibarguchi, 1991). In addition to these lithologies, the Herbeira massif contains dunites and chromitites (Monterrubio Pérez, 1991, Moreno, 1999, Moreno *et al.*, 1999), and abundant spinel- and locally garnet-bearing pyroxenites. This massif is described in detail in the next chapter.

1. Previous geochronological data

The age of Cabo Ortegal peridotites was formerly poorly constrained by whole-rock Rb-Sr ages at 487 ± 122 Ma, or 541 ± 37 Ma if omitting the sample with the lowest Rb/Sr ratio (Van Calsteren *et al.*, 1979). More recently, a whole-rock Sm-Nd isochron of 493 ± 130 Ma and clinopyroxene (cpx)-whole rock pairs at 506 ± 67 Ma (Santos *et al.*, 2002) were reported for pyroxenites and peridotites, which is consistent with U-Pb zircon ages of 520-480 Ma reported for the meta-basic protoliths (Peucat *et al.*, 1990, Ordóñez Casado *et al.*, 2001). However, the significance of these ages is debated as they might record an ancient metamorphic event (Fernández-Suárez *et al.*, 2007, Fernández-Suárez *et al.*, 2002).

A more recent magmatic event was first noticed by Rb-Sr ages of 386 ± 10 Ma for whole-rock lherzolite and phlogopite, and 337 ± 10 Ma for whole-rock and hornblende, in agreement with their K-Ar mineral ages (Van Calsteren *et al.*, 1979), recalculated by Kuijper *et al.* (1982). This is clearly confirmed by U-Pb ages of 392 ± 4 Ma on zircon (Peucat *et al.*, 1990) and 383 ± 1 Ma on rutile (Santos Zalduegui *et al.*, 1996) from a garnet clinopyroxenite vein, and Sm-Nd ages of 392 ± 69 Ma and 394 ± 22 Ma on garnet-cpx-whole-rock aliquots of garnet-, rutile- and zoisite-bearing clinopyroxenites (Santos *et al.*, 2002). This event is coeval with the HP-HT metamorphic event documented by U-Pb zircon, titanite and rutile ages at 382-395 Ma in the adjacent units (Santos Zalduegui *et al.*, 1996, Ordóñez Casado *et al.*, 2001) and confirmed by $^{40}Ar/^{39}Ar$ ages (Gómez Barreiro *et al.*, 2007). A minimum age for the ultramafic rocks is given by a pegmatitic granite that intruded the Uzal peridotite and gave zircon and monazite U/Pb ages of 387 ± 1 and 388 ± 2 Ma, respectively, and Rb-Sr isochron at 395 ± 5 Ma for K-feldspar and muscovite (Santos Zalduegui *et al.*, 1996).

2. Deformation episodes and previous thermobarometric estimates

The ultramafic massifs have experienced high-temperature shear deformation D_{HT} (Ábalos *et al.*, 2003) at > 1000°C. This was recorded by A-type (Jung & Karato, 2001) lattice-preferred orientation (LPO) in olivine ([100](010) slip system), as evidenced by early petrofabric studies (Ben Jamaa, 1988, Girardeau & Gil Ibarguchi, 1991, Girardeau *et al.*, 1990) and confirmed by electron back-scattered diffraction (EBSD) techniques applied to the Limo massif (Puelles *et al.*, 2012) and now to the Herbeira massif (H. Henry, PhD in progress). It resulted in a tectonic foliation parallel to the compositional layering and in isoclinal folding and boudinage (**Fig. III. 2**), including the large-scale boudinage of the pyroxenite-rich domain, from a thickness of more than 300m to less than 30m over a distance of ~3 km (Girardeau *et al.*, 1989, Girardeau *et al.*, 1990).

A subsequent high-pressure episode D_1 (Ábalos *et al.*, 2003) is recorded by a mylonitic foliation near tectonic contacts and extremely elongated sheath folds developed during the thrusting of the ultramafic massifs over the underlying granulites. However, the contacts between Bacariza granulites and the ultramafic massifs have been described as either ductile thrusts (Abalos *et al.*, 1996, Azcárraga *et al.*, 2002, Ábalos *et al.*, 2003, Puelles *et al.*, 2005) or non-tectonic lithological conformities, thus potentially representing a crust-mantle transition (Galán & Marcos, 1997, Galán & Marcos, 2000, Marcos *et al.*, 2002). Nonetheless, until recently, these folds depicting the style of deformation in deep subduction settings (Ábalos *et al.*, 2003) had been recognized in all the units of the Upper Allochthon (Azcárraga *et al.*, 2002) but not in the Limo and Herbeira massifs. The Limo massif was initially described as petrologically and structurally homogeneous (Ben Jamaa, 1988, Girardeau & Gil Ibarguchi, 1991, García Izquierdo *et al.*, 2011) due to the strong alteration of most outcrops inland. However, good exposures of harzburgites were found along the north-western cliffs despite the inaccessibility of the area, and large-scale stacking of extremely elongated sheath folds have been revealed (Puelles *et al.*, 2012). D_1 was accompanied by the injection of pyroxenite and garnet-rich dykes in C′-like[4] tensional fractures, commonly cross-cutting D_{HT} layering at a high angle (> 30°) in the pyroxenite-rich area. This occurred near the peak of metamorphism at 1.65-1.80 GPa and 800°C (Girardeau *et al.*, 1990, Girardeau & Gil Ibarguchi, 1991), while contemporaneous P-T

4 C′-like indicates the orientation of the tensional fractures with respect to the main foliation, *i.e.* the boudinage of pyroxenite layers. It is taken from the microstructural vocabulary used to describe ductile shear zones: C- (*cisaillement*) and S- (*schistosité*) planes. C′-plane, also known as shear bands or secondary shear fabrics specifically corresponds to the new fabric formed after the offset of a pre-existing fabric (C-plane). They form together a crenulation cleavage whose sense of displacement is synthetic to that of the shear zone.

Fig. II. 6. Field pictures illustrating high-temperature deformation features: **a.** thick pyroxenite layers with parallel boundaries contrasting with strongly boudinaged, thinner layers exposed along the shoreline of section 1b (**Fig. III. 1**); **b.** details of the deformed pyroxenite layers (or transposed dykes) with dunite lenses embedded in pyroxenite; **c.** typical boudinage of pyroxenites as observed in the pyroxenite-rich area; **d.** massive dunite with scattered pyroxenite lenses; **e** & **f.** micro-folded pyroxenite layers.

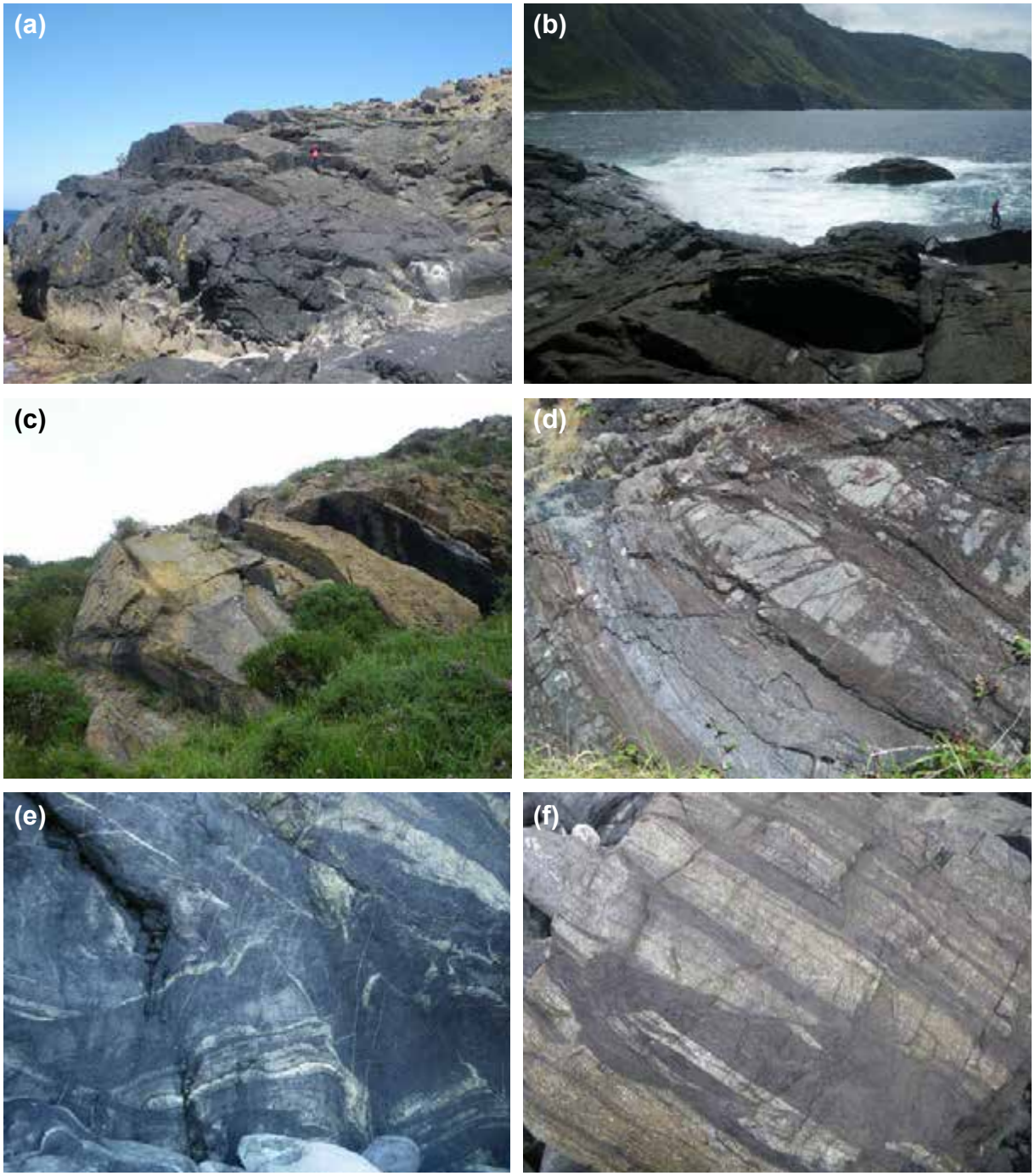

Fig. II. 7. Field pictures illustrating high-shear strain deformation features: **a-d.** sheath-fold deformation affecting harzburgites of the Punta Robaliceira (**a** & **b**); and both dunite (**c**) and interlayered pyroxenite and dunite (**d**) in the lower part of the pyroxenite-rich area; **e.** mylonites; **f.** faults, in interlayered pyroxenite and dunite.

conditions in the eclogites are estimated at 2.2 GPa and 780-800°C (Mendia *et al.*, 2001). These dykes are only deformed in mylonitic bands near the contacts with granulites (**Fig. II. 7e & f**), sealed in turn by undeformed pyroxenite dykes injected in Riedel[5] fractures (Girardeau & Gil Ibarguchi, 1991).

Fast exhumation rapidly follows the HP-HT event as suggested by migmatization of the granulites dated by U/Pb on zircons from a leucosome pod at 397-390 Ma (Fernández-Suárez *et al.*, 2007). Accordingly, carbonate-rich garnet-cpx layers, locally containing fragments of granulites post-dating D_1 in granulites (Gil Ibarguchi *et al.*, 1987, Ábalos *et al.*, 2003) gave U/Pb ages between 406 ± 4 Ma on zircon and 383 ± 3 Ma on rutile with other U/Pb ages on zircon, titanate and epidote lying between these ages (Santos Zalduegui *et al.*, 1996). There is little record of the associated deformation episodes in the ultramafic massifs, apart from the isoclinal folding of the Uzal peridotites and Bacariza granulites, and of their D_1 contact during D_2. This episode (D_2) has mainly been reconstructed from the tectonothermal evolution of the eclogite-facies Banded gneisses (**Fig. II. 8**) and cross-correlations with other structures, notably from the Órdenes Complex (Martínez Catalán *et al.*, 2002). It corresponds to the exhumation and underplating of the HP-HT units to form a unique assemblage at ca. 375 Ma (Ábalos *et al.*, 2003, Albert *et al.*, 2012), after 10-20 My within the subduction conduit (Beaumont *et al.*, 1999). Interestingly, this is in good agreement with structural patterns and exhumation rates predicted by numerical models of syn-convergent extrusion (Chemenda *et al.*, 1995, Doin & Henry, 2001, Warren *et al.*, 2008, Beaumont *et al.*, 2009). This timing was interpreted from $^{40}Ar/^{39}Ar$ dating of the detachment above the Banded gneisses (Ábalos, 1997, Dallmeyer *et al.*, 1997), and similar detachments in the Órdenes complex (Martínez Catalán *et al.*, 2002). Fluidal-like fine-grained assemblage delineating D_2 shear zones (S_2) in granulites were ascribed to shear heating or fluids infiltration close to the contact with peridotites. Similar processes may be responsible for the existence of garnet-biotite-rich migmatitic intercalations recrystallized at ~ 700°C and 1.1 GPa (Ábalos *et al.*, 2003). In addition, near the contact with the Uzal peridotites, the Chimparra gneisses provide evidence of partial melting dated at 391 ± 8 Ma (Ordóñez Casado *et al.*, 2001) and textures resembling those of high-grade contact metamorphism. This indicates a remarkable temperature contrast during the tectonic emplacement and deformation of the gneisses and peridotites and implies that the peridotites were still relatively hot during D_2 (Gayk & Kleinschrodt, 2000, Azcárraga *et al.*, 2002, Ábalos *et al.*, 2003). This overall episode can thus be regarded as a fast exhumation stage of ~ 1 GPa in < 10 Ma (Albert *et al.*, 2012).

5 Riedel shear structures are used in tectonics and micro-tectonics to describe the conjugate sets of fractures or cracks formed during strike-slip faulting (*e.g.* Gamond 1983).

Development of recumbent folds and of a basal thrust (D_3) accompanied retrograde metamorphism under amphibolite-facies conditions. Recumbent folds are younger than the extensional contact between Cariño gneisses and the Banded gneisses, which is similar to the Corredoiras detachments in the Órdenes Complex, dated at 375 Ma (Dallmeyer *et al.*, 1997). The basal thrust cuts amphibolite-facies foliation in Purrido ophiolite dated between 377 and 391 Ma (Peucat *et al.*, 1990, Dallmeyer *et al.*, 1997). However, greenschist-facies foliation in Moeche ophiolite was dated at 364 Ma, implying that D_3 occurred between 364 and 375 Ma (Albert *et al.*, 2012). D_3 recumbent folds are additionally affected by upright folds without axial planar foliation (D_4) such as the large open synform observed in Bacariza granulites and in the Herbeira massif. This last episode occurred under greenschist-facies conditions (Ábalos *et al.*, 2003). Final emplacement of upper allochthonous units on the Iberian parautochthon occurred at ca. 360 Ma (Dallmeyer *et al.*, 1997).

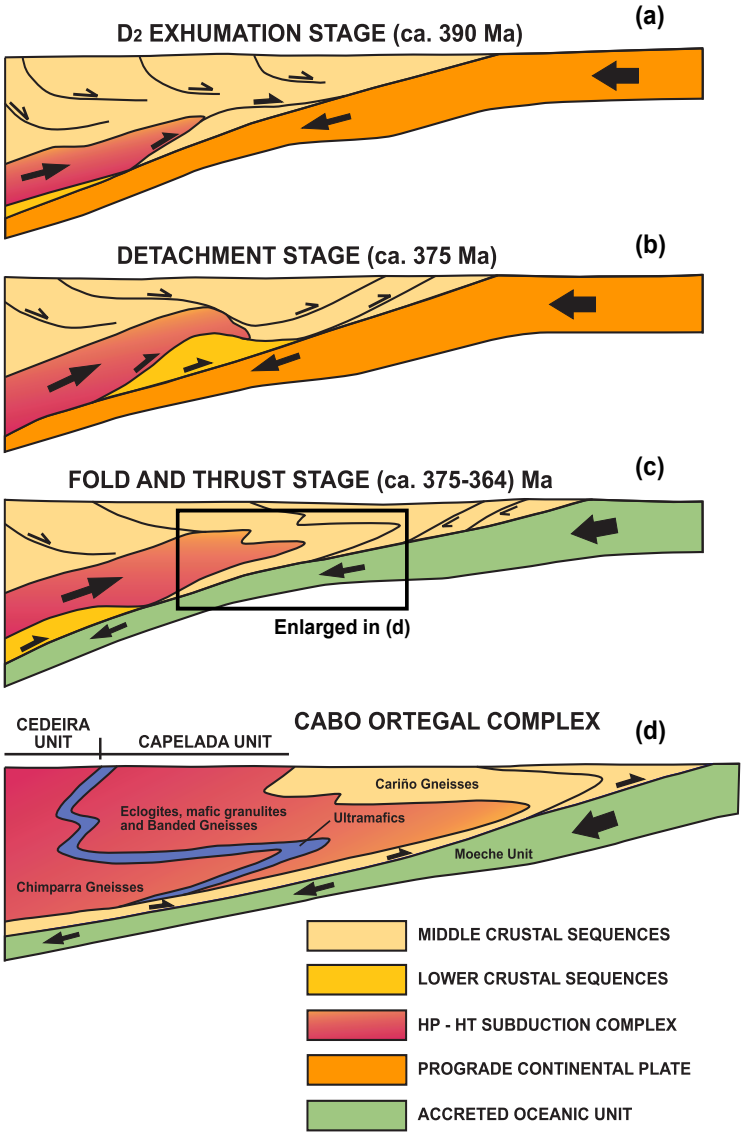

Fig. II. 8. Different stages of exhumation of the HP-HT units interpreted from the tectonothermal evolution of the eclogite-facies gneisses (after Albert *et al.,* 2012): **a.** development of a regional mylonitic foliation S_2; **b.** syn-convergence extensional detachments and **c.** recumbent folds and thrusts; **d.** idealized cross-section of the Cabo Ortegal Complex.

SUMMARY OF CHAPTER II

- The **allochthonous complexes of north-western Iberia** are part of the **Variscan belt** and consist of dismembered terranes, remnants of a **rootless suture**. Their structurally-distinct units record **peri-Gondwanan arc magmatism** and the opening of oceanic domains (potentially the **Rheic Ocean**) during the **Gondwanan-Laurusian convergence**, prior to the **Variscan collision**.

- The Cabo Ortegal Complex notably exposes a **tectonic mélange** along with remnants of the **Gondwanan margin, ophiolites** of debated origin and most importantly for this study, **allochthonous units** of intermediate and high-pressure rocks.

- The **high-pressure units** consist of mantle-derived **ultramafic and mafic rocks** associated with **arc-related granulites** of debated protoliths, homogeneous **MORB-derived eclogites**, **high-pressure gneisses** and their retrogressed products.

- The **ultamafic massifs** of the Cabo Ortegal Complex (Limo, Herbeira and Uzal) are dominated by **amphibole-bearing harburgites** with minor dunites and layered pyroxenites. Their **age is poorly constrained at ~500 Ma.**

- The Herbeira massif is distinctive in exposing **abundant pyroxenites**, **dunites** and **chromitites**, and **mafic dykes** corresponding to a **magmatic/metamorphic event documented at 390 Ma,** which is coeval with the protoliths of the granulites and eclogites.

- The **tectonothermal history** of the ultramafic massifs starts with a mantle-related **high-temperature episode** responsible for the main **tectonic foliation** and **isoclinal folding**. **Sheath folds** and **mylonites** were then developed during a subduction-related **high-pressure episode**. All high-pressure units together were **rapidly exhumed,** partly by **subduction conduit** processes. Their emplacement on the **Iberian autochthon** is estimated to have occurred at *ca* **360 Ma**.

Chapter III.

Structural and Textural Relationships

A. FIELD AND SAMPLING STRATEGY

Two fieldtrips were undertaken in 2012 and 2013 to acquire structural data, observe the main field relationships and collect a representative set of samples from the Herbeira cliffs, where the best exposures of pyroxenites are found, according to previous sampling and field notes by Jacques Girardeau and co-workers (*e.g.* Ben Jamaa, 1988, Girardeau *et al.*, 1989). Two cross sections were sampled in 2012 (**Fig. III. 1**): section 1a throughout the pyroxenite-rich area to the south of the cliffs, and section 2 along the northern boundary of the massif down to the Punta Robaliceira. Additional sampling was undertaken elsewhere in the Herbeira massif, and in the Limo and Uzal massifs, along with granulites, eclogites and gneisses from the other units. Preliminary results pointed to the need for an additional cross section (1b) in the pyroxenite-rich area, which was sampled in 2013, parallel to section 1a. Two structural traverses were undertaken: the first to describe the nature of the contact between dunites and harzburgites along the southern boundary of the massif, the second focused on a complex area at the top of section 2. Targeted sampling of chromitites was also performed at locations indicated by Moreno

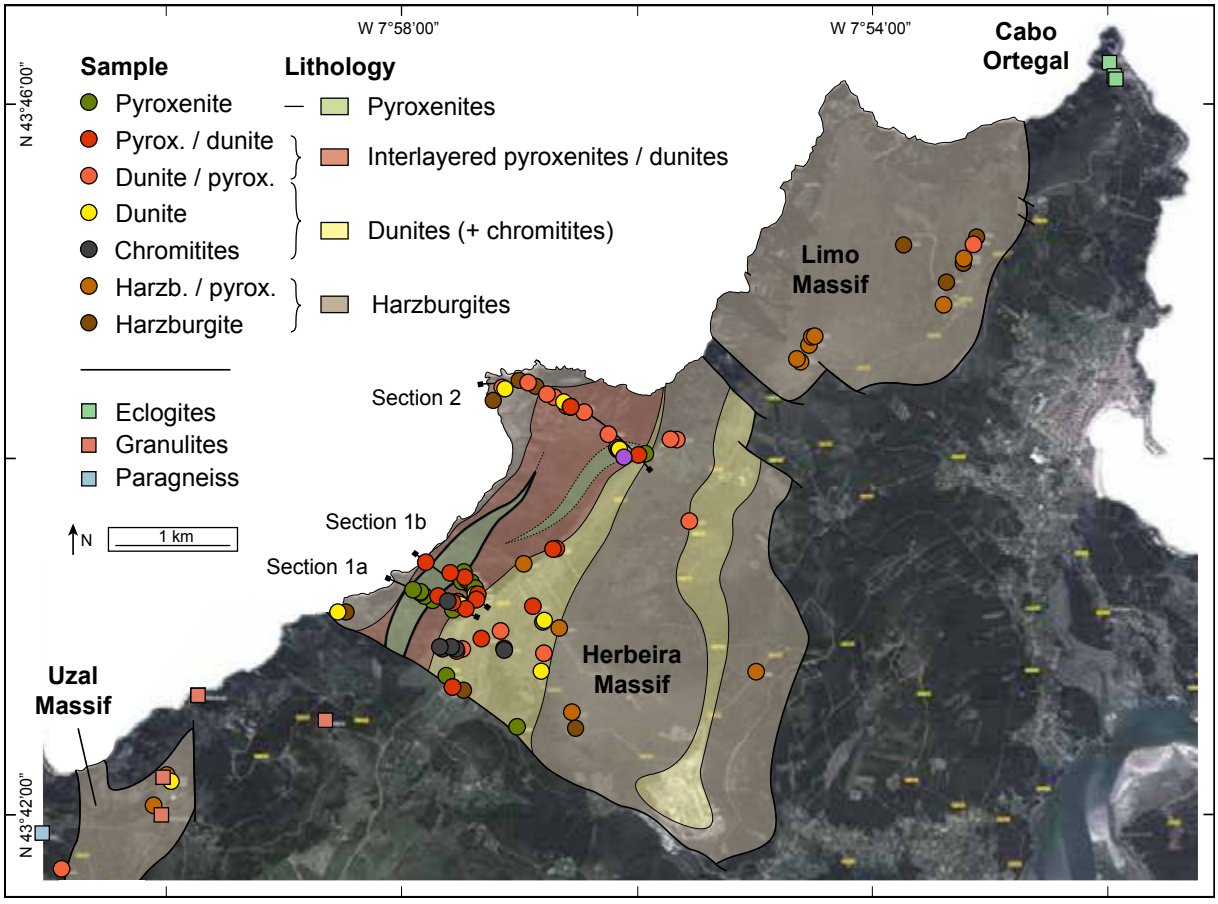

Fig. III. 1. Main lithological units and location of Cabo Ortegal samples (see text for more details).

et al. (2001). The main sample collection includes harzburgites, dunites, chromitites and pyroxenites from layers of different thicknesses. Samples are either homogeneous or composite, preserving layering, lithological contacts and cross-cutting features, when present. They are large enough (up to several kg) to both contain fresh material and preserve the weathered surface so that the geometrical relationships between lithologies can be easily observed (**Appendix A1**). This aims to match the requirements of both whole-rock and in-situ geochemistry.

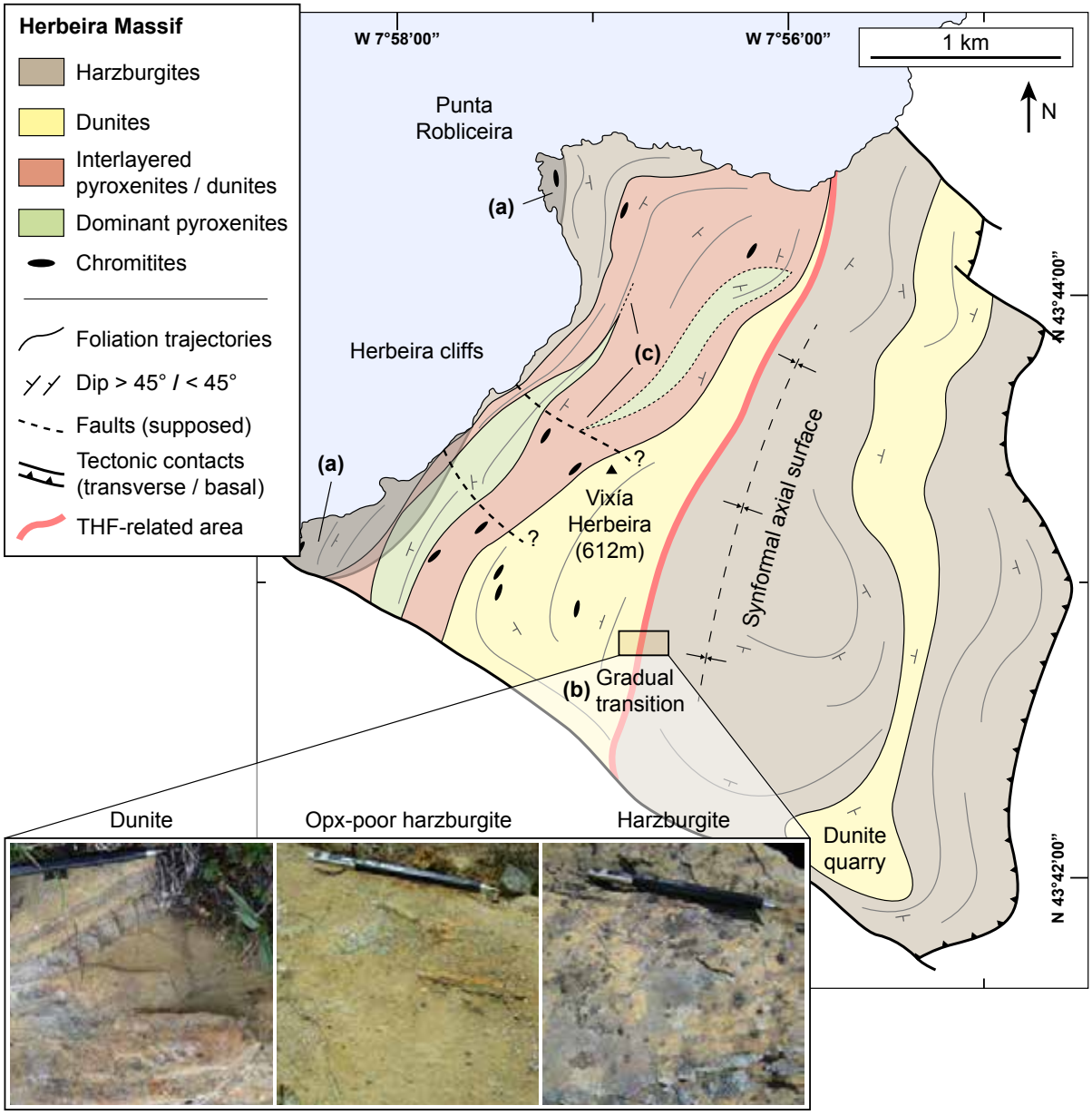

Fig. III. 2. Geological map of the Herbeira massif: **a.** sheath-fold deformation crosscuting lithological contacts on the western bound of the massif; **b.** serpentinized and/or amphibolitized area surrounding the gradual contact between dunite and harzburgite along the synformal axial surface; **c.** uncertainty regarding the outline of the pyroxenite-rich area, as it may consists of a single or several distinct bodies (see text for further details). Fault lines correspond either to transverse (full lines) and basal (thrust patterns) tectonic contacts with granulites, and supposed late strike-slip faults (dashed lines). The outline of the eastern dunite body is modified after Puelles *et al.* (2012).

B. STRUCTURE OF THE HERBEIRA MASSIF

This section discusses the structural features of the Herbeira massif in the light of our new field observations and interpretations.

The Herbeira massif is the largest exposure of ultramafic and related mafic rocks in the Cabo Ortegal Complex (**Fig. III. 1**). It has been proposed that it consists of two tectonically distinct units separated by a near-vertical fault oriented NW-SE (**Fig. III. 2**), the Trans-Herbeira Fault (THF; Moreno *et al.*, 2001, García Izquierdo *et al.*, 2011). Evidence for the existence of this fault may include high degrees of serpentinization and chrysotile veining (asbestos) to the NE and exposure of horizontally-foliated garnet granulites and vertical foliation adjacent to quartz veins to the SW (Moreno, 1999). In addition, ultramafic rocks exposed in excavations to the NE of the Vixía Herbeira are highly brecciated and exhibit a north-dipping lineation and evidence for a dextral shear sense (Moreno, 1999). Our field observations confirm some of these features (**Fig. III. 3**): the area is strongly amphibolitized to the NE and serpentinized with abundant sub-vertical garnet-bearing veins to the SW. However, where fresh outcrops are preserved (*i.e.* to the SW), the contact between harzburgites and dunites can be observed as gradual: the proportion of opx porphyroclasts increases progressively over a few hundred metres. We thus believe that the area has been affected by metasomatism that overprinted the igneous contact between dunites and harzburgites, and probably post-dates the thrusting of the massif on to the granulites, as evidenced by chlorite-talc-serpentine-rich rocks exposed near the contact with granulites. Faulting might have occurred locally, and at most limited to minor displacement; to our understanding, the THF thus does not represent a major structure.

Foliation trajectories indicate that the Herbeira massif is a large and open synformal structure (Ábalos *et al.*, 2003, Girardeau *et al.*, 1990) whose axial plane roughly follows the lithological contact, although it is not possible to directly relate serpentinization, veining and brecciation to the folding episode.

From the base to the top (**Fig. III. 2**), lithological variations can be summarized as follows.

- Serpentinized harzburgites and minor pyroxenite layers occurring along the shore line, well-exposed thanks to marine erosion (**Fig. III. 7a & b**). We have identified in these rocks spectacular sheath folds similar to those described in the Limo massif (Puelles *et al.*, 2012). They exhibit weakly-defined foliation and a well-developed linear fabric. Importantly, the lower part of the overlying pyroxenite-rich domain is also sheath-folded (**Fig. III. 7c & d**),

Fig. III. 3. Field pictures illustrating late features related to the Trans-Herbeira Fault (THF): **a.** complete amphibolitization to the NE, probably after cpx-rich lithologies resulting in hornblendite; **b.** antigorite (asbestos) to the SW, where the THF intersects the contact with granulites; **c.** network of serpentine veins; **d.** breccia made of highly serpentinized dunite fragments embedded in a serpentinite matrix, in the central part of the THF; **e** & **f.** garnet-muscovite-rich veins restricted to the SW of the THF.

suggesting that the Herbeira massif probably underwent the related deformation episode (D_1) as an entity, likely constrained by the presence of abundant pyroxenites, rheologically competent with respect to surrounding peridotites.

- Abundant pyroxenites make up to 80-90 % of a ~ 3 km-long, 300 m-thick lenticular area exposed in the Herbeira cliffs (**Fig. III. 4**). Individual layers may reach up to 3m in thickness with a lateral extent exceeding 100 m. They alternate mostly with dunites, particularly in the core of the pyroxenite-rich body, and with harzburgites in its lower and upper parts (Girardeau & Gil Ibarguchi, 1991). From the study of the detailed cross-sections performed by J. Girardeau and co-workers, and from our own field observations, we suggest that the actual shape of this body may be more complex, potentially consisting of one of several lenticular bodies. As noted on our geological map (**Fig. III. 2**), most pyroxenites are found between altitudes of ~ 150 and ~ 350 m in sections 1a and 1b, whereas they are found at a higher altitude in section 2 (~ 400-500 m), in addition to significant amounts of pyroxenite at ~ 300m. The pyroxenite-rich domain may thus consist of a pile of at least two connected lenticular bodies of varying extent. Near the top, a garnet-rich, 3 to 5 m-thick mafic layer was described by Girardeau and Gil Ibarguchi (1991), as indicated by a purple symbol (**Fig. III. 1**).

- A dunite-dominated domain with abundant chromitites exposed along the western edge of the Herbeira plateau.

- A mainly harzburgitic plateau, with millimetric to decimetric pyroxenite layers representing less than 10 % in volume, resembles exposures of the Limo massif. An elongated lens of dunite[1] is also exposed to the SE.

Pyroxenite and garnet-rich dykes cut the peridotite and pyroxenite foliation as C′-like tensional fractures and Riedel fractures, as detailed above. The latter mostly occur in the dunite-dominated area above the pyroxenite-rich domain, particularly in the area related to the THF, and are also found in the Limo massif. Our field observations indicate that, when intruded into pyroxenitic lithologies, these dykes occur as diffuse garnet-rich bands with a poikilitic texture enclosing pre-existing pyroxenes.

1 These dunites are exploited as refractory material by Pasek España S.A. in the Herbeira quarry.

Fig. III. 4. Field pictures illustrating typical exposures of pyroxenites in the Herbeira cliffs: **a** & **b.** thin layers in moderately serpentinized dunite with white serpentine veins (**a**) and in harzburgites with antiformal fold and regularly-spaced fractures affecting pyroxenites (**b**); **c** & **d** thick layers in dunite with parallel contact (**c**), or slightly boudinaged (**d**); **e.** loose boulder exposing very fresh and finely interlayerd pyroxenite and dunite along the shoreline; **f.** ~ 3 m-thick massive pyroxenites.

C. SAMPLE DESCRIPTION

The next sections provide a summary of the most significant petrographic features of the different types of samples, with emphasis on samples (mainly pyroxenites) used for geochemical investigations. They are mainly based on our own field and petrographic observations, except where otherwise mentioned. A complete description of the sample collection is available in **Appendix A**.

1. Pyroxenites

Four types of pyroxenites have been distinguished mainly from samples collected in the Herbeira massif, on the basis of their mode of occurrence and petrographic features.

- *Type-1* pyroxenites are websterites, olivine websterites, wehrlites and clinopyroxenites containing dunite lenses with sharp or slightly diffuse contacts (**Fig. III. 5a** & **b**);
- *Type-2* pyroxenites are massive websterites and clinopyroxenites and are the most abundant (**Fig. III. 4d**);
- *Type-3* pyroxenites are foliated websterites and clinopyroxenites, commonly strongly amphibolitized; probably representing the deformed products of *type-1* pyroxenites, and to a lesser extent of *type-2* pyroxenites (**Fig. III. 5c-e**). They are particularly abundant in the lower part of the pyroxenite-rich area;
- *Type-4* pyroxenites are subordinate opx-rich (olivine) websterites (**Fig. III. 5f**).

In thin section, all types of pyroxenites have medium- to coarse-grained granoblastic to porphyroclastic textures, although coarse (igneous?) textures may be locally preserved, particularly in *type-1* pyroxenites. However, heterogeneous textures are commonly observed within individual thin sections due to post-kinematic replacement of cpx and spinel by amphibole, as detailed below.

2. Peridotites

Harzburgites (**Fig. III. 6**) sampled in the Herbeira, Limo and Uzal massifs are very strongly serpentinized and amphibolitized, and commonly exhibit unstrained idiomorphic amphibole and antigorite. They preserve few or no relics of olivine, large bastitized opx porphyroclasts (5-10 mm) with undulose extinction, representing 10-30 % by volume (Girardeau & Gil Ibarguchi, 1991) and rare cpx. Amphibole occurs as idiomorphic crystals or as lamellae in cpx, locally

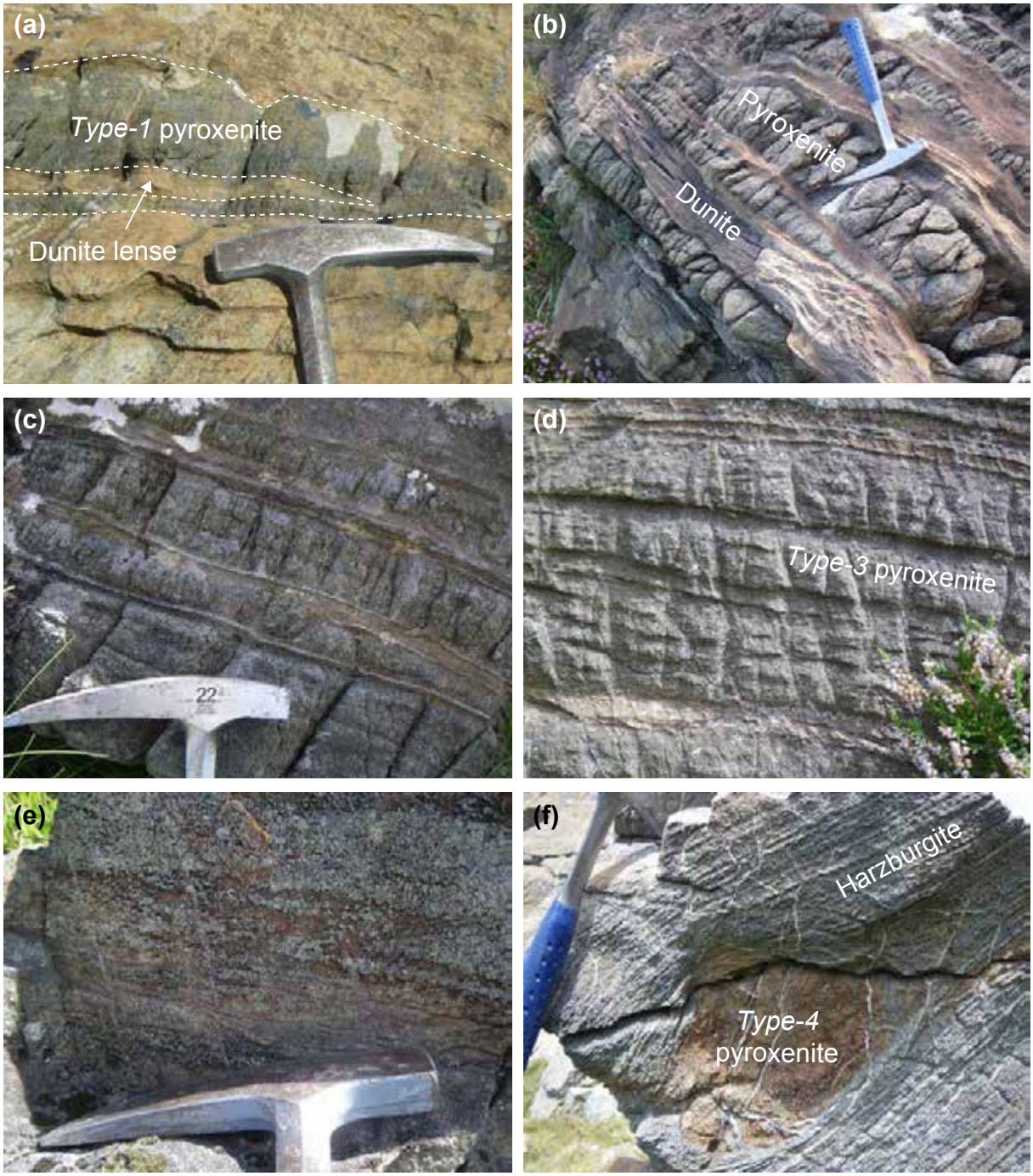

Fig. III. 5. Field pictures illustrating the range of pyroxenite occurrences from dunite-bearing to foliated: **a** & **b.** boudinaged (*type-1)* pyroxenite with dunite lense; **c-e.** foliated (*type-3*) pyroxenite variously preserving dunite layers (**c** & **d**) or folded and stongly amphibolitized (**e**); **f.** opx-rich (*type-4*) pyroxenite in mylonitic harzburgite.

Fig. III. 6. Field pictures of harzburgites: **a.** freshly exposed on the north-western boundary of the Herbeira massif with foliation outlined by aligned opx porphyroclasts and trails of serpentine and spinel; **b.** strongly serpentinized as exposed inland in the Herbeira and Limo massif; **c.** bastitized opx porphyroclasts; **d** & **e.** loose boulder exposing harzburgite with green serpentine veins with boudinaged pyroxenite layers (**e**); **f.** strongly serpentinized harzburgite and thin pyroxenites, as exposed inland.

replaced by antigorite. Opx porphyroclasts and amphibole crystals may derive from disaggregation of boudinaged pyroxenite and hornblendite layers or dykes, particularly in mylonitic samples where they are hardly distinguishable from the actual harzburgite paragenesis. Disseminated fractured grains or elongated and discontinuous aggregates of green (particularly in samples from the Limo massif) to brown spinel constitute 1-3 % in volume (Girardeau & Gil Ibarguchi, 1991). Base-metal sulfides, magnetite and chlorite occur in variable proportions in the serpentine matrix.

Dunites (**Fig. III. 7**) occur sporadically as diffuse pods within harzburgites and abundantly in a dunite-dominated area above the pyroxenite-rich area. They are also strongly serpentinized, with brown to black serpentine associated with magnetite and olivine remnants in a mesh texture, and chrysotile veins. Chlorite and phlogopite occur as minor phases and only rare sulfides are found. Relatively fresh olivine remnants are preserved, particularly where occurring within *type-1* pyroxenites. The freshest olivine remnants may rarely exhibit undulose extinction. Sporadic fine-grained opx was found by Girardeau and Gil Ibarguchi (1991) and interpreted as the result of partial resorption of this phase. Abundant disseminated chromite occurs as 2-3 mm, rounded grains showing no preferred orientations, contrasting with preferentially oriented aggregates of elongated olivine and serpentine veins. Our observations also indicate the existence of elongated and discontinuous aggregates of chromite located at the neck of partly "dissolved" pyroxenite lenses.

Lherzolites and wehrlites occur sporadically, mainly with diffuse contacts to *type-1* pyroxenites in the Herbeira cliffs. They represent the "impregnated" dunites and harzburgites described by Girardeau and Gil Ibarguchi (1991). A comprehensive petrological description of the peridotitic lithologies, which are not the main target of this study, is provided by Girardeau *et al.* (1990) and Santos *et al.* (2002)

3. Chromitites

Chromitites (**Fig. III. 7**) are mostly exposed along the edge of the Herbeira plateau and occur as centimetric to decametric layers or schlieren[2], systematically associated with dunites (with disseminated chromite). They also occur with interlayered pyroxenite and dunite layers exposed in the Herbeira cliffs. Chromitite pods were also reported in harzburgites by Moreno (1999) in two localities on the shoreline of the Herbeira and Uzal massif.

2 From a German word defining optical heterogeneities, here used to describe irregular streaks of igneous rocks differing in composition and texture from the groundmass.

Fig. III. 7. Field pictures of chromitites: **a** & **b.** associated with dunites on the edge of the Herbeira plateau, where most of the chromitites of the Cabo Ortegal Complex are observed; **c-f.** associated with pyroxenite near the area related to the THF (**c** & **d**), exhibiting schlieren and disseminated chromites (**d**) and in the pyroxenite-rich area of the Herbeira cliff (**e** & **f**).

Chromitites have either massive and/or nodular texture, with serpentine (± antigorite) matrix, rarely including sub-idiomorphic chromite. In massive texture, coarse grains, or former coarse grains, are outlined by trails of serpentine inclusions, apparently after olivine. Fine- to medium-grained bands of well-equilibrated, zoned (or rarely unzoned) chromite are observed in samples (commonly amphibole-bearing) that are associated with pyroxenites (**Fig. A3. 6**). They may represent mylonitic bands or healed fractures related to late deformation episodes. Chromite is commonly fractured, locally exhibiting bright rim and drop-shaped along boundaries with serpentine, and/or dendritic alteration rims (**Fig. A3. 7**).

Nodular chromitite is found either within or on the rim of massive chromitite bands, potentially representing "accreted" disseminated chromites. Abundant disseminated chromites are found in the vicinity of chromitite layers, commonly with antigorite. Schlieren of nodular chromite may be associated with clinopyroxenite, wehrlite and dunite, where graded-bedding structures were described by Girardeau and Gil Ibarguchi (1991). Individual nodules commonly exhibit rounded serpentine inclusions after olivine.

Small grains of base-metal sulfides are common, either as fresh association of pentlandite, pyrrhotite and chalcopyrite within chromite, close to grain boundaries, or in the serpentine matrix with various products of serpentinization and supergene alteration. They may host platinum-group minerals (PGM) as single homogeneous or exsolved grains, or as complex aggregates, probably representing very late mineralization. They are commonly Pt-Pd bearing arsenides, tellurides, sulfides, alloys and oxides (**Fig. A3. 9**). These minerals and their host chromitites are described in more detail by Monterrubio Pérez (1991) and Moreno *et al.* (1991; 2001).

4. Subordinate lithologies

A garnet-rich layer near the top of the pyroxenite-rich area consists of 5-20 cm-thick bands ranging from pyroxene-rich at the bottom to garnet-rich at the top, with garnet locally reaching 70 % in volume. They alternate with zoisite- and amphibole-rich (± spinel) bands. Girardeau and Gil Ibarguchi (1991) reported the existence of rutile-rich areas, partly replaced by sphene, and Cr-spinel and pink 0.1mm corundum inclusions in garnet. Our sample exhibit garnet coronas around zoisite (**Appendix A**).

As mentioned above, intrusive rocks (*i.e.* cutting the HT foliation of peridotites and pyroxenites) are observed in the three massifs (**Fig. III. 8**). Amphibole-, olivine- and phlogopite-bearing pyroxenite dykes have dunitic rims when hosted in pyroxenites (**Fig. III. 9a**) and opx-rich,

Fig. III. 8. Field pictures of pyroxenite dykes: **a-c.** cpx-rich with thin (**a**) and thick (**b**) opx-rich rims, or zoned (**c**); **d.** cutting through pyroxenite and dunite at varying angle; **e.** undeformed and sub-vertical across harzburgite foliation as typically exposed to the SW of the THF area and in the Limo massif; **f.** well exposed thanks to marine erosion down section 1a (**Fig. III. 2**).

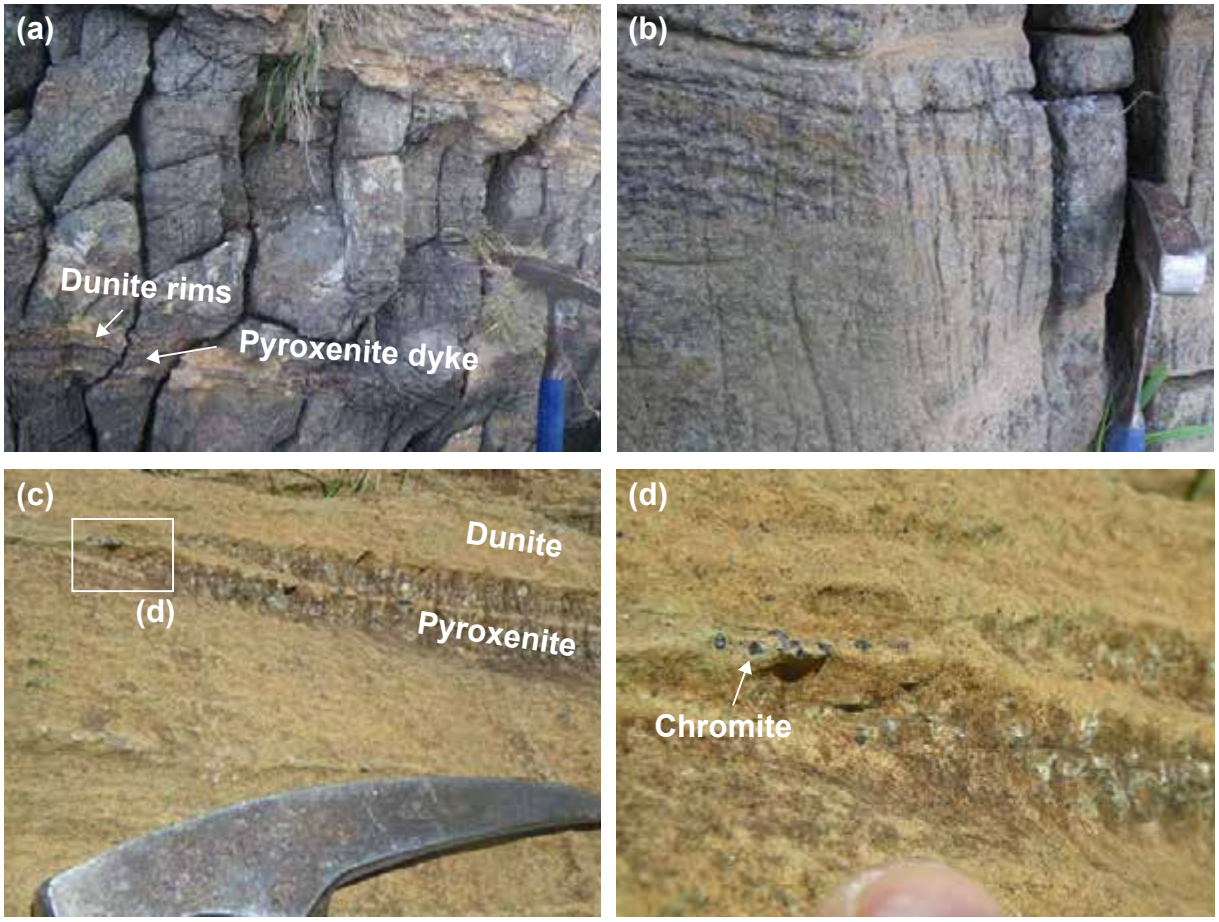

Fig. III. 9. Field pictures illustrating **a.** dunite rim of a pyroxenite dyke represnting the melting/dissolution of a thick pyroxenite layer; **b.** diffuse lens-shaped olivine-rich bands in pyroxenite; **c** & **d.** evidence for incongruent melting of pyroxenes with precipitation of chromite at the termination of a thin pyroxenite layer.

when hosted in peridotites (**Fig. III. 8a**). Such rims may be locally several times thicker than the related cores (**Fig. III. 8b**). These dykes may alternatively have mineralogical assemblages that are very similar to that of their host pyroxenite layers. Girardeau and Gil Ibarguchi (1991) also reported garnet-rich, amphibole- and chlorite-bearing dykes with cpx-rich rims. Minor phases include carbonate, phlogopite and ilmenite and spinel enclosed in garnet as described in concordant pyroxenite layers. In addition, abundant muscovite is observed in our samples, probably related to retrogression into greenschist facies.

D. TEXTURAL RELATIONSHIPS WITHIN PYROXENITES

For clarity, this section includes both the description of textural relationships of pyroxenite-forming phases and their first-order interpretations in terms of petrological processes, which will be in turn incorporated and considered in the framework of the main discussions. Modal proportions given in this section refers to point-counted modes as detailed in the next chapter (**Table IV-1**).

1. Clinopyroxene

Modal proportions of cpx range between 32 and 80 wt % (10-23 wt % in opx-rich websterites) and tend to increase with the thickness of layers. Cpx is well preserved and apparently unstrained (no kink band nor undulose extinction) suggesting deformation at relatively high temperature and/or prolonged static recovery. It occurs as 1-5 mm porphyroclasts (cpx I), locally exhibiting complex (sutured) boundaries (**Fig. III. 10a, c** & **e**), potentially after static recrystallization. They may contain exsolved needles of spinel along cleavages as detailed below. Cpx also commonly occurs as 50-800 μm exsolution-free grains (cpx II) in granoblastic texture or as neoblasts in porphyroclastic texture (**Fig. III. 10c-f**).

2. Orthopyroxene

Modal proportions of opx range between 0 and 45 wt %. It is commonly represented by variably serpentinized 2-5 mm porphyroclasts (**Fig. III. 11a** & **b**). Girardeau and Gil Ibarguchi (1991) also described pegmatoid pyroxenitic facies where opx crystals reach 5 cm. Porphyroclasts locally exhibit undulose extinction, sub-grain boundaries, kink-bands and complex grain boundaries after dynamic recrystallization, particularly outlined by deformed needles of exsolved spinel and cpx (**Fig. III. 11c-f**). Opx can also be found as 50-400 μm fresh neoblasts (opx II) in much lesser proportions (**Fig. III. 11a, b** & **d**).

In opx-rich websterites, where opx ranges between 65-79 wt % and in some harzburgites, opx porphyroclasts are commonly fractured (particularly in samples from the Limo massif) and these fractures filled with exsolution-free opx neoblasts, and less commonly sub-idiomorphic amphibole (**Fig. III. 15e**). The absence of exsolution-free rim along these fractures suggest that they are late features.

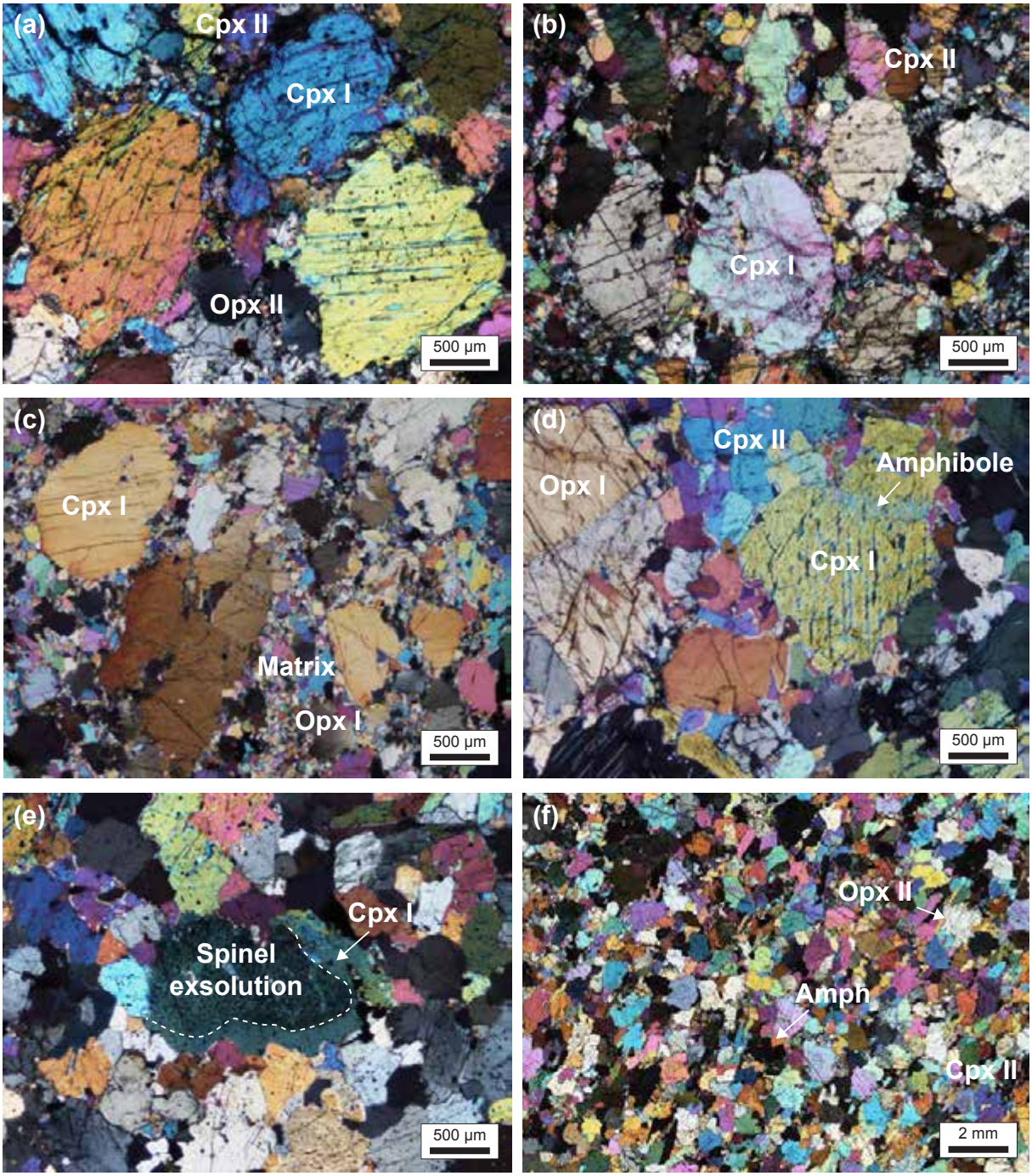

Fig. III. 10. Photomicrographs illustrating the textural relationships of cpx in cross-polarized light: **a.** coarse grains with sutured boundaries in a cpx-rich websterite matrix, note the undulose extinction of opx; **b.** preferentially oriented porphyroclasts within a recrystallized matrix in cpx-rich websterite; **c.** preferentially oriented porphyroclasts with sutured boundaries and fine-grained matrix in websterite; **d.** cpx porphyroclasts with amphibole replacement along cleavage and well-equilibrated granoblasts in porphyroclastic opx-rich websterite, note the kink bands in opx; **e.** t websterite preserving a cpx porphyroclast with exsolutions restricted to the core, note disseminated spinel inclusions; **f.** typical medium-grained granoblastic websterite with abundant amphibole in textural equilibrium with cpx. Back-scattered electron (BSE) images are provided in **Appendix A3** (**Fig. A3. 1** & **2**).

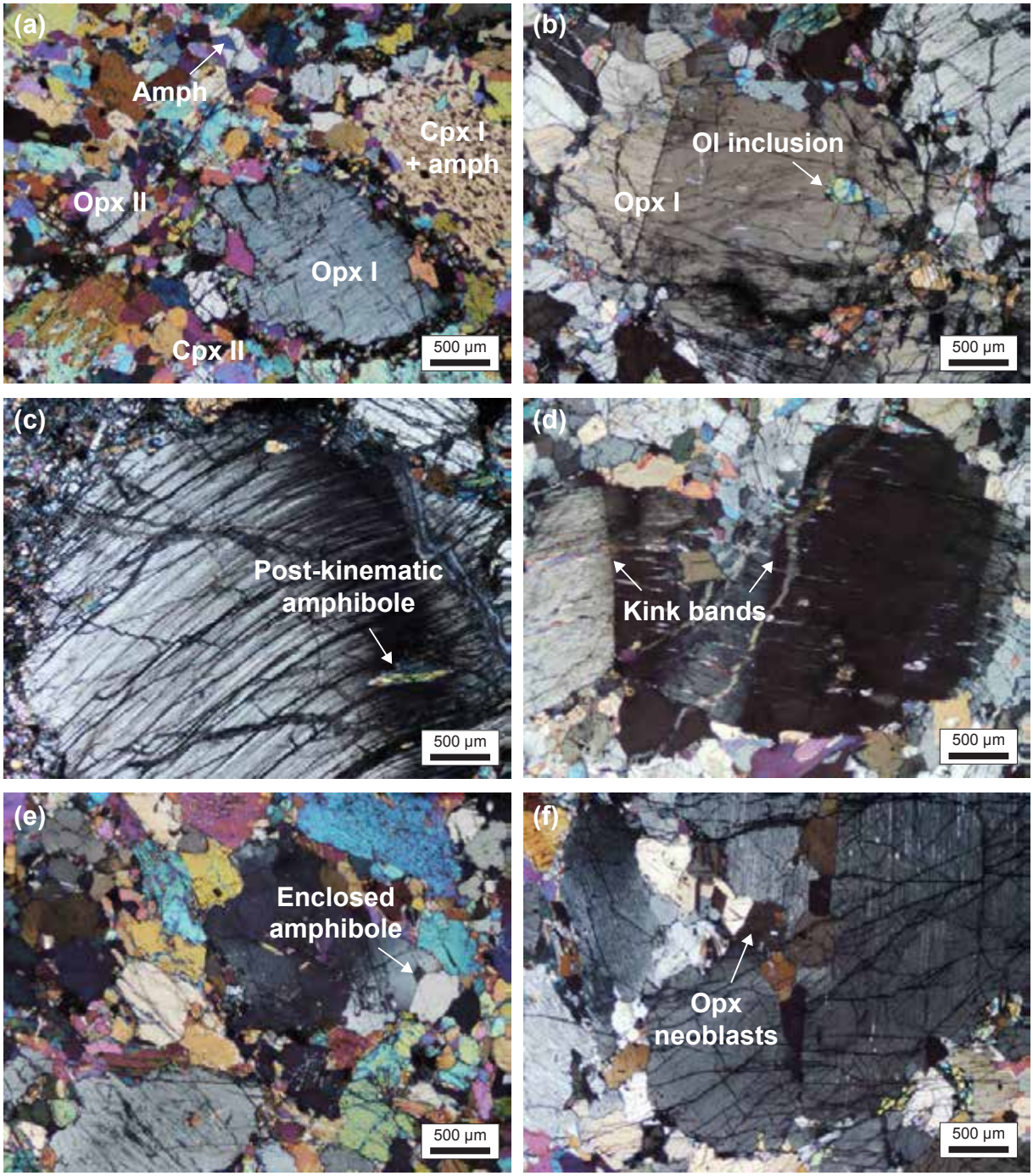

Fig. III. 11. Photomicrographs illustrating the textural relationships of opx in cross-polarized light: **a.** porphyroclast (I) with needle-shaped spinel and cpx exsolution and derived neoblasts in cpx-rich websterite, note strong amphibole replacement in cpx porphyroclast resulting in sutured boundaries and the matrix dominated by sub-idiomoprhic amphibole that preserves only few opx relics and opx II; **b.** opx-rich websterite with olivine inclusion in opx and well-equilibrated medium-grained opx-olivine matrix; **c.** undulose extinction in opx porphyroclast against fine-grained serpentinized matrix in harzburgite, note the post-kinematic amphibole replacement; **d.** undulose extinction and kink bands in porphyroclasts with amphibole replacement and well-equilibrated matrix of opx II; **e.** undulose extinction and sub-grain boundaries nucleated preferentially from enclosed amphibole crystals in a well-equilibrated cpx-amphibole matrix; **f.** neoblasts within fractured opx porphyroclasts with pre-kinematic spinel and cpx exsolution and interstitial olivine within opx-rich matrix. Back-scattered electron (BSE) images are provided in **Appendix A3** (**Fig. A3. 1** & **2**).

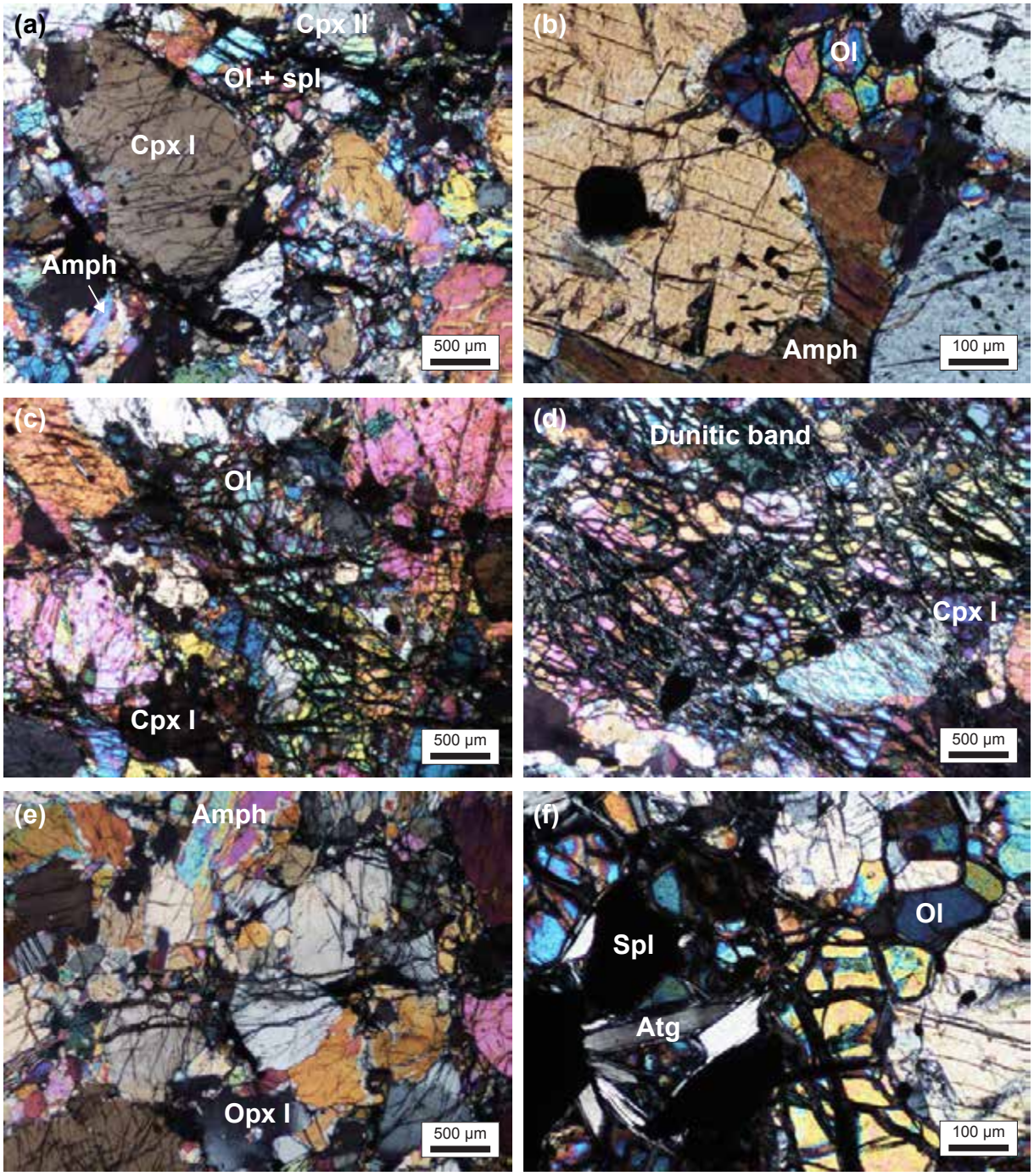

Fig. III. 12. Photomicrographs illustrating the textural relationships of olivine in pyroxenites in cross-polarized light: **a-c**. interstitial trails associated with spinel and amphibole around cpx porphyroclasts in olivine websterite (**a** & **b**) and in olivine clinopyroxenite (**c**), note the fresh contact of olivine (*i.e.* limited serpentinization) against amphibole in **b**; **d.** dunitic band within *type-1* pyroxenite; **e.** opx-rich websterite; **f.** thin *type-2* pyroxenite with antigorite grown on large sub-idiomorphic spinels. Back-scattered electron (BSE) images are provided in **Appendix A3** (**Fig. A3. 3** & **4**).

3. Olivine

Olivine represent up to 5 wt % in point-counted sections of *type-1* pyroxenites, and certainly more in sections where high degrees of serpentinization prevent the determination of an accurate mode. It occurs mainly as interstitial and elongated fine-grained aggregates associated with spinel (**Fig. III. 12**), or as inclusions in pyroxenes (**Fig. III. 11b**), particularly in *type-1* pyroxenites and mostly in opx, where it provides preferential sites for the formation of sub-grain boundaries. Locally, these trails of olivine outline aggregates of cpx and deformed opx (when present), potentially representing former and coarser grains.

4. Amphibole

Modal proportions of amphibole range from 6 to 14 wt % in *type-1*, 4 to 26 wt % in *type-2*, and 8 to 42 wt % in *type-3* pyroxenites. Amphibole occurs in all types, replacing cpx and spinel and preferentially grown among matrix minerals as xenomorphic medium-sized grains in apparent textural equilibrium with cpx (**Fig. III. 10f**). In *type-1* pyroxenites, amphibole is commonly associated with olivine as interstitial minerals (**Fig. III. 12a & b**). Grain boundaries between these minerals are relatively fresh and the very limited serpentinization of olivine rim suggests hydration under conditions exceeding the stability field of serpentine (**Fig. III. 12b**).

Where occurring within pyroxenes, and even at moderate degrees of amphibolitization, sub-idiomorphic to idiomorphic medium-grained crystals are observed (**Fig. III. 13d-f**) and these are preferentially located along cleavages of cpx (**Fig. III. 13a-b**) and replacing cpx exsolution lamellae in opx (**Fig. III. 13c**). The elongated lamellar amphibole may be associated with spinel (**Fig. III. 16d**).

At higher modal proportions of amphibole, disequilibrium textures are observed with interstitial amphibole grown at the expense of porphyroclast (or large granoblast) rims, resulting in sutured grain boundaries, as described above. The range of coarse (igneous?) and variously recrystallized, deformation-related (porphyroclastic and granoblastic) textures is overprinted by this amphibole replacement (**Fig. III. 14**), resulting in composite porphyroclastic textures (*i.e.* with a bimodal grain-size distribution). Well-equilibrated granoblastic texture is locally observed among strongly non-equilibrated and sutured pyroxenes (**Fig. III. 14d**) where static recrystallization of matrix (interstitial) amphibole occurred.

At the most advanced stage of replacement (mainly in *type-3* pyroxenites), amphibole is observed as large crystals, commonly in a sutured granoblastic texture (**Fig. III. 15c**), local-

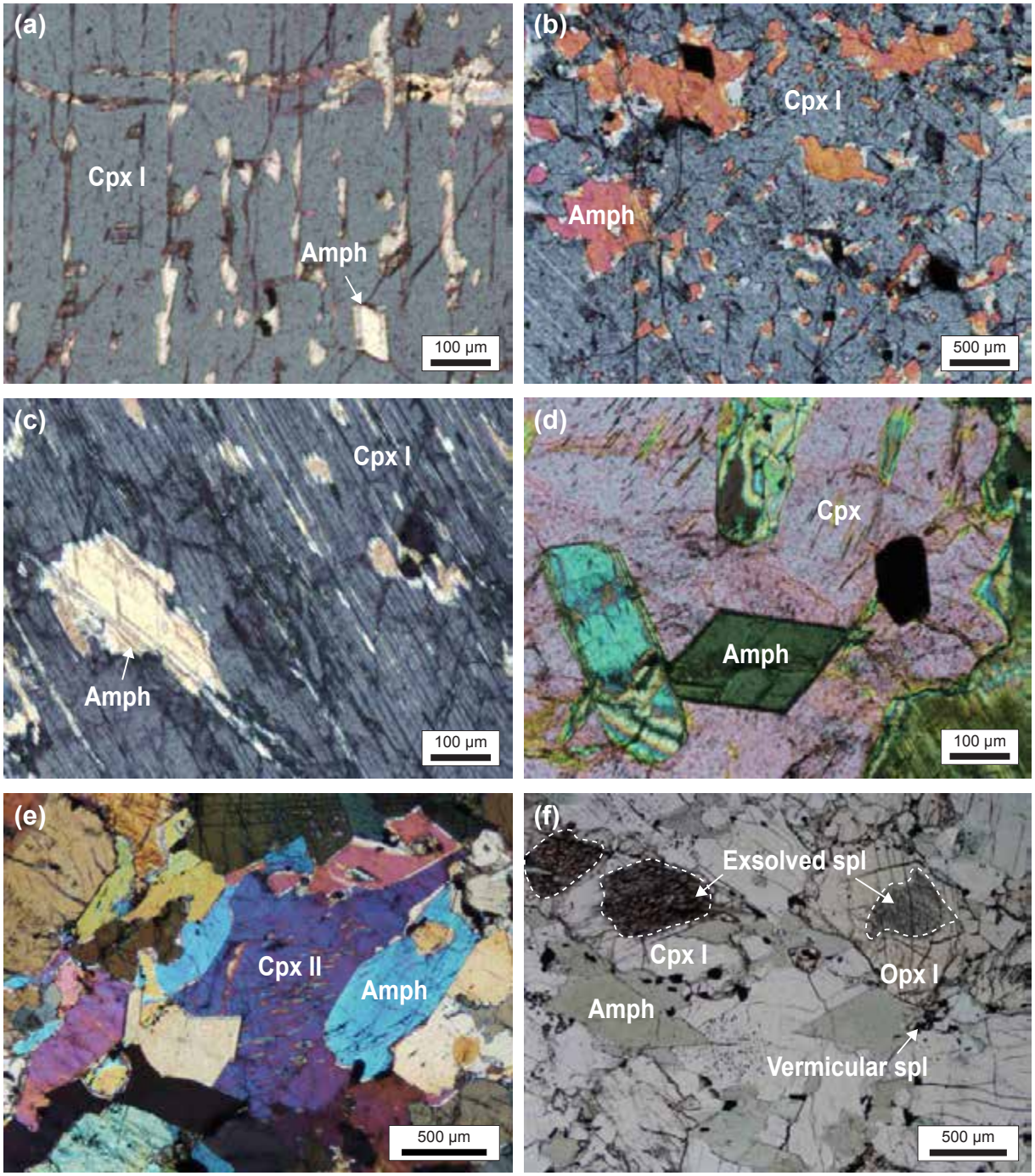

Fig. III. 13. Photomicrographs illustrating the mineralogical features of amphibole in cross-polarized light (**a-e**) and plane-polarized light (**f**): **a-c.** replacement initiated from cleavage of cpx (**a** & **b**) and after needle-shaped exsolution in opx (**c**); **d.** idiomorphic amphibole crystal enclosed in cpx; **e** & **f.** xenomorphic, sub-idiomorphic (**e**) and idiomorphic (**f**) amphibole crystals grown within variously recrystallized cpx-rich matrix. Note that in plane-polarized light, amphibole is pale green, cpx is white and opx is pinkish brown. Back-scattered electron (BSE) images are provided in **Appendix A3** (**Fig. A3. 1** & **2**).

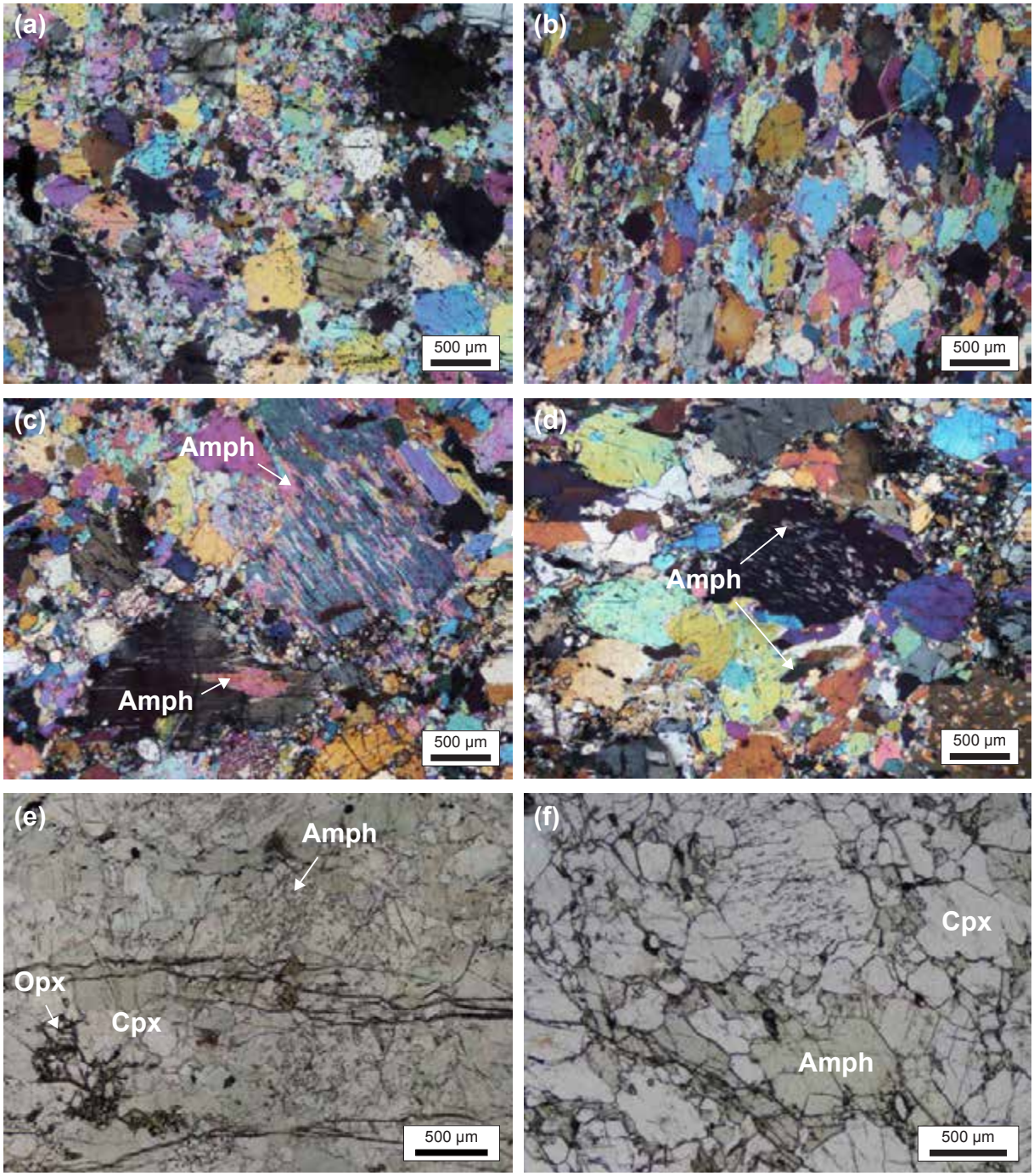

Fig. III. 14. Photomicrographs illustrating the textural overprint of amphibole replacement in cross-polarized light (**a-d**) and plane-polarized light (**e** & **f**): **a.** on a coarse texture, resulting in sutured grain boundaries and poorly equilibrated fine-grained matrix; **b.** on a preferentially oriented granoblastic texture, resulting in interstitial neoblasts between formerly equilibrated granoblasts; **c** & **d.** on a medium-grained granoblastic texture with amphibole occurring both as idiomorphic crystals and in apparent textural equilibrium with cpx; **e** & **f.** on porphyroclastic textures, initiated within matrix minerals and replacing cpx along cleavage and after exsoltion in opx (**e**) then resulting in partly-equilibrated matrix as observed in former granbolastic texture (**f**). Back-scattered electron (BSE) images are provided in **Appendix A3** (**Fig. A3. 1** & **2**).

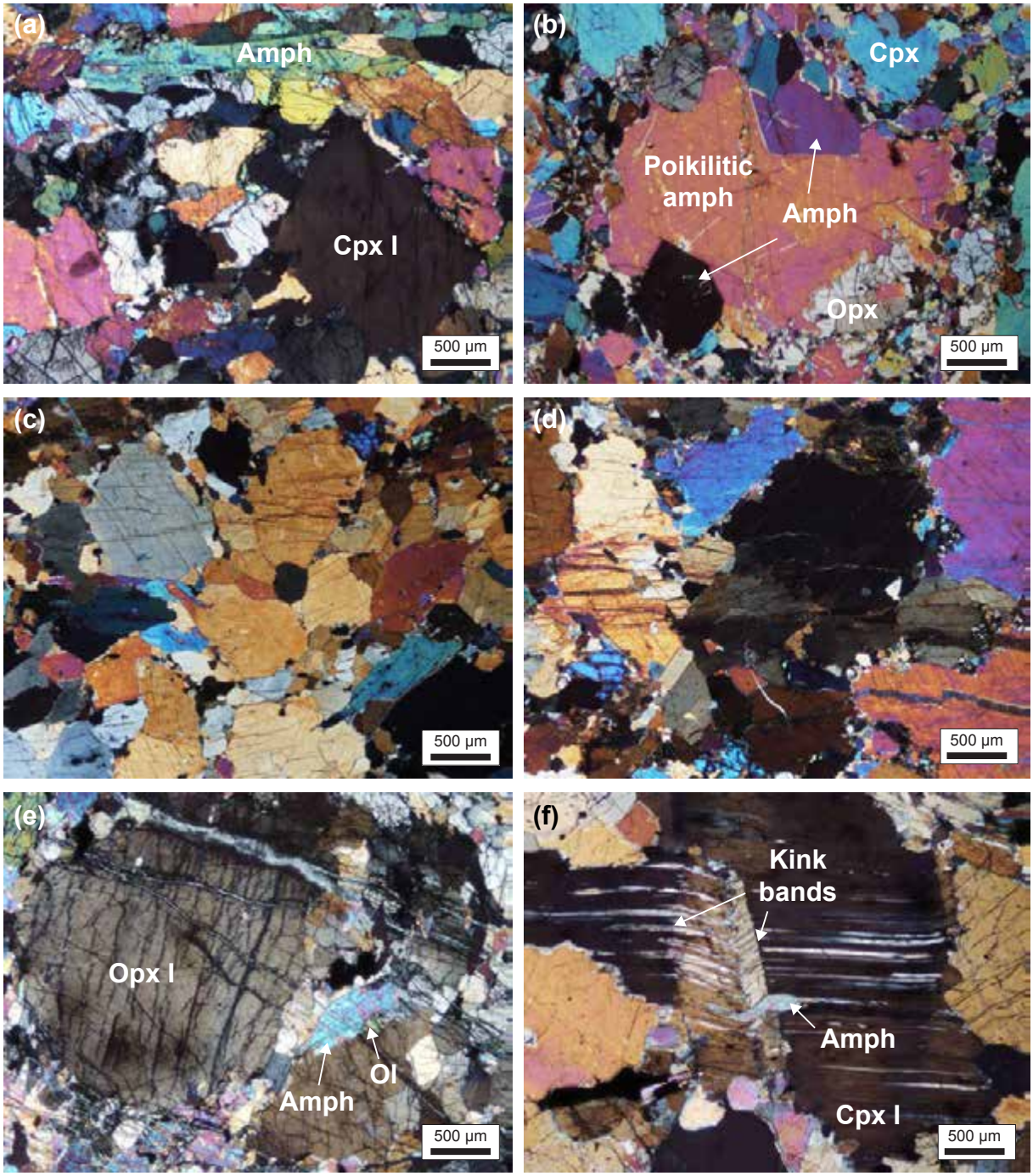

Fig. III. 15. Photomicrographs illustrating chronological constraints on amphibole replacement in cross-polarized light: **a.** elongated sub-idiomorphic crystal post-dating deformation and recrystallization that led to the the partly-equilibrated medium-grained matrix; **b.** poikilitic amphibole enclosing idiomorphic amphibole crystals and pyroxene relics in hornblendite, which suggests (at least) two phases of amphibole growth; **c.** well-equilibrated granoblastic hornblendite including sub-idiomorphic amphibole crystals, indicating an extensive period of annealing between different phases of amphibole growth, note relics of interstitial olivine preserved; **d.** undulose extinction and sub-grain boundaries in large and fractured amphibole; note the incomplete reequilibration of the grain boundaries; **e.** idiomorphic amphibole crystal and opx neoblasts post-dating fracturing of an opx porphyroclast, note the fresh olivine preserved against the amphibole crystal; **f.** sub-idiomorphic amphibole grown after a kink band and cpx exsolution in opx porphyroclast with undulose extinction. Back-scattered electron (BSE) images are provided in **Appendix A3** (**Fig. A3. 1** & **2**).

ly sub-idiomorphic and elongated (**Fig. III. 15a**). In rare cases of extreme amphibolitization (hornblendite), amphibole exhibits a poikilitic texture enclosing other amphiboles (**Fig. III. 15b**), relics of pyroxenes and trails of vermicular spinel, although these minerals are very rarely preserved in such samples

In most cases, amphibole appears unstrained, and clearly post-dates the HT deformation of the pyroxenes (**Fig. III. 15f**), as suggested for instance by undeformed sub-idiomorphic crystals nucleated within kink bands in opx porphyroclasts. Exceptions include samples collected near tectonic contacts where amphibole may exhibit undulose extinction (**Fig. III. 15d**).

5. Spinel

Spinel ranges in modal proportion from 2 to 8 wt % in pyroxenites (< 1 wt % in opx-rich websterites). It is mainly found as rounded or idiomorphic 20-60 μm crystals included in silicates, preferentially cpx and opx I and amphibole (**Fig. III. 16a, b & e**). These inclusions may be restricted to the cores of grains, potentially resulting from diffusion and dynamic recrystallization, but do not define clearly delineated areas. Spinel occurs less commonly as elongated interstitial grains, locally associated with sulfides (**Fig. III. 17f** & **Fig. III. 20c-e**), and as large idiomorphic crystals (**Fig. III. 17e** & **Fig. III. 18a**).

In addition, spinel is observed as needles along cleavages of pyroxene porphyroclasts (**Fig. III. 16a-e**), rarely associated with lamellar amphibole (**Fig. III. 17a** & **d**). They may cover entire porphyroclasts or just the cores (**Fig. III. 17b**), commonly outlining rectangular areas, contrasting with the complex sutured boundaries of the host pyroxenes. This observation may indicate pre-cooling diffusion, or alternatively post-cooling (and/or compositionally distinct) overgrowth of pyroxenes followed by recrystallization and/or annealing. Although these processes are not mutually exclusive, the shape of the exsolved areas suggest that they may represent former well-equilibrated grains. In strongly serpentinized samples, these exsolved phases might be preferentially altered resulting in "corroded" cpx cores (**Appendix A1**).

Less commonly, the exsolved areas have more complex shapes, outlining exsolution-free cracks or rounded shapes, potentially after formerly enclosed spinels (**Fig. III. 17c**), and coronas around the lamellar amphibole-spinel assemblage described above (**Fig. III. 17d-e**). This may indicate that amphibolitization pre-dated exsolution of spinel in pyroxenes upon cooling, or a reverse scenario, in which small-scale, and very localized (particularly along cleavage) partial melting of pyroxenes upon hydration was rapidly followed by co-precipitation of idiomorphic spinel and lamellar amphibole. A similar process within matrix minerals is suggested

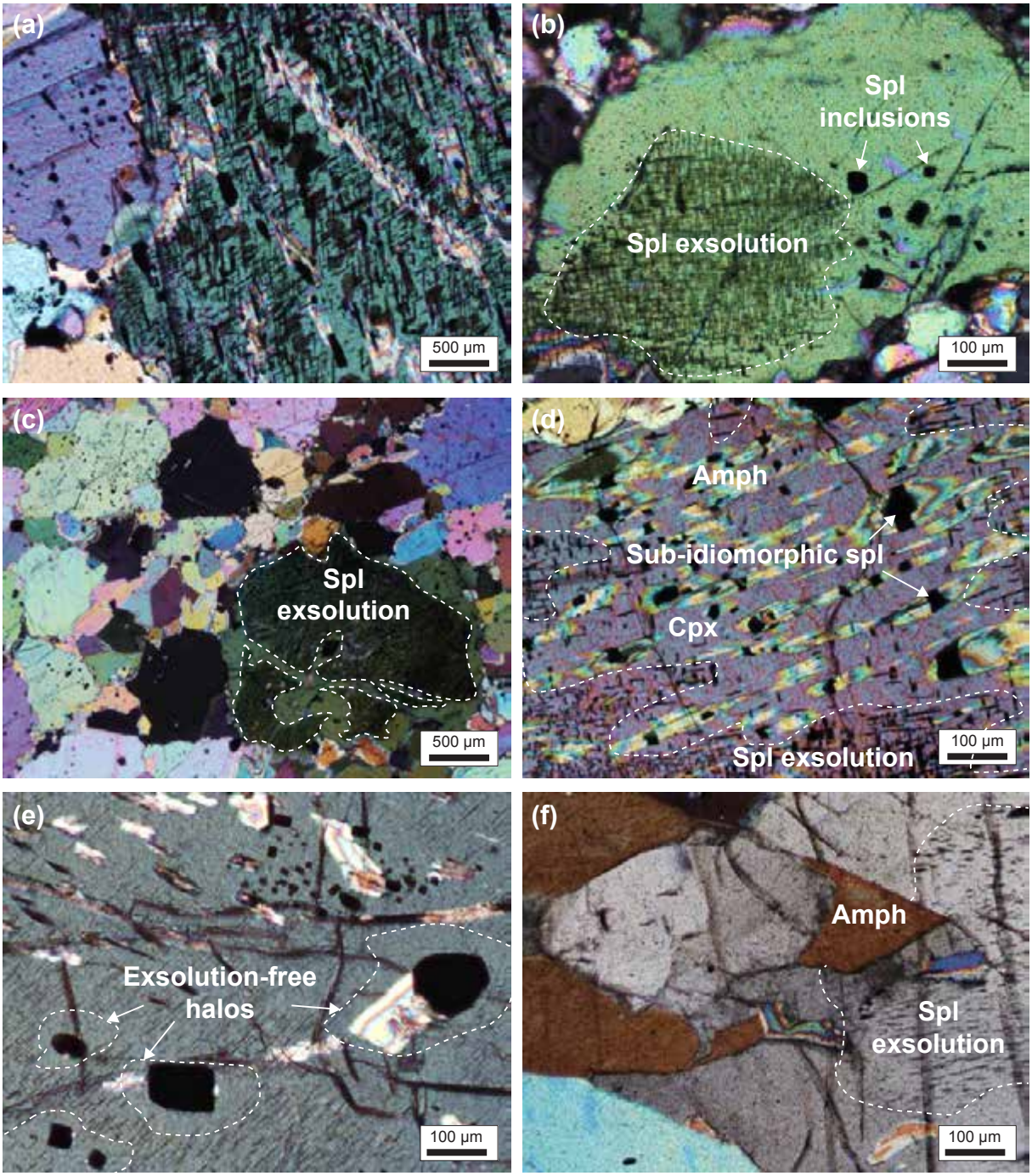

Fig. III. 16. Photomicrographs illustrating the exsolution patterns of spinel in pyroxenes in cross-polarized light: **a-c.** network covering entire cpx grains around spinel inclusions and amphibole (**a**), or outlining rectangular (**b**) or curve-bounded shapes with "negative" cracks and former spinel inclusions (**c**); **d.** amphibole replacement along cleavage associated with (sub-)idiomorphic spinel crystals surrounded by exsolution-free areas in the host cpx; potentially indicating very localized partial melting and re-precipitation upon hydration; **e.** needle-shaped exsolution with exsolution-free halos around spinel inclusions and amphibole; **f.** similar exsolution against sub-idiomorphic amphibole crystal. Back-scattered electron (BSE) images are provided in **Appendix A3** (**Fig. A3. 2**).

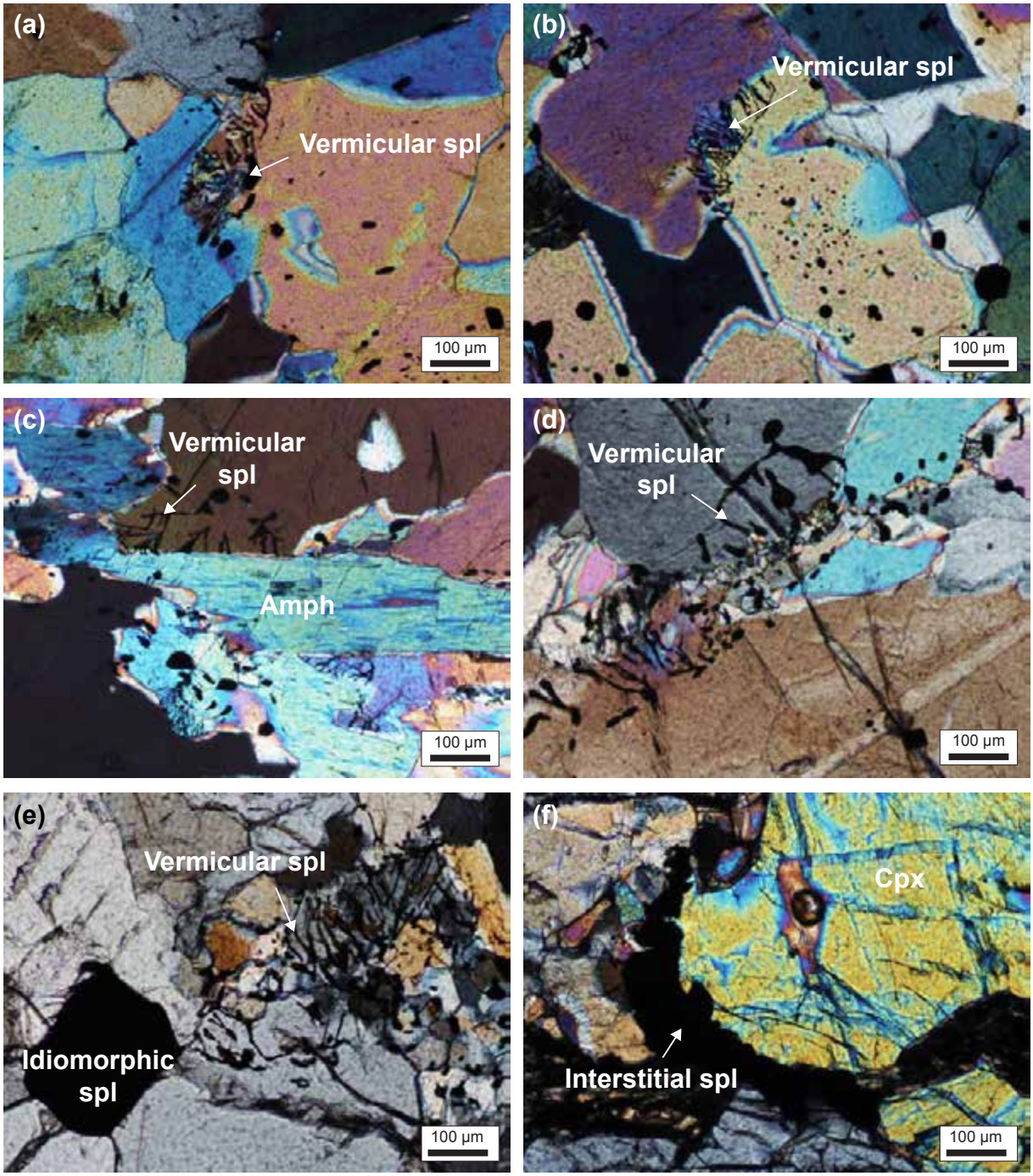

Fig. III. 17. Photomicrographs illustrating vermicular and interstital spinel in cross-polarized light: **a-d.** vermicular in cpx against xenomorphic (**a** & **b**) and sub-idiomorphic amphibole (**c**), and between cpx grains outlining a "path" connected to a xenomorphic amphibole (**d**); **e.** vermicular and idiomorphic in recrystallized opx-rich assemblage; **f.** interstitial grain associated with a base-metal sulfide around cpx.

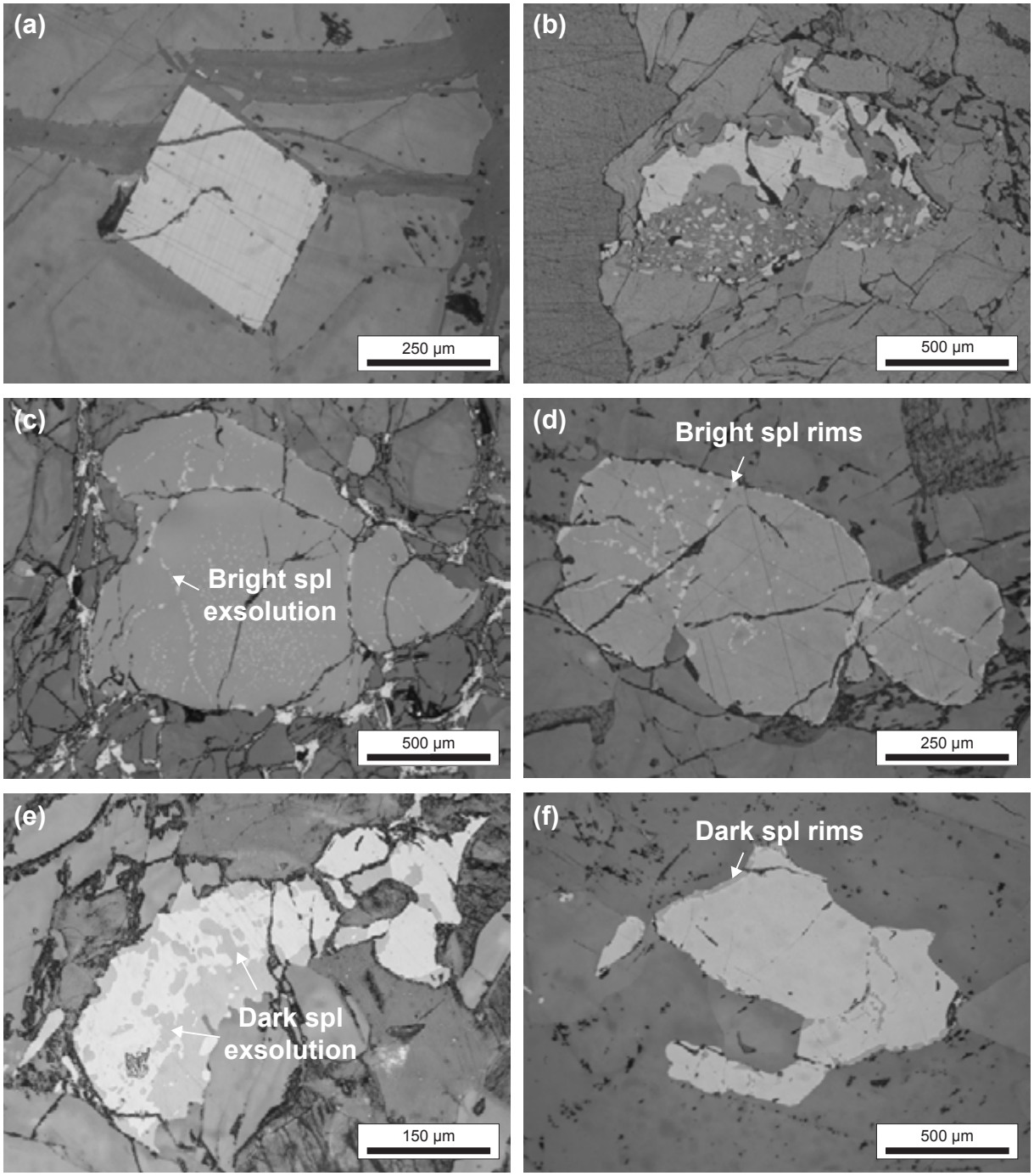

Fig. III. 18. Photomicrographs illustrating mineralogical features of large interstitial spinel in reflected light: **a.** idiomorphic; **b.** leaf-shaped and vermicular, potentially after garnet breakdown; **c** & **d.** with brighter rims and exsolution aligned along cracks and potentially former grain boundaries; **e** & **f.** with darker exsolution (**e**) and rims (**f**).

by the existence of vermicular spinel systematically located near amphibole (**Fig. III. 19a-c**). If this process actually occurred, it implies that amphibolitization may have significantly modified the grain boundaries of pyroxenes even where amphibole is not observed, as suggested by trails of vermicular spinel bridging over distinct pyroxenes (**Fig. III. 19d & e**), potentially following fluid paths.

Spinel may be internally heterogeneous, exhibiting darker (**Fig. III. 18f**) or brighter (**Fig. III. 18c & d**) rims, commonly outlining discrete shapes, or aligned along former cracks or grain boundaries (**Fig. III. 18c-e**). Such internal structures may be observed in enclosed, interstitial or vermicular spinel, although they tend to be more common in enclosed spinel and spinel associated with amphibole, where dark rims outline their common boundaries.

6. Garnet

Garnet occurs in different textural assemblages and represents 6-7 wt % in point-counted samples. It occurs in apparent equilibrium with pyroxenes (**Fig. III. 19a**), as coronas around spinel (**Fig. III. 19e**) or symplectites of spinel and pyroxenes (**Fig. III. 18b** ± amphibole and ilmenite; **Fig. III. 19f**). It also occurs interstitially associated with amphibole, and grown within pyroxenes (**Fig. III. 19d**) in a *type-2* pyroxenite, in a hornblendite layer and in an olivine websterite from the Limo massif.

Garnet is also found in garnet-rich areas, either representing bands in pyroxenite or veins in mylonitic harzburgite, where it encloses cpx, opx and olivine (± spinel) in a poikilitic texture (**Fig. III. 19b & c**), and in the garnet-rich layer located near the top of the pyroxenite-rich area, where it occurs as coronas around zoisite. Andradite-grossular garnet is also observed in the serpentine matrix near tectonic contacts with granulites (**Appendix A**).

7. Accessory minerals

Large interstitial grains of base-metal sulfides (up to 1 wt %) occur as pyrrhotite, pentlandite and chalcopyrite associated with various products of serpentinization and supergene alteration. Chalcopyrite-rich grains are commonly associated with amphibole (**Fig. III. 20f**). Sulfides are also locally associated with Al-rich rimmed Cr-spinel (**Fig. III. 20c-e**), and very rarely occur as rounded homogeneous inclusions in silicates (**Fig. III. 20a & b**), possibly as a result of grain growth during recrystallization. Among the samples checked for the presence of PGM, one sample yielded a number of Pt-Pd-rich tellurides, bismuthides and arsenides with traces of Au and Ag, hosted as needles in sulfides (**Fig. A3. 9**). However, this constitutes

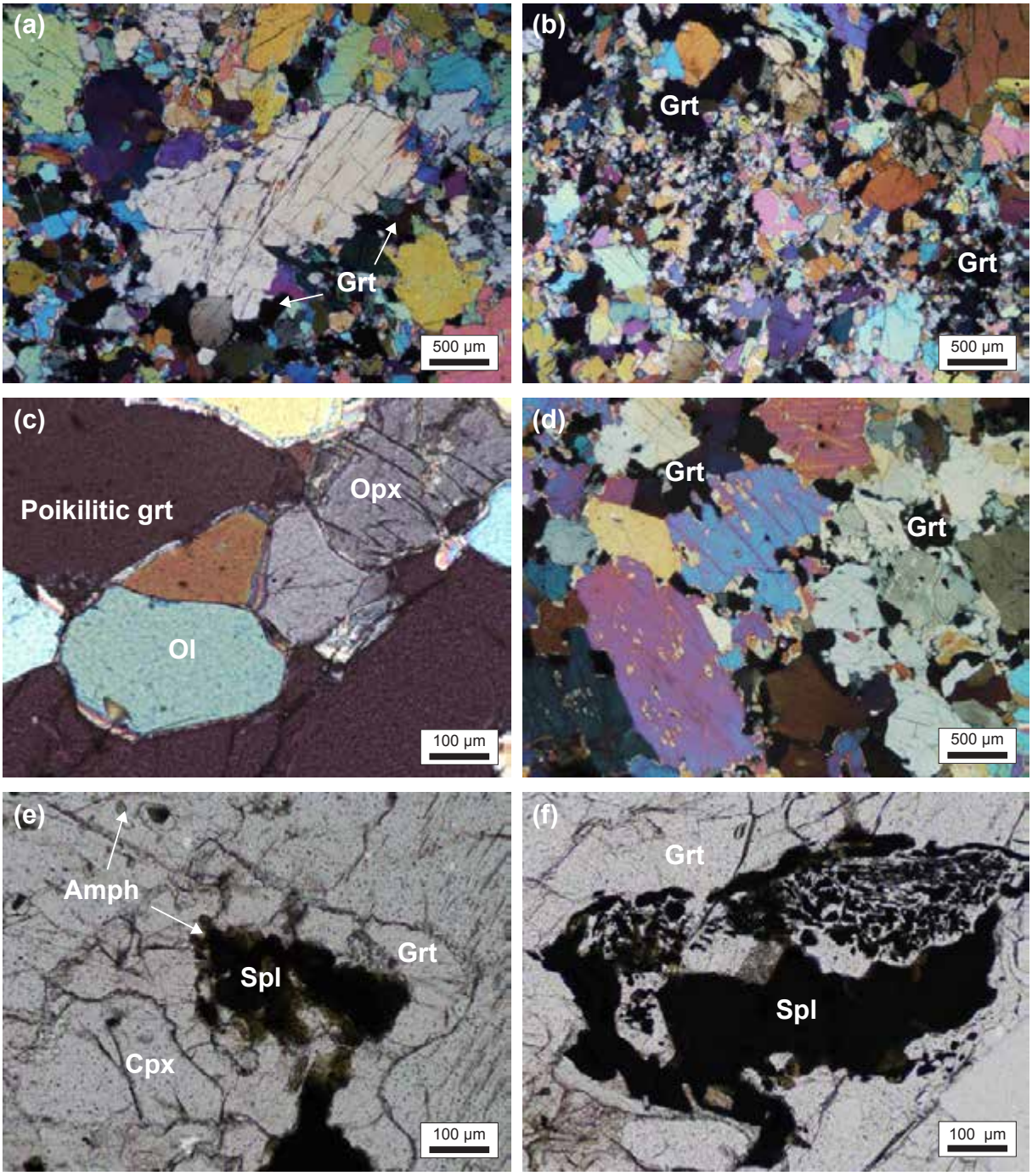

Fig. III. 19. Photomicrographs illustrating textural relationships of garnet in cross-polarized light (**a-d**) and plane-polarized light (**e** & **f**): **a.** as matrix mineral equilibrated with pyroxenes; **b** & **c.** as a poikilitic texture enclosing pyroxenes and olivine; **d.** equilibrated with amphibole grown from matrix minerals and after pyroxenes along cleavage in texture similar to that commonly observed for amphibole (**Fig. III. 14d**); **e.** as corona around spinel (with amphibole along the interface), indicating a prograde reaction; **f.** enclosing a vermicular assemblage of spinel (±ilmenite and amphibole) indicating a retrograde reaction. Back-scattered electron (BSE) images are provided in **Appendix A3** (**Fig. A3. 5**).

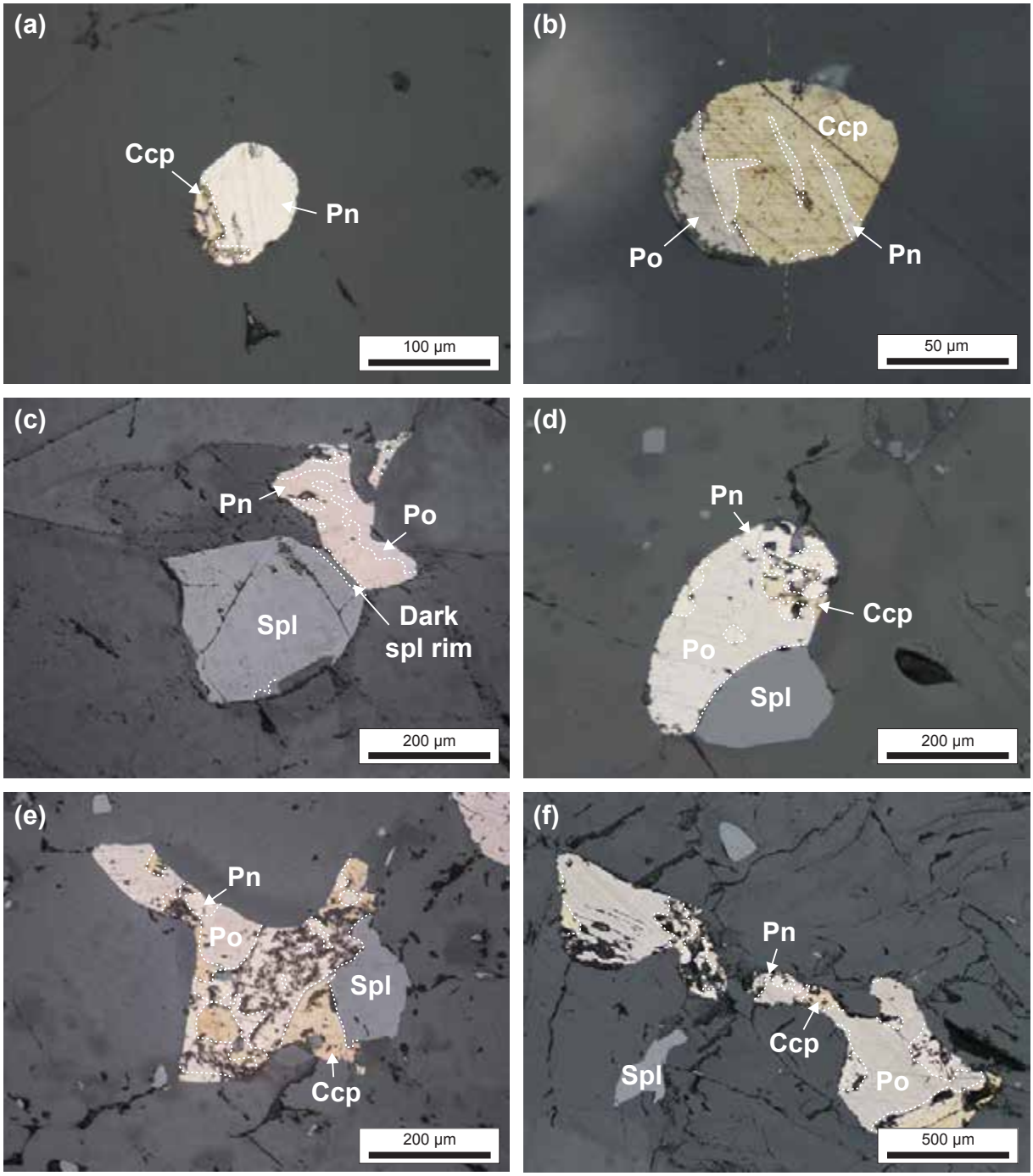

Fig. III. 20. Photomicrographs illustrating mineralogical features of base-metal sulfides in reflected light: **a** & **b**. enclosed; **c-f.** interstital associated with spinel with (**c** & **d**) or without (**e**) darker rim and amphibole (**f**). Note the different proportions of exsolved pyrrhotite (po), pentlandite (pn) and chalcopyrite (ccp) and the textural association of pentlandite and chalcopyrite. Back-scattered electron (BSE) images are provided in **Appendix A3** (**Fig. A3. 8** & **9**).

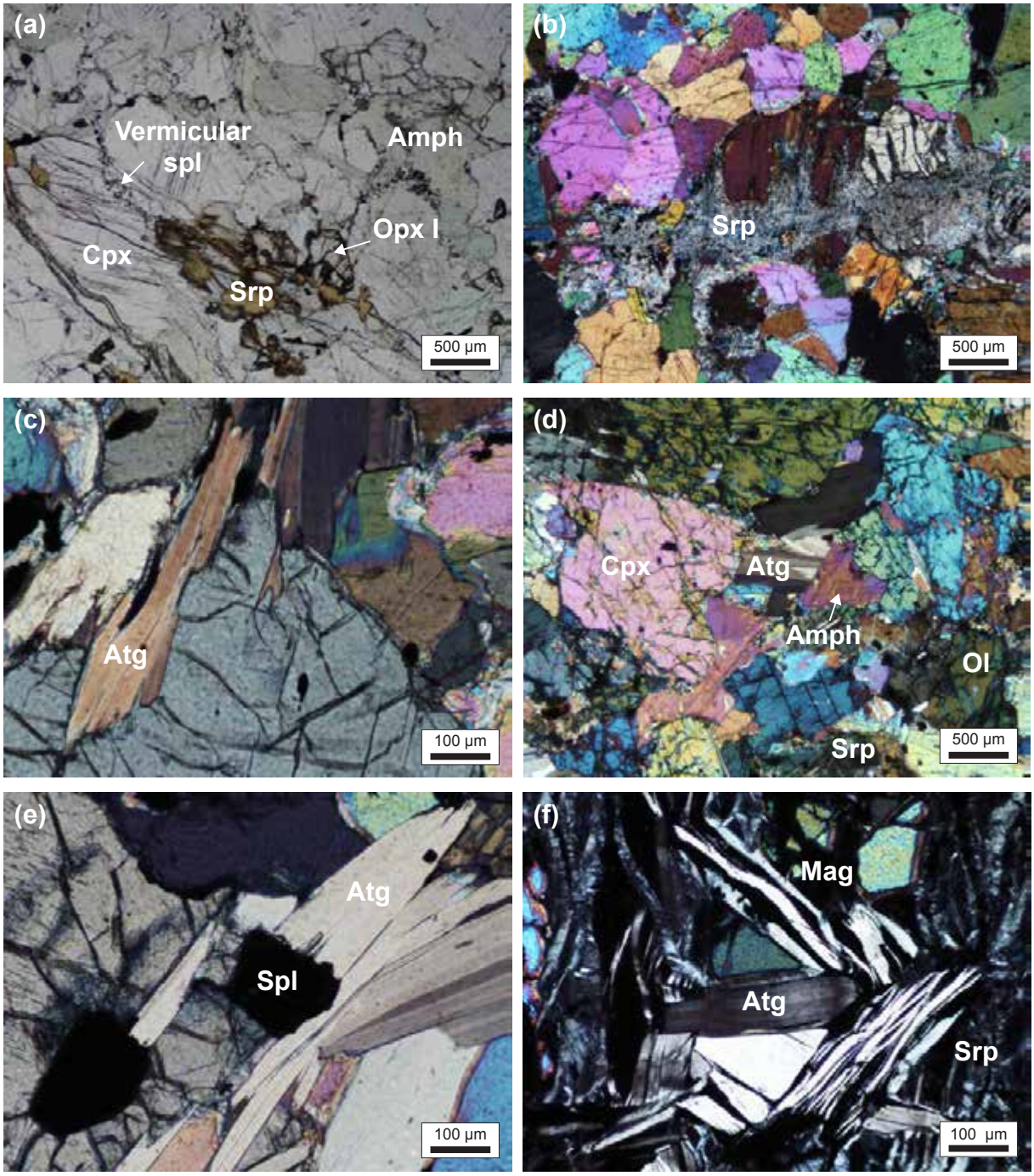

Fig. III. 21. Photomicrographs illustrating the textural relationship of low-temperature minerals in plane-polarized light (**a**) and cross-polarized light (**b-f**): **a.** replacement of opx "connected" to cracks, note trails of vermicular spinels; **b.** after pyroxenes and preferentially along cleavage; **c-f.** antigorite post-dating pyroxenes (**c**) and amphibole (**d**), preferentially grown on spinels (**e**) and associated with low-temperature serpentine (**f**). Back-scattered electron (BSE) images are provided in **Appendix A3** (**Fig. A3. 4**).

only a preliminary investigation.

Serpentine after olivine is abundant in *type-1* pyroxenites and thinly layered *type-2* pyroxenites (< 5 cm) but is otherwise limited (< 1 wt %). Serpentinization after opx is independent of the type of pyroxenites and is instead associated with the development of late fractures (**Fig. III. 21 a & b**). Antigorite may occur as late clusters of platy crystals representing < 2 wt %, preferentially grown on spinel and after or contemporaneously with amphibole (**Fig. III. 21c-f**).

Interstitial phlogopite associated with ilmenite and chlorite was reported by Girardeau & Gil Ibarguchi (1991) near late tectonic contacts, along with zoisite in retrogressed pyroxenites. Magnetite and carbonates also occur sporadically.

SUMMARY OF CHAPTER III

- The **lithological heterogeneity** of the massif is dominantly **igneous** (*i.e.* non-tectonic) and **pre-dates** the development of sheath folds and mylonites related to **high-shear strain deformation.** It also predates most **high-temperature deformation**, although thin pyroxenite layers may have recorded additional deformation with respect to massive pyroxenites of greater thickness.

- **Foliated (*type-3*)** pyroxenites may represent the **hydrated** (*i.e.* commonly amphibolitized) and **deformed** products of **dunite-bearing (*type-1*)** and, to a minor extent, **massive (*type-2*)** pyroxenites. **Tectonic slicing** is likely to explain most of the range in thickness of the pyroxenite layers (from < 1 cm to several meters) thus **hindering** the observation of **original magmatic layering**.

- Petrographic observations strikingly indicate **extensive sub-solidus re-equilibration**. This includes the development of:

  - **garnet coronas around spinel** and pyroxenes-spinel-amphibole (± ilmenite) **symplectites after garnet breakdown**;
  - **abundant amphibole** (up to 40 wt %), including idiomorphic crystals;
  - **exsolution** of needle-shaped **spinel** in pyroxenes, commonly restricted to the cores or parts of porphyroclasts, and preferentially **replaced by amphibole.**

- **Amphibolitization** at least partly **post-dates** the development of deformation-related textures, ranging from **porphyroclastic** to **granoblastic**. This **textural overprint** consists in the preferential replacement of matrix pyroxenes (within interstitial trails of olivine in *type-1* pyroxenites), of the rims of porphyroclasts or granoblasts (which results in **sutured grain boundaries**) and along their cleavage. **Vermicular spinels** and **sulfides** are commonly associated with amphibole.

Chapter IV.

Major- and Trace-Element Geochemistry

A. WHOLE-ROCK COMPOSITIONS

1. Mineral modes

Mineral modes were estimated by point counting and converted to wt % from mineral densities[1]. Least-squares fitted modes were calculated from whole-rock and mineral major-element compositions using MINSQ (Herrmann & Berry, 2002). The solving method of Solver in Microsoft Excel™ was set to the GRG Nonlinear engine for most samples, and to the Evolutionary engine for samples where satisfactory values (*i.e.* < 1) of residual sum of squares (RSSQ) values could not be reached. A constrained minimization of 0-100 wt % was used for all minerals apart from spinel, which was constrained to a maximum set to the counted value when available, or arbitrarily to 5 wt %.

Point-counted modes are consistent with mineral modes calculated using the least-squares method for the pyroxenites (**Table IV-1**), although the latter tends to give slightly lower cpx/opx ratios and higher olivine proportions than the former. Point counting yields 32-80 wt % cpx (10-23 wt % in opx-rich, *type-4* websterites) and 0-45 wt % opx (65-79 wt % in *type-4* websterites). Pyroxenites with dunite lenses (*type 1*) and foliated (*type-3*) pyroxenite have higher cpx/opx ratios than massive (*type-2*) pyroxenites (**Fig. IV. 1**). Olivine is mostly restricted to

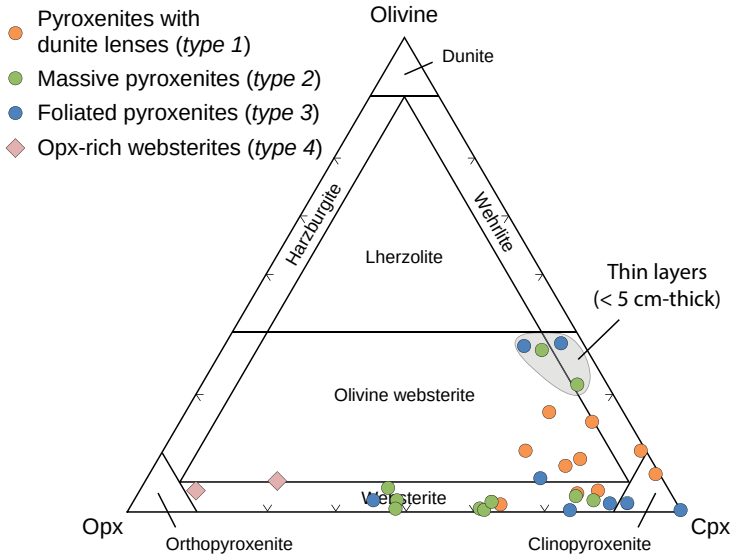

Fig. IV. 1. Point-counted modal compositions of Cabo Ortegal pyroxenites recalculated into proportions of olivine (including serpentine), clinopyroxene (cpx) and orthopyroxene (opx).

1 d = 3.1 (cpx), 3.3 (opx), 3.2 (olivine), 3.2 (amphibole), 4.6 (spinel), 3.8 (garnet), 2.6 (serpentine), from Deer *et al.* (2013).

Table IV-1. Point-counted and calculated modal compositions

Mineral		Cpx	Opx	Ol	Amph	Spl	Grt		Sulf	Srp	Other	RSSQ	Total
Pyroxenites with dunite lenses (*type 1*)													
CO-012-A		57.4 (57.3)	27.4 (24.0)	0 (10.6)	6.0 (1.5)	6.6 (5.8)			0.4	1.1	1.4[2]	0.04	99.1
CO-013-A		62.1 (53.8)	5.6 (6.8)	0 (17.8)	8.9 (12.8)	4.7 (3.5)			1.4	15.7	1.9[1]	0.01	94.7
CO-013-C		63.1 (45.8)	13.8 (14.8)	0.3 (14.0)	8.2 (21.8)	4.4 (0)			0.7	7.9	2.0[1]	0.03	96.5
CO-066-B2	*	55.1	18.1	6.2	11.2	4.1			1.0	4.3			
CO-091-A		72.2 (67.4)	0.9 (10.0)	3.3 (10.3)	11.1 (2.2)	4.9 (4.9)			0.3	7.3		0.30	94.8
CO-094-B		79.9 (56.3)	0.6 (9.1)	4.9 (20.4)	8.0 (8.1)	3.8 (3.8)				1.9	1.1[1]	0.09	97.8
CO-095-A		74.4 (79.6)	11.6 (13.6)	1.7 (1.2)	6.7 (0)	2.8 (2.8)			0.6	2.2		1.08	97.2
CO-096-A		63.4	10.5	6.6	14.1	3.1				2.4			
CO-096-B		69.5 (58.8)	14.8 (11.5)	2.1 (10.5)	8.3 (14.4)	3.8 (3.8)			0.4	1.0		0.54	99.0
CO-096-C		33.6	7.1	13.8	6.4	4.8			0.2	34.0			
CO-100	*	52.0	10.5	7.5	15.2	5.7			0.1	8.9			
Massive pyroxenites (*type 2*)													
CO-006-A		45.3 (50.5)	24.8 (29.6)	0 (0.9)	26 (13.3)	3.4 (3.4)			0.4	0.1		0.41	97.8
CO-006-B		46.2 (54.2)	26.3 (21.4)	0 (1.7)	15.6 (16.9)	3.1 (3.1)	6.8 (0.9)		0.3	0.5		0.00	98.3
CO-007		55.9 (53.4)	28.5 (24.2)		10.9 (19.1)	2.9 (2.9)			0.2	1.6		0.72	99.5
CO-019-A		34.4 (56.9)	38.5 (21.9)	0 (1.3)	20.2 (16.6)	2.5 (2.5)			0.7	3.8		0.16	99.1
CO-024		33.8 (41.9)	35.5 (22.1)	0 (0.1)	17.9 (32.7)	2.5 (2.5)	6.0 (0.7)		1.4	1.6	0.2[1]	0.16	100.0
CO-025		59.8 (60.1)	13.1 (25.2)	0 (1.0)	18.9 (7.4)	5.1 (4.6)			0.9	2.3		0.04	98.3
CO-045-A		42.9 (54.1)	45.2 (31.1)	0 (2.4)	8.3 (6.8)	2.3 (2.3)			0.9	0.5		0.07	96.8
CO-046-A		66.3 (70.2)	11.6 (14.8)	0 (0.1)	11.4 (4.6)	7.7 (6.4)			1.0	1.9		0.07	96.0
CO-046-C	*	57.2	4.6		9.7	4.7			1.4	22.4			
CO-065	*	55.1	7.9	4.8	4.5					27.6	0.2[1]		
Foliated pyroxenites (*type 3*)													
CO-004-A		57.3 (57.9)	0 (4.8)		42.5 (37.3)					0.2		0.07	100.0
CO-009		69.2 (77.5)	9.8 (2.8)	0 (7.9)	11.1 (5.2)	6.0 (5.2)			1.0	1.3	2.0[2]	0.03	98.5
CO-010-A	*	48.0	3.1	1.6	14.3	4.4			2.3	26.3			
CO-010-B	*	47.3 (55.7)	9.7 (9.6)	0 (24.7)	7.9 (4)	4.6 (1.3)			0.3	30.2		0.01	95.3
CO-020-C	*		1.7	0.6	64.6	1.9			30.8		0.4[1]		
CO-044-C		30.5 (32.3)	37.9 (37.6)		23.7 (27.5)	5.2 (1.6)			1.0	1.6		0.88	98.9
CO-067		63.9 (46.8)	6.3 (20.3)		25.7 (29.3)	2.5 (2.5)			0.4	1.1		0.46	98.9
CO-098		54.7 (48.4)	16.9 (15.1)	0 (2.0)	21.1 (31.1)	1.8 (1.8)			0.3	5.3		0.06	98.4
CO-101		46.4 (32.5)	11.6 (12.9)		38.1 (49.8)	3.2 (3.2)			0.6	0.2		0.66	98.4
Opx-rich websterites (*type 4*)													
CO-002-A	*	9.8	79.4	0.6	5.0	1.0			0.7	3.5			
CO-048		22.6 (5.4)	64.9 (79.9)	3.9 (6.3)	5.9 (3.7)	0.3 (0.3)			0.3	2.1		3.64	95.5
Pyroxenite dyke													
CO-064-C	*	55.7 (19.5)	16 (32.5)	1.8 (31.6)	9.1 (5)	4.2 (4.2)			0.6	12.0	0.9[1]	7.99	92.7
Other													
CO-069		71.2				4.7	7.0			19.5	1.4[3]		
Dunites													
CO-012-D		(8.1)	(13.6)	(65.0)		(0.3)						0.03	87.0
CO-013-B	*	18.5 (7.5)	2.6 (17.2)	7.6 (59.9)	6.3 (1.0)	0.8 (1.4)			0.3	62.7	1.1[1]	0.01	87.0
CO-022-A			(18.7)	(61.9)		(1.6)				(0.3)		0.25	82.2
Harzburgites													
CO-003†			(26.0)	(49.4)	(7.5)	(2.1)						1.10	85.0
CO-015-B	*	1.4 (0.1)	3.0 (27.3)	4.2 (52.6)	10.2 (5.3)	1.5 (0.0)				82.6	0.4[1]	0.29	85.3
CO-031A*			(26.9)	(43.8)	(14.8)	(0.9)						0.29	86.5
CO-035*			(21.8)	(43.6)	(17.9)	(4.0)						0.20	87.3
CO-052		(0.9)	(23.9)	(45.4)	(13.8)	(4.3)						0.13	88.3
CO-084			(23.1)	(52.9)	(7.8)	(5.0)						1.10	88.8

* Heterogeneous sections (see text for further details); other minerals include: [1] antigorite, [2] chlorite, [3] wollastonite. Total values are those from the least-squares method calculation.

type-1 pyroxenites with the exception of thin pyroxenite layers (< 5 cm) where it may result from mechanical mixing with host peridotites (**Fig. IV. 1**). Modal proportions of amphibole range from 6-14 wt % in *type-1* and 4-26 wt % *type-2* pyroxenites to 8-42 wt % in *type-3* pyroxenites. Spinel represents 2-8 wt % (< 1 wt % in opx-rich websterites), garnet 6-7 wt % when present, and sulfides never exceed 1 wt %.

As for the modal compositions of peridotites, there is a discrepancy between the calculated mode and petrographic observations as dunites have apparent lherzolitic compositions. This is inherent to the least-square calculation which does not take into account serpentine or other hydrous alteration minerals. Indeed, Si/(Fe + Mg) in serpentine (~ 1/2) is higher than in olivine (~ 1/2). This induces an overestimation of the proportion of pyroxenes, which have high Si/(Fe+Mg) (~ 1). In addition, these calculations had high residual sums of squares (RSSQ) due to the overestimation of Al_2O_3 and CaO, hence again the overestimation of the proportion of pyroxenes (**Table IV-1**). This may be also due to the high Al_2O_3 of chlorite or the presence of disseminated carbonates related to serpentinization.

2. Major elements

Whole-rock major-element compositions were determined in two different batches by ALS minerals, Seville, Spain and by the Service d'Analyse des Roches et des Minéraux of the Centre de Recherches Pétrographiques et Géochimiques (CRPG), Nancy, France, using inductively coupled plasma atomic-emission spectroscopy (ICP-AES); loss on ignition (LOI) was also determined at 1000°C for each sample.

Whole-rock major- and trace-element compositions of Cabo Ortegal pyroxenites with dunite lenses (*type-1*), massive (*type-2*), foliated (*type-3*) and opx-rich (*type-4*) pyroxenites from this study are reported in **Table IV-2**. Major-oxide compositions are plotted against MgO in **Fig. IV. 2** along with compositions of Cabo Ortegal peridotites and mafic rocks. Compared with pyroxenite xenoliths and pyroxenites from orogenic and ophiolitic massifs worldwide, Cabo Ortegal *type-1*, *-2* and *-3* pyroxenites are very rich in CaO (11.2-20.1 wt %), SiO_2 (47.0-52.7 wt %) and Cr_2O_3 (0.23-1.93 wt %) and have low TiO_2 (< 0.20 wt %) and Al_2O_3 (1.29-6.59 wt %) resulting in high CaO/Al_2O_3 ratios (2.2-11.3) and Cr#[2] (0.04-0.37). They also have relatively high Mg# ranging between 0.83 and 0.89, which is intermediate between Cabo Ortegal peridotites and mafic rocks. *Type-1* pyroxenites are restricted to high values (0.87-0.89), overlapping

2 Molar Cr/(Al + Cr)

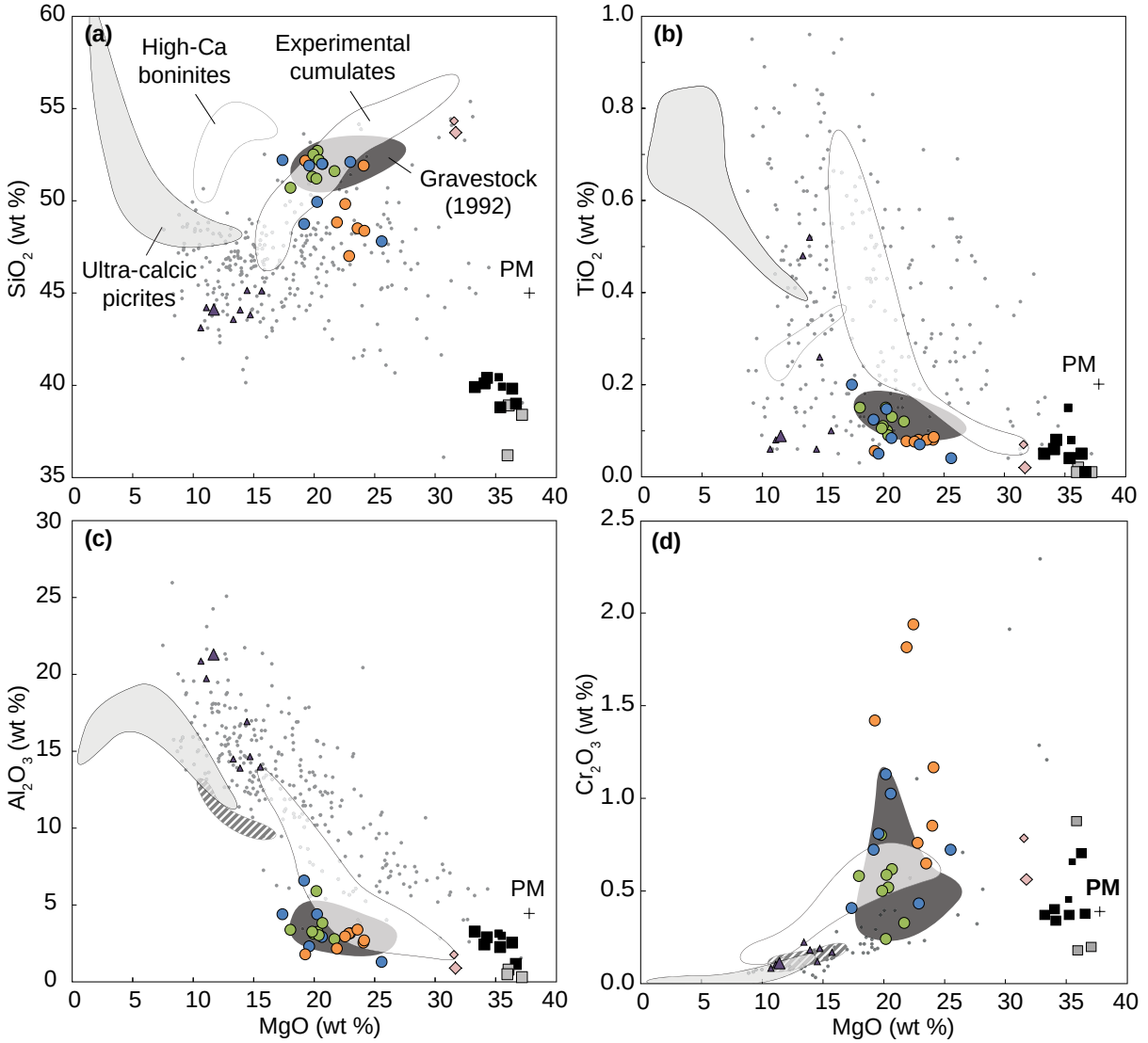

(continued on next page)

the compositions of Cabo Ortegal dunites and some harzburgites, although these have much higher MgO and FeO. Our data overlap the range of compositions previously reported for Cabo Ortegal pyroxenites (Gravestock, 1992), but extend it to slightly higher CaO and lower TiO_2. The content of most major oxides is directly related to modal variations. Opx-rich websterites accordingly have higher MgO and SiO_2, and lower CaO, Al_2O_3, and TiO_2 than other types of pyroxenite.

Alkalis are generally very low in all types of pyroxenite, including opx-rich websterites, although K_2O reaches 0.27 wt % in amphibole-rich, *type-3* pyroxenites. Cabo Ortegal pyroxenites are thus comparable in terms of major-element chemistry with the pyroxenitic compositions reconstructed by Müntener *et al.* (2001) from the experimental products of crystallization of hydrous basaltic andesite and high-Mg# andesite at 1.2 GPa (**Fig. IV. 2**). Differences include

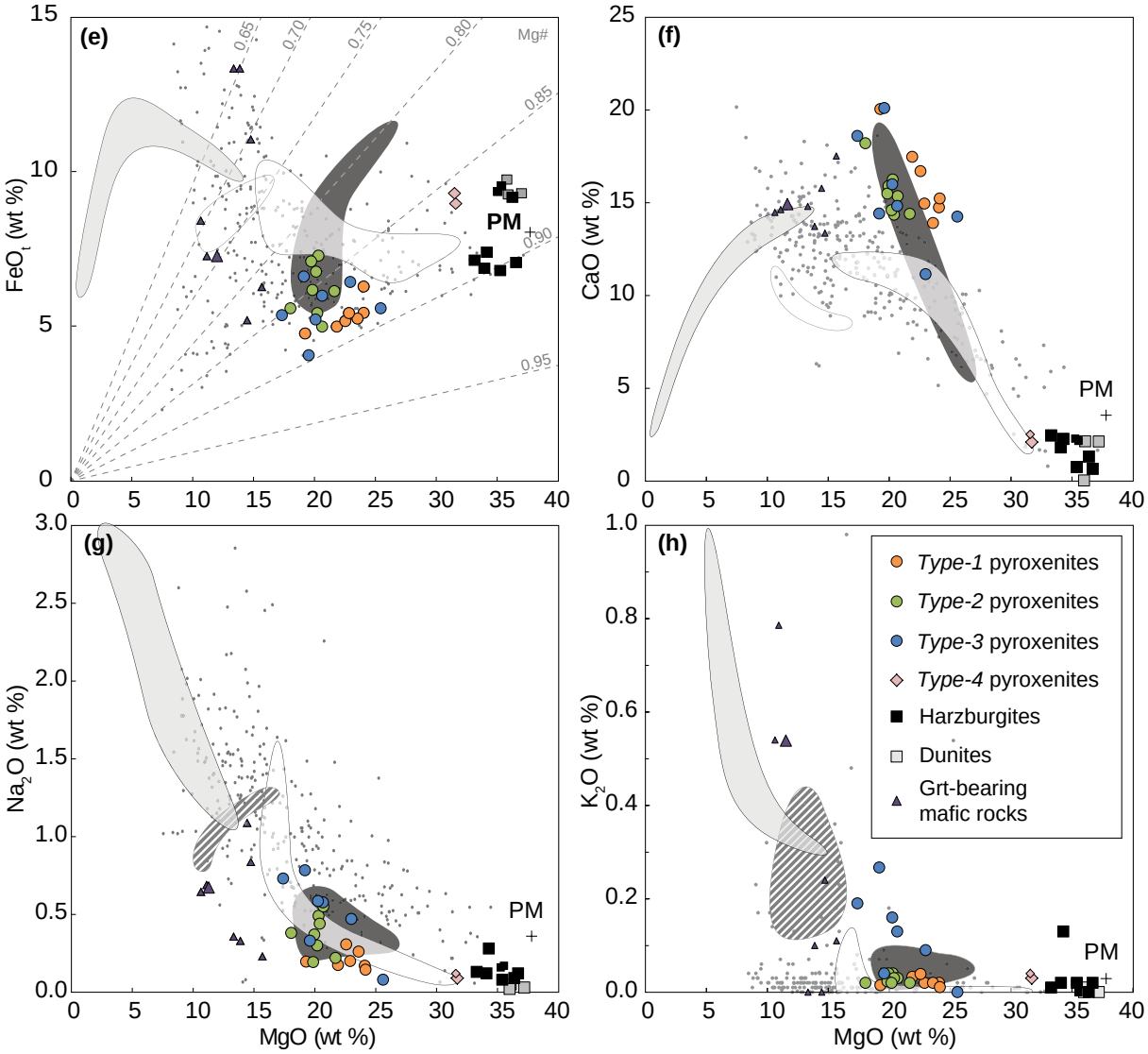

Fig. IV. 2. Whole-rock major-element compositions of Cabo Ortegal pyroxenites, peridotites and mafic rocks: MgO *vs* **a.** SiO_2; **b.** TiO_2; **c.** Al_2O_3; **d.** Cr_2O_3; **e.** FeO_t, with corresponding Mg#; **f.** CaO; **g.** Na_2O; **h.** K_2O. Additional data for Cabo Ortegal pyroxenites from Gravestock (1992) are shown for comparison.Samples of opx-rich websterites, peridotites and mafic rocks from Santos *et al.* (2002) are also shown, with smaller symbols. Experimental cumulates refer to pyroxenite compositions reconstructed by Müntener *et al.* (2001) from the products of crystallization of hydrous basaltic andesite and high-Mg# andesite at 1.2 GPa. Ultra-calcic picrites refer to whole-rock compositions of ankaramitic lavas reported by Barsdell and Berry (1990) from Western Epi, Vanuatu. High-Ca boninites refer to whole-rock compositions of lavas from the Troodos ophiolite, Cyprus and from the north Tonga trench, which were used by Crawford *et al.* (1989) in their classification of boninites. A worldwide database of mantle pyroxenites (massifs and xenoliths) is shown for comparison (Xiong *et al.*, 2014). PM, Primitive mantle; Mg#, molar ratio of $Mg^{2+}/(Mg^{2+} + Fe^{tot})$.

higher CaO and lower FeO_t and TiO_2 for Cabo Ortegal pyroxenites, and lower SiO_2 and higher Cr_2O_3 in the case of *type-1* pyroxenites. Comparison with the compositions of ultra-calcic picrites and high-Ca boninites is also shown here and discussed in **Chapter VI** in terms of melt differentiation.

Table IV-2. a. Whole-rock compositions of Cabo Ortegal *type-1* pyroxenites

Sample	CO-012-A	CO-013-A	CO-013-C	CO-091-A	CO-094-B	CO-095-A	CO-096-B
wt %	*	*	*	†	†	†	†
SiO_2	51.90	47.00	48.50	48.83	48.37	52.16	49.82
TiO_2	0.08	0.08	0.08	0.08	0.09	0.06	0.08
Al_2O_3	2.55	3.14	3.39	2.16	2.69	1.78	2.94
Cr_2O_3	0.84	0.75	0.64	n.a.	n.a.	n.a.	n.a.
FeO_t	5.44	5.41	5.23	4.97	6.26	4.77	5.16
MnO	0.13	0.12	0.12	0.12	0.13	0.13	0.12
MgO	24.10	22.90	23.60	21.90	24.16	19.28	22.58
CaO	14.75	14.95	13.90	17.47	15.23	20.04	16.70
Na_2O	0.17	0.20	0.26	0.17	0.14	0.20	0.31
K_2O	0.02	0.02	0.02	0.03	0.01	0.02	0.04
P_2O_5	< dl	< dl	< dl	< dl	< dl	< dl	< dl
LOI	0.95	5.45	5.21	3.40	1.93	0.93	1.58
Total	101.54	100.64	101.54	99.68	99.72	99.89	99.91
Mg#	0.89	0.88	0.89	0.89	0.87	0.88	0.89
ppm							
Li	1.4	1.9	1.9	1.0	1.0	2.6	0.7
Be	n.a.	n.a.	n.a.	0.50	0.04	0.40	0.16
B	5	8	8	12.3	13.2	13.5	10.9
Sc	159	189	211	41	38	44	29
V	135	189	202	256	252	240	181
Cr	n.a.	n.a.	n.a.	6194	3959	4833	6616
Co	197	71	71	43	55	43	45
Ni	764	1125	781	527	500	380	633
Cu	183	353	159	122	68	182	278
Zn	19.3	29.2	24.0	19.6	27.6	19.5	14.5
Ga	1.71	2.27	2.78	1.51	1.99	1.67	1.56
Rb	0.86	0.43	0.63	0.30	0.27	0.53	0.46
Sr	18	27	38	55	9	33	17
Y	3.17	3.87	4.07	2.41	2.60	1.47	2.08
Zr	0.81	0.94	2.39	2.02	1.75	2.46	1.50
Nb	n.a.	n.a.	n.a.	n.a.	0.05	0.06	0.10
Cs	0.09	0.14	0.15	0.03	0.04	0.10	0.03
Ba	9.2	12.1	17.5	11.2	6.3	6.2	13.5
La	0.33	0.23	0.39	1.09	0.22	1.10	0.20
Ce	0.36	0.36	1.02	2.37	0.44	2.09	0.36
Pr	0.06	0.06	0.15	0.26	0.06	0.22	0.04
Nd	0.39	0.34	0.67	1.03	0.36	0.80	0.24
Sm	0.20	0.17	0.20	0.23	0.17	0.17	0.12
Eu	0.08	0.07	0.08	0.09	0.07	0.07	0.05
Gd	0.33	0.37	0.38	0.31	0.28	0.22	0.20
Tb	0.06	0.08	0.09	0.06	0.06	0.04	0.04
Dy	0.50	0.59	0.64	0.40	0.43	0.25	0.32
Ho	0.11	0.13	0.15	0.09	0.10	0.05	0.08
Er	0.34	0.41	0.44	0.25	0.28	0.16	0.22
Tm	n.a.	n.a.	n.a.	n.a.	n.a.	n.a.	n.a.
Yb	0.32	0.40	0.46	0.22	0.25	0.15	0.21
Lu	0.05	0.06	0.07	0.03	0.04	0.02	0.03
Hf	0.10	0.09	0.14	0.08	0.09	0.08	0.07
Ta	n.a.	n.a.	n.a.	n.a.	0.002	0.003	0.004
Pb	0.3	0.9	1.1	1.0	0.4	1.1	0.6
Th	0.42	0.33	0.18	0.08	0.06	0.12	0.06
U	0.11	0.10	0.11	0.08	0.06	0.09	0.05

Table IV-2. b. Whole-rock compositions of Cabo Ortegal *type-2* pyroxenites

Sample	CO-006-A	CO-006-B	CO-007	CO-019-A	CO-024	CO-025	CO-045-A	CO-046-A
wt %	*	†	*	*	*	*	*	*
SiO_2	52.20	51.30	52.00	52.70	51.20	52.50	51.60	50.70
TiO_2	0.09	0.11	0.13	0.10	0.15	0.11	0.12	0.15
Al_2O_3	3.03	3.26	3.82	3.25	5.89	3.13	2.77	3.38
Cr_2O_3	0.51	n.a.	0.61	0.58	0.23	0.49	0.32	0.57
FeO_t	7.27	7.07	4.98	5.44	6.73	6.17	6.12	5.57
MnO	0.16	0.18	0.12	0.13	0.16	0.15	0.12	0.13
MgO	20.40	19.85	20.70	20.30	20.20	19.95	21.70	18.05
CaO	14.35	15.49	15.35	16.25	14.60	15.90	14.40	18.20
Na_2O	0.44	0.19	0.55	0.49	0.30	0.37	0.22	0.38
K_2O	0.03	0.02	0.03	0.04	0.02	0.04	0.02	0.02
P_2O_5	< dl	< dl	< dl	< dl	< dl	< dl	< dl	< dl
LOI	0.99	0.48	1.39	1.26	0.88	1.05	1.09	0.97
Total	100.29	98.74	100.24	101.17	101.12	100.56	99.18	98.76
Mg#	0.83	0.83	0.88	0.87	0.84	0.85	0.86	0.85
ppm								
Li	1.9	2.4	2.3	2.4	1.7	2.0	1.2	1.8
Be	n.a.	0.63	n.a.	n.a.	n.a.	n.a.	n.a.	n.a.
B	5	18.1	5	< dl	< dl	6	< dl	5
Sc	281	73	318	230	246	277	211	332
V	209	438	283	256	241	244	231	261
Cr	n.a.	2707	n.a.	n.a.	n.a.	n.a.	n.a.	n.a.
Co	86	74	76	57	61	58	108	56
Ni	358	217	799	531	230	353	770	267
Cu	95	174	232	197	41	118	524	208
Zn	31.6	34.2	25.2	19.8	43.0	30.5	29.0	22.6
Ga	3.24	3.52	4.24	11.60	4.58	3.88	3.25	2.54
Rb	0.50	0.61	1.05	0.84	0.78	0.65	0.63	0.55
Sr	13	57	45	49	42	90	49	47
Y	2.08	3.33	2.41	3.07	2.78	3.74	1.37	3.46
Zr	1.00	5.40	1.51	1.15	3.11	1.89	1.42	5.31
Nb	0.06	n.a.	n.a.	n.a.	0.11	0.56	n.a.	n.a.
Cs	0.05	0.07	0.15	0.27	0.16	0.12	0.09	0.10
Ba	21.9	14.0	23.5	123.0	22.0	26.3	19.0	13.3
La	0.00	0.91	1.30	0.46	0.82	2.05	0.44	0.91
Ce	0.17	2.80	1.47	0.55	1.82	7.81	0.74	1.95
Pr	0.05	0.42	0.12	0.07	0.22	1.22	0.11	0.28
Nd	0.36	2.00	0.50	0.40	1.01	4.91	0.52	1.26
Sm	0.16	0.51	0.24	0.17	0.30	0.89	0.24	0.39
Eu	0.09	0.17	0.14	0.10	0.15	0.28	0.10	0.17
Gd	0.24	0.53	0.35	0.34	0.43	0.71	0.31	0.49
Tb	0.05	0.08	0.06	0.06	0.08	0.11	0.05	0.09
Dy	0.34	0.54	0.42	0.52	0.51	0.66	0.30	0.60
Ho	0.08	0.12	0.09	0.11	0.11	0.13	0.05	0.13
Er	0.24	0.35	0.27	0.35	0.29	0.42	0.12	0.39
Tm	n.a.	n.a.	n.a.	n.a.	n.a.	n.a.	n.a.	n.a.
Yb	0.23	0.34	0.25	0.34	0.27	0.37	0.08	0.35
Lu	0.04	0.05	0.04	0.05	0.04	0.05	0.01	0.05
Hf	0.14	0.20	0.19	0.10	0.20	0.09	0.09	0.20
Ta	0.002	n.a.	n.a.	n.a.	0.002	0.014	n.a.	n.a.
Pb	0.7	1.4	1.2	1.9	0.7	0.9	1.1	1.0
Th	0.30	0.09	0.84	0.21	0.23	0.31	0.09	0.22
U	0.06	0.14	0.27	0.19	0.13	0.24	0.22	0.20

Table IV-2. c. Whole-rock compositions of Cabo Ortegal *type-3* pyroxenites

Sample	CO-004-A	CO-009	CO-010-B	CO-044-C	CO-067	CO-098	CO-101
wt %	*	*	*	*	†	†	†
SiO_2	52.20	51.90	47.80	52.10	52.00	49.93	48.74
TiO_2	0.20	0.05	0.04	0.07	0.08	0.15	0.12
Al_2O_3	4.39	2.30	1.29	3.15	2.92	4.39	6.59
Cr_2O_3	0.40	0.80	0.71	0.42	n.a.	n.a.	n.a.
FeO_t	5.36	4.05	5.57	6.43	5.99	5.18	6.62
MnO	0.15	0.12	0.12	0.15	0.15	0.11	0.16
MgO	17.40	19.60	25.60	23.00	20.66	20.26	19.18
CaO	18.60	20.10	14.25	11.15	14.83	15.99	14.42
Na_2O	0.73	0.33	0.08	0.47	0.58	0.59	0.78
K_2O	0.19	0.04	< dl	0.09	0.13	0.16	0.27
P_2O_5	< dl	< dl	< dl	< dl	< dl	< dl	< dl
LOI	1.59	1.48	5.39	1.33	1.92	2.82	1.91
Total	101.87	101.24	101.48	99.12	99.93	100.16	99.53
Mg#	0.85	0.90	0.89	0.86	0.86	0.88	0.84
ppm							
Li	3.9	1.4	1.3	1.8	3.5	5.8	2.0
Be	n.a.	n.a.	n.a.	n.a.	2.52	0.88	2.36
B	5	6	7	< dl	12.9	12.7	13.2
Sc	395	292	171	186	37	36	60
V	246	191	155	183	255	224	305
Cr	n.a.	n.a.	n.a.	n.a.	3475	3835	2446
Co	52	44	71	80	42	51	46
Ni	258	428	1022	417	373	352	257
Cu	74	109	202	92	170	85	159
Zn	29.0	10.6	23.1	31.4	21.9	17.1	16.9
Ga	8.04	3.54	1.20	5.83	2.25	3.20	4.10
Rb	1.58	0.57	0.10	1.61	1.11	2.54	2.83
Sr	425	97	16	108	146	104	139
Y	6.31	2.55	1.68	1.96	1.61	1.90	4.58
Zr	5.47	2.08	0.01	5.14	4.72	12.96	15.39
Nb	0.80	n.a.	n.a.	n.a.	n.a.	n.a.	1.19
Cs	0.03	0.05	0.02	0.14	0.07	0.26	0.16
Ba	68.6	28.2	7.1	54.5	28.1	54.4	84.5
La	7.27	3.40	0.55	1.64	2.07	2.44	1.95
Ce	14.09	5.58	0.34	3.66	4.42	5.15	4.48
Pr	1.69	0.52	0.02	0.48	0.55	0.55	0.61
Nd	6.68	1.52	0.11	2.03	2.18	2.03	2.73
Sm	1.22	0.26	0.08	0.44	0.38	0.38	0.62
Eu	0.40	0.10	0.04	0.12	0.13	0.16	0.23
Gd	1.17	0.33	0.16	0.37	0.34	0.40	0.63
Tb	0.17	0.07	0.04	0.06	0.05	0.06	0.10
Dy	1.12	0.44	0.26	0.35	0.26	0.34	0.69
Ho	0.23	0.09	0.06	0.07	0.05	0.07	0.16
Er	0.63	0.27	0.19	0.21	0.16	0.20	0.47
Tm	n.a.	n.a.	n.a.	n.a.	n.a.	n.a.	n.a.
Yb	0.54	0.25	0.17	0.21	0.15	0.17	0.49
Lu	0.08	0.04	0.02	0.03	0.02	0.02	0.07
Hf	0.30	0.12	0.06	0.21	0.15	0.36	0.75
Ta	0.021	n.a.	n.a.	n.a.	n.a.	n.a.	0.081
Pb	2.5	1.6	0.7	1.3	2.1	1.6	3.2
Th	0.51	0.52	0.40	0.28	0.21	0.30	0.23
U	0.28	0.20	0.11	0.32	0.16	0.14	0.36

Table IV-2. d. Whole-rock compositions of Cabo Ortegal peridotites

	Dunites			Harzburgites					
Sample	CO-012-D	CO-013-B	CO-022-A	CO-003	CO-015-B	CO-031-A	CO-035	CO-052	CO-084
wt %	*	*	*	*	*	*	*	*	†
SiO_2	38.40	38.90	36.20	38.80	39.00	40.10	39.90	40.40	39.81
TiO_2	0.01	0.02	0.01	0.04	0.01	0.06	0.05	0.08	0.05
Al_2O_3	0.30	0.79	0.49	2.25	1.16	2.42	3.26	2.89	2.55
Cr_2O_3	0.19	0.17	0.87	0.36	0.37	0.39	0.36	0.33	n.a.
FeO_t	9.26	9.21	9.71	6.81	7.05	6.85	7.12	7.38	9.13
MnO	0.14	0.14	0.12	0.10	0.11	0.11	0.12	0.12	0.11
MgO	37.20	36.10	36.00	35.40	36.70	34.10	33.30	34.30	36.39
CaO	2.13	2.14	0.03	0.75	0.66	1.81	2.45	2.26	1.32
Na_2O	0.03	0.05	0.02	0.08	0.12	0.12	0.13	0.28	0.09
K_2O	< dl	0.01	< dl	0.02	0.02	0.02	0.01	0.13	< dl
P_2O_5	< dl	< dl	< dl	< dl	< dl	< dl	< dl	0.01	< dl
LOI	11.70	11.20	16.00	15.70	15.30	11.25	11.35	11.25	11.60
Total	100.40	99.77	100.54	101.07	101.29	98.00	98.85	100.26	100.07
Mg#	0.89	0.89	0.89	0.89	0.89	0.89	0.89	0.89	0.89
ppm									
Li	< dl	0.6	< dl	< dl	0.5	1.1	0.6	0.7	2.1
Be	n.a.	n.a.	n.a.	n.a.	n.a.	n.a.	n.a.	n.a.	< dl
B	9	12	11	5.0	7.0	31.0	12.0	5.0	< dl
Sc	5	4	< dl	< dl	< dl	0.1	9	3	11
V	42	45	39	54	45	69	76	61	93
Cr	n.a.	n.a.	n.a.	n.a.	n.a.	n.a.	n.a.	n.a.	2376
Co	147	124	123	114	108	101	98	98	82
Ni	1539	1441	1427	1808	1776	1624	1572	1464	1596
Cu	< dl	< dl	< dl	< dl	< dl	< dl	< dl	< dl	17
Zn	36.7	34.1	59.8	48.5	45.8	47.2	42.5	45.0	36.6
Ga	0.66	0.67	0.65	1.98	1.28	2.93	2.49	4.07	1.73
Rb	0.05	0.08	0.01	0.28	0.25	0.47	0.27	1.71	0.29
Sr	15	9	2	19	20	23	17	35	4
Y	0.39	0.65	0.05	1.33	0.32	1.44	2.34	2.58	1.57
Zr	< dl	0.11	< dl	0.99	0.33	0.53	0.13	2.80	1.26
Nb	n.a.	n.a.	n.a.	n.a.	0.07	n.a.	n.a.	n.a.	0.03
Cs	0.00	0.01	0.004	0.03	0.02	0.11	0.02	0.03	0.04
Ba	5.4	4.2	3.4	12.3	9.3	21.5	16.3	34.7	6.8
La	0.58	< dl	0.40	0.65	1.21	0.86	0.74	0.89	0.11
Ce	1.32	0.02	1.00	0.93	1.55	1.76	0.91	2.52	0.16
Pr	0.15	0.01	0.11	0.09	0.11	0.20	0.08	0.43	0.01
Nd	0.51	0.06	0.31	0.33	0.24	0.76	0.29	2.19	0.07
Sm	0.06	0.02	0.02	0.08	0.01	0.18	0.12	0.58	0.05
Eu	0.02	0.01	0.01	0.04	0.01	0.06	0.05	0.18	0.03
Gd	0.05	0.06	0.01	0.13	0.02	0.20	0.20	0.54	0.12
Tb	0.01	0.01	0.00	0.03	0.005	0.04	0.05	0.08	0.03
Dy	0.07	0.10	0.01	0.19	0.04	0.23	0.35	0.43	0.23
Ho	0.01	0.03	0.002	0.05	0.01	0.05	0.08	0.09	0.06
Er	0.04	0.08	0.01	0.14	0.04	0.15	0.27	0.24	0.18
Tm	n.a.	n.a.	n.a.	n.a.	n.a.	n.a.	n.a.	n.a.	n.a.
Yb	0.04	0.08	0.02	0.16	0.06	0.15	0.26	0.24	0.19
Lu	0.01	0.01	0.00	0.02	0.01	0.02	0.04	0.04	0.03
Hf	< dl	0.07	< dl	0.10	0.02	0.04	0.03	0.10	0.06
Ta	n.a.	n.a.	n.a.	n.a.	0.003	n.a.	n.a.	n.a.	0.001
Pb	0.2	0.3	0.1	0.2	0.5	0.3	0.3	0.5	0.2
Th	< dl	0.33	< dl	0.24	0.32	0.18	0.12	0.03	0.01
U	0.08	0.03	0.05	0.06	0.10	0.12	0.07	0.06	0.01

Table IV-2. e. Other whole-rock compositions

	Opx-rich wbt.	Pyr. dyke	Grt-bearing	Other
Sample	CO-048	CO-064-C	CO-026	CO-069
wt %	*	*	†	†
SiO_2	53.70	44.40	44.08	49.27
TiO_2	0.02	0.09	0.09	0.05
Al_2O_3	0.89	2.25	20.71	1.81
Cr_2O_3	0.56	0.47	0.06	1.03
FeO_t	8.98	11.17	7.20	4.46
MnO	0.17	0.16	0.12	0.16
MgO	31.70	29.90	11.19	20.38
CaO	2.10	6.10	14.96	19.52
Na_2O	0.09	0.15	0.65	0.09
K_2O	0.03	0.02	0.55	< dl
P_2O_5	< dl	< dl	< dl	< dl
LOI	1.03	5.23	1.05	3.50
Total	98.28	98.70	99.54	99.39
Mg#	0.89	0.89	0.73	0.89
ppm				
Li	5.4	0.9	10.5	2.7
Be	n.a.	n.a.	0.14	1.04
B	5	n.a.	n.a.	14.0
Sc	10	28	37	48
V	45	213	141	275
Cr	n.a.	n.a.	194	6274
Co	81	93	46	46
Ni	843	1059	58	633
Cu	109	306	49	106
Zn	38.1	38.2	28.6	24.9
Ga	3.49	2.30	12.26	1.22
Rb	1.41	0.25	7.96	0.05
Sr	80	5	360	57
Y	0.31	2.60	2.01	1.77
Zr	0.39	2.53	1.46	1.25
Nb	0.08	0.02	0.09	0.33
Cs	0.99	0.04	0.07	0.01
Ba	33.9	3.1	131.7	3.5
La	0.81	0.07	2.40	1.04
Ce	1.91	0.17	4.34	1.85
Pr	0.23	0.03	0.71	0.18
Nd	0.78	0.25	2.80	0.59
Sm	0.10	0.14	0.62	0.13
Eu	0.03	0.06	0.29	0.04
Gd	0.08	0.25	0.48	0.21
Tb	0.01	0.05	0.06	0.04
Dy	0.05	0.41	0.31	0.29
Ho	0.01	0.09	0.07	0.06
Er	0.02	0.28	0.19	0.19
Tm	n.a.	n.a.	0.10	1.08
Yb	0.05	0.29	0.18	0.19
Lu	0.01	0.04	0.03	0.03
Hf	0.07	0.12	0.05	0.05
Ta	0.003	0.001	0.003	0.038
Pb	0.4	0.3	0.8	1.3
Th	0.07	0.02	0.04	0.13
U	0.05	0.02	0.16	0.16

* Major-element compositions were determined by solution ICP-AES after $LiBO_2$ fusion at ALS Minerals, Spain; trace-element compositions (except Li and B) were determined by solution ICP-MS at GET, Toulouse, France; Li and B were analysed at SARM, CRPG, Nancy, France by flame AAS after acid digestion and by UV-Vis after Na_2Co_3 fusion, respectively.

† Major-element compositions (except Cr_2O_3) were determined after $LiBO_2$ fusion by solution ICP-AES, and Cr by ICP-MS, at SARM, CRPG, Nancy, France; trace-element compositions (including Li, B and Be) were determined by solution ICP-MS at GET, Toulouse, France.

FeO_t, total Fe as FeO; LOI, loss on ignition; < dl, below detection limit; n.a., not analyzed.

3. Trace elements

Whole-rock trace-element compositions were analysed in two different batches by solution inductively-coupled plasma mass spectrometry (ICP-MS) on an Agilent 7500ce system and on a high-resolution (HR)-ICP-MS Element XR at Géosciences Environnement Toulouse (GET), Toulouse, France. Homogeneous sections of samples were cut and cleared of patina using a rock saw and then powdered in an agate mill for 2-5 min.; the mill was cleaned between samples using MQ water and ethanol. Prior to powdering, samples were rinsed, cleaned ultrasonically in Milli-Q® water and oven-dried to eliminate potential contamination from the saw. Powders were digested following method C of Yokoyama *et al.* (1999) and spiked with a solution of pure Tm, following Barrat *et al.* (2012). USGS standard BHVO-2 was used to check measurements and instrumental drift, and analyses of IWG-GIT standard PM-S and CRPG standard UB-N were included as unknown samples for quality control. Corresponding analyses are reported along with details of sample digestion and data collection in **Appendix B**.

The different types of pyroxenite have very distinctive whole-rock REE compositions (**Fig. IV. 3**). Most *type-1* pyroxenites have a characteristic spoon-shaped pattern with flat HREE [$(Gd/Lu)_{CN}$ = 0.73-1.3; CN indicates chondrite-normalized], whereas *type-3* pyroxenites have enriched and strongly fractionated LREE and MREE [$(La/Gd)_{CN}$ = 2.6-8.6]. Exceptions include a LREE-enriched *type-1* pyroxenite (CO-092-A) sampled near a pyroxenite dyke with dunitic rims (**Fig. III. 9a**). *Type-2* pyroxenites exhibit a range of REE patterns with progressive LREE enrichment [$(La/Gd)_{CN}$ = 1.1-3.2], including a very LREE-depleted sample (CO-006-A) with $(La/Gd)_{CN} < 0.01$ and a sample (CO-045A) with a saddle-shaped REE pattern. Most LREE-enriched *type-2* and *-3* samples also exhibit slightly negative slopes from MREE to HREE [$(Gd/Lu)_{CN}$ = 1.1-2.0]. Among all types, only the least enriched *type-2* samples and two *type-3* samples exhibit a slightly positive Eu anomaly [$(Eu/Eu^*)_{CN}$ = 1.1-1.4]. Trace-element compositions of Cabo Ortegal peridotites and other rocks (including samples from Santos *et al.*, 2002) can be found in the **Appendix C1**.

In a multi-element diagram normalized to primitive-mantle values, whole-rock trace elements exhibit strong enrichment of most large-ion lithophile elements (LILE) and other fluid-mobile elements, relative to neighbouring lithophile elements (**Fig. IV. 4**). This enrichment is pronounced, although variable (regardless of the types of pyroxenite) for Cs, Ba, U, Pb and Sr. Rb, Th and K are enriched with respect to neighbouring lithophile elements only in foliated (*type-3*) pyroxenites. Variations in Li content in *type-2* and *-3* pyroxenites result in zero to

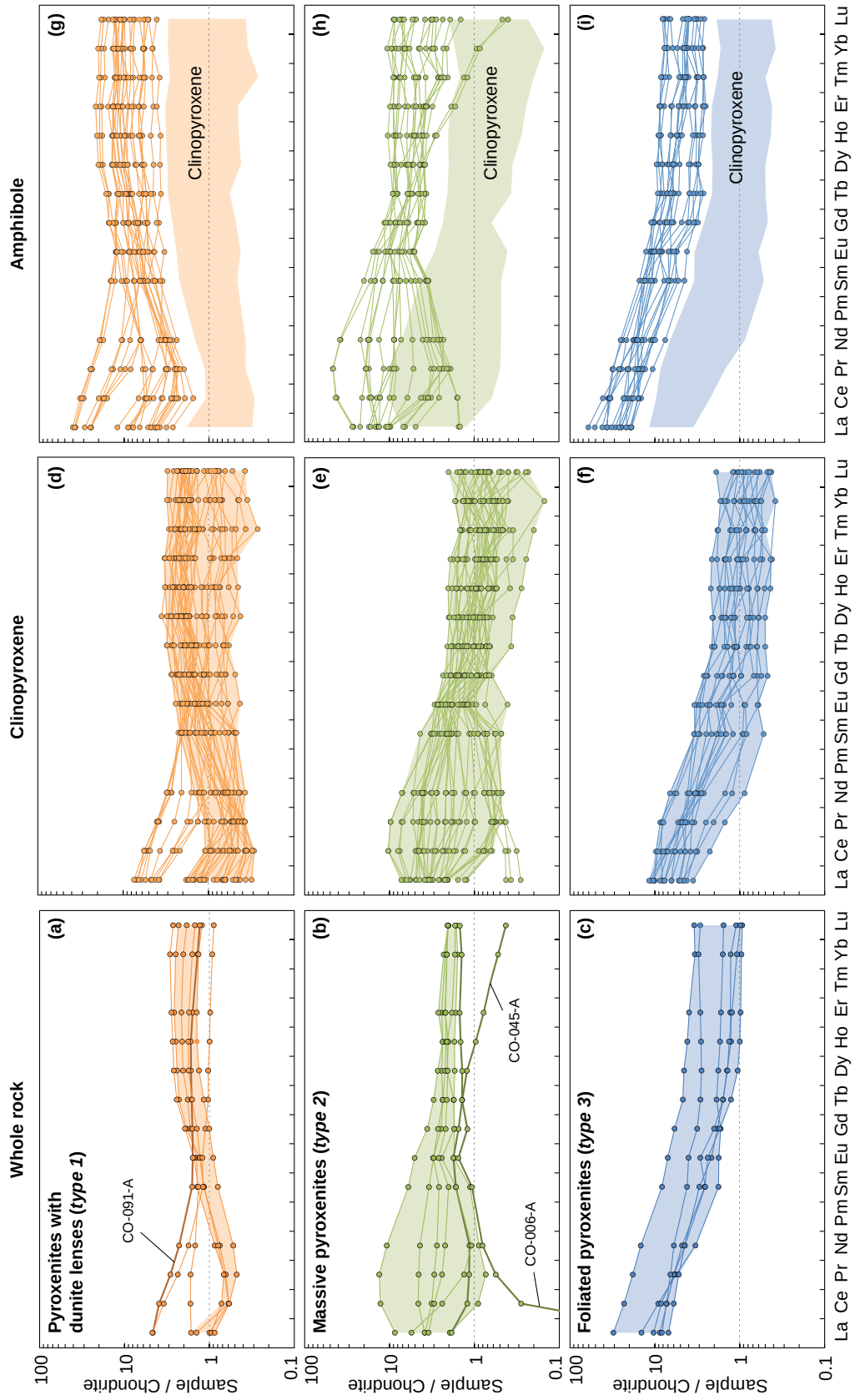

Fig. IV. 3. Chondrite-normalized REE patterns of Cabo Ortegal pyroxenites: **a-c.** whole-rock samples; **d-f.** cpx; **g-i.** amphibole. *Type-1* (**a**, **d** & **g**), *type-2* (**b**, **e** & **h**) and *type-3* (**c**, **f** & **i**) pyroxenites are distinguished. Chondrite composition from McDonough and Sun (1995).

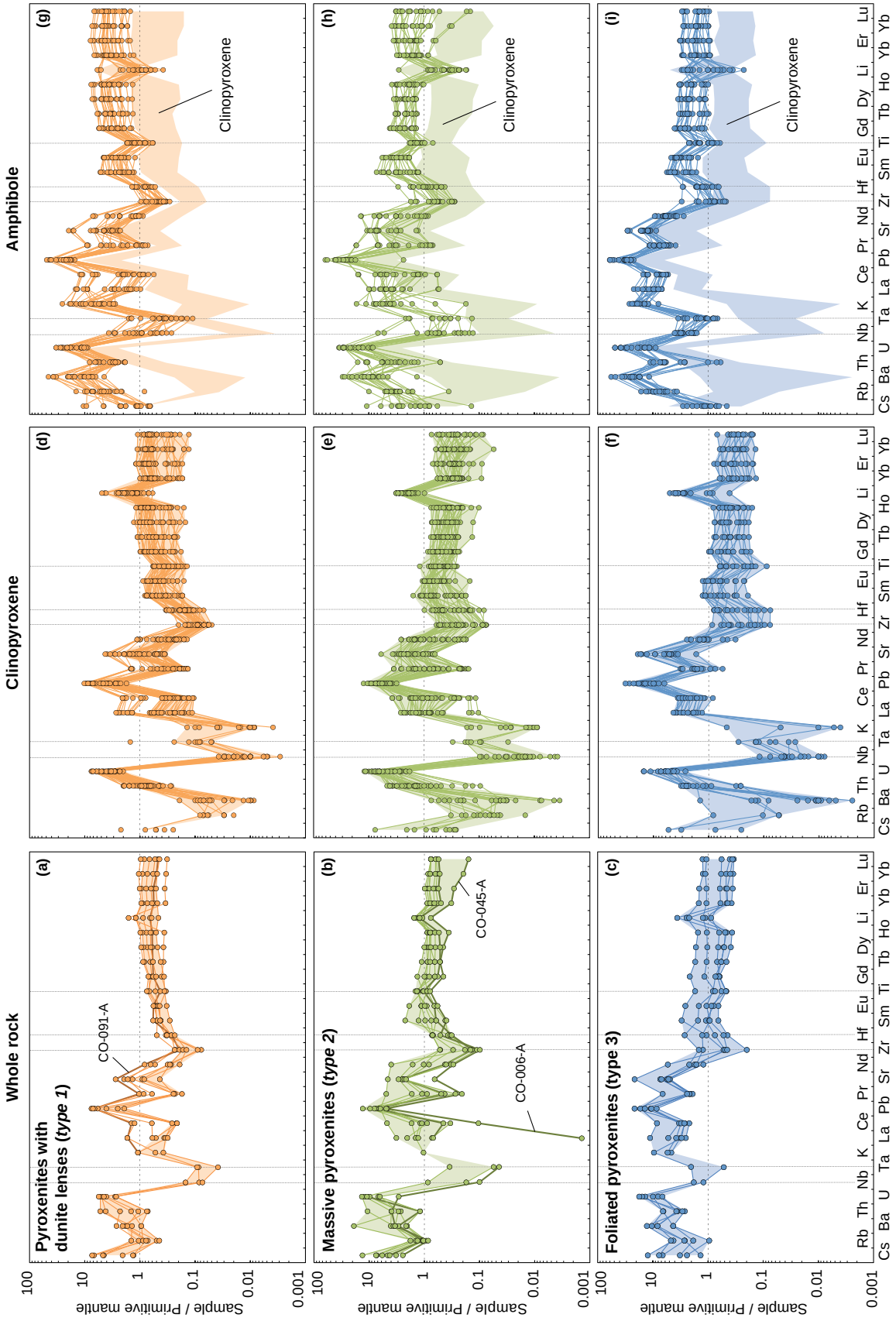

Fig. IV. 4. Primitive-mantle-normalized trace-element patterns of Cabo Ortegal pyroxenites: **a-c.** whole-rock samples; **d-f.** cpx; **g-i.** amphibole. *Type-1* (**a**, **d** & **g**), *type-2* (**b**, **e** & **h**) and *type-3* (**c**, **f** & **i**) pyroxenites are distinguished. Primitive-mantle composition from McDonough and Sun (1995).

strongly positive anomalies relative to neighbouring elements [*e.g.* $(Li/Dy)_{PM}$ = 1.2-7.1; PM indicate primitive-mantle-normalized], whereas *type-1* samples have weak anomalies [$(Li/Dy)_{PM}$ < 1.4 with one sample reaching 4.3]. The high-field strength elements (HFSE) are strongly depleted, with particularly low Ta (Nb/Ta = 14.7-50.9) and variable Zr-Hf fractionation (Zr/Hf = 7.1-36.0). All *type-3* pyroxenites exhibit negative Ti anomalies [$(Ti/Ti^*)_{PM}$ = 0.36-0.57] whereas *type-1* and *type-2* pyroxenites have either positive or negative anomalies [$(Ti/Ti^*)_{PM}$ = 0.36-1.2].

The abundance of transition elements is related to modal variations. Sc, V and Zn are the highest in *type-2* pyroxenites and lowest in *type-1* pyroxenites and opx-rich (*type-4*) websterites, whereas *type-3* pyroxenites overlap the whole range of compositions (**Table IV-2**). Co, Ni and particularly Cr show less clear variation although they are slightly more abundant in *type-1* and *type-4* pyroxenites. Cu appears uncorrelated to the types of pyroxenite, probably due to variations in modal proportion of Cu-bearing sulfides.

Trace-element compositions of Cabo Ortegal *type-4* pyroxenites, peridotites and mafic rocks are available in **Appendix C1**.

B. MINERAL CHEMISTRY

Electron microprobe (EMPA) and laser ablation (LA)-ICP-MS analyses were performed at the Geochemical Analysis Unit (GAU) of GEMOC/CCFS at Macquarie University, Australia. For that purpose, polished thin (~ 30 μm) and thick (~ 100 μm) sections were prepared and examined under an optical microscope. Backscattered electron (BSE) images were acquired on a Zeiss EVO MA15 scanning electron microscope (SEM) using a beam current of 20 nA and an accelerating voltage of 15 kV (for silicates and oxides) and 20 kV (for sulfides).

1. Major elements

Mineral major-element compositions were determined by electron microprobe analysis (EMPA) using a CAMECA SX100 instrument fitted with five wavelength-dispersive spectrometers, at an accelerating voltage of 15 kV, a beam current of 20 nA, a beam size of 1-2 μm and a counting time of 10 seconds on peaks and 5 seconds on background, on each side of the peak. Natural minerals and synthetic oxides were used as standards following the PAP correction method of Pouchou and Pichoir (1984). Relative standard deviations on standard analyses are better than 1 %. Representative major-element compositions of cpx, opx, amphibole, olivine and garnet are reported in **Table IV-3**; the entire dataset is presented in **Appendix C4**.

a. Clinopyroxene

The composition of cpx (diopside) differs in the different types of pyroxenite (**Fig. IV. 5**). Cpx in (*type-1*) pyroxenites with dunite lenses has higher Mg# (0.91-0.94) than in massive (*type-2*) pyroxenites (0.88-0.92), which has highest Al_2O_3 (1.12-2.79 wt %) and TiO_2 (up to 0.25 wt %), outlining well-defined trends for Al_2O_3 or TiO_2 *vs* Mg#. Cpx in harzburgites and mafic rocks defines a similar trend with a much steeper slope on the Al_2O_3 *vs* Mg# plot; cpx in mafic rocks also have a very low TiO_2. In addition, cpx in *type-1* pyroxenites has the lowest SiO_2 (51.7-54.5 wt %) and highest CaO (24.1-25.1 wt %). Cpx in foliated (*type-3*) pyroxenites overlaps other types of pyroxenites in terms of Mg# (0.87-0.94), although a significant proportion of these values are greater than 0.92, and thus follows a similar trend in most oxides. However, its Al_2O_3 is lower by ~ 0.4 wt % (**Fig. IV. 5a**) and TiO_2 is also slightly lower. In addition, cpx in low-Mg# *type-3* pyroxenites has relatively high Na_2O and K_2O. Cpx in opx-rich (*type-4*) pyroxenites is similar to that of *type-1* pyroxenites, differing only by its lower Al_2O_3 (0.47-1.15 wt %), and thus higher Cr#. Along with those of cpx in high-Mg# *type-3* pyroxenites, these compositions overlap the compositions of cpx in dunites. The range of Mg# of cpx in pyroxenites results

Table IV-3. Representative major-element compositions of silicates in Cabo Ortegal pyroxenites

Rock type	Pyroxenites with dunites (*type 1*)				Massive pyroxenites (*type 2*)				Foliated pyroxenites (*type 3*)				Opx-rich wbt (*type 4*)		
Mineral	Cpx														
wt %	amph	I (core)	I (rim)	II	amph	I (core)	I (rim)	II	amph	I (core)	I (rim)	II	I	II	II
SiO_2	53.16	53.20	53.94	53.46	53.18	53.34	53.46	54.31	53.83	54.48	53.12	54.63	54.01	54.32	55.05
TiO_2	0.11	0.03	0.08	0.04	0.19	0.10	0.13	0.10	0.07	0.04	0.04	0.03	0.02	0.01	0.01
Al_2O_3	1.95	1.38	1.07	1.16	2.00	1.75	1.61	1.38	1.10	1.23	0.96	0.91	0.76	0.76	0.47
Cr_2O_3	0.37	0.39	0.35	0.20	0.11	0.33	0.11	0.20	0.42	0.30	0.41	0.28	0.36	0.31	0.23
FeO_t	2.72	2.26	2.32	2.31	3.27	3.33	2.97	3.19	2.27	2.36	3.34	2.36	2.20	2.09	1.97
MgO	17.24	17.67	17.48	17.80	16.61	16.51	16.80	16.55	17.59	17.00	17.57	17.07	17.91	17.83	17.75
NiO	0.04	0.04	0.02	0.05	0.04	0.00	0.00	0.02	0.08	0.02	0.05	0.05	0.04	0.10	0.07
MnO	0.09	0.08	0.06	0.09	0.09	0.15	0.09	0.13	0.09	0.08	0.16	0.10	0.11	0.02	0.08
CaO	24.22	24.89	24.46	24.76	24.29	24.31	24.71	24.04	24.44	24.71	24.20	24.52	24.48	24.40	24.59
Na_2O	0.10	0.10	0.10	0.14	0.09	0.15	0.05	0.17	0.17	0.17	0.37	0.16	0.18	0.18	0.13
K_2O	< dl	< dl	< dl	0.01	< dl	< dl	0.01	0.01	0.01	0.01	0.01	0.01	< dl	< dl	< dl
Total	100.01	100.06	99.90	100.02	99.88	99.96	99.94	100.09	100.07	100.41	100.22	100.12	100.07	100.02	100.34
Mg#	0.92	0.93	0.93	0.93	0.90	0.90	0.91	0.90	0.93	0.93	0.90	0.93	0.94	0.94	0.94
	Opx														
wt %	I (core)	I (core)	I (rim)	II	cpx	I (core)	I (rim)	II	amph	I (core)	I (rim)	II	I (core)	I (rim)	II
SiO_2	55.76	55.73	55.99	56.54	56.07	55.65	56.39	54.22	54.18	53.52	55.30	55.28	55.96	56.86	56.82
TiO_2	0.02	0.04	0.03	0.06	0.05	0.05	0.05	0.03	0.03	0.03	0.03	0.01	0.03	0.01	0.03
Al_2O_3	1.56	2.18	1.48	1.61	1.92	2.38	1.63	2.71	1.83	3.10	1.82	1.51	1.42	1.15	0.76
Cr_2O_3	0.22	0.37	0.17	0.20	0.15	0.30	0.20	0.29	0.34	0.20	0.16	0.18	0.29	0.23	0.23
FeO_t	8.96	7.70	9.11	8.49	10.61	11.21	12.04	12.96	11.45	11.02	10.98	10.05	7.57	7.67	7.76
NiO	0.03	0.02	0.01	0.08	0.05	0.00	0.01	0.01	0.03	0.00	0.03	0.04	0.08	0.05	0.09
MnO	0.25	0.21	0.29	0.22	0.15	0.33	0.37	0.27	0.32	0.28	0.26	0.22	0.19	0.22	0.16
MgO	33.30	33.41	33.14	33.26	31.53	29.96	29.50	29.49	31.68	31.80	31.83	32.55	34.18	34.36	33.77
CaO	0.26	0.56	0.25	0.21	0.24	0.25	0.26	0.21	0.24	0.23	0.26	0.24	0.24	0.22	0.33
Na_2O	< dl	< dl	< dl	< dl	0.03	0.01	0.01	< dl	< dl	< dl	< dl	0.01	< dl	0.01	0.01
K_2O	< dl	< dl	0.01	0.01	0.01	< dl	< dl	< dl	0.02	0.02	0.01	0.01	< dl	< dl	0.02
Total	100.37	100.21	100.47	100.68	100.81	100.13	100.45	100.18	100.12	100.18	100.65	100.12	99.96	100.79	99.99
Mg#	0.87	0.89	0.87	0.87	0.84	0.83	0.81	0.80	0.83	0.84	0.84	0.85	0.89	0.89	0.89
	Amph														
wt %	idio	sub	xeno	encl	idio	sub	xeno	encl	idio	sub	xeno	encl	xeno	sub	sub
SiO_2	46.68	49.16	46.70	47.41	48.38	47.04	49.53	47.65	45.63	48.40	47.70	49.46	48.06	54.64	49.16
TiO_2	0.26	0.22	0.26	0.22	0.32	0.28	0.36	0.36	0.27	0.32	0.16	0.33	0.15	0.04	0.12
Al_2O_3	10.18	9.03	9.90	8.17	10.13	10.78	8.62	10.21	10.10	8.95	9.85	8.43	9.28	3.29	8.31
Cr_2O_3	0.77	0.55	1.11	0.71	1.09	0.65	0.76	0.30	0.72	0.88	1.00	0.57	1.25	0.33	0.96
FeO_t	4.74	4.39	4.22	3.71	5.76	5.67	5.36	5.32	6.26	7.60	4.30	7.01	4.28	3.05	4.10
NiO	0.06	0.05	0.10	0.10	0.06	0.02	0.05	0.04	0.03	0.00	0.05	0.01	0.11	0.05	0.03
MnO	0.08	0.06	0.08	0.06	0.08	0.01	0.00	0.05	0.10	0.09	0.05	0.09	0.06	0.06	0.10
MgO	19.69	19.76	19.65	21.31	18.20	18.63	19.08	17.50	19.06	17.24	18.84	18.14	19.78	22.55	19.97
CaO	12.69	12.71	12.82	12.82	12.27	12.36	12.73	12.73	12.61	12.39	12.79	12.35	12.44	12.82	12.60
Na_2O	1.81	1.16	1.77	1.63	1.53	1.85	1.12	1.27	1.62	1.44	1.67	1.34	1.94	0.56	1.52
K_2O	0.26	0.22	0.33	0.17	0.08	0.20	0.19	0.08	0.43	0.51	0.47	0.49	0.13	0.13	0.54
Total	97.21	97.31	96.94	96.30	97.90	97.50	97.78	95.52	96.84	97.82	96.90	98.23	97.47	97.53	97.43
Mg#	0.88	0.89	0.89	0.91	0.85	0.85	0.86	0.85	0.84	0.80	0.89	0.82	0.89	0.93	0.90
	Ol				Grt										
wt %					core	rim	coro								
SiO_2	40.06	40.11	39.89	40.04	39.84	40.48	40.38	40.16							
TiO_2	< dl	0.02	0.02	< dl	0.10	0.14	0.02	0.02							
Al_2O_3	< dl	< dl	0.02	0.01	21.48	21.24	22.57	22.27							
Cr_2O_3	< dl	0.03	0.01	0.02	1.09	1.01	0.19	0.66							
FeO_t	11.57	13.32	10.99	11.76	16.15	16.35	15.27	15.61							
NiO	0.15	0.23	0.29	0.23	0.00	0.00	0.06	0.01							
MnO	0.22	0.24	0.21	0.21	1.03	0.95	0.82	0.94							
MgO	48.02	46.10	48.22	48.15	12.57	12.44	14.68	14.48							
CaO	0.03	0.03	0.03	0.03	7.90	7.82	6.03	6.14							
Na_2O	0.02	0.01	0.02	< dl	0.01	0.00	0.01	0.01							
K_2O	< dl	< dl	0.04	0.01	0.01	0.00	0.02	< dl							
Total	100.08	100.14	99.71	100.44	100.18	100.44	100.04	100.31							
Mg#	0.88	0.86	0.89	0.88	0.58	0.58	0.63	0.62							

Amph, abundant amphibole; idio, idiomorphic; sub, sub-idiomorphic; xeno, xenomorphic; encl., enclosed; coro, corona around spinel; FeO_t, total Fe as FeO; < dl, below detection limit.

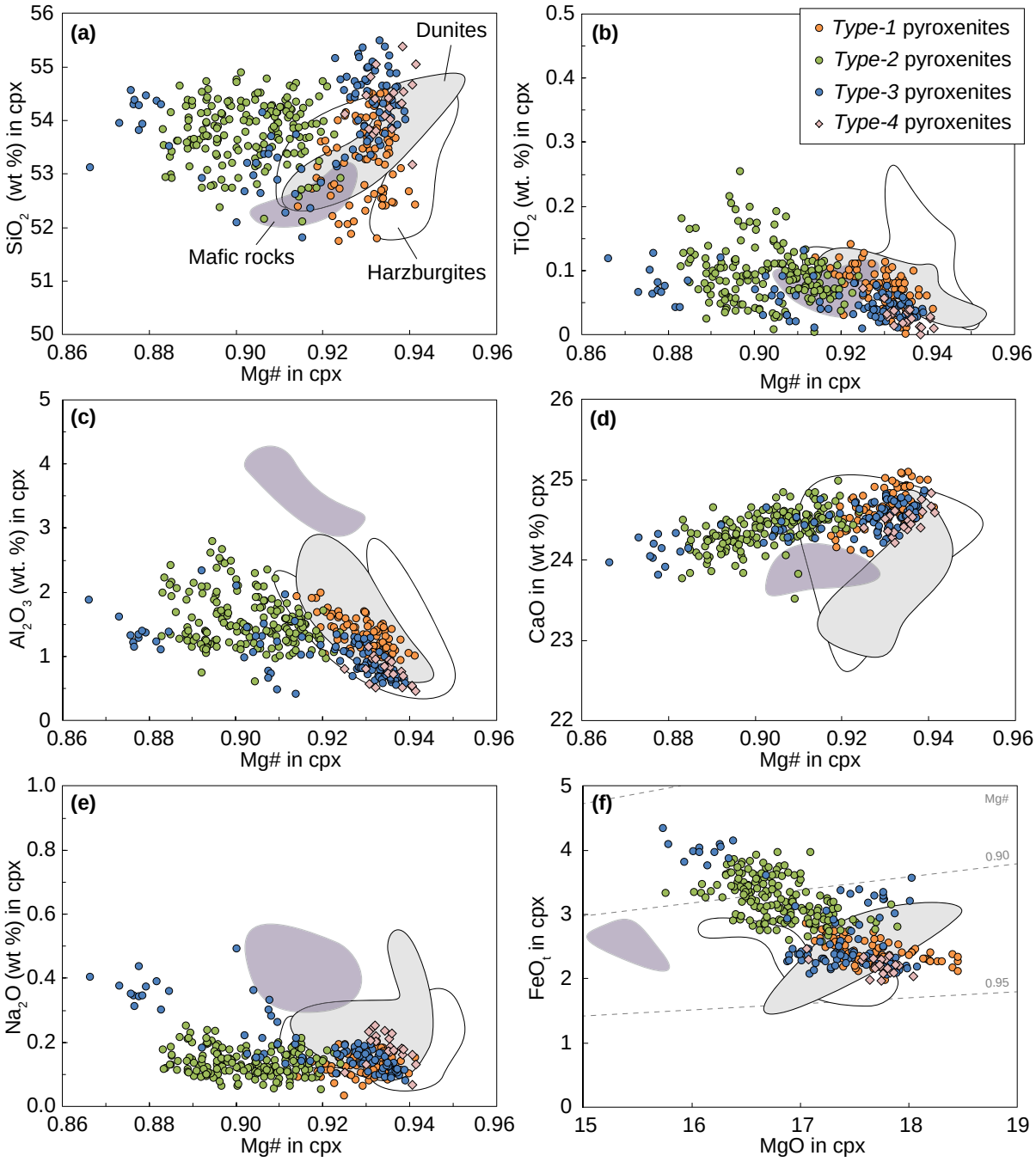

Fig. IV. 5. Compositions of cpx in Cabo Ortegal pyroxenites, peridotites and mafic rocks: **a-e.** plotted *vs* Mg#, SiO_2 (**a**), TiO_2 (**b**), Al_2O_3 (**c**), CaO (**d**) and Na_2O (**e**); **f.** FeO_t *vs* MgO with corresponding Mg#. Data from peridotites and mafic rocks are mainly from Santos *et al.* (2002).

from decreasing MgO at constant FeO_t for the highest Mg# (*i.e. type-1* and *-4* and some *type-3* pyroxenites), and decreasing MgO and FeO_t for lower Mg# (*i.e. type-2* pyroxenites, mainly).

Within individual samples, cores of cpx I commonly have higher Al_2O_3 (by up to 1 wt %), and to a minor extent, TiO_2, and lower SiO_2 and Mg# (by up to 0.017 units) than rims. On average, this difference represents ~ 0.05 in Mg# and 0.3-0.4 wt % in Al_2O_3, because it is not observed systematically in strongly amphibolitized areas. Neoblasts or matrix grains (cpx II) have compositions similar to those of the rims of cpx I, and may have even lower Al_2O_3. In addition, no systematic significant variation was observed between the core of cpx I porphyroclasts exhibiting a dense concentration of exsolved needle-shaped spinel (± amphibole) and the core of exsolution-free porphyroclasts. However, this may imply a significant difference in composition between them if exsolved spinel is re-integrated into the composition of cpx, although this is difficult to quantify due to the small size and density of spinel exsolution.

b. Orthopyroxene

Opx (enstatite) shows more limited variations between the different types of pyroxenite except in terms of Mg# which increases from *type-1* and *-4* pyroxenites to *type-2* pyroxenites, with *type-3* being intermediate between them (**Fig. IV. 6**). The trends of increasing Al_2O_3 and TiO_2 at decreasing Mg# observed in cpx are very weakly defined in opx, and non-existent for TiO_2. However, like the cpx, opx from *type-3* pyroxenites has slightly lower Al_2O_3 over the range of Mg# and opx from *type-4* pyroxenites has a narrow range of high Mg# (0.89) and lower Al_2O_3 (0.39-1.42) than any other types of pyroxenite. Compared with peridotites, while opx in *type-1* and *-4* pyroxenites is close to that in dunites, opx in harzburgites strongly differs. It has indeed a wide range of Al_2O_3 (up to 7.13 wt %) and CaO, (up to 3.19 wt %), and to a minor extent TiO_2 and Cr_2O_3, but its Mg# (0.86-0.92) is fairly limited and similar to that in dunites (0.89-0.91), although over a wider range of MgO. The difference in Mg# between peridotites and most pyroxenites results from a 1-4 wt % difference in FeO at relatively similar MgO (**Fig. IV. 6d**).

Compositional variations similar to those observed between core and rims of cpx I, and cpx II may be observed in opx, but they are restricted to opx I porphyroclasts in contact with other porphyroclasts. However, even in this case, the difference is only significant in terms of Al_2O_3 (up to 1.5 wt %) and SiO_2 while Mg# is similar within ± 0.008 units. In contrast, porphyroclasts in contact with abundant neoblasts and opx II in granoblastic texture show no systematic difference between core and rims, which have homogeneous core-like values. Neoblasts show rim-like values. As in the case of cpx, no additional variation associated with the presence of

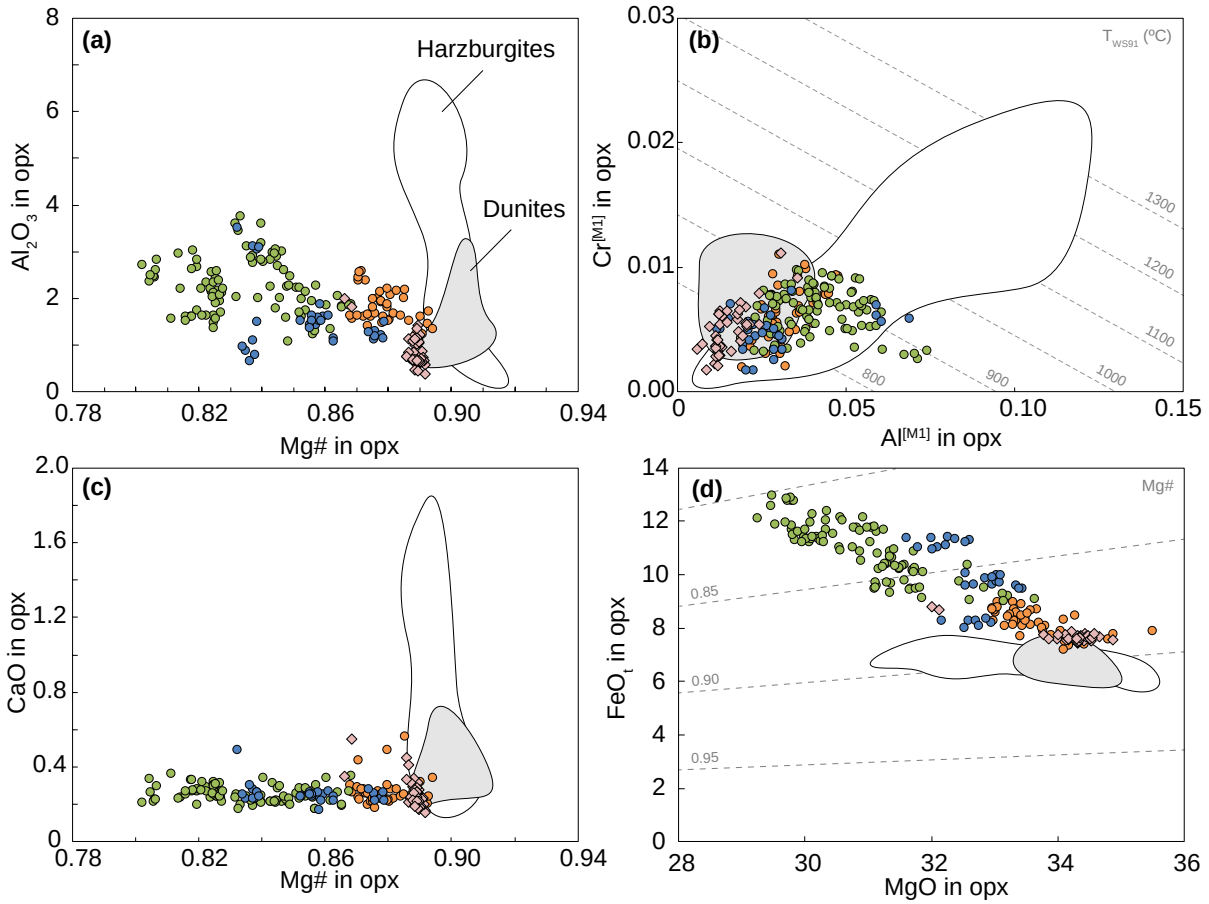

Fig. IV. 6. Compositions of opx in Cabo Ortegal pyroxenites and peridotites: **a** & **c.** plotted *vs* Mg#, Al_2O_3 (**a**) and CaO (**c**); **b.** $Cr^{[M1]}$ *vs* $Al^{[M1]}$, with corresponding temperatures estimated from Witt-Eickschen & Seck 1991; **d.** FeO_t *vs* MgO, with corresponding Mg#. Data from peridotites are mainly from Santos *et al.* (2002). Symbols as in **Fig. IV. 15.**

needle-shaped spinel exsolution was observed.

c. Olivine

Olivine (only analysed in *type-1* and *-4* pyroxenites) has lower Mg# (0.86-0.89) than olivine from dunites and harzburgites (**Fig. IV. 7**). When plotted against Cr# of spinel from corresponding samples, Mg# of olivine in dunite is on the edge of the olivine-spinel mantle array (OSMA, Arai, 1987; Arai, 1994) while that of olivine in pyroxenites plots 2-4 Mg# units outside the OSMA (Santos *et al.*, 2002). This difference in Mg# reflects a ~ 2 wt % drop in FeOt at similar MgO (**Fig. IV. 7d**). When plotted against Mg#, there is an increasing trend in NiO (decreasing in MnO) from *type-1* pyroxenites to dunites and harzburgites. From this trend, olivine in opx-rich (*type-4*) pyroxenites has commonly higher NiO (0.27-0.48 wt %) than in *type-1* pyroxenites (0.15-0.37 wt %).

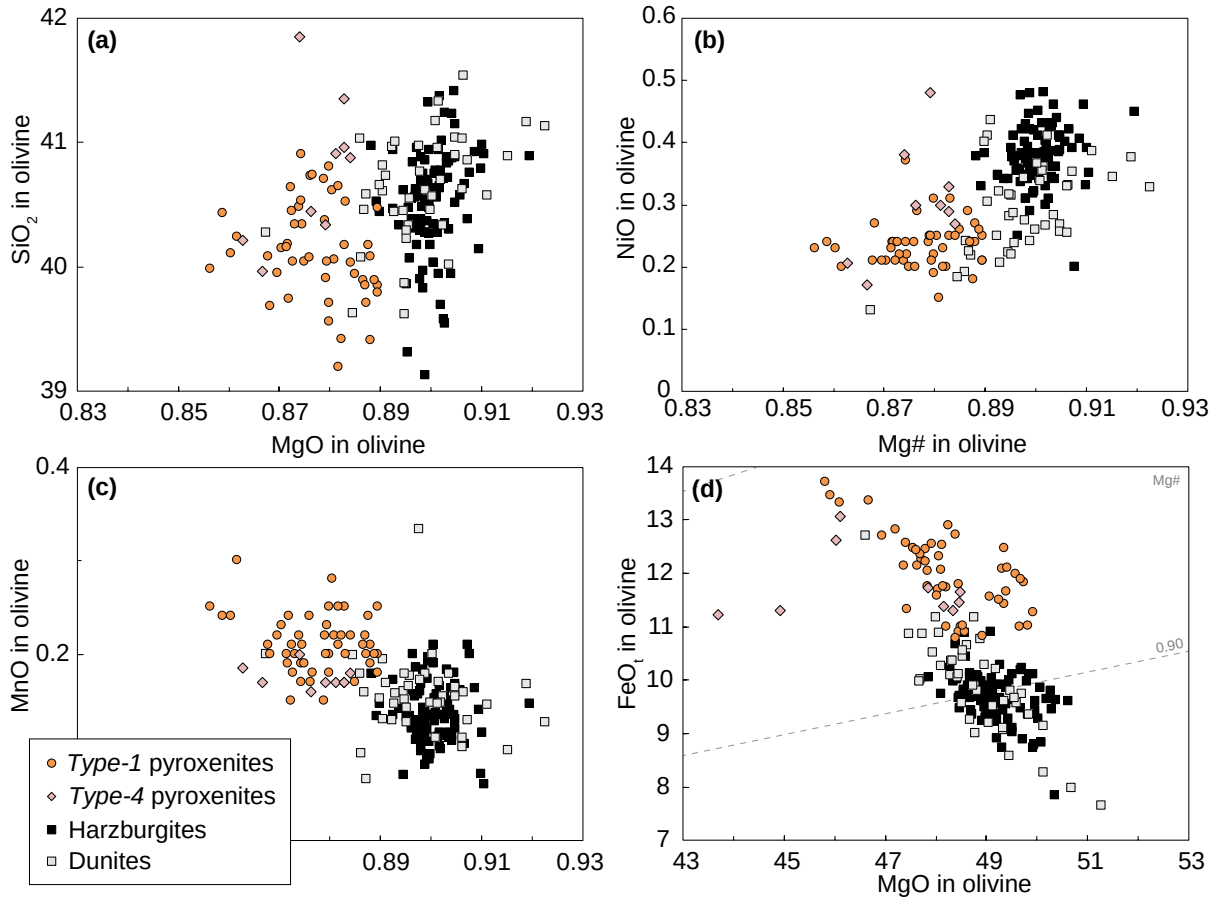

Fig. IV. 7. Compositions of olivine in Cabo Ortegal pyroxenites, dunites (grey) and harzburgites (black): **a-c.** plotted *vs* Mg#, SiO_2 (**a**); NiO (**b**) and MnO (**c**); **d.** FeO_t *vs* MgO, with corresponding Mg#.

d. Amphibole

Amphibole (magnesio-hornblende, following the classification of Leake *et al.*, 1997) also shows limited variations (compared with cpx) among the different types of pyroxenites (**Fig. IV. 8**). The trend of increasing Al_2O_3 and TiO_2 at decreasing Mg# observed in cpx is only weakly defined in amphibole. However, like cpx, amphibole in *type-1* pyroxenites has lower SiO_2. In addition, K_2O and to a lesser extent Na_2O, are systematically higher in amphibole from *type-3* pyroxenites (0.12-0.69 wt %) over a similar range of Mg#, while amphibole in *type-1* and *-2* pyroxenites outlines a slightly increasing trend at increasing Mg#. Similar patterns are observed for Cr_2O_3. Amphibole in dunite constitutes the high-Mg# end member of the compositional trend from *type-1* to *type-2* pyroxenites. However, in harzburgites, the composition of amphibole is dramatically different: it has high Al_2O_3 (16.9-20.7 wt %) and a wide range of Cr_2O_3 and K_2O. Its Mg# is similar to that of low-Mg# *type-2* pyroxenites, but at a much lower MgO and FeO_t. Amphibole in *type-4* pyroxenites has a composition roughly similar to that in *type-1*

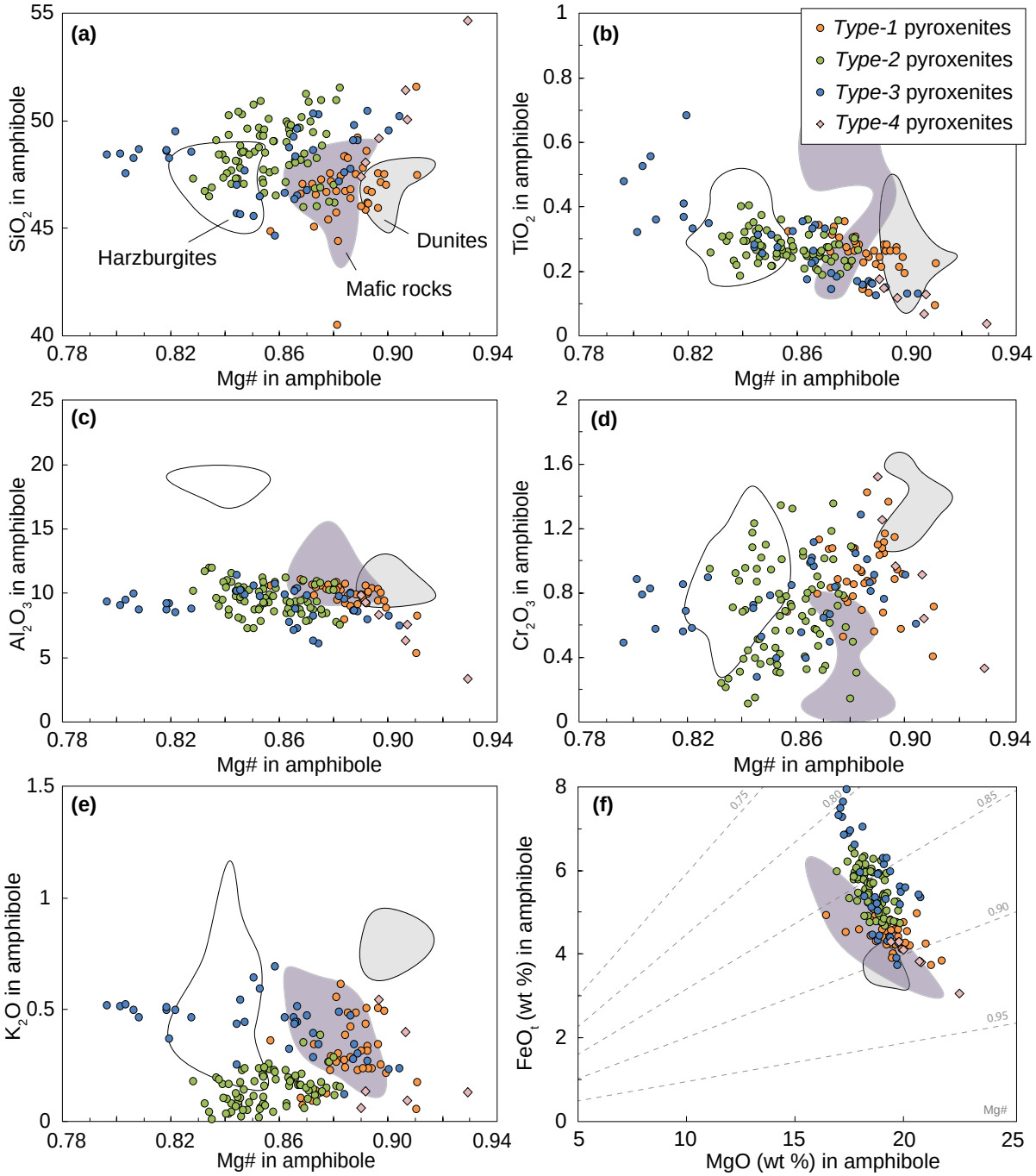

Fig. IV. 8. Compositions of amphibole in Cabo Ortegal pyroxenites, peridotites and mafic rocks: **a-e.** plotted *vs* Mg#, SiO_2 (**a**); TiO_2 (**b**); Al_2O_3 (**c**); Cr_2O_3 (**d**); K_2O (**e**); **f.** FeO_t *vs.* MgO (d), with corresponding Mg#.

pyroxenites, although these data are relatively limited. Within individual samples, there is no systematic compositional difference between idiomorphic, sub-idiomorphic and xenomorphic or enclosed amphibole; Al_2O_3 varies within ± 1 wt % from sample averages.

e. Spinel

In addition to silicates, the compositions of oxide minerals, mostly spinel, were investigated. For the sake of simplicity, both major and minor elements are reported here. On a Cr-Al-Fe^{3+} + 2 Ti triplot, the data outline a convex trend towards the Cr pole (**Fig. IV. 9a**). This trend is correlated with decreasing Mg# [increasing $Fe^{2+}/(Fe^{2+}+Mg)$; **Fig. IV. 10a**) and increasing TiO_2 (**Fig. IV. 10b**). The field and textural distinctions between pyroxenites, which coincide with major-element compositions of whole rocks and silicates, are also reflected in the spinels. Spinel in *type-1* pyroxenites and harzburgites (Santos *et al.*, 2002) constitutes an Al-rich end member while spinel in most *type-2* pyroxenites is an Fe^{3+}+Ti-rich end member. In other *type-2* pyroxenites, spinel has a composition similar to that in *type-1* pyroxenites. Between the Al- and Fe^{3+}+Ti-rich end members, the compositions of spinel in *type-3* pyroxenites overlap those of spinel in *type-1* and -2 pyroxenites and dunites (Santos *et al.*, 2002) and *type-4* pyroxenites constitute a Cr-rich end member.

From the data of this study alone, the compositions of spinel in chromitites fall in two groups, which are both Cr-rich when compared to pyroxenite spinels (**Fig. IV. 9b**). Group A represents massive chromitites hosted in dunites along the edge of the Herbeira plateau, which are the richest in Cr. Group B represents chromitites associated with pyroxenites in the Herbeira cliffs and from the THF-related area; their compositions overlap that of spinel in dunites and *type-1* pyroxenites.

Within individual pyroxenite samples, interstitial spinel and spinel enclosed in amphibole

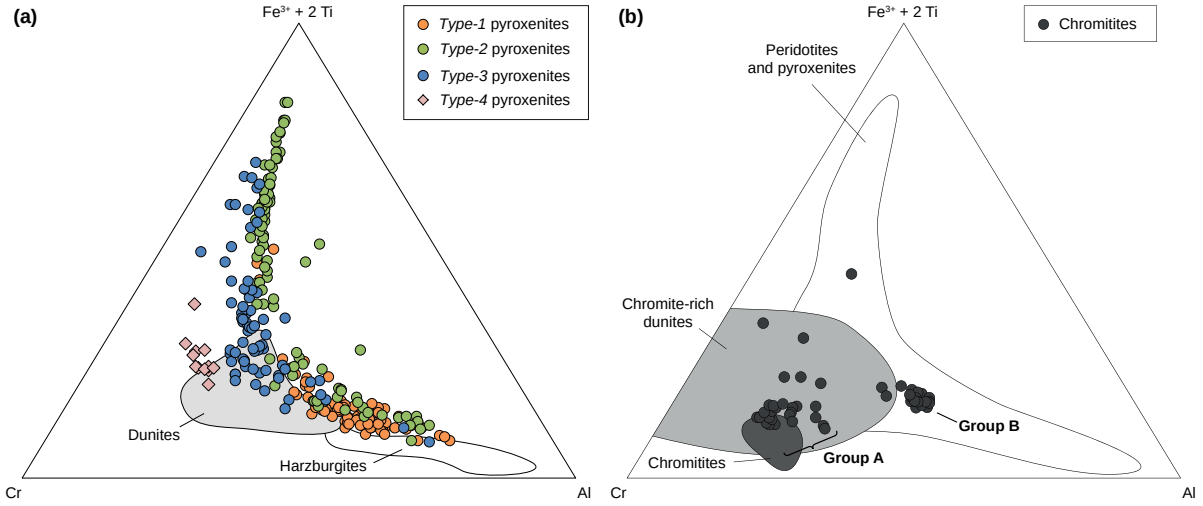

Fig. IV. 9. Compositions of spinel in Cabo Ortegal recalculated into Cr- Al- and Fe^{2+} + 2 Ti- end members: **a.** pyroxenites and peridotites; **b.** chromitites Compositional fields are from Santos *et al.* (2002) for peridotites and from Moreno *et al.* (2002) for chromitites (> 75 wt % spinel) and chromite-rich dunites (< 75 wt % spinel). Black symbols show chromitites from this study.

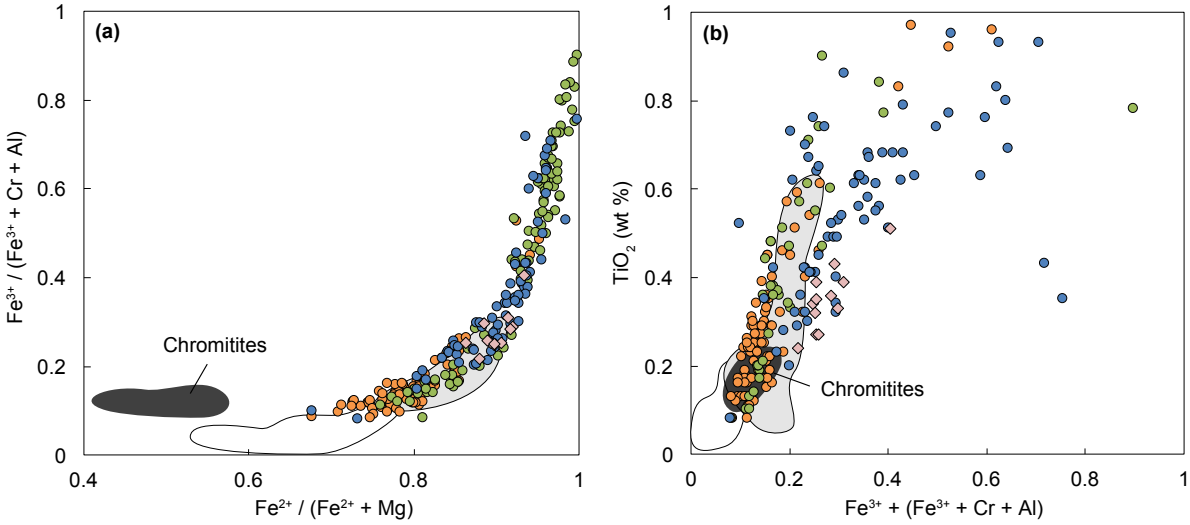

Fig. IV. 10. a. $Fe^{3+}/(Fe^{3+}+Cr+Al)$ *vs* $Fe^{2+}/(Fe^{2+}+Mg)$; **b.** TiO_2 *vs* $Fe^{3+}/(Fe^{3+}+Cr+Al)$ of spinel in Cabo Ortegal pyroxenites, peridotites and chromitites (both groups A and B from this study). Compositional fields for peridotites are from Santos *et al.* (2002). Fields and symbols as in **Fig. IV. 19.**

have higher FeO_t (particularly Fe^{3+}) and TiO_2 (up to 3.4 wt %) than spinel enclosed in silicates, which is richer in Cr_2O_3 and particularly Al_2O_3. As described above, spinel may be internally heterogeneous with dark areas corresponding to Al_2O_3- (~ 30-40 wt %) and Cr_2O_3-rich (~ 20-25 wt %) spinel with < 0.2 wt % TiO_2 and bright areas with high FeO_t (~ 65-75 wt %) and TiO_2 (~ 1.5-2.5 wt %).

Due to the small size (< 2-10 μm) of some spinel grains approaching the spatial resolution of standard EMPA, one sample was investigated using the field-emission gun (FEG) EMPA on a Cameca SX Five FE at the Centre de Micro Caractérisation Raimond Castaing (UMS 3623), Toulouse, France. No systematic difference was observed between needle-shaped exsolved grains, spinel inclusions and vermicular spinel, although data scatter significantly about the sample average (particularly in terms of FeO_t). This indicates that the estimation of sample averages could be strongly biased by the assumed proportion of the different types of spinel and thus the importance of reporting individual analyses as in **Fig. IV. 9**.

Spinel compositions in chromitites are quite homogeneous; most data range within ± 2 wt % from the sample average in terms of major oxides (*e.g.* Cr_2O_3, Al_2O_3, FeO_t). There is no systematic compositional difference between nodular and coexisting massive spinel, nor between their cores and rims apart from localized bands of zoned neoblasts, as described above, which have Al-rich cores and Cr-rich rims. However, disseminated spinels commonly have lower Cr_2O_3 and higher Al_2O_3 and FeOt, with similar TiO_2. Bright rims along boundaries with serpentine-filled cracks, and the dendritic alteration features have Cr-spinel compositions rich

in FeO_t, and locally in MnO (up to 9.13 wt%).

f. Garnet

Due to the limited occurrence of garnet in Cabo Ortegal pyroxenites, there are few garnet compositions reported from this study, but they are very similar to data from Girardeau & Gil Ibarguchi, 1991). In the two garnet-bearing samples investigated (*type-2* pyroxenites), garnet is mainly pyrope (46-53 %), almandine (27-32 %) and grossular (~ 14 %), a composition similar to that of garnet in the mafic layer near the top of the pyroxenite-rich area (CO-026). Poikilitic garnet from CO-006-B has lower Mg# and Al_2O_3 and higher CaO, Cr_2O_3 and TiO_2 than coronitic garnet from CO-024, which is similar to the composition of garnet from a mafic dyke (CO-073).

2. Trace elements

The trace-element compositions of minerals were determined on thick sections (after being examined and imaged under an optical microscope) by laser ablation inductively-coupled plasma mass spectrometry (LA-ICP-MS) using a Photon Machine Excite 193 nm ArF Excimer laser attached to an Agilent 7700 ICP-MS system. Beam size ranged between 30 and 60 μm at a pulse rate of 5 Hz, and an energy density of 3.0-4.4 $J.cm^{-2}$. Each analytical sequence started with 60 seconds of background, followed by 120 seconds of ablation and 30 seconds of wash-out. NIST SRM610 was used as an external standard, and ^{43}Ca was taken as the internal standard for cpx, garnet and amphibole whereas ^{29}Si was used for opx and olivine, ^{27}Al for spinel. Internal standard values were EMPA data averaged on thin sections of homogeneous samples, or taken from the same spot on thick sections of heterogeneous samples. The data reduction software GLITTER 4.4 (Griffin *et al.*, 2008) was used to calibrate the fractionation induced by ablation, transportation and excitation processes. Analyses of BCR-2G and BHVO-2 were made as unknown samples in each batch for quality control (**Appendix B**).

a. Clinopyroxene

Representative trace-element compositions of cpx are reported in **Table IV-4**. The REE compositions of cpx are consistent with the whole-rock data (**Fig. IV. 3**). *Type-1* cpx (*i.e.* cpx from *type-1* pyroxenites) commonly has spoon-shaped patterns with $(La/Gd)_{CN} < 1.3$, with a few exceptions. *Type-2* cpx has a range of LREE enrichment [$(La/Gd)_{CN}$ = 0.39-5.8] extended to higher values by *type-3* cpx with $(La/Gd)_{CN}$ reaching 9.1. Cpx from the most enriched samples has strongly fractionated LREE relative to MREE and flattened LREE distributions. Cpx from most *type-1* pyroxenites and the least LREE-enriched *type-2* pyroxenites have flat or slightly negative MREE-to-HREE slopes, whereas cpx from LREE-enriched *type-2* and most *type-3* py-

Table IV-4. Representative trace-element compositions of cpx in Cabo Ortegal pyroxenites

Rock type	*Type-1* pyroxenites			*Type-2* pyroxenites			*Type-3* pyroxenites			*Type-4* wbt	
ppm	I (core)	I (rim)	II	amph	I (core)	I (rim)	amph	I (core)	I (rim)	I (core)	I (core)
Li	2.7	1.7	0.9	3.4	2.8	3.6	1.2	6.1	0.9	3.6	2.3
Be	< dl	< dl	0.16	0.14	0.43	0.40	0.15	1.04	0.10	0.60	< dl
Sc	50	53	65	73	47	59	64	85	56	59	50
V	116	104	149	214	136	118	113	196	84	85	106
Cr	2340	1970	1550	2130	820	1300	1140	1780	850	3570	1560
Co	21	18	17	26	20	23	21	22	18	23	21
Ni	162	187	166	103	78	110	185	84	141	n.a.	247
Cu	< dl	< dl	0.1	< dl	< dl	0.1	5.8	0.2	0.1	< dl	< dl
Zn	5.6	2.8	2.8	14.6	9.2	12.6	5.2	20.3	3.8	n.a.	5.4
Ga	1.23	0.84	0.92	2.53	2.26	1.48	1.27	3.06	0.75	1.09	0.68
Rb	< dl	< dl	< dl	0.10	< dl	0.03	0.25	0.06	0.01	< dl	< dl
Sr	39	20	80	88	42	78	111	376	103	166	28
Y	0.90	2.94	2.43	1.50	1.10	1.31	1.87	2.36	1.18	1.68	1.25
Zr	0.8	1.2	1.3	3.5	3.5	1.1	1.6	4.0	1.0	1.8	0.3
Nb	0.01	< dl	0.01	0.03	0.01	0.02	0.15	0.02	< dl	< dl	< dl
Cs	< dl	< dl	< dl	< dl	< dl	< dl	< dl	0.11	< dl	< dl	< dl
Ba	< dl	0.1	0.1	n.a.	0.2	0.4	13.0	0.5	< dl	0.1	< dl
La	0.41	0.92	1.45	0.95	0.83	1.04	2.77	1.92	1.94	4.78	0.16
Ce	0.59	1.34	3.08	2.96	2.18	3.95	4.59	5.15	3.26	11.54	0.14
Pr	0.06	0.14	0.37	0.47	0.30	0.60	0.44	0.76	0.31	1.43	0.02
Nd	0.23	0.59	1.25	2.51	1.48	2.30	1.35	3.02	0.87	4.87	0.08
Sm	0.07	0.25	0.33	0.55	0.27	0.37	0.17	0.50	0.19	0.69	0.04
Eu	0.05	0.06	0.10	0.19	0.08	0.11	0.09	0.19	0.05	0.17	0.03
Gd	0.12	0.28	0.33	0.40	0.18	0.32	0.21	0.52	0.14	0.34	0.12
Tb	0.02	0.06	0.06	0.06	0.03	0.04	0.05	0.07	0.03	0.06	0.02
Dy	0.19	0.49	0.48	0.38	0.15	0.19	0.28	0.40	0.24	0.24	0.24
Ho	0.04	0.10	0.10	0.06	0.03	0.06	0.07	0.09	0.04	0.06	0.05
Er	0.10	0.30	0.31	0.12	0.09	0.14	0.19	0.24	0.15	0.16	0.13
Tm	0.02	0.05	0.03	0.01	0.01	0.02	0.04	0.03	0.02	0.02	0.02
Yb	0.11	0.28	0.26	< dl	0.14	0.18	0.18	0.26	0.11	0.18	0.15
Lu	0.02	0.05	0.04	0.01	0.01	0.02	0.03	0.03	0.02	0.02	0.02
Hf	0.05	0.08	0.04	0.22	0.12	0.03	0.06	0.18	0.05	0.04	< dl
Ta	0.003	< dl	< dl	< dl	0.005	< dl	0.004	0.001	< dl	< dl	< dl
Pb	1.1	0.6	1.4	1.3	1.0	0.9	1.9	2.4	1.5	2.8	1.2
Th	0.06	0.11	0.09	0.03	0.22	0.05	0.24	0.02	0.10	0.14	0.01
U	0.11	0.09	0.09	0.09	0.08	0.10	0.13	0.12	0.07	0.06	0.01

Amph, abundant amphibole along cleavage (see text for details on the petrographic features); < dl, below detection limit; n.a., not analyzed.

roxenites show the steepest slopes [$(Gd/Lu)_{CN}$ up to 3]. Cpx from garnet-bearing *type-2* samples has strongly negative MREE-to-HREE slopes [$(Gd/Lu)_{CN}$ = 2.1-3.9 where Lu is not below detection limit]. Cpx with the lowest ΣREE contents, particularly from *type-1* and *-2* samples, has positive Eu anomalies, with $(Eu/Eu^*)_{CN}$ reaching 1.4. LREE-depleted and saddle-shaped REE patterns are observed in cpx from samples CO-006-A and CO-045-A, respectively, consistent with their whole-rock compositions. In addition, cpx has extreme REE compositions in *type-4* pyroxenites, from the highest $(La/Gd)_{CN}$ to the most pronounced spoon-shaped patterns observed in Cabo Ortegal pyroxenites. Cpx from a pyroxenite dyke (CO-064-C) yields a LREE-depleted pattern with the highest HREE content observed.

The trace-element compositions of cpx are characterized by HFSE depletion, which is particularly strong for Nb and Ta (**Fig. IV. 4**). Very low Nb concentrations result in Nb/Ta = 0.46-17.42; most values are < 4. Zr-Hf fractionation in cpx is consistent with the fractionation observed in whole-rock samples (Zr/Hf = 12-44). Cpx exhibits negative Ti anomalies similar to whole-rock values; $(Ti/Ti^*)_{PM}$ ranges between 0.22 and 1.5 in *type-2* and *type-3* cpx, but never exceeds 0.59 in *type-3* cpx. Cpx from the LREE-enriched opx-rich websterite (CO-048) has even larger anomalies [$(Ti/Ti^*)_{PM}$ = 0.06]. The most incompatible fluid-mobile elements have very heterogeneous abundances. Pb and Sr, and to a lesser extent U and Th, increase from *type-1* to *type-2* and *type-3* cpx. U and Pb are strongly enriched with respect to primitive-mantle values in cpx from all types of pyroxenites. Rb, Ba and K are moderately to strongly depleted in cpx depending on rock type. Li exhibits a range of positive anomalies with respect to the neighbouring REE, resulting in (Li/Dy) = 1.6-22.5 in *type-2* and *-3* pyroxenites, whereas this ratio is restricted to 0.46-12.7 in *type-1* pyroxenites. Cpx from the pyroxenite dyke (CO-064-C) has no Li anomaly, low Nb and Ta and the lowest abundances of LILE, U and Th.

b. Amphibole

Representative trace-element compositions of amphibole are reported in Table IV-5. REE patterns of amphibole are very similar to those of cpx (**Fig. IV. 3**); higher ΣREE contents result in $D^{\Sigma REE}_{amph/cpx}$ ~ 4-7 with no LREE-to-HREE fractionation. Partition coefficients between amphibole and cpx are reported and discussed in Chapter VI. On a multi-element diagram (**Fig. IV. 4**), a major difference between amphibole and cpx is the strong enrichment of the most incompatible fluid-mobile elements in the former. Rb, Ba and K are strongly partitioned into amphibole with Damph-cpx generally well above 15, whereas U, Th, Pb and Sr partition similarly to the REE. However, Li is partitioned into cpx ($D^{Li}_{amph-cpx}$ = 0.1-0.8) resulting in negative Li anomalies in amphibole [$(Li/Li^*)_{PM}$ = 0.06-0.76]. Exceptions, including *type-4* pyroxenites

Table IV-5. Representative trace-element compositions of amphibole in Cabo Ortegal pyroxenites

Rock type	*Type-1* pyroxenites			*Type-2* pyroxenites			*Type-3* pyroxenites			*Type-4* wbt	
ppm	idio	sub	xeno	anhed	idio	xeno	idio	sub	sub	xeno	sub
Li	1.0	0.6	1.3	1.2	0.6	4.6	1.6	3.5	0.6	9.2	15.5
Be	0.07	0.12	0.09	< dl	0.11	0.46	1.45	0.82	0.35	0.16	1.25
Sc	110	169	115	118	101	55	99	73	107	112	98
V	402	577	375	386	480	289	428	371	487	324	182
Cr	5862	2679	5555	5032	5573	1638	3794	5094	4113	7471	6097
Co	41	38	33	65	42	18	47	45	47	39	34
Ni	451	508	519	359	569	115	248	459	272	734	553
Cu	0.1	0.125	3.5	0.117	0.1	0.1	0.2	0.5	0.1	0.084	0.192
Zn	9.4	7.1	5.0	20.9	9.0	9.3	46.1	32.0	22.4	9.4	10.2
Ga	5.23	3.84	4.53	6.60	7.69	1.94	11.14	6.86	9.40	4.64	4.76
Rb	3.2	2.1	4.4	1.6	2.0	0.2	5.5	3.6	4.5	3.0	2.5
Sr	122	47	69	27	62	50	577	250	309	57	416
Y	5.61	25.17	13.83	6.89	4.79	6.57	12.26	4.11	7.42	6.44	7.08
Zr	3.5	5.3	3.6	3.3	2.9	6.9	8.9	5.6	10.1	2.1	13.5
Nb	0.77	0.27	0.62	0.12	0.14	0.41	2.57	1.24	2.04	0.10	2.81
Cs	0.02	0.05	0.04	0.01	0.02	0.06	0.01	0.02	0.01	0.04	< dl
Ba	73	81	133	78	44	9	170	114	237	50	126
La	2.11	1.88	1.03	0.35	2.33	3.13	8.69	6.28	4.48	0.74	22.18
Ce	2.76	3.52	1.59	0.96	2.39	7.88	21.21	11.88	9.71	0.65	51.52
Pr	0.29	0.56	0.21	0.20	0.22	1.08	2.85	1.32	1.47	0.07	6.23
Nd	1.09	2.92	1.52	1.38	1.05	6.05	11.57	5.15	7.15	0.48	21.82
Sm	0.56	1.39	0.89	0.52	0.54	1.30	2.25	0.85	1.93	0.28	3.14
Eu	0.19	0.58	0.35	0.28	0.29	0.49	0.72	0.31	0.59	0.11	0.83
Gd	0.83	2.70	1.38	0.90	0.76	0.95	2.06	0.78	1.73	0.50	1.85
Tb	0.13	0.55	0.30	0.17	0.14	0.14	0.33	0.12	0.26	0.11	0.20
Dy	0.93	4.38	2.45	1.09	0.97	0.93	2.35	0.75	1.54	0.99	1.24
Ho	0.20	0.99	0.54	0.28	0.22	0.20	0.47	0.16	0.30	0.25	0.26
Er	0.66	2.94	1.45	0.77	0.63	0.50	1.42	0.44	0.82	0.86	0.75
Tm	0.09	0.42	0.23	0.12	0.06	0.06	0.19	0.07	0.11	0.13	0.11
Yb	0.75	2.76	1.57	0.93	0.60	0.49	1.13	0.43	0.73	0.94	0.82
Lu	0.10	0.38	0.24	0.12	0.08	0.06	0.20	0.08	0.10	0.17	0.15
Hf	0.18	0.38	0.23	0.14	0.12	0.29	0.31	0.19	0.46	0.12	0.47
Ta	0.010	< dl	0.016	< dl	< dl	0.012	0.061	0.038	0.088	< dl	0.104
Pb	4.5	3.3	3.1	2.6	3.7	0.4	4.9	3.8	8.2	2.6	5.0
Th	0.20	0.23	0.20	0.04	0.83	0.46	0.06	0.25	0.49	0.05	0.73
U	0.46	0.39	0.24	0.17	0.59	0.21	0.34	0.25	0.77	0.10	0.43

Idio, idiomorphic; sub, sub-idiomorphic; xeno, xenomorphic; < dl, below detection limit.

and several *type-3* pyroxenites, have both positive anomalies in amphibole and cpx, and positive $D^{Li}_{amph\text{-}cpx}$ values. As in cpx, HFSE are strongly depleted in amphibole. Nb is partitioned into amphibole more strongly than Ta, resulting in $D^{Nb}_{amph\text{-}cpx}$ = 13-117 and $D^{Ta}_{amph\text{-}cpx}$ = 0.7-26.1. $D^{Nb}_{amph\text{-}cpx}$ and $D^{Ta}_{amph\text{-}cpx}$ are variable in *type-1* and *-2* pyroxenites and much higher in *type-3* pyroxenites. Zr and Hf also partition into amphibole but with limited differences between the different types of pyroxenites. Ti partitions into amphibole with lower $D^{Ti}_{amph\text{-}cpx}$ than that of neighbouring REE, which results in stronger negative anomalies in amphibole.

c. Olivine and orthopyroxene

Olivine (only analysed in *type-1* pyroxenites) and opx has depleted REE patterns and very low contents of most lithophile trace elements (**Appendix C**). Only incompatible fluid-mobile elements (Cs, U and Th) and Li reach near-chondritic abundances. Opx shows slightly positive anomalies in Zr and Ti whereas very low Nb and Zr in olivine result in positive Nb-Ta and Zr-Hf anomalies.

d. Spinel

Compared to the composition of chromite in MORB (Pagé & Barnes, 2009), the minor- and trace-element compositions of spinel in Cabo Ortegal pyroxenites are enriched in Ti, Zn, Co,

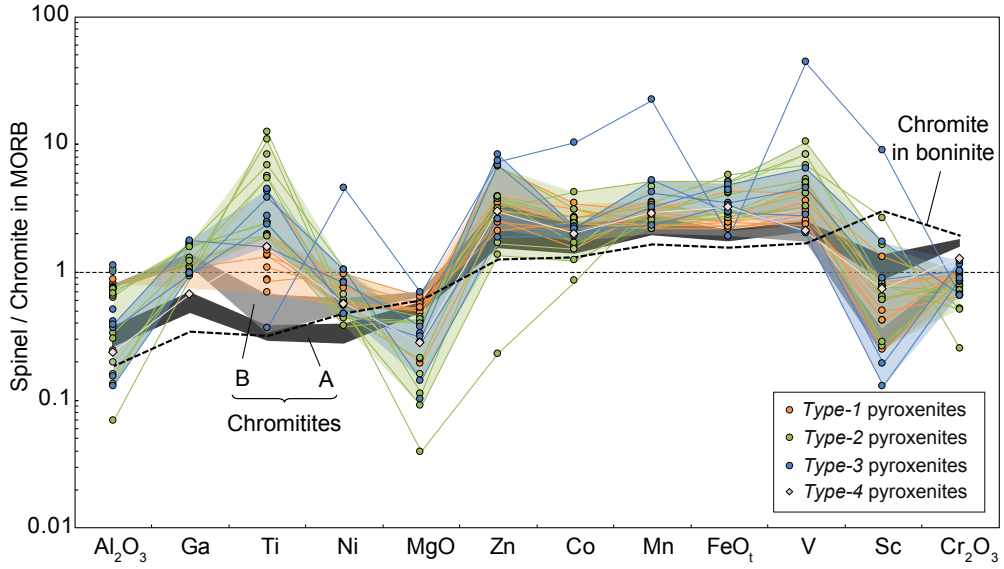

Fig. IV. 11. Spider diagrams showing the compositions of spinel in Cabo Ortegal pyroxenites and chromitites compared to chromite in boninites, normalized to chromite in MORB. Each individual line corresponds to a sample average excluding magnetite rims. The composition of chromite in MORB used for normalization is from a sample from the East Pacific Rise and that of chromite in boninites is from a sample from Bonin Island (Pagé & Barnes, 2001). Concentrations reported as oxides (Al_2O_3, MgO, FeO and Cr_2O_3) were acquired by EMPA while elemental concentrations (Ga, Ti, Ni, Zn, Co, Mn, V and Sc) were analysed by LA-ICP-MS.

Mn and V and strongly depleted in Sc (0.7-14.1 ppm). Ti enrichment is related to the different types of pyroxenite, increasing from *type-1* to *type-2* and *-3*, as described above. The minor- and trace-element compositions of spinel in chromitites are similar, with slightly higher Ga and Ni, and lower Sc in group B.

e. Garnet

Garnet analysed in two massive (*type-2*) pyroxenites has depleted HREE patterns with various degrees of LREE enrichment, rarely exceeding chondritic values, and exhibits negative anomalies in Sr, Ti and Li, and positive U anomalies (**Appendix C4**).

3. Major- and trace-element profiles

In addition to the set of mainly homogeneous samples described above, the composition of cpx has been investigated by coupled EMPA/LA-ICP-MS profile analysis of two heterogeneous samples (**Appendix C4**): a composite sample of *type-1* and *type-3* pyroxenite (CO-010) and a sample that preserves the contact between a *type-1* pyroxenite and its host dunite, and thinly layered pyroxenites (CO-013). Changes in modal composition along the profiles were investigated by point counting over small areas assumed to be homogeneous. Limited major and trace-element data were also collected for other minerals, but their lower abundance does not allow for sufficient spatial resolution and these data are thus not described as profiles.

a. Sample CO-010

Along the 8 cm-long profile, the modal proportion of amphibole increases steadily from 4 to 14 wt % (**Fig. IV. 12a**) along with the cpx/opx ratio and the modal proportion of sulfides (< 1 to 2 wt %). This roughly corresponds to a change from *type-1*- to *type-3*-like compositions. However, the major-element composition of cpx exhibits only limited change throughout the profile apart from SiO_2 decreasing from ~ 54.5 to 54.0 wt % while Mg# roughly increases.

A selective enrichment of LREE (**Fig. IV. 12b** & **Fig. IV. 13a**), LILE and other fluid-mobile elements (**Fig. IV. 13b**) accompanies the changes in modal composition. The range of cpx LREE compositions [$(La/Gd)_{CH}$ = 1.37-19.0] overlaps the entire range observed from *type-1* to *type-3* pyroxenites. At ~ 4 cm, the LREE distribution flattens and the enrichment progressively shifts towards MREE (**Fig. IV. 13a**). Sr and Pb also increase significantly along the profile but not linearly with respect to their neighbouring REE, which results in the transient evolution of $(Pb/Pb^*)_{PM}$ (**Fig. IV. 12d**) and $(Sr/Sr^*)_{PM}$ (**Fig. IV. 12c**). Most other LILE, Th, Zr, Hf and Li remain unchanged or slightly increase. Apart from Li, these elements partition more readily

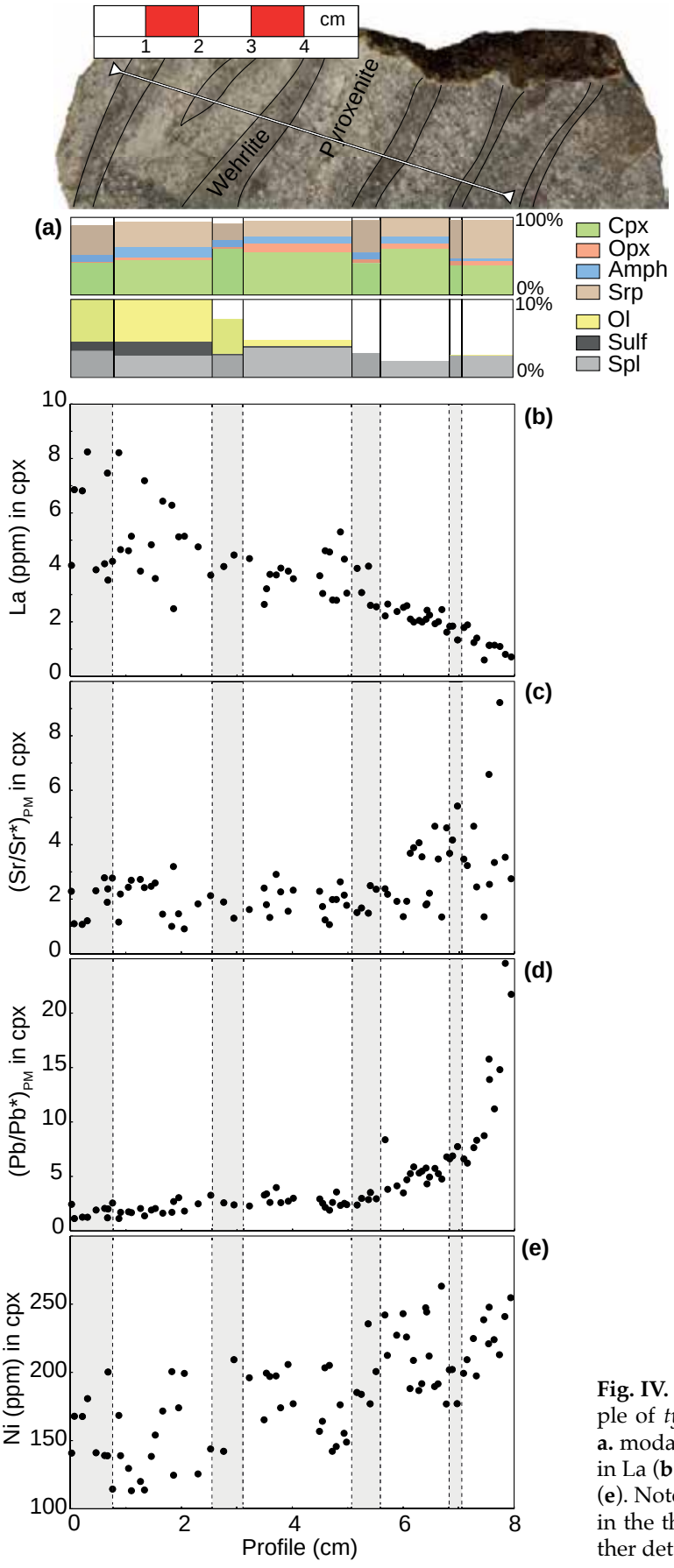

Fig. IV. 12. Profile study of a composite sample of *type-1* and *type-3* pyroxenite (CO-010): **a.** modal compositions; **b-e.** cpx compositions in La (**b**), $(Sr/Sr^*)_{PM}$ (**c**), $(Pb/Pb^*)_{PM}$ (**d**) and Ni (**e**). Note the thin dunitic lens preserved within the thick pyroxenite layer (see text for further details).

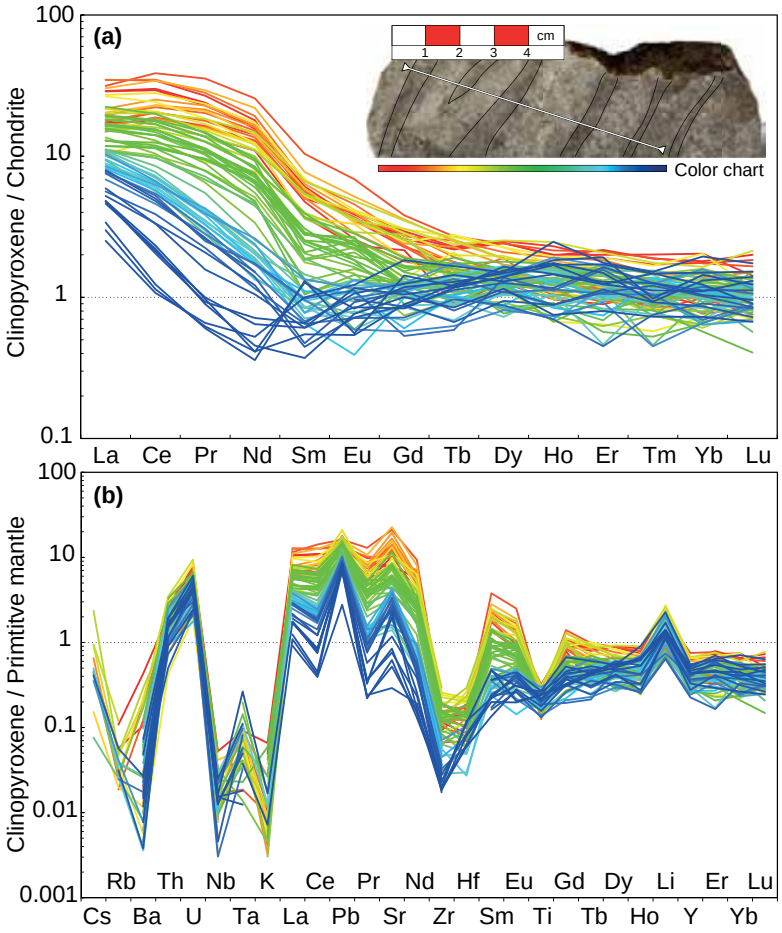

Fig. IV. 13. Cpx compositions along the profile of **Fig. IV. 12** (also reproduced here): **a.** chondrite-normalized REE patterns; **b.** primitive-mantle normalized multi-element patterns. Colour code relates to positions along the profile. Chondrite and primitive mantle compositions from McDonough and Sun (1995).

into amphibole; their concentration in cpx may thus respond to small-scale variations of modal proportion. The contribution of olivine (± opx) is also suggested by the variations in compatible elements such as Ni and Co (**Fig. IV. 12e**), while Cr is buffered by the presence of Cr-spinel throughout the profile.

b. Sample CO-013

The 12 cm-long profile can be described as two distinct trends. From 0 to 7 cm, corresponding to the *type-1* pyroxenite itself, the cpx/opx ratio increases while the modal proportion of amphibole decreases from 12 to 7 wt % (**Fig. IV. 14a**). From 7 to 12 cm, which includes the contact between the pyroxenite and thinly layered pyroxenites and dunite, the cpx/opx ratio decreases while serpentinization dramatically increases from ~ 30 to 70 wt % as the modal proportion of amphibole keeps decreasing from 7 to 5 wt %. Throughout the profile and across

the contact between pyroxenite and dunite, the proportion of spinel decreases constantly from ~ 5 to 0.5 wt %.

SiO_2 is maximum at the core of the pyroxenite layer (~ 53.5 wt %) and decreases towards both rims (~ 52.5 wt %). Throughout the profile, Al_2O_3 roughly decreases from ~ 2.0 to 1.5 wt % while Mg# increases from 0.92 to 0.93. However, the dispersion of data is almost of the same amplitude, particularly in the core of the profile (~ 4-8 cm). CaO is slightly lower in the first 4 cm (~ 24.5 wt %) than in the rest of the profile (~ 25 wt %).

In terms of minor and trace elements, the concentration of the lightest REE (La to Nd) and Zr, and to a minor extent Nb, decreases from 0 to 7 cm (**Fig. IV. 14c & d**). From 7 to 12 cm, which includes the contact between the pyroxenite and thinly layered pyroxenites and dunite, Li significantly increases (**Fig. IV. 14b**), from 1.6 to 7.0 ppm [$(Li/Dy)_{PM}$ = 1.1-5.3] along with the lightest REE only (La and Ce). Ni (F**Fig. IV. 14e**), and to a lesser extent Co, exhibit similar small-scale variations probably related to changes in the modal proportion of olivine, as described in sample CO-010. The concentration of most other trace elements exhibits no significant trend although the dispersion data is particularly large in the core of the pyroxenite layer for the MREE and HREE, V and Y, and for certain fluid-mobile elements (Th, U, Pb and Sr).

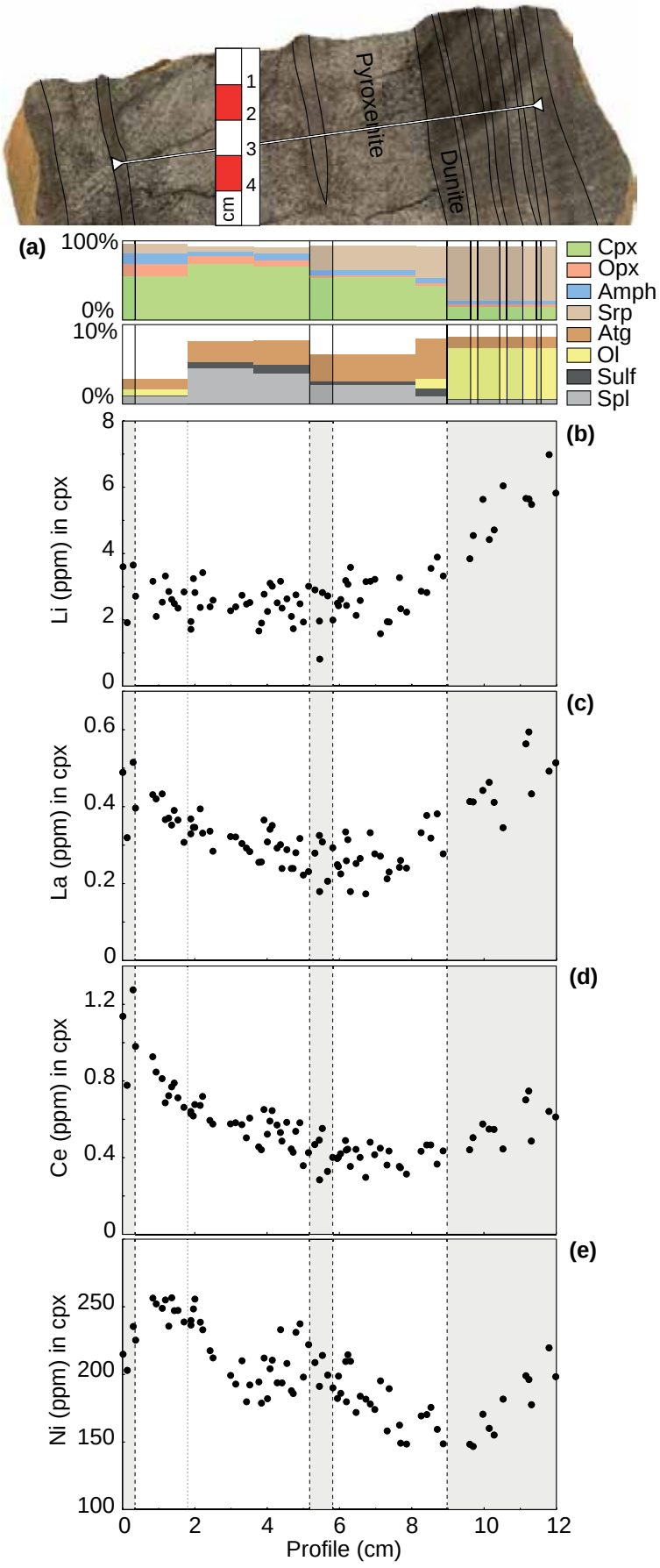

Fig. IV. 14. Profile study of a sample of *type-1* pyroxenite and its host dunite and thin-layered pyroxenites (CO-013): **a.** modal compositions; **b-e.** cpx compositions in Li (**b**), La (**c**), Ce (**d**) and Ni (**e**). Note the dunite lens preserved within the pyroxenite layer as in **Fig. IV. 12** (see text for further details).

C. BULK-ROCK RECONSTRUCTIONS AND TRACE-ELEMENT DISTRIBUTION

Bulk-rock trace-element compositions were reconstructed from mineral chemistry and mineral modes obtained from point counting and least-square calculation. For the 20 homogeneous samples investigated (**Appendix C2**), the reconstructed compositions are consistent with measured whole-rock compositions as illustrated in **Fig. IV. 15**. No modal correction was applied to fit the trace-element data but it clearly appears for some samples that discrepancies between measured and reconstructed compositions simply relate to misestimation of the proportion of minerals that may be heterogeneously distributed, such as amphibole and garnet.

Moderately incompatible trace elements are satisfactorily accounted for by the cpx-opx-amphibole (± olivine ± garnet) assemblage (**Fig. IV. 16** and **Appendix C3**). Cpx and amphibole host most REE, LILE and HFSE; amphibole dominates the budget of most fluid-mobile elements (K, Rb, Ba), whereas cpx controls Li. Nb is also preferentially partitioned into amphibole, which commonly results in low reconstructed Nb/Ta ratios, contrasting with the high measured values, due to underestimated amphibole proportions. Opx only contributes to the budget of Ni, Cr, V and Sc, and hosts a minor proportion of the HFSE (Ta, Hf and Ti), HREE, Y and some fluid-mobile elements (U, Th and Li). Olivine contributes to the budget of some HFSE, Ni, Li and other fluid-mobile elements in *type-1* pyroxenites. Garnet, when present, dominates the budget of HREE and hosts minor proportions of HFSE, Y, Sc and Cr. In *type-4*

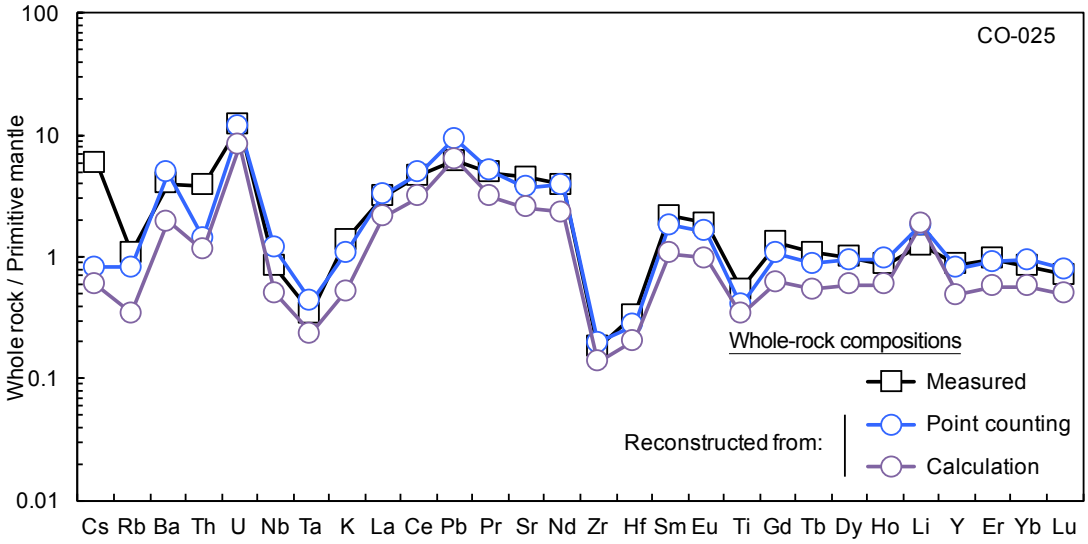

Fig. IV. 15. Comparison between whole-rock compositions and bulk-rock reconstructions of a representative *type-2* pyroxenite plotted on a primitive-mantle normalized multi-element diagram. Both reconstructions from point-counted and least-square fitted modes are shown. Primitive mantle composition from McDonough and Sun (1995).

(opx-rich) pyroxenites, cpx, opx and amphibole share most moderately incompatible elements. Amphibole hosts a significant proportion of LILE and opx controls Ni, Cr, HREE and to a lesser extent MREE. Olivine contributes to the budget of V and Sc.

Missing amounts of compatible lithophile (Cr and V), siderophile (Ni and Co) and chalcophile (Cu and Zn) elements are attributed to sulfides (< 1 wt %) and spinels (< 5 wt %) that were not taken into account in the calculation. Whole-rock concentration of HFSE (mainly Ti, Zr and Hf) are not fully accounted for by the analysed minerals, which suggests that a minor phase such as phlogopite or rutile has not been identified. Very low whole-rock TiO_2 probably excludes that rutile was a liquidus phase (Lee *et al.*, 2006), but it might have exsolved from Ti-bearing phases (amphibole, cpx and spinel), which are now recrystallized. Alternatively, spinels included in amphibole are typically richer in TiO_2 than spinels enclosed in other silicates could be associated with metasomatic micro-phases, such as Ti oxides and phlogopite. These phases would contribute to the budget of highly incompatible elements (Bodinier *et al.*, 1996, Condie *et al.*, 2004), in addition to material at grain boundaries, cracks and fluid inclusions. Ti oxides in particular can both accommodate both LILE and HFSE because of their structural flexibility (Haggerty, 1989, Haggerty, 1991).

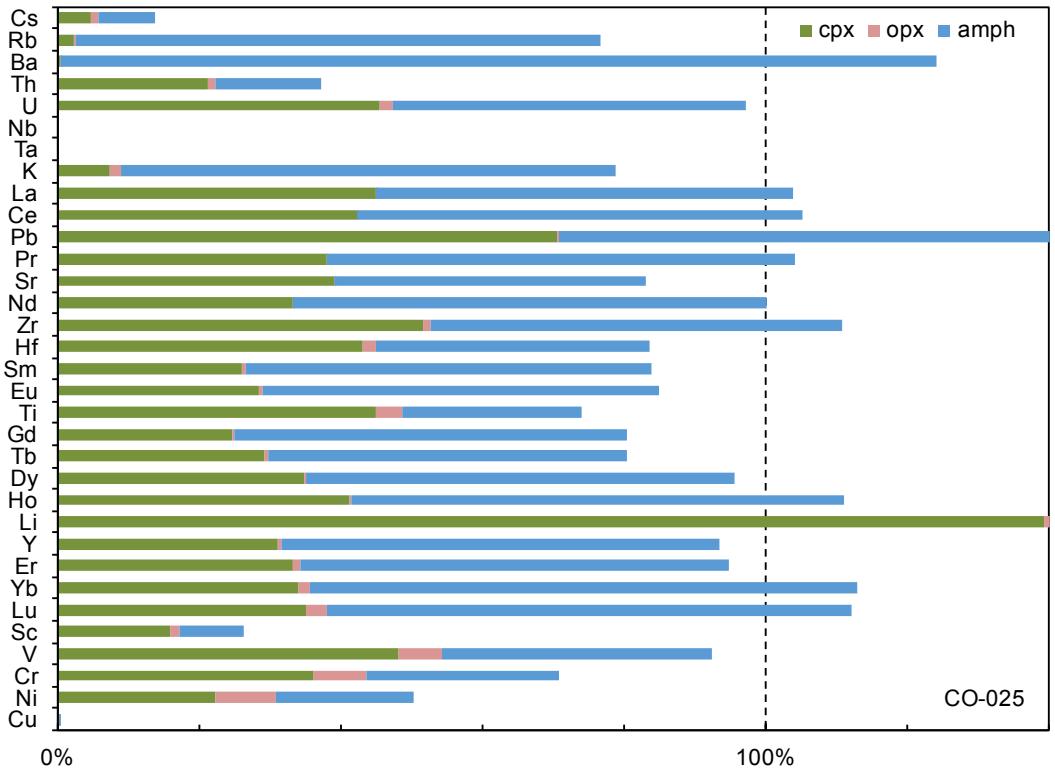

Fig. IV. 16. Distribution of trace elements among the main rock-forming phases of a representative *type-2* pyroxenite, as estimated from point-counted modes (see text for further details).

D. THERMOBAROMETRIC CALCULATIONS

The Fe-Mg, Ca-Na exchange (opx-cpx solvus) thermometer of Brey and Köhler (1990) and the Ca-in-opx thermometer of Brey *et al.* (1990) were used, along with the Al-in-opx thermometer for spinel peridotites of Witt-Eickschen and Seck (1991), to estimate the temperatures of last equilibration of Cabo Ortegal pyroxenites (**Table IV-6**), assuming a pressure of 1.6 GPa (Girardeau & Gil Ibarguchi, 1991). The Ca-in-opx thermometer gives temperatures between 742 and 856°C with limited differences between the different types of pyroxenite and in agreement with the Al-in-opx thermometer (706-854°C). However, the opx-cpx-solvus thermometer yields lower (629°C on average) and very dispersed values ranging between 472 and 796°C. When compared with the values obtained for pyroxenites, the Al-in-opx thermometer gives for harzburgites a wide range of temperatures reaching much higher values (> 1100°C; **Fig. IV. 6**).

The Al-in-opx barometers of McGregor (1974), Nickel and Green (1985) and Brey and Köhler (1990) were used to estimate equilibrium pressures of two garnet-bearing samples, assuming an equilibration temperature of 800°C. Estimates from the McGregor (1974) and Nickel and Green (1985) barometers are mutually consistent, ranging respectively between 1.4 and 1.8 GPa, and 1.1 and 1.5 GPa, whereas the Brey and Köhler (1990) barometer yields much lower values (0.2-0.4 GPa). The former estimates are in agreement with values previously reported by Girardeau and Gil Ibarguchi (1991) for Cabo Ortegal pyroxenites (800°C, 1.65 GPa).

Table IV-6. Equilibration temperature (°C) of Cabo Ortegal pyroxenites assuming 1.6 GPa

Method	Brey & Köehler (1990) Cpx-opx solvus	Brey & Köehler (1990) Na in opx-cpx	Brey *et al.* (1990) Ca in opx	Witt-Eickschen *et al.* (1991 Al in opx
Pyroxenites with dunite lenses (*type 1*)				
CO-012-A	682	1388	776	805
CO-013-A	685	1056	760	813
CO-013-C	606	1206		
CO-066-B2	596		856	854
CO-091-A	593			706
CO-094-B				
CO-095-A	636			779
CO-096-A	503		760	739
CO-096-B	472	1028	784	792
CO-100	538	1041	807	825
Massive pyroxenites (*type 2*)				
CO-006-A	684	482	800	
CO-006-B	730	1244	776	
CO-007	616	993	808	
CO-019-A	649	628	745	
CO-024	651	952	742	
CO-025	696	781	765	
CO-045-A	697	1004	758	
CO-046-A	796	930	783	
CO-046-C	665		766	777
CO-065	508		792	726
Foliated pyroxenites (*type 3*)				
CO-004-A				
CO-009	664	811	767	
CO-010-A				
CO-010-B				
CO-044-C	510	744	788	
CO-067	708	956	781	
CO-098	654		744	
CO-101	631	1064	821	
Opx-rich websterites (*type 4*)				
CO-002-A	667	573	742	
CO-048	635	954	797	728

Equilibrium temperatures were estimated from averaged core compositions of olivine, cpx I and opx I.

SUMMARY OF CHAPTER IV

- Cabo Ortegal pyroxenites are characterised by very **high CaO** and **low Al_2O_3** and alkalis and are comparable to the experimental products of crystallization of **primitive hydrous arc magmas**. They also have a ubiquitous **selective enrichment** of **LILE/HFSE**.

- ***Type-1* pyroxenites** have **higher cpx/opx** ratios and **Cr_2O_3** and **lower SiO_2** than other types of pyroxenite. Their pyroxenes and amphibole have **higher Mg#** than those of ***type-2* pyroxenites**, while those of ***type-3* pyroxenites** overlap this range at **lower Al_2O_3**.

- Each type of pyroxenite (and their main host minerals) has a **distinctive REE pattern**. ***Type-1* pyroxenites** display **spoon-shaped REE** while ***type-3* pyroxenites** have **LREE-enriched** pattern; ***type-2* pyroxenites** range **between these two extremes**.

- The **whole range of LREE enrichment** is found within individual samples and is partly correlated with the **modal proportion of amphibole**. Only **limited enrichment** is associated with **serpentinization**.

- **Mineral-chemistry** data and **modal proportions** satisfactorily reproduce **whole-rock** trace-element compositions. **REE patterns** of **amphibole** are **strikingly parallel** to those of **cpx**, but most **REE, LILE** and **HFSE partition preferentially** into amphibole.

- **Spinel** is mainly **Al-rich in *type-1* pyroxenites**, **Fe-Ti-rich** in t***ype-2*** and **Cr-rich** in ***type-3* pyroxenites**. Its **trace-element** composition is roughly **similar** to that of spinel crystallized from **boninites**.

- **Thermobarometric** estimates for pyroxenites are in **good agreement** with published values (**1.6-1.8 GPa** and **780-800°C**). Higher temperatures are preserved in harzburgites.

Chapter V.

Radiogenic-Isotope Geochemistry and Geochronology

A. STRONTIUM, NEODYMIUM AND HAFNIUM ISOTOPES

Sr-, Nd- and Hf-isotope compositions were measured on cpx and amphibole separates and whole-rock powders from pyroxenites (and two whole-rock samples of peridotites) in the GAU of GEMOC/CCFS at Macquarie University, Australia. The same portions of samples used for whole-rock elemental analysis were disaggregated using high-voltage pulses in a Selfrag® apparatus and sieved into three fractions (< 100 μm, 100-600 μm and > 600 μm). Clean mineral separates were then hand-picked from the two coarser fractions under a binocular microscope to avoid weathered surfaces and cloudy grains. Due to their low Nd and Hf concentrations, large quantity of material (~ 100-450 mg) were digested and processed using ion-exchange techniques described by Blichert-Toft *et al.* (1997) and Pin and Santos Zalduegui (1997). For cpx and whole-rock samples, 2 or 3 columns per sample were used depending on the concentrations. Separated minerals were optically pure apart from variable amounts of spinel inclusions that could not be avoided. Their effect was tested for amphibole by preparing distinct aliquots of coarse grains (> 600 μm) with abundant inclusions and finer-grained (100-600 μm) with fewer inclusions, for the same sample (CO-004-A). A subset of mineral separates was also analysed after leaching in 6N HCl for 2h at 80°C, although sample disaggregation seemed to have mainly produced grains with fresh surfaces. Procedures for sample digestion, ion-exchange chromatographic separation and data collection are detailed in **Appendix B**.

Sr and Nd isotopic ratios were obtained by thermal ionization mass spectrometry (TIMS) on a Thermo Finnigan Triton system. SRM-987 and JMC-321 were measured to check instrument status and sensitivity for Sr and Nd, respectively and followed by reference samples BHVO-2 and BCR-2. SRM-987 yielded $^{87}Sr/^{86}Sr = 0.710218 \pm 3$ (in-run error) and $^{143}Nd/^{144}Nd = 0.511128 \pm 2$ (in-run error), which are within error of the GeoRem recommended values. Three analyses of BCR-2 yielded $^{87}Sr/^{86}Sr = 0.704998 \pm 6$ (2σ) and $^{143}Nd/^{144}Nd = 0.512634 \pm 7$ (2σ) and two analysis of BHVO-2 yielded $^{87}Sr/^{86}Sr = 0.703473 \pm 40$ (2σ) and $^{143}Nd/^{144}Nd = 0.512986 \pm 30$ (2σ); these are comparable to values from Jweda *et al.* (2016) for BCR-2 ($^{87}Sr/^{86}Sr = 0.705000 \pm 11$; $^{143}Nd/^{144}Nd = 0.512637 \pm 13$) and to GeoRem preferred values for BHVO-2 ($^{87}Sr/^{86}Sr = 0.703469 \pm 34$; $^{143}Nd/^{144}Nd = 0.512980 \pm 12$). Ratios were normalized to $^{86}Sr/^{88}Sr = 0.1194$ and $^{146}Nd/^{144}Nd = 0.7219$) to correct for mass fractionation. Blanks were generally below 1000 and 80 pg for Sr and Nd, respectively.

Hf isotopic data were acquired in solution on a Nu Plasma multi-collector ICP-MS. JMC-475 gave $^{176}Hf/^{177}Hf = 0.282155 \pm 14$ (2σ; n = 37) within the uncertainty of GeoRem recom-

mended value (0.282159 ± 26). BCR-2 ($^{176}Hf/^{177}Hf$ = 0.282836 ± 100; 2σ; n = 3) and BHVO-2 ($^{176}Hf/^{177}Hf$ = 0.283100 ± 20; 2σ; n = 9) were also in good agreement with values from Jweda *et al.* (2016) for BCR-2 (0.282866 ± 11) and GeoRem recommended value for BHVO-2 (0.283109 ± 12), respectively. Blanks were generally below 60 pg.

$^{87}Rb/^{86}Sr$, $^{147}Sm/^{144}Nd$ and $^{176}Lu/^{177}Hf$ ratios were calculated from relative isotopic abundances and elemental ratios measured by LA-ICP-MS for cpx and amphibole, and by solution ICP-MS data for whole rocks. Accepted decay constants (λ_{Rb} = 1.42 x 10-11 a^{-1}; λ_{Sm} = 6.54 x 10-12 a^{-1}; λ_{Lu} = 1.865 x 10-11 a^{-1}) were used in the calculation of initial ratios at 390 Ma. Present-day ratios were taken as $^{87}Rb/^{86}Sr$ = 0.8603 and $^{87}Sr/^{86}Sr$ = 0.7047 (Zindler & Hart, 1986), $^{147}Sm/^{143}Nd$ = 0.1960, $^{143}Nd/^{144}Nd$ = 0.512630, $^{176}Lu/^{177}Hf$ = 0.0336 and $^{176}Hf/^{177}Hf$ = 0.282785 (Bouvier et al., 2008), for the chondritic uniform reservoir (CHUR), and $^{87}Rb/^{86}Sr$ = 0.022 and $^{87}Sr/^{86}Sr$ = 0.7025 (Zindler & Hart, 1986), $^{147}Sm/^{144}Nd$ = 0.2137 and $^{143}Nd/^{144}Nd$ = 0.513215 (Jacobsen & Wasserburg, 1980), and $^{176}Lu/^{177}Hf$ = 0.0384 and $^{176}Hf/^{177}Hf$ = 0.283251 (Blichert-Toft & Albarède, 1997), for the depleted MORB mantle (DMM).

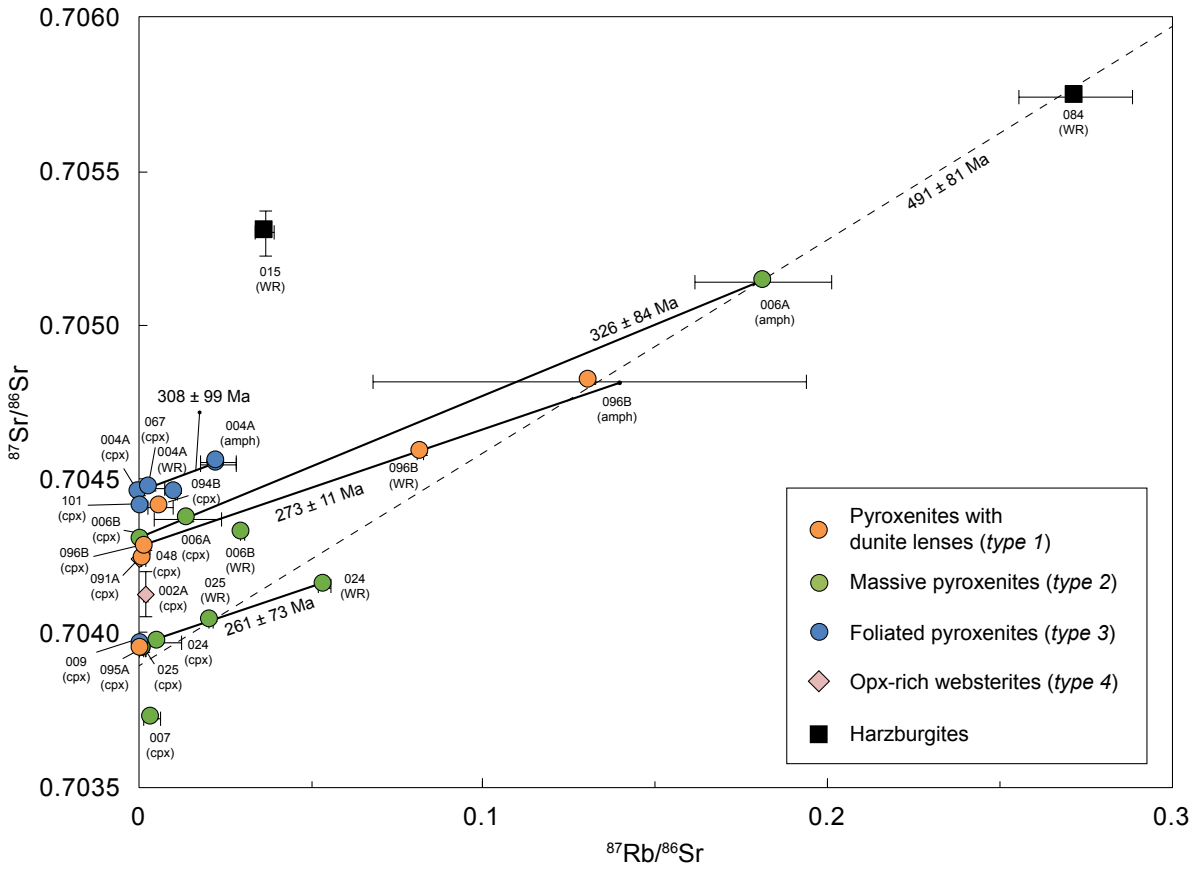

Fig. V. 1. Measured $^{87}Sr/^{86}Sr$ *vs* Rb/Sr for cpx, amphibole and whole rocks of Cabo Ortegal pyroxenites (and peridotites) and potential internal (full lines) and external (dashed lines) Rb-Sr isochrons. Error used are the in-run errors for $^{87}Sr/^{86}Sr$ and standard deviations (2σ) for $^{87}Rb/^{86}Sr$.

Table V-1. Sr-isotope data for Cabo Ortegal pyroxenites (and peridotites)

Sample		Rb (ppm)	Sr (ppm)	$^{87}Rb/^{86}Sr$	$^{87}Sr/^{86}Sr$	±	$^{87}Sr/^{86}Sr$ at 390 Ma
Type-1 pyroxenites							
CO-091-A	cpx	0.02	51	0.0014	0.704245	2	0.704237
CO-094-B	cpx	0.02	9	0.0064	0.704411	3	0.704375
CO-095-A	cpx	0.02	49	0.0010	0.703946	3	0.703940
	leached cpx	0.02	49	0.0010	0.704134	51	0.704129
CO-096-B	cpx	0.02	20	0.0023	0.704276	2	0.704264
	leached cpx	0.02	20	0.0023	0.704310	5	0.704297
	amph	3.64	81	0.1307	0.704816	3	0.704091
	WR	0.46	16	0.0819	0.704586	2	0.704131
Type-2 pyroxenites							
CO-006-A	cpx	0.07	13	0.0143	0.704370	2	0.704291
	amph	1.74	28	0.1813	0.705144	3	0.704138
CO-006-B	cpx	0.02	84	0.0007	0.704301	3	0.704297
	WR	0.61	59	0.0300	0.704329	2	0.704162
CO-007	cpx	0.02	18	0.0039	0.703727	2	0.703705
	leached cpx	0.02	18	0.0039	0.704032	18	0.704010
CO-024	cpx	0.05	27	0.0058	0.703975	3	0.703942
	leached cpx	0.05	27	0.0058	0.703922	9	0.703889
	WR	0.78	42	0.0540	0.704154	3	0.703854
CO-025	cpx	0.02	58	0.0012	0.703949	2	0.703942
	leached cpx	0.02	58	0.0012	0.703952	9	0.703945
	WR	0.65	90	0.0210	0.704045	2	0.703929
Type-3 pyroxenites							
CO-004-A	cpx	0.03	345	0.0003	0.704455	3	0.704453
	amph	4.43	558	0.0230	0.704551	2	0.704424
	amph*	4.43	558	0.0230	0.704557	3	0.704430
	WR	1.58	425	0.0108	0.704458	2	0.704398
CO-009	cpx	0.02	75	0.0007	0.703966	3	0.703962
	leached cpx	0.02	75	0.0007	0.705806	113	0.705801
	leached amph	2.31	210	0.0318	0.703984	3	0.703808
CO-067	cpx	0.25	217	0.0034	0.704470	2	0.704451
CO-101	cpx	0.02	98	0.0007	0.704410	2	0.704406
Type-4 pyroxenites							
CO-002-A	cpx	0.02	22	0.0020	0.704128	3	0.704117
CO-048	cpx	0.03	261	0.0003	0.704244	3	0.704242
Harzburgites							
CO-015-B	WR	0.25	20	0.0365	0.705300	72	0.705097
CO-084	WR	0.29	3	0.2720	0.705739	3	0.704228
Pyroxenite dyke							
CO-064-C	cpx	0.03	6	0.0153	0.704168	2	0.704083
Other							
CO-069	cpx	0.02	173	0.0004	0.704284	3	0.704283

WR, whole rock; cpx, clinopyroxene; amph, amphibole. *coarse (> 600 μm) amphibole separates. Errors are given for the last dig it on $^{87}Sr/^{86}Sr$.

1. Sr-isotope systematics

Sr-isotope compositions are reported in **Table V-1**. Cpx from *type-1*, *-2* and *-3* pyroxenites have low $^{87}Rb/^{86}Sr$ (< 0.18). They have $^{87}Sr/^{86}Sr$ ranging between 0.7039 and 0.7044 while most cpx in *type-3* pyroxenites are restricted to radiogenic values (~ 0.7045). When compared with corresponding cpx, *type-1* and *-2* amphiboles have more radiogenic values and higher Rb/Sr, whereas *type-3* amphibole is similar to its corresponding cpx (**Fig. V. 1**). Whole rocks plot close to the mixing lines between cpx and amphibole, where data are available. Additional whole-rock data for *type-2* pyroxenites show higher Rb/Sr and more radiogenic $^{87}Sr/^{86}Sr$. Cpx from a LREE-depleted *type-4* pyroxenite plots among *type-1* and *-2* cpx while that from a LREE-enriched sample is slightly more radiogenic at higher Rb/Sr. Sr isotopes in the two analysed samples of harzburgites are significantly more radiogenic than in any pyroxenites.

When excluding *type-3* pyroxenites and a few exceptions among other types, cpx, amphibole and whole-rock compositions from all samples plot on a line which includes one of the harzburgite samples as the most radiogenic end member. This line would correspond to an isochron age of 491 ± 81 Ma and an initial ratio of 0.7039. Internal isochrons that could be calculated from cpx, amphibole and/or whole-rock aliquots give ages between 261 and 326 Ma, including a well-defined age of 273 ± 11 Ma for sample CO-096-B (**Fig. V. 1**).

Leached separates yielded similar ($^{87}Sr/^{86}Sr$ within ± 2 x 10^{5}), or slightly more radiogenic Sr (by up to 3 x 10^{4}) than their non-leached replicates. This confirms that most grains were free of surface contamination in terms of Sr isotopes, indicating the reliability of the data collected on non-leached minerals. One exception has much more radiogenic Sr in the leached aliquot, although the corresponding error is very high (± 113 x 10^{6}); this may be due to the removal of surface contaminants with non-radiogenic Sr, such as carbonates.

2. Nd-isotope systematics

Nd-isotope compositions are reported in **Table V-2**. Cpx, amphibole and whole-rock compositions from the different types of pyroxenite have distinctive Nd-isotope compositions (**Fig. V. 2**). All *type-3* pyroxenites plot within a narrow range of low $^{143}Nd/^{144}Nd$ (0.5126-0.5127) and low $^{147}Sm/^{144}Nd$ (0.08-0.16) while most *type-1* pyroxenites have more radiogenic $^{143}Nd/^{144}Nd$ (0.5130-0.5132) at higher $^{147}Sm/^{144}Nd$ (0.15-0.31). Two exceptions are the LREE-enriched *type-1* samples, one of which was sampled near a pyroxenite dyke; these plot near the field of *type-3* pyroxenites. The least LREE-enriched *type-2* pyroxenites plot between *type-1* and *-3* pyrox-

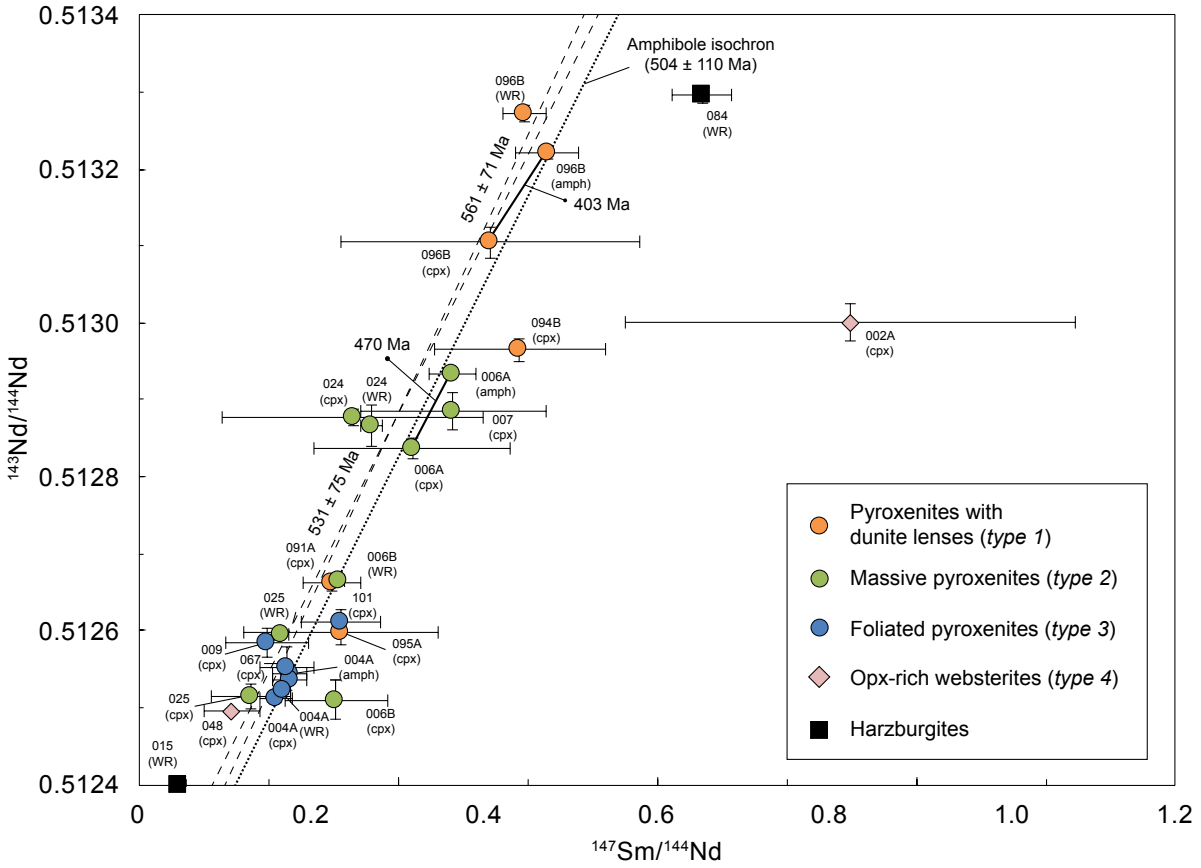

Fig. V. 2. Measured $^{143}Nd/^{144}Nd$ *vs* Sm/Nd for cpx, amphibole and whole-rock samples of Cabo Ortegal pyroxenites (and peridotites) and potential internal (full lines) and external (dashed lines) Sm-Nd isochrons. Error used are the in-run errors for $^{143}Nd/^{144}Nd$ and standard deviations (2σ) for $^{147}Sm/^{144}Nd$.

enites while the most enriched ones overlap *type-3* pyroxenites. As for Sr, Nd in amphibole is more radiogenic and $^{147}Sm/^{144}Nd$ higher than in cpx, but this difference is very small in the case of *type-3* pyroxenites. Whole-rock Nd is systematically more radiogenic than Nd in cpx, either plotting near the mixing lines of cpx and amphibole (*type-3*) or at higher $^{143}Nd/^{144}Nd$ and intermediate $^{147}Sm/^{144}Nd$ (*type-1*), suggesting the involvement of a component with more radiogenic Nd than that in cpx and amphibole. An exception is a garnet-bearing sample (CO-024) with very similar $^{143}Nd/^{144}Nd$ and $^{147}Sm/^{144}Nd$ in cpx and the whole rock. The compositions of the LREE-enriched *type-4* pyroxenite is similar that of *type-3* pyroxenites while the LREE-depleted one exhibit very high $^{147}Sm/^{144}Nd$ (0.55) at moderately radiogenic $^{143}Nd/^{144}Nd$.

The positive correlation between $^{147}Sm/^{144}Nd$ and $^{143}Nd/^{144}Nd$ indicates that the range of Nd-isotope compositions of Cabo Ortegal pyroxenites is directly related to the ingrowth of radiogenic Nd. The three types of pyroxenite indeed fall on a line whose slope would equate an isochron age of 561 ± 71 Ma, or 531 ± 75 Ma if excluding *type-3* pyroxenites, and an ini-

Table V-2. Nd-isotope data for Cabo Ortegal pyroxenites and peridotites

Sample		Sm (ppm)	Nd (ppm)	$^{147}Sm/^{144}Nd$	$^{143}Nd/^{144}Nd$	±	ε_{Nd}	τ_{DM} (Ma)	$^{143}Nd/^{144}Nd$ at 390 Ma	ε_{Nd} at 390 Ma	$\tau_{DM(2)}$ (Ma)
Type-1 pyroxenites											
CO-091-A	cpx	0.30	1.24	0.148	0.512662	10	0.6	1285	0.512284	3.0	665
CO-094-B	cpx	0.28	0.57	0.293	0.512965	15	6.5	-481	0.512215	1.7	714
CO-095-A	cpx	0.27	1.06	0.156	0.512598	15	-0.6	1620	0.512200	1.4	724
	leached cpx	0.27	1.06	0.156	0.512595	8	-0.7	1627	0.512198	1.3	726
CO-096-B	cpx	0.15	0.33	0.270	0.513103	19	9.2	-302	0.512413	5.5	572
	leached cpx	0.15	0.33	0.270	0.513251	10	12.1	96	0.512561	8.4	468
	amph	0.84	1.61	0.315	0.513221	8	11.5	8	0.512417	5.6	570
	WR	0.12	0.24	0.297	0.513271	12	12.5	102	0.512512	7.5	502
Type-2 pyroxenites											
CO-006-A	cpx	0.10	0.30	0.210	0.512837	13	4.0	15922	0.512300	3.3	654
	amph	0.53	1.32	0.242	0.512933	4	5.9	-1554	0.512316	3.6	642
CO-006-B	cpx	0.51	2.02	0.152	0.512511	25	-2.3	1725	0.512124	-0.1	779
	WR	0.51	2.00	0.154	0.512666	5	0.7	1389	0.512274	2.8	672
CO-007	cpx	0.10	0.26	0.242	0.512886	24	5.0	-1791	0.512268	2.7	676
	leached cpx	0.10	0.26	0.242	0.512891	13	5.1	-1764	0.512273	2.8	673
CO-024	cpx	0.22	0.82	0.164	0.512878	10	4.8	1043	0.512458	6.4	541
	leached cpx	0.22	0.82	0.164	0.512937	3	6.0	861	0.512517	7.6	499
	WR	0.30	1.01	0.178	0.512866	26	4.6	1500	0.512411	5.5	574
CO-025	cpx	0.38	2.72	0.086	0.512515	17	-2.2	833	0.512297	3.3	656
	leached cpx	0.38	2.72	0.086	0.512609	3	-0.4	722	0.512390	5.1	589
	WR	0.89	4.91	0.109	0.512595	2	-0.7	905	0.512316	3.6	642
Type-3 pyroxenites											
CO-004-A	cpx	0.48	2.74	0.106	0.512512	4	-2.3	990	0.512243	2.2	694
	amph	2.07	10.80	0.116	0.512545	2	-1.7	1042	0.512250	2.3	689
	amph*	2.07	10.80	0.116	0.512537	3	-1.8	1054	0.512242	2.2	695
	WR	1.22	6.68	0.110	0.512523	5	-2.1	1021	0.512241	2.2	695
CO-009	cpx	0.19	1.17	0.098	0.512586	19	-0.9	828	0.512336	4.0	627
	leached cpx	0.19	1.17	0.098	0.512580	18	-1.0	836	0.512330	3.9	632
	leached amph	2.81	22.11	0.077	0.512605	6	-0.5	680	0.512409	5.5	576
CO-067	cpx	0.24	1.30	0.114	0.512552	29	-1.5	1014	0.512260	2.6	681
CO-101	cpx	0.44	1.73	0.156	0.512613	17	-0.3	1583	0.512215	1.7	714
Type-4 pyroxenites											
CO-002-A	cpx	0.12	0.13	0.549	0.513000	24	7.2	-98	0.511598	-10	1153
CO-048	cpx	0.50	4.23	0.071	0.512497	1	-2.6	767	0.512316	3.6	642
Harzburgites											
CO-015-B	WR	0.01	0.24	0.030	0.512401	8	-4.5	675	0.512325	3.8	636
CO-084	WR	0.05	0.07	0.435	0.513294	10	13.0	55	0.512184	1	736
Pyroxenite dyke											
CO-064-C	cpx	0.46	0.88	0.313	0.513328	7	13.6	174	0.512529	7.8	490
Other											
CO-069	cpx	0.28	1.82	0.094	0.512621	10	-0.2	757	0.512381	5	596

WR, whole rock; cpx, clinopyroxene; amph, amphibole. *coarse (> 600 μm) amphibole separate. Errors are given for the last digit on $^{143}Nd/^{144}Nd$. $\varepsilon_{Nd} = [(^{143}Nd/^{144}Nd_{sample})/(^{143}Nd/^{144}Nd_{CHUR})-1] \times 10000$.

tial $^{143}Nd/^{144}Nd$ of ~0.5121. However, it may be related to the resetting of the system during amphibolitization as suggested by the location of amphiboles on a line that would give an isochron age of 504 ± 110 Ma and an initial ratio of 0.5122. Cpx-amphibole pairs would give isochron ages ranging between 403 and 470 Ma.

Depleted mantle model ages (τ_{DM}) calculated from Nd-isotope compositions gives three different groups (**Table V-2**). The first one corresponds to the cluster of radiogenic samples and gives a relatively narrow range of τ_{DM} between -481 and 102 Ma, while the other two are either very high (767-1725 Ma) or high values of meaningless future ages; both correspond to the cluster of LREE-enriched samples with non-radiogenic Nd compositions. Nonetheless, considering the ingrowth of radiogenic Nd, these (single-stage) model ages calculated from the present-day Nd-isotope compositions are probably mostly meaningless. We thus have used two-stage model ages, first calculating initial $^{143}Nd/^{144}Nd$ at 390 Ma then minimum depleted mantle model ages $\tau_{DM(2)}$ from these ratios assuming that no Lu was present. For *type-1*, *-2* and *-3* pyroxenites, these range between 502 and 779 Ma and are normally distributed around ~ 650 Ma.

Leached separates yielded very similar or slightly more radiogenic Nd (less 15 x 10^5 difference in $^{143}Nd/^{144}Nd$) than their non-leached replicates indicating the reliability of the data collected on non-leached minerals. If any, leaching has removed a surface contaminant with Nd slightly less radiogenic than cpx.

3. Combined Sr and Nd isotopes

On a plot of present-day ε_{Nd} *vs* $^{87}Sr/^{86}Sr$ (**Fig. V. 3**), most samples of cpx, amphibole and whole rocks are comparable to data previously reported for Cabo Ortegal pyroxenites, which plot within the field of ocean island basalts (OIB). However, apart from the LREE-enriched ones, *type-1* pyroxenites exhibit more radiogenic Nd compositions (up to ε_{Nd} = 12.5). Within the field of OIB, *type-3* pyroxenites, along with most LREE-enriched *type-1* and *-2* pyroxenites plot close to the EM I end member. Cabo Ortegal pyroxenites thus have heterogeneous Nd-isotope compositions (~ 15 ε_{Nd} units) over a narrow range of Sr-isotope compositions. Compared with the pyroxenites, Cabo Ortegal eclogites have quite homogeneous Sr- and Nd-isotope compositions, ε_{Nd} being similar to those of *type-1* pyroxenites over a range of $^{87}Sr/^{86}Sr$. However, like the garnet-bearing mafic layer sampled near the top of the pyroxenite-rich area in the Herbeira massif, Cabo Ortegal granulites are more scattered in Sr-Nd space, overlapping the whole range of pyroxenite compositions.

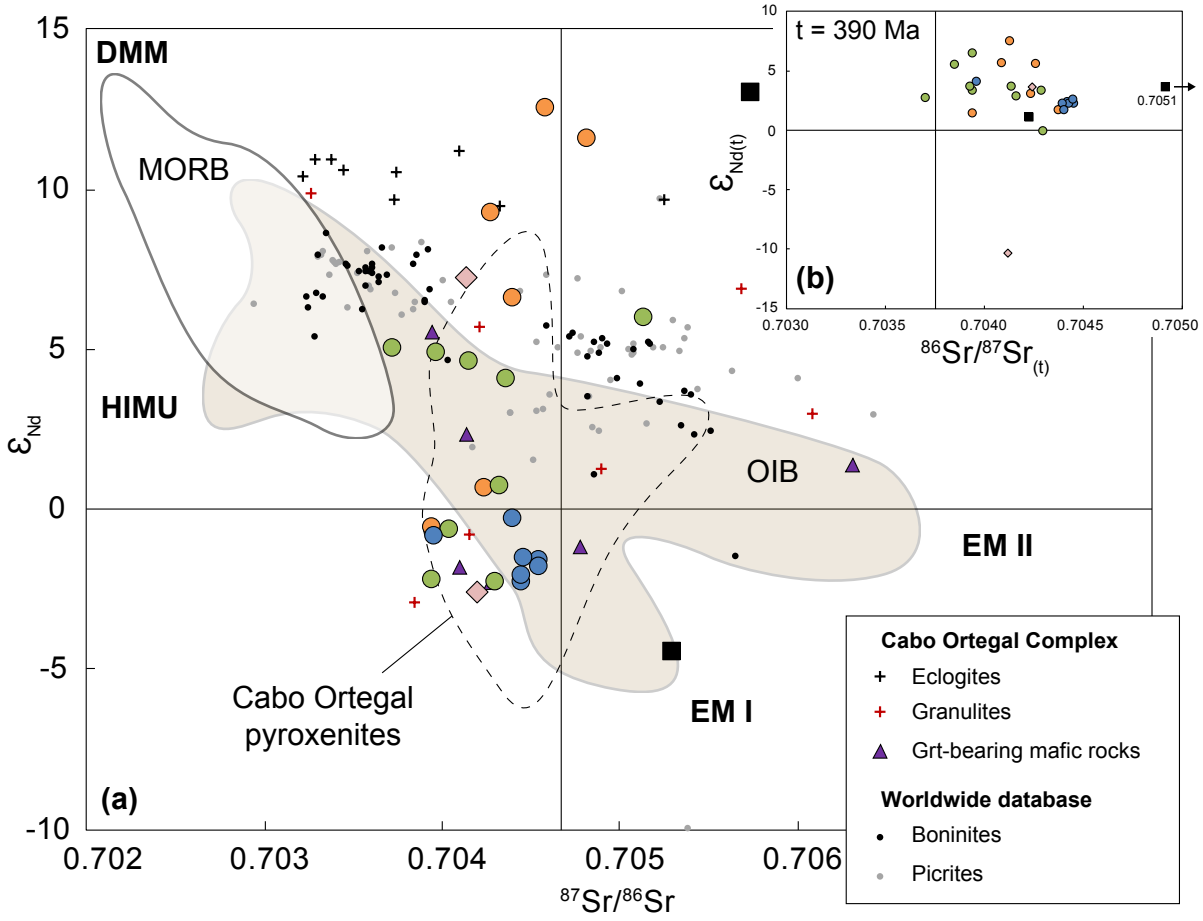

Fig. V. 3. a. Present-day ε_{Nd} *vs* $^{87}Sr/^{86}Sr$ for non-leached cpx, amphibole and whole-rock samples of Cabo Ortegal pyroxenites (and peridotites) compared with previous data on Cabo Ortegal pyroxenites (Gravestock, 1992; Santos et al., 2002), eclogites and granulites (Gravestock et al., 1992) and garnet-bearing mafic rocks (Peucat et al., 1990). A worldwide database of boninites and picrites sampled at convergent margins (Georock) and the compositional fields of MORB and OIB are also shown with DMM, EM I, EM II and HIMU end members (Hofmann, 2014). **b.** Initial ε_{Nd} *vs* $^{87}Sr/^{86}Sr$ calculated at t = 390 Ma (see text for more details). Other symbols as in **Fig. V. 2.**

Initial ratios calculated for Cabo Ortegal pyroxenites at t = 390 Ma are more homogeneous: ε_{Nd} lies mostly between 0 and 7.5, with the exception of the LREE-enriched *type-4* pyroxenite, and $^{87}Sr/^{86}Sr$ between 0.7037 and 0.7044. One of two analysed samples of peridotites has very radiogenic initial $^{87}Sr/^{86}Sr$.

4. Hf-isotope systematics

These data are the first Hf-isotope compositions reported for Cabo Ortegal pyroxenites and peridotites (**Table V-3**). Cpx, amphibole and whole-rock aliquots have $^{176}Hf/^{177}Hf$ ranging between 0.2822 and 0.2855, but there is no clear correlation with $^{176}Lu/^{177}Hf$ and no systematic distinction between the different types of pyroxenite (**Fig. V. 4**). However, *type-1* pyroxenites

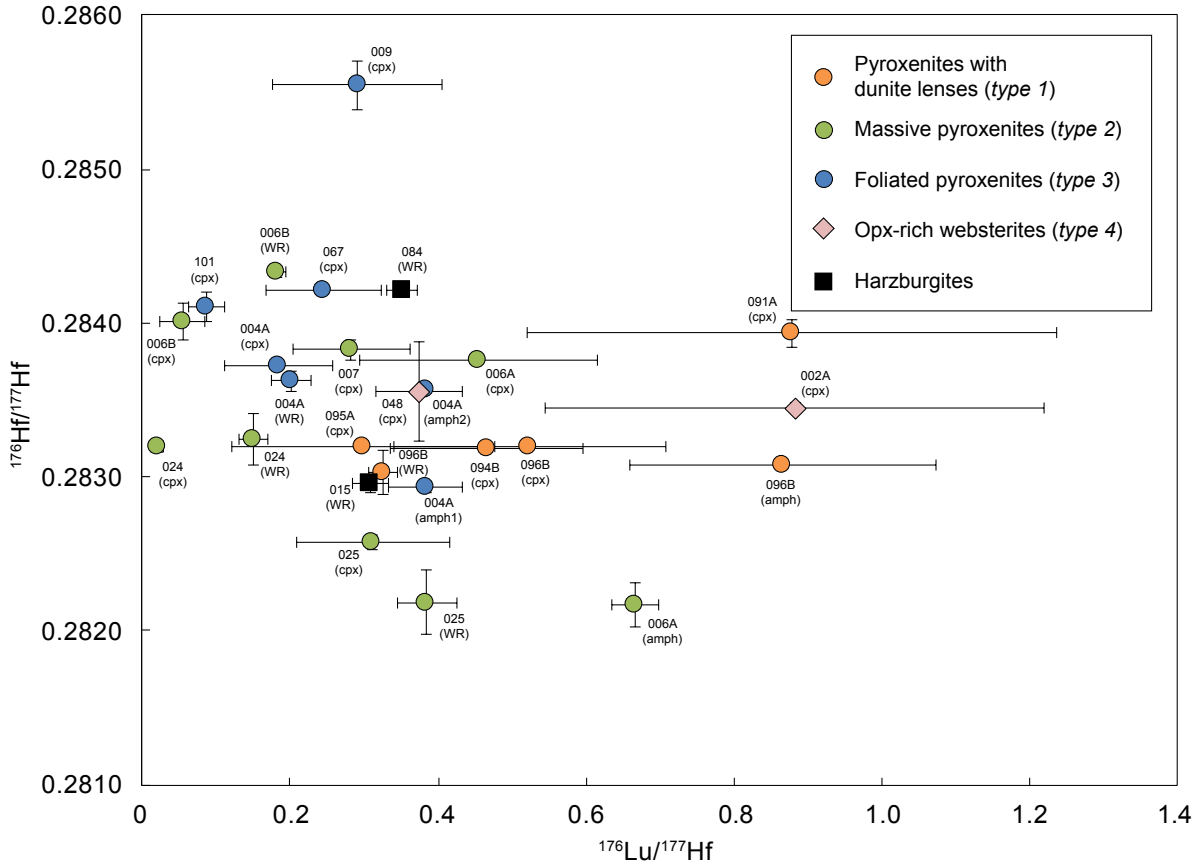

Fig. V. 4. Measured $^{176}Hf/^{177}Hf$ *vs* Lu/Hf for cpx, amphibole and whole-rock samples of Cabo Ortegal pyroxenites (and peridotites). Error used are the in-run errors for $^{176}Hf/^{177}Hf$ and standard deviations (2σ) for $^{176}Lu/^{177}Hf$.

have slightly higher $^{176}Lu/^{177}Hf$ and *type-2* pyroxenites reach lower $^{176}Hf/^{177}Hf$ while *type-3* pyroxenites tend to be restricted to higher values. Amphibole has higher $^{176}Lu/^{177}Hf$ than cpx and may either have similar or lower $^{176}Hf/^{177}Hf$. This isotopic disequilibrium cannot have simply been produced by ingrowth of radiogenic Hf from different initial $^{176}Lu/^{177}Hf$ related to partitioning between cpx and amphibole. This rather suggests the addition of non-radiogenic Hf during amphibolitization, as discussed in the next chapter. As a consequence, and with the exception of a *type-1* pyroxenite, whole rock samples have higher $^{176}Lu/^{177}Hf$ but variably lower, similar or higher $^{176}Hf/^{177}Hf$ than corresponding cpx.

Considering the large uncertainties associated with the calculation of initial Hf-isotope compositions, essentially due to the unknown extent to which $^{176}Lu/^{177}Hf$ has been changed, no meaningful two-step model ages can be calculated. The ingrowth of radiogenic Hf also render meaningless single-step model ages, ranging from future ages to > 5 Ga (**Table V-3**).

Table V-3. Hf-isotope data for Cabo Ortegal pyroxenites (and peridotites)

Sample		Lu (ppm)	Hf (ppm)	$^{176}Lu/^{177}Hf$	$^{176}Hf/^{177}Hf$	±	ε_{Hf}	τ_{DM} (Ma)	$^{176}Hf/^{177}Hf$ at 390 Ma	ε_{Hf} at 390 Ma
Type-1 pyroxenites										
CO-091-A	cpx	0.05	0.04	0.88	0.283930	93	40	433	0.277518	-178
CO-094-B	cpx	0.06	0.09	0.47	0.283187	25	14	-80	0.279782	-98
CO-095-A	cpx	0.02	0.05	0.30	0.283199	8	15	-108	0.281019	-54
	leached cpx	0.02	0.05	0.30	0.283439	32	23	386	0.281259	-45
CO-096-B	cpx	0.04	0.05	0.52	0.283193	7	14	-64	0.279368	-112
	leached cpx	0.04	0.05	0.52	0.283464	43	24	235	0.279638	-103
	amph	0.24	0.20	0.87	0.283075	21	10	-114	0.276748	-205
	WR	0.03	0.07	0.33	0.283028	141	8.6	-417	0.280653	-67
Type-2 pyroxenites										
CO-006-A	cpx	0.02	0.03	0.46	0.283762	14	35	656	0.280435	-74
	amph	0.13	0.14	0.67	0.282167	148	-22	-926	0.277300	-185
CO-006-B	cpx	0.01	0.15	0.05	0.284011	121	43	25529	0.283617	38
	WR	0.05	0.20	0.18	0.284331	36	55	4014	0.283001	16.3
CO-007	cpx	0.02	0.04	0.28	0.283823	67	37	1253	0.281758	-28
	leached cpx	0.02	0.04	0.28	0.283018	24	8	-512	0.280953	-56
CO-024	cpx	0.01	0.20	0.02	0.283192	37	14	1715	0.283047	18
	leached cpx	0.01	0.20	0.02	0.283130	41		3490	0.282985	16
	WR	0.04	0.20	0.15	0.283245	168	16	-28	0.282143	-14
CO-025	cpx	0.03	0.07	0.31	0.282574	49	-7.5	-1330	0.280297	-79
	leached cpx	0.03	0.07	0.31	0.282986	56	7.1	-520	0.280709	-65
	WR	0.05	0.09	0.38	0.282184	206	-21	-1653	0.279374	-112
Type-3 pyroxenites										
CO-004-A	cpx	0.03	0.14	0.18	0.283723	18	33	1735	0.282379	-6
	amph	0.18	0.34	0.38	0.282936	37	5.3	-490	0.280136	-85
	amph*	0.18	0.34	0.38	0.283564	10	28	486	0.280764	-63
	WR	0.08	0.30	0.20	0.283624	66	30	1230	0.282157	-14
CO-009	cpx	0.02	0.05	0.29	0.285545	166	98	4867	0.283428	31.4
	leached cpx	0.02	0.05	0.29	0.284062	46	45	1727	0.281946	-21.0
	leached amph	0.16	0.35	0.32	0.283427	51	23	341	0.281122	-50.2
CO-067	cpx	0.02	0.05	0.25	0.284210	22	50	2472	0.282415	-4
CO-101	cpx	0.02	0.18	0.09	0.284104	91	47	9443	0.283473	33
Type-4 pyroxenites										
CO-002-A	cpx	0.03	0.03	0.88	0.283443	35	23	122	0.276996	-196
CO-048	cpx	0.02	0.05	0.37	0.283557	323	27	487	0.280820	-61
Harzburgites										
CO-015-B	WR	0.01	0.02	0.31	0.282952	57	5.9	-593	0.280700	-65
CO-084	WR	0.03	0.06	0.35	0.284209	9	50	1639	0.281644	-32
Pyroxenite dyke										
CO-064-C	cpx	0.09	0.22	0.29	0.284015	35	43.5	1600	0.281869	-24
Other										
CO-069	cpx	0.03	0.03	0.68	0.282589	51	-7	-552	0.277606	-175

WR, whole rock; cpx, clinopyroxene; amph, amphibole. *coarse (> 600 μm) amphibole separate. Errors are given for the last digit on $^{143}Nd/^{144}Nd$. $\varepsilon_{Nd} = [(^{176}Hf/^{177}Hf_{sample})/(^{176}Hf/^{177}Hf_{CHUR})-1] \times 10000$.

Leached separates yielded similar or slightly more radiogenic Hf (less than 4 x 10^4 difference in $^{176}Hf/^{177}Hf$) than their non-leached replicates, with one exception less radiogenic. This indicates the overall reliability of the data acquired on non-leached minerals considering the range of variation observed between samples. However, it also suggests the significant contribution of surface contaminant with non-radiogenic Hf (compared to cpx). This is in agreement with coarse amphibole having higher $^{176}Hf/^{177}Hf$ (0.2836) than fine-grained amphibole (0.2829), while there is virtually no difference in terms of Sr and Nd isotopes.

5. Combined Nd and Hf isotopes

On a plot of present-day ε_{Hf} *vs* ε_{Nd} (**Fig. V. 5**), most *type-1* pyroxenites plot within or near the mid-ocean ridge basalts (MORB) array while *type-3*, and to a lesser extent, *type-2* pyroxenites have a wide range of radiogenic Hf-isotope compositions (ε_{Hf} = 5-98) plotting above the mantle array, with few exceptions of *type-2* pyroxenites plotting below. This shift from the mantle array towards more radiogenic Hf, and non-radiogenic Nd is roughly correlated with the metasomatic enrichment of LREE, LILE and other fluid-mobile elements described in the previous chapter. It would require the contribution of a highly radiogenic component with very low Nd/Hf and a comparatively high-Nd/Hf melt from the oceanic mantle array. However, calculation of initial ratios at t = 390 Ma provides a very different range of highly non-radiogenic Hf-isotope compositions with ($\varepsilon_{Hf(t)}$ = -205-18) mostly restricted to slightly non-radiogenic ε_{Nd}. This dramatic change in Hf compositions owes to the high $^{176}Lu/^{177}Hf$ of most samples and is highly dependent on the relatively large error propagated from $^{176}Lu/^{177}Hf$, particularly for the lowest ε_{Hf} with high $^{176}Lu/^{177}Hf$. Nonetheless, such low initial ε_{Hf} imply extremely old depleted-mantle model ages, even assuming unrealistically low $^{176}Lu/^{177}Hf$. This may suggest the involvement of an old, highly non-radiogenic component but mainly indicates that the present-day $^{176}Lu/^{177}Hf$ has been significantly increased since the last isotopic equilibrium. Implications of both of these observations are discussed in the next chapter in terms of petrogenetic processes and constraints on the nature of the source region.

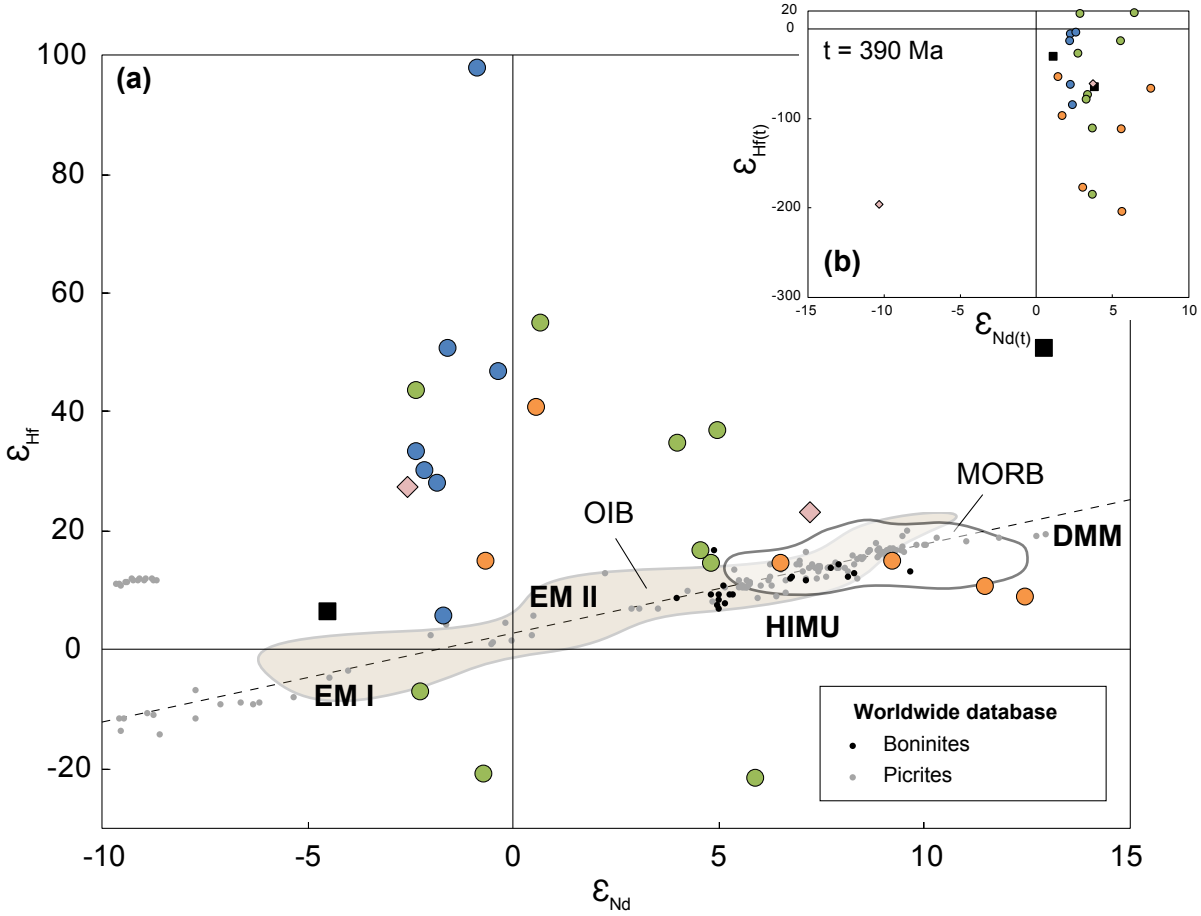

Fig. V. 5. a. Present-day ε_{Hf} *vs* ε_{Nd} for cpx, amphibole and whole rock of Cabo Ortegal pyroxenites (and peridotites). A worldwide database of boninites and picrites sampled at convergent margins (Georock) and the compositional fields of MORB and OIB are also shown with DMM, EM I, EM II and HIMU end members (Hofmann, 2014). **b.** Initial ε_{Hf} *vs* ε_{Nd} calculated at t = 390 Ma (see text for more details). Other symbols as in **Fig. V. 4.**

B. OSMIUM ISOTOPES

A set of samples from each type of pyroxenite, peridotite and chromitite was selected for analysis of Os-isotope composition. 2 g of powder was spiked with ^{190}Os and ^{185}Re for isotope-dilution measurement, and then digested in reverse aqua regia by Carius tube dissolution followed by solvent extraction, as described in detail by Shirey and Walker (1995) and Cohen and Waters (1996). 100 mg were weighed for chromitite assuming ~ 20 ppb Os. Re separation after removal of Os involved further solvent extraction. Detailed procedures for sample digestion, Os and Re separation and purification, and data collection carried out in the GAU of GEMOC/CCFS at Macquarie University are available in **Appendix B**.

Os concentrations and isotopic ratios were measured by negative-ion TIMS on a Thermo Finnigan Triton TIMS system. All analyses were carried out using a secondary electron multiplier via ion counting, in peak hopping mode using a $Ba(OH)_2$ activator solution. Os total procedural blanks (TPB) levels of 1-3 pg represent contributions of less than 0.5 % with the exceptions of 4 samples with Os concentrations < 140 ppt, where blank contributions were between 1 and 3 %. Two batches of analyses yielded ^{187}Os/^{188}Os of 0.14436 ± 5 and 0.14415 ± 6 for reference sample WPR-1 (in-run errors) and long-term lab running of has yielded ^{187}Os/^{188}Os= 0.14466 ± 80 (n = 28), which is good agreement with Day *et al.* (2016) for comparable dissolution techniques (^{187}Os/^{188}Os = 0.1449 ± 13). The measured ^{187}Os/^{188}Os of the TPB was 0.1590 and 0.1642. Re concentrations were measured on an Agilent 7700 ICP-MS as detailed in **Appendix B**. TPB for Re were 12.5 and 15 pg for the two different batches, which represent in most cases < 0.1 % of the dissolution of 2 g samples. Os-isotope compositions are reported in **Table V-4**.

As for Hf, these data are the first Os-isotope compositions reported for the Cabo Ortegal Complex. Os concentration in pyroxenites ranges between 0.05 and 0.86 ppb; *type-1* pyroxenites are mainly restricted to the low concentrations while *type-3* pyroxenites may reach the higher values. Harzburgites have 3.2-3.8 ppb Os while chromitites range between 25 and 77 ppb. One sample of the garnet-rich mafic layer near the top of the pyroxenite-rich area (CO-026) has extremely low Os (0.016 ppb). Re concentration is very variable, ranging from 0.36 ppb to 137 ppb in pyroxenites, with one sample exceeding 7 ppm. The two samples of harzburgites have 1.1-4.8 ppb Re while chromitites range between 7 and 480 ppb. The garnet-bearing mafic sample (CO-026) is also quite Re-rich with 22.6 ppb.

^{187}Os/^{188}Os generally ranges between 0.16 and 0.54 in pyroxenites (one sample reaches 1.4) while peridotites and chromitites have relatively homogeneous compositions around 0.13-

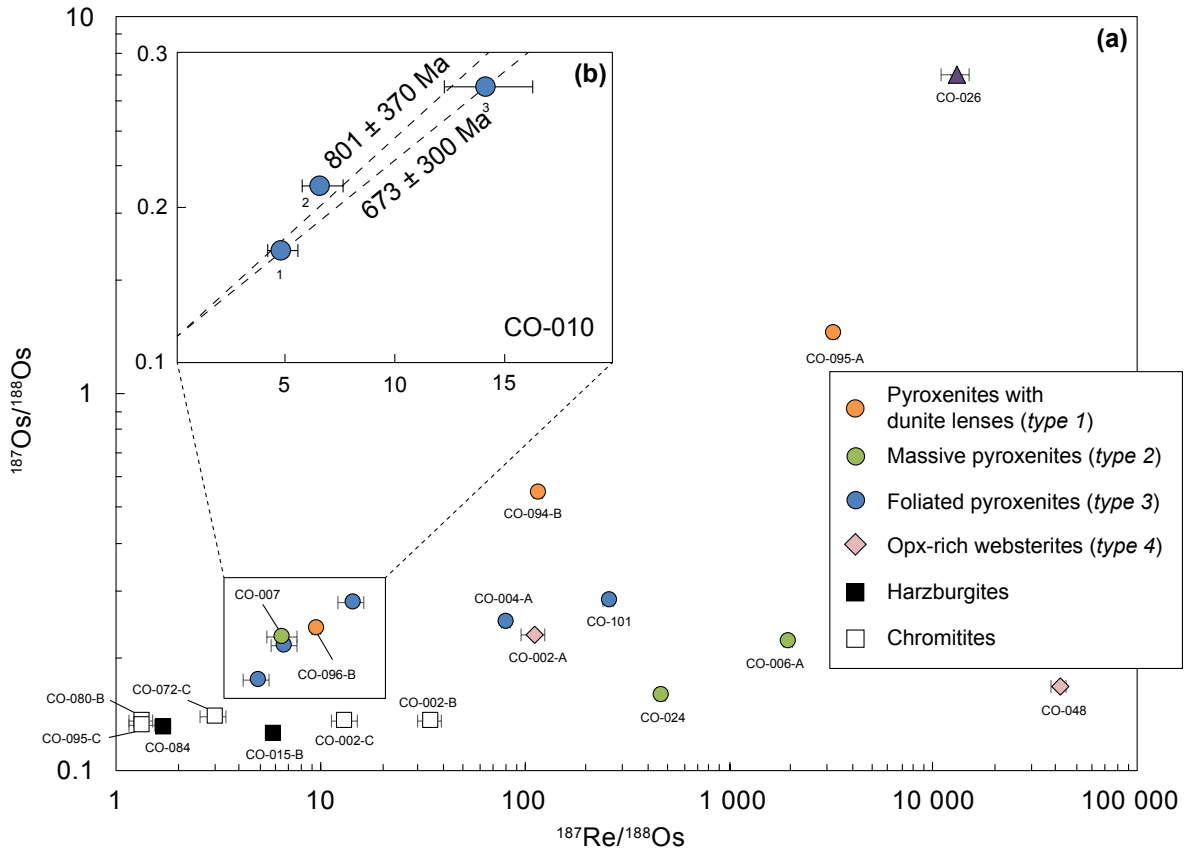

Fig. V. 6. a. Measured whole-rock $^{187}Os/^{188}Os$ *vs* $^{187}Re/^{188}Os$ for Cabo Ortegal pyroxenites, peridotites and chromitites. Both axes are in log scale. **b.** Measured whole-rock $^{187}Os/^{188}Os$ *vs* Re/Os and potential isochrons calculated for three portions of sample CO-010 plotted in linear scales (see text for further details). Errors used are the in-run errors (2σ) for both $^{187}Os/^{188}Os$ and $^{187}Re/^{188}Os$.

0.14. The garnet-bearing mafic sample has extremely radiogenic Os ($^{187}Os/^{188}Os = 7.1$). On an isochron diagram (**Fig. V. 6a**) plotted with log scale due to the large range of values on both axis, these data exhibit an increasing scattering from homogeneously low $^{187}Os/^{188}Os$ at low Re/Os to very dispersed at the highest parent-daughter ratios. The garnet-bearing mafic sample (CO-026) and the LREE-enriched *type-4* pyroxenite are respectively the most and the least radiogenic end members at high parent/daughter ratios; chromitites and harzburgites represent the low $^{187}Os/^{188}Os$-low $^{187}Re/^{188}Os$ end members of this triangular compositional field.

To investigate the impact of melt-induced metasomatism as evidenced by trace-element compositions (particularly the enrichment of LREE, LILE, U and Th), three portions of the heterogeneous sample described in the previous chapter (CO-010) were analysed. Portion 1, which represents the least-enriched part of the sample, accordingly has the least radiogenic Os, while portions 2 and 3, which are increasingly enriched in terms of trace elements, also have more radiogenic Os (**Fig. V. 6b**). A potential isochron age has been calculated from these

Table V-4. Whole-rock Os-isotope data for Cabo Ortegal pyroxenites, peridotites and chromitites

Sample	Re (ppb)	Os (ppb)	$^{187}Re/^{188}Os$	$^{187}Os/^{188}Os$	±	τ_{MA} (Ma)	τ_{RD} (Ma)
Type-1 pyroxenites							
CO-094-B	1.51	0.065	117	0.54253	21	212	
CO-095-A	26.2	0.046	3232	1.44200	23	24.4	
CO-096-B	1.68	0.857	9.55	0.23620	5	708	
Type-2 pyroxenites							
CO-006-A*	137	0.341	1962	0.21984	7	2.8	
CO-007	0.363	0.271	6.52	0.22530	4	6.5	
CO-024	63.1	0.650	469	0.15823	10	3.9	
CO-025		0.086		0.50054	12		
Type-3 pyroxenites							
CO-004-A	2.17	0.131	81.0	0.24594	18	81	
CO-010-1	1.75	0.603	14.3	0.27823	3	648	
CO-010-2	0.971	0.710	6.7	0.21431	4	825	
CO-010-3	0.643	0.635	4.9	0.17268	4	597	
CO-101	18.8	0.360	256	0.28008	15	256	
Type-4 pyroxenites							
CO-002-A	11.2	0.493	111	0.22926	4	111	
CO-048*	7058	0.827	41307	0.16708	11	0.06	
Harzburgites							
CO-015-B	4.73	3.89	5.86	0.12439	2		588
CO-084	1.14	3.21	1.71	0.12948	2	87	
Pyroxenite dyke							
CO-064-C	21.2	0.293	359	0.37507	35	41	
Other							
CO-026	22.6	0.016	12958	7.08507	463	32	
Chromitites							
CO-072-C	15.7	25.3	3.00	0.13818	3	244	
CO-002-B	480	67.0	34.5	0.13519	3	13	
CO-002-C	101	37.2	13.1	0.13506	3	35	
CO-080-B	21.2	76.8	1.33	0.13440	3	440	
CO-095-C	6.98	25.1	1.34	0.13189	2	275	

τ_{MA}, Os model ages (i.e. assuming the ingrowth of Os from the present-day $^{187}Re/^{188}Os$); τ_{RD}, rhenium-depletion model ages (i.e. assuming no ingrowth of Os).

three points at 801 ± 370 Ma (initial $^{187}Os/^{188}Os$ = 0.111 ± 40; MSWD = 2.2), while a two-point isochron excluding the intermediate value provides an age of 673 ± 300 Ma (initial $^{187}Os/^{188}Os$ = 0.117 ± 33).

Os model ages (τ_{MA}) are very scattered but as a significant proportion of them are restricted to the last 60 Ma (**Table V-4**). Among them, a cluster appears between 24 and 41 Ma, potentially corresponding to the crude isochron that could be calculated from the whole dataset at 30 Ma. Os model ages also span to much older ages (213-951 Ma) without clustering. In addition, one sample of harzburgite (CO-015-B) has sub-chondritic present-day $^{187}Os/^{188}Os$ that allows for the calculation of a Re-depletion model age (τ_{RD}) at 588 Ma.

SUMMARY OF CHAPTER V

- Cabo Ortegal pyroxenites have **homogeneous Sr-isotope** compositions ($^{87}Sr/^{86}Sr$ ~ 0.704-0.705). ***Type-3*** **pyroxenites** are distinctive with **radiogenic** $^{87}Sr/^{86}Sr$ at low $^{87}Rb/^{86}Sr$. Amphibole and whole rocks have higher $^{87}Rb/^{86}Sr$ than cpx providing **internal Sr isochrons** with apparent ages around **300 Ma** *Type-1* and -2 pyroxenites along with one of the harzburgite samples give an **external isochron** age of **491 ± 81 Ma**.

- *Type-1*, *-2* and *-3* have **increasingly unradiogenic Nd-isotope** compositions ($-3 < \varepsilon_{Nd} < 12$), which are directly **correlated with their LREE enrichment** and trend towards the **EM I / II end members** of the OIB array in initial Sr-Nd space. **Internal** and **external Nd isochrons** give apparent ages between **403 and 561 Ma**. Two-stage **Nd model ages** range between **502 and 779 Ma**.

- In Nd-Hf space, the **wide range** of present-day Hf-isotope compositions of most pyroxenites ($^{176}Hf/^{177}Hf = 0.282\text{-}0.286$) is shifted from the OIB array towards **extremely radiogenic Hf-isotope** compositions (ε_{Hf} close to 100). This contrasts with **unrealistically unradiogenic initial ratios** (ε_{Hf} = -205-18) potentially suggesting the involvement of an old, **highly non-radiogenic component**, but mainly indicating the recent **modification of $^{176}Lu/^{177}Hf$**. This modification and the ingrowth of radiogenic Hf render meaningless single- and two step Hf model ages.

- Pyroxenites comparatively have a **wide range of radiogenic Os-isotope** compositions ($^{187}Os/^{188}Os = 0.16\text{-}1.44$) with respect to the **homogeneous peridotites and chromitites** (0.12-0.14). A linear correlation between the three portions of an increasingly LREE-enriched sample give an **isochron age of ~ 800** Ma. A sample of harzburgite with sub-chondritic present-day $^{187}Os/^{188}Os$ gives a **Re-depletion model age of 588 Ma**.

Chapter VI.

Discussion

A. IMPACT OF SECONDARY PROCESSES

In the Herbeira massif of the Cabo Ortegal Complex, pyroxenite layers vary in thickness from a few millimetres up to 3 m. This may reflect inheritance of intrusive magmatic layering strongly overprinted by tectonic slicing and transposition, as suggested by Girardeau and Gil Ibarguchi (1991). Cabo Ortegal pyroxenites also bear evidence of prograde metamorphism, from the stability field of spinel pyroxenite to that of garnet pyroxenite, and of hydration during retrograde metamorphism, notably under amphibolite-facies conditions, and serpentinization. Selective enrichment of LILE, LREE and other fluid-mobile elements over HFSE is also characteristic of these pyroxenites and may relate to fluid/melt percolation. A preliminary requirement is thus to assess the impact of these secondary processes in order to envision the magmatic significance of Cabo Ortegal pyroxenites, based on the consistency between the petrological and geochemical systematics.

1. Serpentinization

Cabo Ortegal pyroxenites, and particularly olivine-bearing (*type-1*) pyroxenites have been subjected to various degrees of serpentinization. To investigate the role of this process, the composition of cpx was analysed across the contact between a *type-1* pyroxenite and its host dunite and thinly layered pyroxenites (**Fig. IV. 14**). As serpentinization increases from ~ 30 to 70 %, Li content in cpx increases significantly from 1.6 to 7.0 ppm but this is only accompanied by moderated enrichment of the lightest REE (La and Ce). This trend very likely represents the diffusional modification of a sharp gradient, formerly located at the contact between moderately-serpentinized pyroxenite and highly-serpentinized dunite. An additional enrichment of highly fluid-mobile elements can thus be potentially ascribed to serpentinization but it seems restricted to the lightest REE and Li, as only observed in certain *type-1* pyroxenites.

2. Fluid/melt percolation

Cpx, amphibole and whole-rock samples consistently show REE patterns ranging from spoon-shaped in (*type-1*) pyroxenites with dunite lenses, to variously LREE-enriched and LREE-to-MREE fractionated in massive (*type-2*) and foliated (*type-3*) pyroxenites (**Fig. VI. 1**). Gravestock (1992) noted that, among melting models, only fractional disequilibrium melting could produce such a selective enrichment of LREE (Bédard, 1989, Prinzhofer & Allègre, 1985). However, this process would result in a positive MREE-to-HREE slope which is not observed in the Cabo Ortegal pyroxenites. The range of spoon-shaped to continuously-enriched REE

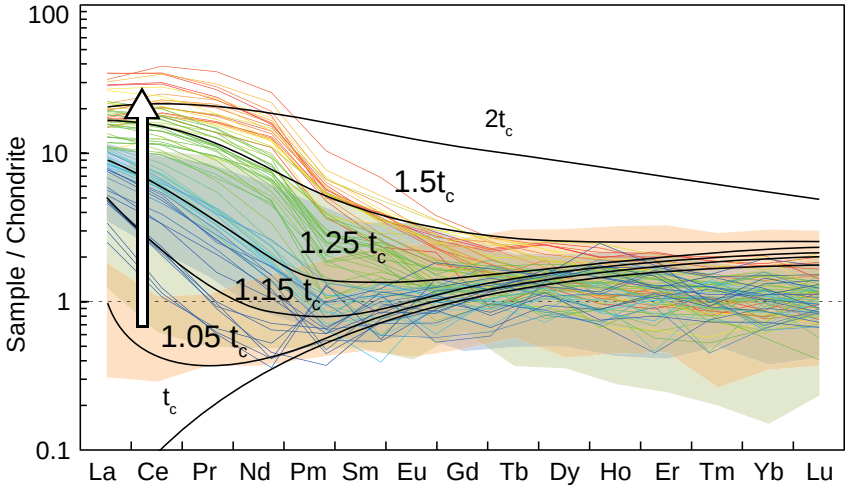

Fig. VI. 1. Comparison between REE compositions of cpx in Cabo Ortegal pyroxenites and predictions from the chromatographic model as illustrated in Fig 4 of Navon & Stopler (1987). Compositional fields correspond to cpx in *type-1*, *-2* and *-3* pyroxenites, as in **Fig. IV. 3** and **4**. Individual lines correspond to the compositions of cpx along the profile of sample CO-010, as in **Fig. IV. 12**. t_c corresponds to the nondimensional time required for the metasomatic agent to pass through the column. The vertical scale of the modelled REE patterns have been modified to fit the data thus only providing a qualitative comparison of their evolution; original La abundance ranges between 0.01 and 0.3 times its concentration in chondrites (McDonough and Sun, 1995).

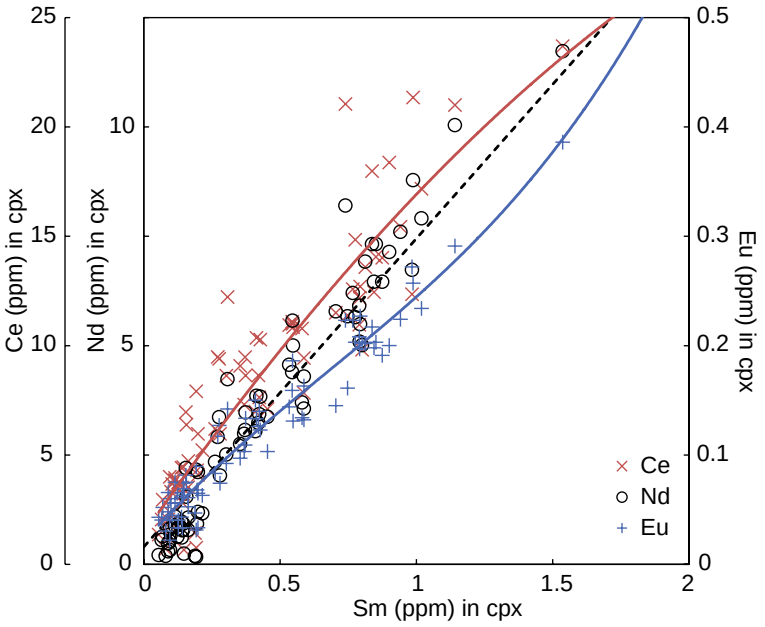

Fig. VI. 2. Concentrations of Ce, Nd and Eu in cpx along the profile shown in **Fig. IV. 12** plotted *vs* that of Sm. Scale on the y axis is adjusted so that end-member samples plot at approximately the same position, as in Navon and Stolper (1987). Red and blue lines represent best-fit regression lines for Ce and Eu, respectively. Dashed black line represents the linear trend expected from simple mixing between end-member samples from which data deviate.

patterns can instead be reproduced by percolation of fluids or melts according to the chromatographic model of Navon and Stolper (1987), as illustrated in **Fig. IV. 1** and reported in many localities (*e.g.* Batanova *et al.*, 1998, Bodinier *et al.*, 1990, O'Reilly *et al.*, 1991, Takazawa *et al.*, 1992, Ionov *et al.*, 2002, Powell *et al.*, 2004, Gysi *et al.*, 2011). This process can potentially generate extreme fractionation at small scales (*e.g.* Rampone & Morten, 2001), such as the progressive enrichment of LREE and MREE observed within individual samples and between the different types of pyroxenite. Accordingly, the deviation of Ce or Nd from a simple mixing line when plotted against Sm (**Fig. VI. 2**) and the transient evolution of $(Pb/Pb^*)_{PM}$ and $(Sr/Sr^*)_{PM}$ (**Fig. IV. 11**) are predicted between elements of different degrees of incompatibility by chromatographic reequilibration (Navon & Stolper, 1987).

The good correlation between LREE enrichment (*i.e.* decreasing $^{147}Sm/^{144}Nd$) and Nd-isotope compositions allows for a reliable discrimination between the different types of pyroxenite. This implies that the Nd-isotope compositions (**Fig. V. 2**) are simply related to the ingrowth of Nd following the chromatographic reequilibration of Cabo Ortegal pyroxenites with an enriched metasomatic agent. The overall agreement between the compositions of leached and unleached minerals signifies that this enrichment is probably not a late superficial feature (although this cannot be ruled out altogether), implying that exotic Sr and Nd were introduced into the clinopyroxene structure through recrystallization and/or diffusion. The narrow range of initial ratios calculated at t = 390 Ma ($^{143}Nd/^{144}Nd_{(t)}$ = 0.5117-0.5122) indicates that the metasomatic enrichment probably occurred following the formation of the pyroxenites, although the external Nd isochrons (531 and 561 Ma) are too old when compared with the commonly accepted ages reported for Cabo Ortegal pyroxenites (~ 390 Ma; Santos *et al.*, 2002). The significance of these ages will be discussed below.

Potential metasomatic agents responsible for the chromatographic reequilibration of Cabo Ortegal pyroxenites include:

- (1) hydrous metamorphic fluids;
- (2) residual melts left after fractional crystallization;
- (3) low-degree partial melts.

These alternatives have very distinctive petrogenetic implications closely related to the origin of amphibole as discussed below. In terms of isotope systematics, we suggest that the metasomatic enrichment can be represented by mixing with a Nd-rich component (compared

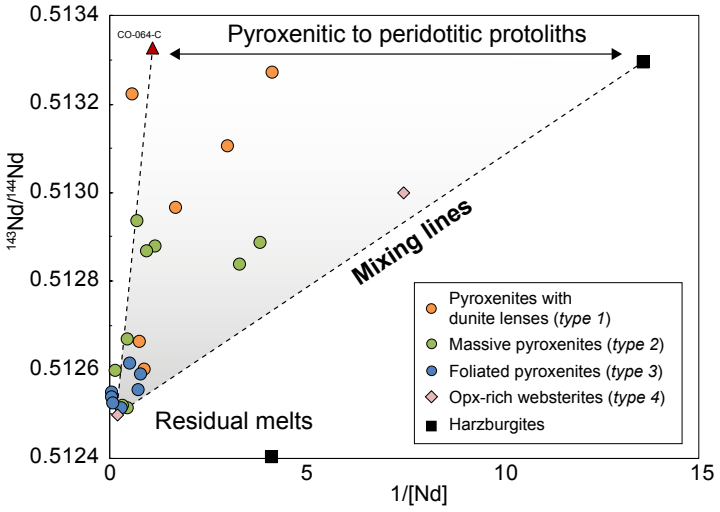

Fig. VI. 3. Measured $^{143}Nd/^{144}Nd$ *vs* 1/[Nd] and potential mixing lines between pyroxenitic and peridotitic protoliths and *type-3* pyroxenites, potentially representing the composition of residual melts.

to cpx and amphibole). This implies that it had a comparatively unradiogenic composition; the opposite situation is excluded because it would require an unrealistically high fluid-melt/rock ratio. The convergence of potential mixing lines towards the compositions of *type-3* pyroxenites on a $^{143}Nd/^{144}Nd$ *vs* 1/[Nd] plot (**Fig. VI. 3**) more particularly indicates that the Nd contents and isotopic compositions of the metasomatic agents were very similar to those in *type-3* pyroxenites, or generally to LREE-enriched pyroxenites. These interpretations support the concept of late-magmatic migration of residual melts (*i.e.* in isotopic equilibrium with the LREE-enriched pyroxenites), although the contribution of hydrous fluids cannot be excluded, particularly if this fluid was extracted from the silicate melt upon solidification (Menzies *et al.*, 1987).

No correlation was observed between $^{87}Sr/^{86}Sr$ and 1/[Sr], which suggests that at least one of the mixing components (*i.e.* protolith or metasomatic agent) had a heterogeneous Sr-isotope composition, or alternatively that they had similar compositions. Nonetheless, the relatively homogeneous compositions of *type-3* pyroxenites are probably representative of that of the metasomatic agent (~ 0.7045), without providing further constraints on its fluid or melt nature. Similarly, the unsupported (*i.e.* by greater $^{176}Lu/^{177}Hf$) radiogenic Hf-isotope compositions of most LREE-enriched samples is likely to be related to metasomatic addition of radiogenic Hf, but this again does not constrain the nature of the agent involved.

Alternatively, the migration of low-degree partial melts could be envisaged if small-vol-

ume melts are able to percolate through a solid matrix (Mckenzie, 1984). Unrealistically low (*i.e.* less radiogenic than the primitive mantle at 4.6 Ga) initial Hf compositions (mostly for *type-1* pyroxenites) imply that the $^{176}Lu/^{177}Hf$ ratios of the Cabo Ortegal pyroxenites have been modified by the addition of Lu, subsequently to the isotopic equilibrium. This strongly suggests that *type-1* pyroxenites may have experienced late partial melting in the presence of garnet. The involvement of garnet is indeed one of the only means to fractionate $^{147}Sm/^{144}Nd$ from $^{176}Lu/^{177}Hf$ as observed here (*e.g.* Salters & White, 1998). This would imply that the apparent primitive characteristics of *type-1* pyroxenites might be the consequence of melt extraction. However, the high uncertainty associated with the calculation of initial Hf compositions renders these data alone insufficient to support this scenario.

Nonetheless, post-kinematic migration of low-degree partial melts may be indicated by pyroxenite and garnet-rich mafic dykes in the Herbeira massif, among which some exhibit

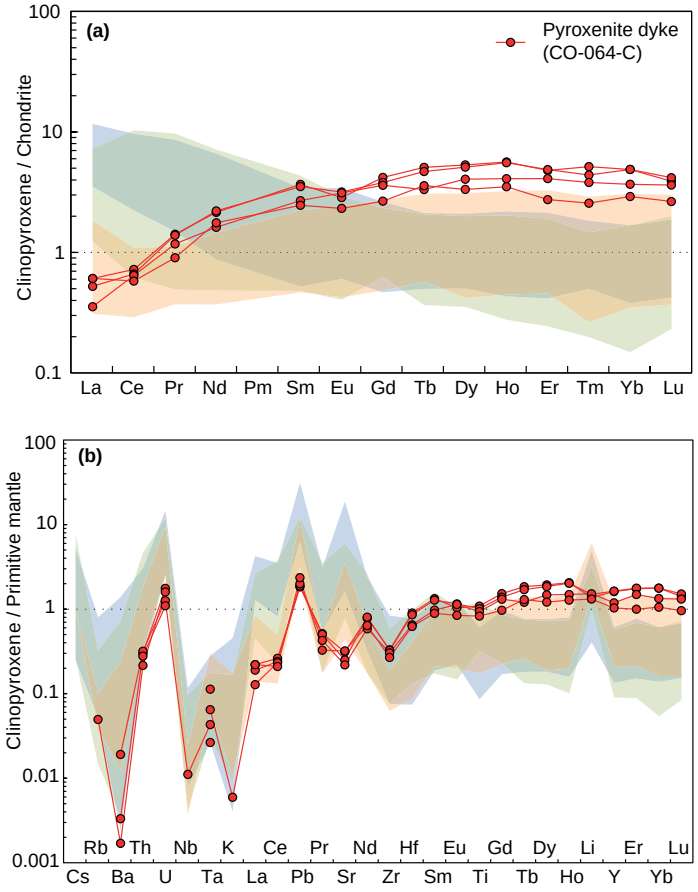

Fig. VI. 4. a. REE and **b.** trace-element compositions of cpx in a pyroxenite dyke (CO-064-C). Orange, blue and green compositional fields correspond to cpx in *type-1*, *-2* and *-3* pyroxenites, respectively, as in **Fig. IV. 3** and **4**. Chondrite and primitive mantle compositions from McDonough and Sun (1995).

opx-rich rims characteristic of the reaction between Si-rich melt and peridotite (*e.g.* Borghini *et al.*, 2013). Although the presence of such dykes in the vicinity of LILE- and LREE-enriched *type-1* pyroxenites is demonstrated for one sample (CO-091-A), we believe that this non-pervasive process cannot be responsible for the ubiquitous metasomatic signature of Cabo Ortegal pyroxenites. In addition, the very limited enrichment of LREE, LILE and other fluid-mobile elements observed in such dykes (**Fig. VI. 4**) confirms that their intrusion post-dated the main magmatic/metasomatic episode. Accordingly, these veins are also mostly undeformed, except where occurring near tectonic contacts.

3. Metamorphic *vs* late magmatic/metasomatic amphibolitization

The origin of amphibole, which represents at the thin-section scale between 4 and 42 wt % of Cabo Ortegal pyroxenites, is ambiguous. Following the above discussion, two scenarios, not mutually exclusive, are envisaged, excluding the migration of partial melts for being volumetrically limited. According to these, amphibole may represent the product of either:

- (1) hydration (± addition of other volatiles) and reaction of cpx and spinel during retrograde metamorphism
- (2) crystallization of percolating or trapped residual melts.

The first scenario is supported by textural observations, and particularly the post-kinematic character of amphibole and its dominantly interstitial position, which clearly indicate that it is a secondary phase. It is also consistent with the observation that cpx and opx from the

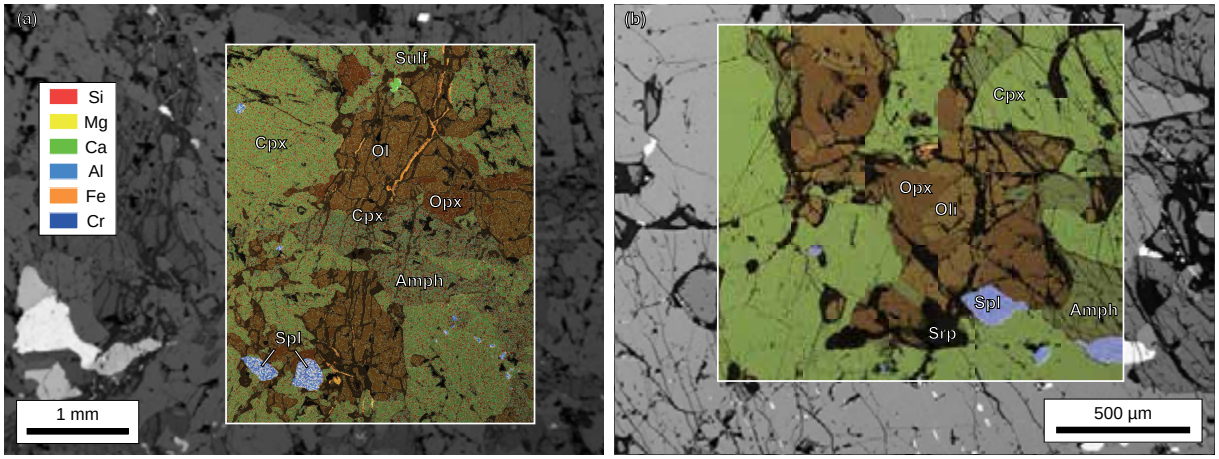

Fig. VI. 5. Back-scattered electron (BSE) images with overlapping energy-dispersive X-ray spectroscopy (EDS) maps illustrating the textural relationships between amphibole, olivine and pyroxenes in *type-1* pyroxenites: **a.** idiomorphic amphibole grown within an olivine trail; **b.** opx enclosing olivine against a sub-idiomorphic amphibole. EDS maps are color-coded by element as indicated. See **Appendix A3** (**Fig. A3. 3**) for further details.

most amphibolitized (*type-3*) pyroxenites overlap the range of Mg# of both *type-1* and *type-2* pyroxenites and have lower Al_2O_3 contents as the result of sub-solidus reequilibration with amphibole (**Fig. IV. 5**).

The partitioning of most incompatible elements (apart from REE, as discussed below) reported in **Table VI-1**, is similar to values reported in mantle-derived xenoliths (O'Reilly *et al.*, 1991, O'Reilly & Griffin, 1995, Vannucci *et al.*, 1995, Chazot *et al.*, 1996, Ionov *et al.*, 1997, Grégoire *et al.*, 2000b). This may indicate a chemical equilibrium between the two phases, in good agreement with the similarities between their REE patterns (**Fig. IV. 3**), which is in turn consistent with a metamorphic origin for amphibole.

In addition, *type-3* pyroxenites plot parallel to the Fo-An join following *type-1* pyroxenites on a pseudoternary forsterite (Fo)-Ca-tschermak pyroxene (CaTs)-quartz (Qz) diagram projection, as detailed below (**Fig. VI. 9**), which suggests that primitive olivine-clinopyroxenitic and olivine-websteritic protoliths were preferentially amphibolitized, in agreement with textural relationships in *type-1* pyroxenites (**Fig. VI. 5**). Conversely, the preservation of dunite lenses within them is indicative of limited metasomatic/metamorphic overprint and deformation. *Type-3* pyroxenites may indeed simply have formed through greater amphibolitization (*i.e.* hydration) of the same protoliths as those of *type-1* and -2 pyroxenites. This implies that more deformed protoliths were subsequently exposed to greater hydration, hence amphibolitization (**Fig. VI. 6**). Accordingly, spinel in *type-3* pyroxenites exhibit a strong Fe-Ti trend (as dis-

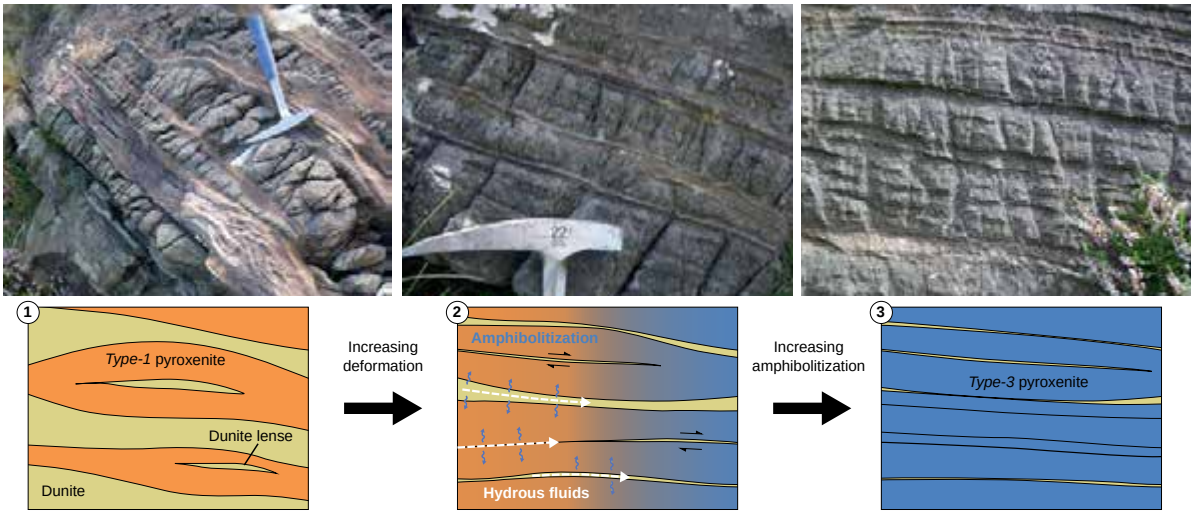

Fig. VI. 6. Field pictures and schematic illustrations of the deformation/hydration (amphibolitization) of the protolihs of *type-1* pyroxenites to *type-3* pyroxenites. (**1**) *Type-1* pyroxenite layers exhibiting high-temperature boudinage preserve dunite lenses; (**2**) dunitic layers and lenses are preferentially deformed and percolated by hydrous fluids; as a consequence, (**3**) *type-3* pyroxenites are highly amphibolitized, their foliation results from stretched-out dunites. Field of view of the third field picture is similar to that of the second.

Table VI-1. Representative partition coefficients between amphibole and cpx in Cabo Ortegal

Rock type	*Type-1* pyroxenites			*Type-2* pyroxenites			*Type-3* pyroxenites			*Type 4*
$D_{amph\text{-}cpx}$										
Li	0.62	0.21	0.47	0.29	0.09	0.38	0.61	0.76	0.15	2.39
Be	1.7	1.2	1.7	1.3	1.2	1.3	1.7	1.2	1.1	0.8
Sc	2.5	2.1	2.6	1.7	2.0	1.6	1.4	1.7	1.6	1.2
Ti	2.9	2.9	4.5	4.4	3.4	2.8	6.0	3.6	3.8	4.8
V	3.3	3.5	4.0	2.6	3.0	2.4	2.6	2.8	2.5	1.2
Cr	2.1	4.2	3.6	2.3	2.5	3.1	3.2	3.1	3.0	0.5
Co	1.9	1.8	2.0	1.9	1.9	1.9	1.8	1.9	2.0	1.4
Ni	2.9	2.9	2.9	2.8	2.8	2.7	3.0	2.7	2.7	n.a.
Cu	3.3	1.4	1.1	2.1	12.7	1.3	9.9	2.9	5.3	0.0
Zn	1.6	1.4	1.7	1.8	1.4	1.5	1.8	1.5	2.0	n.a.
Ga	3.3	4.0	4.7	3.7	3.8	3.3	4.4	3.7	3.3	2.3
Rb	118	114	157	26	82	48	15	309	267	78
Sr	5.7	4.0	3.6	2.1	3.5	4.9	1.2	2.2	3.3	6.3
Y	7.5	5.9	7.1	5.9	5.4	5.6	4.5	5.6	5.3	2.3
Zr	3.8	3.9	6.2	3.8	3.6	2.5	4.5	3.2	2.5	2.9
Nb	36	71	82	28	16	73	46	117	79	70
Cs	12.9	7.8	3.3	1.4	3.0	2.2	0.7	3.7	1.7	21.7
Ba	571	207	493	144	244	3362	501	1990	671	366
La	5.5	5.3	6.9	4.2	4.8	4.2	3.8	4.4	4.0	2.2
Ce	5.8	4.6	6.7	4.1	4.8	4.2	3.7	4.3	3.9	2.1
Pr	5.4	4.5	6.8	4.2	3.9	4.1	3.8	4.2	3.7	2.1
Nd	5.1	4.7	6.3	4.4	4.4	4.3	4.0	4.2	4.1	2.2
Sm	5.3	5.5	6.4	5.1	5.2	4.1	3.7	5.3	4.1	2.2
Eu	5.8	5.5	5.4	5.3	4.5	4.6	3.8	4.8	4.3	2.2
Gd	6.3	5.4	5.9	5.1	5.3	4.8	4.5	4.6	4.3	2.9
Tb	6.3	4.8	6.2	4.7	5.7	5.2	4.2	5.5	5.1	2.0
Dy	7.0	5.0	6.7	5.3	5.2	5.3	4.5	5.2	4.8	2.5
Ho	7.2	5.6	6.4	5.4	5.5	5.7	3.9	5.7	5.2	2.5
Er	7.3	5.7	8.2	5.7	4.6	5.9	4.0	5.0	5.4	2.7
Tm	7.4	5.9	8.1	5.3	6.4	6.1	4.7	5.4	4.9	3.9
Yb	7.9	5.9	7.7	6.4	7.3	7.0	3.6	5.8	5.4	3.1
Lu	7.3	6.2	6.9	6.5	4.8	5.0	4.2	7.0	4.8	4.8
Hf	3.9	3.2	7.3	4.5	3.6	2.7	3.9	3.1	2.4	4.7
Ta	2.1	1.9	5.6	0.9	1.6	5.1	10.0	9.7	13.2	48.2
Pb	6.6	6.0	5.2	3.1	5.7	6.4	1.1	3.0	4.0	0.5
Th	3.3	4.1	4.9	3.8	2.9	3.2	2.2	3.1	2.7	1.4
U	4.6	4.0	5.7	4.2	4.2	3.7	2.3	3.6	3.2	2.2

Partition coefficients were calculated from averaged grain cores of cpx and amphibole.

cussed below) interpreted as the result of extensive fluid infiltration and preferential lost of Al during amphibolite-facies metamorphism (Barnes, 2000, Barnes & Roeder, 2001). The common development of magnetite and "ferritchromit" is also consistent with a metamorphic scenario involving relatively high grades (Barnes, 2000), as detailed below.

On the other hand, the late-magmatic appearance of hornblende has been previously reported for similar bulk compositions (Green *et al.*, 2004) and several observations support this scenario in Cabo Ortegal pyroxenites. For instance, strong partitioning of the REE into amphibole ($D^{\Sigma REE}_{amph/cpx}$ ~ 4-7) as measured in Cabo Ortegal pyroxenites has only been reported in few other localities (Vannucci *et al.*, 1995, Witt-Eickschen & Harte, 1994). In the East Eifel xenoliths of the Rhenish Massif, similar $D^{\Sigma REE}_{amph/cpx}$ (3-8) were interpreted as the result of a crystal-chemical control from low Na and K, and high Ca in cpx, similar to cpx compositions in Cabo Ortegal pyroxenites. In these xenoliths, amphibolitization was attributed to the interaction of rising peridotites with small fractions of low-density, CO_2-H_2O-bearing fluids present along grain boundaries during cooling, without additional supply of percolating fluids (Witt & Seck, 1989).

We suggest that the presence of small volumes of incompatible- and volatile-enriched residual melts after the segregation of Cabo Ortegal pyroxenites may have been responsible for the late magmatic/metasomatic crystallization of hornblende. Similar processes have been documented in other arc-related pyroxenites (*e.g.* Burg *et al.*, 1998). Such metasomatic infill, referred to as "percolative fractional crystallization" by Harte *et al.* (1993), would account for the correlation between the modal proportion of amphibole and the selective enrichment of incompatible trace elements described above, due to the combination of porosity-reducing reactions (fractional crystallization) and chromatographic effects (Navon & Stolper, 1987, Bodinier *et al.*, 1990, Vasseur *et al.*, 1991). It is also expected from experimental studies that amphibole precipitation can lead to a compositional shift from H_2O-rich to CO_2-rich in the residual liquid, which would consequently reduce the solubility of the REE, thus incorporated into cpx and amphibole (Moine *et al.*, 2004, Schneider & Eggler, 1986).

For the reasons above, we believe that the existence of late magmatic/metasomatic amphibole is likely. However, compelling textural evidence supports the existence of at least some metamorphic amphibole. It is thus envisaged that two distinct episodes of amphibolitization occurred (*i.e.* late magmatic/metasomatic and metamorphic). Nonetheless, both episodes may be regarded as virtually occurring in closed systems (apart from hydration and addition of volatiles), which allows us to speculate on the petrogenetic processes and on the nature of

melts involved.

From the perspective of Hf-isotope systematics, a simple replacement of cpx (and spinel) by amphibole seems unlikely. Indeed, if amphibole was simply the product of a metamorphic reaction from cpx and spinel (and assuming a negligible contribution of spinel), the higher $^{176}Lu/^{177}Hf$ in amphibole would have generated more radiogenic Hf than in cpx. However, the opposite is observed. This unsupported radiogenic Hf in amphibole could be explained by either of the following hypotheses.

Addition of non-radiogenic Hf

This hypothesis would imply that the residual melt or hydrous fluid responsible for amphibole crystallization had experienced a low time-integrated $^{176}Lu/^{177}Hf$ and was thus generated in the presence of garnet. We have no other evidence to support this alternative.

Addition of Lu subsequent to the closure of the system

This can be envisaged if, during the crystallization of amphibole, the breakdown of garnet occurred in the presence of a mineral with high partition coefficient for the HFSE, such as zircons or Ti-rich oxides (*e.g.* Green & Pearson, 1987, Foley *et al.*, 2000, Münker *et al.*, 2004). In other words, it would imply that the late-magmatic or metamorphic event responsible for amphibolitization was coeval with the breakdown of garnet. This scenario may be supported by the association of ilmenite and Fe-Ti-rich spinel and amphibole in symplectite that were

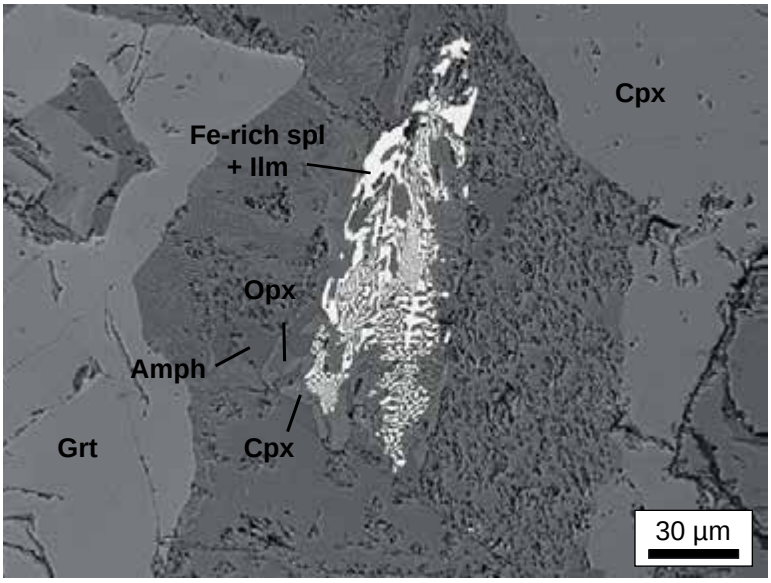

Fig. VI. 7. BSE image illustrating the association of cpx, opx, amphibole, Fe-rich spinel and ilmenite as distinct symplectites after garnet. See **Appendix A3** (**Fig. A3. 5**) for further details.

probably formed after garnet (**Fig. VI. 7**). These symplectites may have subsequently (and preferentially) been replaced by amphibole while the preferential host mineral of the HFSE, and thus of Hf (*e.g.* ilmenite) was preserved as a distinct phase. This could be consistent with the higher $^{176}Hf/^{177}Hf$ measured in coarse-grained amphibole although we did not find any textural evidence for this replacement.

Lack of initial equilibrium between cpx and amphibole

This is not supported by the isotopic equilibrium between these two phases in terms of Nd isotopes unless the blocking temperature of Lu-Hf is significantly higher than that of Sm-Nd (*e.g.* Scherer *et al.*, 2000), but this is not documented for amphibole to our knowledge. Nonetheless, the preservation of fresh olivine rims in textural equilibrium with amphibole grains suggests that amphibole crystallized at relatively high temperatures (**Fig. VI. 5b**), at least exceeding the stability field of serpentine, and probably the blocking temperature of Sm-Nd.

From the perspective of Sr and Nd isotopes, internal isochrons calculated from cpx-amphibole pairs are respectively younger (261-326 Ma) and older (403-470 Ma) than the ages commonly accepted for Cabo Ortegal pyroxenites (~ 390 Ma). These observations may indicate that amphibole crystallization was accompanied by the addition of an enriched component (*i.e.* with radiogenic Sr and unradiogenic Nd), potentially represented by hydrous fluids (*e.g.* Downes, 2001), without ruling out the existence of late-magmatic amphibole.

B. ORIGIN OF CABO ORTEGAL PYROXENITES

Girardeau and Gil Ibarguchi (1991) estimated that 80-90 % of the 300 m-thick, 3 km-long pyroxenite-rich area exposed in the Herbeira massif of the Cabo Ortegal Complex is made up of pyroxenites, which is consistent with our observations. This amount of relatively homogeneous pyroxenites requires a significant volume of compositionally similar melts. It is unlikely that these were produced in situ (*i.e.* in a closed system) by low-degree partial melting of lherzolite, as formerly proposed (Van Calsteren, 1978). Instead, high-pressure crystallization of an external melt intruding and reacting with the ambient peridotite is a more reasonable scenario, as later suggested (Girardeau & Gil Ibarguchi, 1991, Girardeau *et al.*, 1989, Gravestock, 1992). More recently, based on the presence of high-Pd and -Pt chromitites exposed within high-Cr# dunites, Moreno *et al.* (2001) interpreted the western part of the Herbeira massif as a (crustal) cumulate sequence. In addition, Santos *et al.* (2002) indicated the residual origin of the harzburgites and showed a fractionation trend between dunites and pyroxenites. However, a comprehensive model accounting for the formation of Cabo Ortegal pyroxenites based on petrological and geochemical constraints is still missing. This is thus the aim of the following discussion.

We suggest that the lithological variations observed among Cabo Ortegal pyroxenites (*e.g.* olivine clinopyroxenites, clinopyroxenites, websterites and opx-rich websterites), and their association with dunites, relate to an intricate combination of fractional crystallization and melt/peridotite interaction. For that purpose, several assumptions have been made.

- All pyroxenites are cogenetic and related to a single partial melting episode of a homogeneous or homogeneously heterogeneous mantle source (on the scale of melt extraction), in agreement with homogeneous Pb-, Sr-, Nd-isotope compositions reported by Gravestock (1992), Santos *et al.* (2002) and in this study; Hf- and Os-isotope systematics may indicate a more complex situation as discussed below.

- They do not represent the metamorphic products of plagioclase-bearing mafic lithologies, as supported by the absence of strong positive Eu anomalies.

- Their whole-rock major-element compositions were preserved (± volatiles addition) during amphibolitization, as discussed above.

1. Major-element characteristics of the parental melts

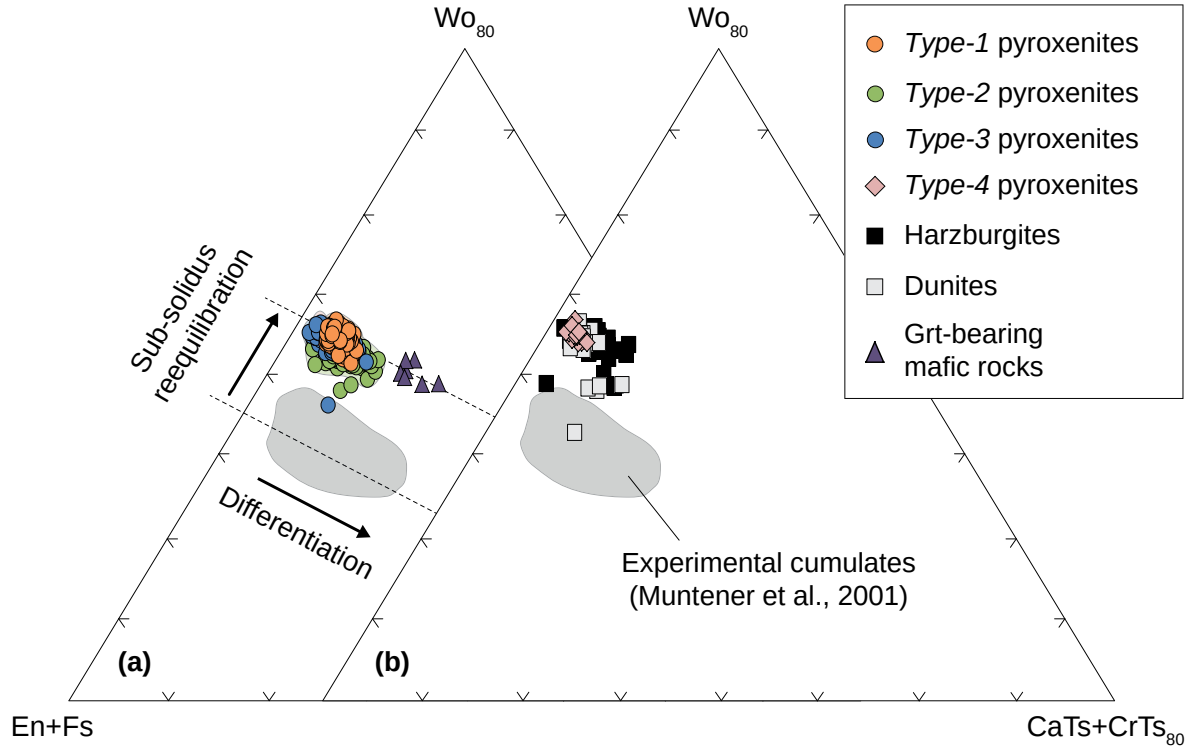

Fig. VI. 8. Compositions of cpx in **a.** *type-1*, *-2* and *-3* pyroxenites and garnet-bearing mafic rocks, and **b.** *type-4* pyroxenites and peridotites compared to experimental cumulates from Müntener *et al.* (2001) and recalculated into end-member components wollastonite (Wo) – enstatite + ferrosilite (En+Fs) – Ca- and Cr-Tschermaks (CaTs+CrTs) as in O'Hara (1968).

The whole-rock major-element compositions of Cabo Ortegal pyroxenites are characterised by very high CaO and low Al_2O_3, TiO_2 and alkalis. They are thus comparable to the pyroxenitic compositions reconstructed by Müntener *et al.* (2001) from the experimental products of crystallization of hydrous basaltic andesite and high-Mg# andesite at 1.2 GPa. The corresponding experimental cpx have low Ca- and Cr-Tschermaks (CaTs + CrTs) indicative of near-liquidus crystallization where the partitioning of Al between cpx and melt increases with water content and decreases with temperature (Gaetani *et al.*, 1993, Sisson & Grove, 1993, Müntener *et al.*, 2001). From these initial compositions, CaTs + CrTs components may then increase during fractional crystallization due to the combined effect of high pressure and high water content in the melt (> 3 %) preventing the appearance of plagioclase. This trend is observed for cpx in Cabo Ortegal pyroxenites and arc-related pyroxenites and gabbronorites from the Tonsina complex (DeBari & Coleman, 1989), but their wollastonite (Wo) content is shifted away from the compositional field of experimental cpx (**Fig. VI. 8**). This shift is ascribed to the widening of the immiscibility gap between enstatite and diopside at lower temperature, due to sub-solidus reequilibration and/or the presence of water during crystallization (Gaetani & Grove,

1998, Müntener *et al.*, 2001). Accordingly, our data show that cpx in *type-1* and *-4* pyroxenites have slightly higher Wo content than *type-2* pyroxenites, potentially due to sub-solidus re-equilibration with higher modal olivine.

In addition to the effect of pressure and water content, experiments have shown that, provided that no Al-rich phases are present, a positive correlation exists between the partitioning of Al into cpx and the Al/Si of the coexisting melt (Gaetani & Grove, 1995, Müntener *et al.*, 2001). Low-Al pyroxenes like those reported in this study are thus likely to be produced from hydrous melts with low Al/Si such as boninites or high-Mg# andesites, as suggested by Müntener *et al.* (2001) for being two-pyroxene saturated melts. However, we believe that Si-undersaturated melts such as picrites cannot be excluded at this stage, because the extent of olivine fractionation and melt-rock interaction is uncertain. It should be emphasized here that the terms *boninite* and *picrite* are strictly used to describe the affinities of their parental melts, and not the Cabo Ortegal pyroxenites themselves. These are defined on a petrogenetic basis for describing magmatic rocks "demonstrably derived from parental magmas meeting […] compositional requirements[1]" (Crawford *et al.*, 1989). The very high CaO/Al_2O_3 (2.2-11.3) of Cabo Ortegal pyroxenites more specifically suggest high-Ca boninites (Crawford *et al.*, 1989) or ultra-calcic picrites (Schiano *et al.*, 2000, Kogiso & Hirschmann, 2001), also referred to as island-arc ankaramites.

After constraining the extent of melt-peridotite interaction, inferences on the potential source region of these melts will be proposed in the light of trace-element and isotope geochemistry.

2. Melt differentiation and melt-peridotite interaction

High concentrations of compatible elements (*i.e.* $Cr_2O_3 > 0.4$ wt %) in the Cabo Ortegal pyroxenites suggest that they crystallized from primitive melts, which are known to produce olivine-bearing assemblages at relatively low pressures, if generated in equilibrium with peridotite at higher pressures (Kushiro & Yoder, 1966, O'Hara, 1968, Green & Ringwood, 1969). Apart from very thin layers (< 5 cm-thick) that may have mechanically included olivine from the host rock (**Fig. IV. 1**), olivine-bearing samples are restricted to the most primitive (*type-1*) pyroxenites (*i.e.* with the highest Mg# and Cr#). Their high cpx/opx ratios point to crystallization

1 As revised by Le Bas (2000), these requirements are, for boninites, high SiO_2 (> 52 wt %) and MgO (> 8 wt %) and low TiO_2 (< 0.5 wt %), and for picrites, high MgO (> 12 wt %), and low SiO_2 (< 52%) and alkalis (< 3 wt % $Na_2O + K_2O$).

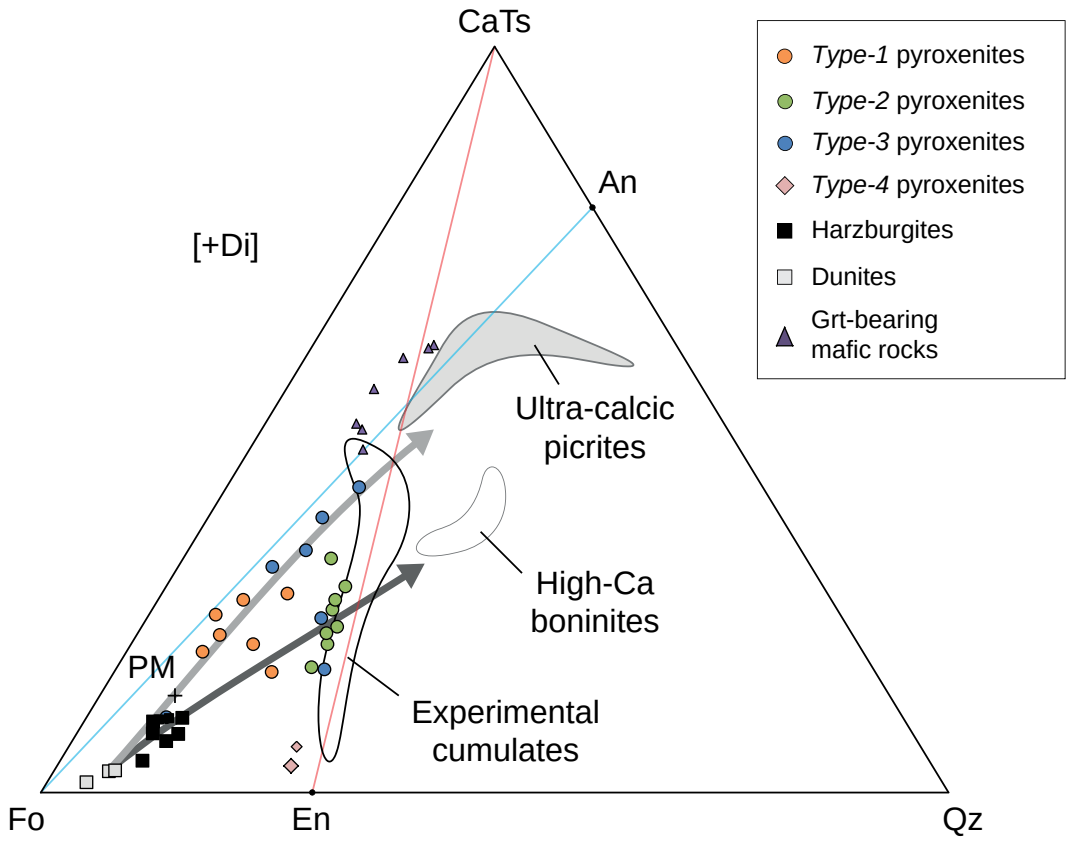

Fig. VI. 9. Normative compositions of Cabo Ortegal pyroxenites in the pseudoternary system Fo-CaTs-Qz projected from Di using the method of O'Hara (1968). Nepheline- and hypersthene-normative compositions are separated by the Di-Fo-An plane (blue line). Silica-deficient and silica-excess compositions are divided by the Di-CaTs-En plane (red line). Light and dark grey arrows correspond to the potential differentiation trends for *type-1* and *type-2* pyroxenites, towards picrites and boninites, respectively (see text for further details). Fo, forsterite; CaTs, Ca-Tschermak pyroxene; Qz, quartz; An, anorthite; En, enstatite; Di, diopside. References for ultra-calcic picrites, high-Ca boninites and the experimental cumulates are in **Fig. IV. 2**.

along a cpx-olivine cotectic line, as expected from the crystallization of ultra-calcic picrites, but contrasting with the early appearance of opx during the crystallization of boninites (Barsdell & Berry, 1990, Eggins, 1993). A picritic parental melt is thus suggested for *type-1* pyroxenites.

However, the existence of dunite lenses within *type-1* pyroxenites cannot be simply explained by melt differentiation following a single magmatic event and probably resulted from incomplete reaction between their parental melts and the dunitic host. This is consistent with the interpretation of dunite lenses preserved in the pyroxenites of the Jijal Complex as due to partial replacement of peridotites at decreasing melt/rock ratios (Burg *et al.*, 1998, Garrido *et al.*, 2007, Bodinier *et al.*, 2008). Accordingly, *type-1* pyroxenites plot close to the Fo-An join within the nepheline-normative, silica-deficient field because of their lower SiO_2 at similar MgO

compared to other types, and compared to the experimental pyroxenites mentioned above (**Fig. IV. 2**). This trend towards the peridotite array (*i.e.* close to the Fo apex) is seen in other orogenic pyroxenites, and has been ascribed to melt-peridotite interaction (Bodinier *et al.*, 2008, Lambart *et al.*, 2012).

By contrast, olivine-free massive (*type-2*) pyroxenites plot close to the experimental cumulates along the En-CaTs join on the Fo-CaTs-Qz diagram (**Fig. VI. 9**) and may thus represent the crystallization products of two-pyroxene saturated melts (*e.g.* boninites) comparable with those used in the experiments by Müntener *et al.* (2001). This may have occurred following the completion of a peritectic reaction of the type Fo + Si-rich melt = En (*e.g.* Kelemen, 1986, Kelemen & Ghiorso, 1986, Burg *et al.*, 1998) if under sufficiently low-pressure conditions (< 1.2 GPa), and/or by segregation from differentiated melts into dykes or veins. In any cases, *type-2* pyroxenites were produced at greater melt/rock ratios than *type-1* pyroxenites, as required

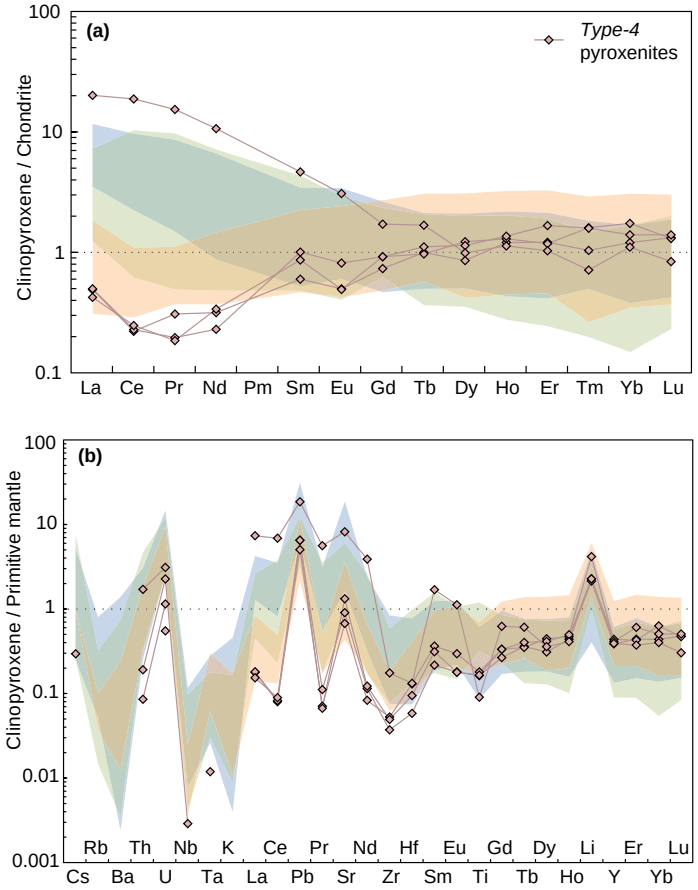

Fig. VI. 10. a. REE and **b.** trace-element compositions of cpx in opx-rich (*type-4*) websterites. Orange, blue and green compositional fields correspond to cpx in *type-1*, *-2* and *-3* pyroxenites, respectively, as in **Fig. IV. 3** and **4**. Chondrite and primitive mantle compositions from McDonough and Sun (1995).

either to ensure the completion of the peritectic reaction or to permit melt migration though open fractures. Distinct tectonic implications follow, as discussed below.

Consequently, the combination of low melt/rock ratios in *type-1* pyroxenites and low time-integrated amount of metasomatic agent inferred from their limited enrichment of LREE and LILE confirms that residual melts may indeed represent the main metasomatic agent, as postulated above. This process corresponds to the percolative fractional crystallization of Harte *et al.* (1993) and may account for the correlation between the abundance of layered pyroxenites and the extent of LREE enrichment observed in the host harzburgites (Gravestock, 1992). Such melt-induced metasomatism would also account for the fact that the whole-rock budget of Li is dominated by cpx, because Li preferentially partitions into cpx instead of olivine in the presence of melt (Scambelluri *et al.*, 2006).

Constraints provided by spinel compositions

The compositions of Cr-spinels in Cabo Ortegal pyroxenites and peridotites show a strong control of both Cr-Al and Fe-Ti trends, resulting in a well-defined spinel gap (**Fig. VI. 11**), which relates to a solvus in the spinel solid solution (Sack & Ghiorso, 1991).

The Cr-Al trend, which is commonly observed in high-pressure mantle xenoliths and abyssal, ophiolitic and orogenic peridotites, is mainly defined by spinel in *type-1* (and some *type-2* and *-3*) pyroxenites and accompanied by decreasing Mg#. This trend is interpreted as the result of reequilibration between spinel and silicates (Barnes & Roeder, 2001), and more specifically following the subsolidus reequilibration with cpx exsolving Al (Sinton, 1977), thus overprinting the initial variation of whole-rock compositions. Conversely, chromitites (and to a minor extent, chromite-rich dunites) are more preserved from this reequilibration process, hence their high Cr. This is confirmed by their narrow range of Mg# (0.35-0.50). Accordingly, chromite in chromitites associated with pyroxenites (group B) has lower Cr# and the difference in spinel compositions between dunites and harzburgites relates to their respective refractory and fertile character (Bonatti & Michael, 1989).

The Fe-Ti trend, which is commonly observed in continental mafic intrusions and arc-related ultramafic complexes, is represented by spinel in most *type-2* and *-3* pyroxenites and particularly well defined by *type-2* pyroxenites (comparatively less scattered than *type-3* pyroxenites). This may be the result of:

- fractional crystallization of olivine and pyroxenes as Fe/Mg and Ti increase in the residual melt (particularly in the case of *type-2* pyroxenites). This effect can be accentuated if

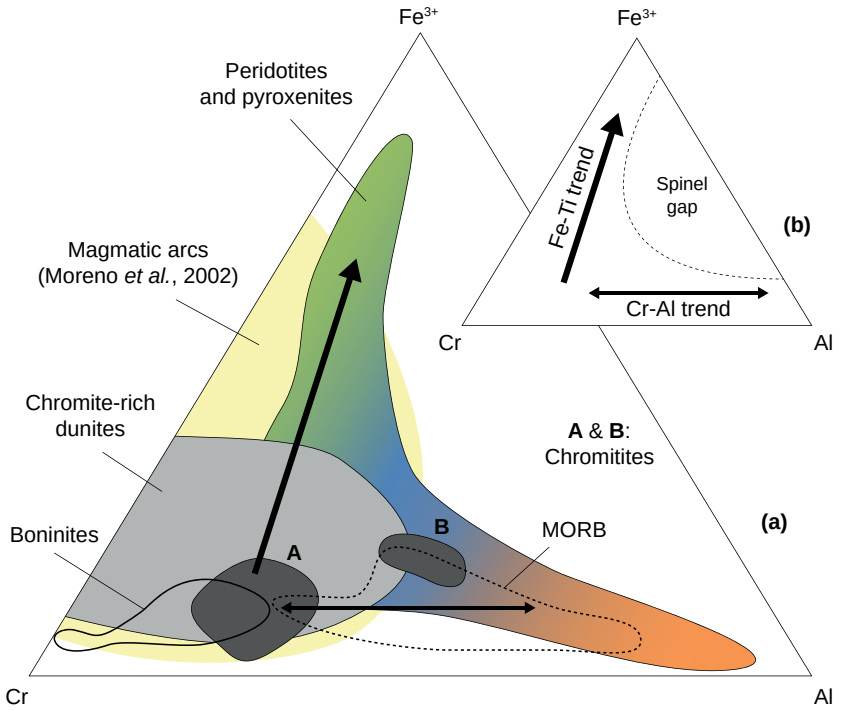

Fig. VI. 11. a. Compositionnal fields of spinel in Cabo Ortegal pyroxenites, peridotites and chromitites compared with that of chromite in boninites and MORB. **b.** Schematic representation of the main trends governing the compositions of terrestrial spinels after Barnes & Roedder (2001). **A** and **B** correspond to the groups of chromitite defined in **Fig. IV. 9b**; **A** also includes chromitites from Moreno *et al.* (2001).

spinel is reacting with evolving trapped melt (Barnes & Roeder, 2001, and references therein), which could be indicated by the continuity of compositions from Cr-rich to Fe^{3+}-rich;

- increasing oxidation accompanying melt differentiation as suggested by the correlation between Fe^{3+} and V (Pagé & Barnes, 2009).

Decreasing Mg# accompanying these trends is ascribed to evolving melt compositions (late-magmatic metasomatism) and reequilibration with coexisting silicates at decreasing temperatures (Irvine, 1965) and/or to alteration (Pagé & Barnes, 2009). The relatively limited enrichment of Ti (mainly < 1 wt %) specified the competition of other phases for Ti, and notably amphibole (Barnes & Roeder, 2001). Greater Ti enrichment is restricted to Cr-rich magnetites[2] as Ti preferentially partitionned in spinels with high magnetite component (Barnes & Roeder, 2001). Limited development of the Fe-Ti trend in chromitites is ascribed to the buffering effect

2 Such Fe^{3+}-Cr-rich composition represents a product of metamorphism and alteration that has been frequently referred to as "ferritchromit", which, although not officially recognised as a mineral, is clearly distinct from igneous magnetite that has lower Cr# due to its late appearance in the crystallization sequence (*i.e.* as Cr has been mainly consummed from the melt).

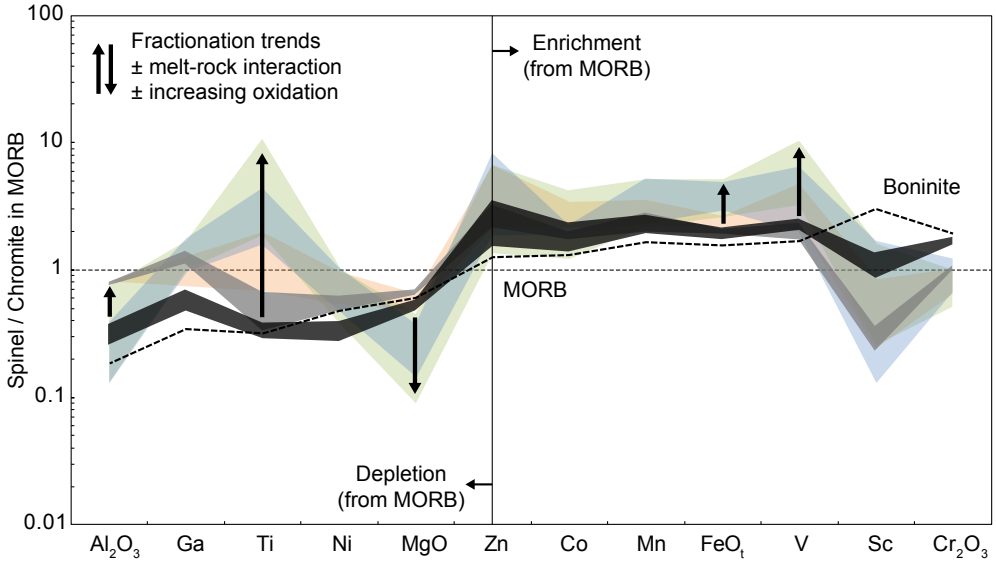

Fig. VI. 12. Spider diagram illustrating the affinity of Cabo Ortegal chromitites with boninites and the effect on pyroxenitic spinels of reequilibration with silicates during fractional crystallization, among other processes (see text for further details). The compositional fields of the different types of pyroxenite and chromitites shown here are related to **Fig. IV. 11**.

of high-modal chromites thus less sensitive to reaction with trapped liquids.

The composition of spinel in *type-1* pyroxenites overlaps that of spinel in MORB. However, the combination of melt differentiation and reequilibration with silicates and/or residual fluids hinder the interpretation of peridotitic, and particularly pyroxenitic, spinels in terms of the composition of their parental melts. This apparent MORB-like compositions is simply the result of the above-mentioned processes. On the other hand, chromite in chromitites that are not directly associated with pyroxenites mostly fall within the compositional field of boninitic chromites, which probably reflects the actual compositions of their parental melts. This is confirmed by their minor- and trace-element compositions (**Fig. VI. 12**).

Boninites are the only natural magmas (apart from kimberlites) that contain chromites as Cr-rich as those in ophiolitic chromitites (Barnes & Roeder, 2001). This strong affinity has been previously used to suggest that boninites may be the parental melts for ophiolitic podiform chromitites in agreement with the large proportion of boninites associated with ophiolitic complexes (Cameron, 1985, Coish, 1989). The reason for this lies both in the highly depleted source of boninitic melts (hence the high Cr#, low Fe^{3+} and low Ti; Crawford & Cameron, 1985, Sobolev & Danyushe*vsk*y, 1994) and their high content of water leading to the earlier crystallization of spinel than Cr-bearing pyroxenes (Bannister *et al.*, 1998). Such requirements may also be met in the case of other primitive mantle-derived magmas such as picrites.

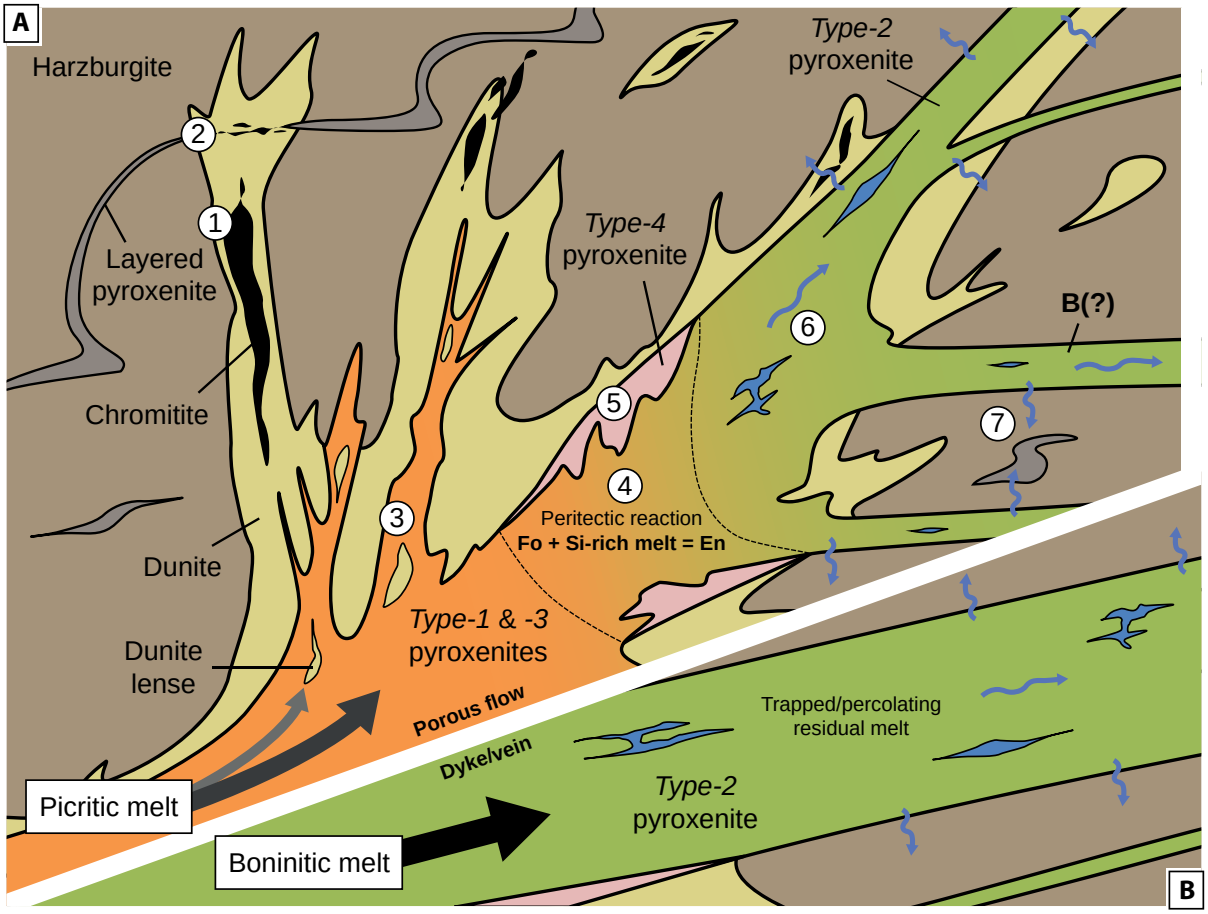

Fig. VI. 13. A. Schematic representation of the proposed model for the main magmatic/metasomatic episode in the petrogenesis of Cabo Ortegal pyroxenites, dunites and chromitites assuming an initial picritic melt. (**1**) Dunites and chromitites represent the first products of crystallization of a primitive picritic melt reacted with host peridotite. (**2**) Extremely deformed pyroxenites, potentially resulting from former partial melting of the host harzburgites, are locally dissolved at the contact with dunites where disseminated chromites are precipitated. (**3**) Melt differentiation along the cpx-olivine cotectic line produces cpx-rich *type-1* (and the protolith of *type-3*) pyroxenites, partially replacing the host dunites at decreasing melt/rock ratio, in a porous flow regime. (**4**) Further melt differentiation led to the saturation of Si in the melt thus intersecting a peritectic reaction in which opx replaces olivine; this produces *type-2* websteritic pyroxenites at relatively high melt/rock ratios. (**5**) Subordinate opx-rich (*type-4*) websterites are produced as olivine and melt are simultaneously consumed by the peritectic reaction where Si-rich melts interact with dunites. (**6**) Excess of residual melt in *type-2* pyroxenites either is trapped or percolates, leading to the precipitation of late-magmatic interstitial amphibole upon cooling and to metasomatic enrichment via the combination of porosity-reducing reaction and chromatographic reequilibration (percolative fractional crystallization). (**7**) Sideways migration of residual melts (or hydrous fluids liberated from the silicate melt upon cooling) affect all surrounding rocks leading to their amphibolitization and metasomatic enrichment. **B.** A boninitic melt is alternatively envisaged for the petrogenesis of *type-2* pyroxenites. It may represent the segregation of evolved melts as represented on the right-hand side in (A), but this alternative is to be considered both in time and in a three-dimensional space, as boninitic dykes and veins may also represent either a subsequent stage or a zone of higher melt influx. For the sake of simplicity, potential partial melting of the *type-1* pyroxenites and magmatic activity associated with garnet-rich pyroxenite and mafic dykes have been deliberately omitted as they relate to the metamorphic episode associated with the late hydration of the massif (see text for further details). Similarly, the subsequent formation *type-3* pyroxenites from the protoliths of *type-1* pyroxenites is detailed in the text and in **Fig. VI. 10**.

We conclude that the Cabo Ortegal pyroxenites, dunites and chromitites resulted from melt-peridotite interaction initially involving picritic melts, which produced *type-1* pyroxenites (and the protoliths of *type-3* pyroxenites), then evolved towards boninitic compositions, crystallizing *type-2* pyroxenites at greater melt/rock ratios. This scenario, illustrated in **Fig. VI. 13A**, validates *a posteriori* the initial assumption of the cogenetic character of the different types of pyroxenite, although *type-2* pyroxenites may represent distinct boninitic dykes and veins as suggested in **Fig. VI. 13B**. It is also supported by the normative compositions of *type-1* and *-3* pyroxenites, and *type-2* pyroxenites, trending towards ultra-calcic picrites and high-Ca boninites, respectively (**Fig. VI. 9**). In addition, we suggest that the formation of opx-rich (*type-4*) websterites occurred where boninitic melts interacted with dunites. This is consistent with the relatively high NiO in olivine from *type-4* pyroxenites, which reflects the concentration of Ni in smaller amounts of olivine (**Fig. IV. 7**) and the extreme REE patterns measured in their low-modal cpx (**Fig. VI. 10**), as predicted by the chromatographic model.

C. TECTONIC AND GEODYNAMIC SIGNIFICANCE

There are relatively robust constraints on the geodynamic setting associated with the metamorphic complexes of north-western Iberia (*e.g.* Martínez Catalán *et al.*, 2009, Arenas *et al.*, 2014a). However, the origin of some of the high-pressure allochthonous units remains uncertain. In the Cabo Ortegal Complex, the ultramafic massifs are structurally associated with granulites, and the nature of their protoliths is debated, as reviewed in **Chapter II**. Nonetheless, for the purpose of the following discussion, we assume that the Cabo Ortegal granulites represent remnants of a volcanic-arc crust, consistent with the volcano-sedimentary protolith inferred for the associated HP gneisses (Gil Ibarguchi *et al.*, 1990). Accordingly, the dominantly harzburgitic compositions of Cabo Ortegal peridotites and the existence of dunitic bodies containing podiform chromitites are consistent with an arc-related origin, and potentially more specifically indicative of a fore-arc environment (*e.g.* Pagé *et al.*, 2008, Pagé & Barnes, 2009).

1. Formation of Cabo Ortegal pyroxenites

Assuming a sub-arc environment, Cabo Ortegal pyroxenites may represent layered cumulates, along with the associated dunites ± chromitites (*e.g.* Moreno *et al.*, 2001). This has been documented in arc-related ophiolites where ultramafic cumulates may reach several hundred meters in thickness (*e.g.* Bédard & Hébert, 1996, Ceuleneer & Le Sueur, 2008, Clénet *et al.*, 2010). However, we are aware of only very limited evidence of magmatic stratigraphy; variations of modal proportions across layers, as reported in this study (**Fig. IV. 14a**) or by Girardeau and Gil Ibarguchi (1991), are rare in Cabo Ortegal. The increasing content of platinum-group elements (PGE) and Cr# in chromitites exposed in the Herbeira cliffs (Moreno, 1999, Moreno *et al.*, 2001) has been suggested as indicative of magmatic stratigraphy, but it is constrained by the arguable existence of the Trans-Herbeira Fault (THF), as discussed in **Chapter III**. In addition, although the overall lithological stratigraphy of the Herbeira massif could be compared to a cumulate series such as that of the supra-subduction zone Trinity ophiolite (Ceuleneer & Le Sueur, 2008) it is also comparable to the transition from the peridotite to the pyroxenite zones of the Jijal ultramafic section in the Kohistan complex, where the formerly-proposed cumulative origin (Khan *et al.*, 1993) has been strongly questioned. The preservation of dunite "flames, streaks and wisps" in websterites of the peridotite zone is now indeed regarded as resulting from partial replacement of peridotite following melt-rock interaction at decreasing melt/rock ratios, close to the peridotite solidus (Burg *et al.*, 1998, Garrido *et al.*, 2007, Bodinier *et al.*, 2008). These websterites are comparable to *type-1* pyroxenites in Cabo Ortegal while the

final products of reaction at higher melt/rock ratios, represented by olivine-free websterites in the pyroxenite zone, are similar to *type*-2 pyroxenites, as discussed above. This may relate to the transition from channeled porous flows to dykes and veins (*e.g.* Bodinier *et al.*, 2008), suggesting the existence of a thermally-controlled permeability barrier, which in turn may be indicative of regional tectonic processes (Van der Wal & Bodinier, 1996, Burg *et al.*, 1998, Garrido & Bodinier, 1999, Python & Ceuleneer, 2003, Rabinowicz & Ceuleneer, 2005, Bouilhol *et al.*, 2011). Significant modification of melt distribution may also be envisaged if a carbonatite component was involved in the source region, as experiments show that degassing of C-H-O fluids at < 1 GPa should increase melt viscosity (Green *et al.*, 2004). However, the strong deformational overprint resulting in the transposition of lithological contacts hinders further interpretation.

2. Inferences on the source region

The characteristics of the source region of the parental melts of Cabo Ortegal pyroxenites are imposed by the petrogenesis of boninitic or picritic melts and the particular conditions associated with their high CaO/Al_2O_3. Although it also has been reported in various other contexts (Salters & Shimizu, 1988, Benoit *et al.*, 1999, Nonnotte *et al.*, 2005), the relative enrichment of LILE/HFSE observed in Cabo Ortegal pyroxenites is a characteristic fingerprint of subduction-related magmatic rocks (*e.g.* Kelemen *et al.*, 1993, Foley *et al.*, 2000, Münker *et al.*, 2004). We thus assume such an environment for the purpose of this discussion.

a. Constraints imposed by the petrogenesis of boninites/picrites

Experimental studies have suggested that these magmas are generated in equilibrium with refractory sources, representing the residue of earlier melt extraction (Crawford *et al.*, 1989, and references therein). Accordingly, like present-day boninitic and picritic lavas, the parental melts of Cabo Ortegal pyroxenites probably acquired their relatively high concentration of compatible elements such as Ni, Mg and Cr from a depleted mantle source.

The presence of water is required to reach the solidus of a refractory peridotite under realistic conditions of pressure and temperature in the upper mantle. Indeed, anhydrous melting would otherwise only generate boninitic compositions at crustal depths (*i.e.* < 0.5 GPa). Nonetheless, such flux melting is reasonable in a mantle-wedge environment within the metasomatic aureole of a subducting slab and is consistent with the trace-element characteristics of Cabo Ortegal pyroxenites. The consistency between the depletion of HFSE in cpx and amphibole and their depletion in the whole-rock samples indeed indicates that it must be a primary

feature inherited from the composition of the parental melts of the Cabo Ortegal pyroxenites. High LILE/HFSE confirms a metasomatic contribution in the source, in good agreement with the metasomatized harzburgitic source suggested by Gravestock (1992), but in contrast to the primitive-mantle source advocated by Laribi-Halimi (1992)

Assuming a mantle-wedge source, metasomatic contributions may be related to percolation of slab- or mantle-wedge-derived fluids or melts (Meijer, 1980, Hickey & Frey, 1982, Hawkesworth *et al.*, 1993, Tatsumi & Eggins, 1995, Grégoire *et al.*, 2001, Gregoire *et al.*, 2008). Preferential partitioning of LILE into hydrous fluids or melts extracted from the slab is indeed one of the mechanisms invoked to account for relative depletion of HFSE (*e.g.* Tatsumi *et al.*, 1986, Saunders *et al.*, 1991, Tatsumi & Eggins, 1995, Kelemen *et al.*, 2014). In addition, the presence of Ti-rich minerals (Foley *et al.*, 2000, Barth *et al.*, 2002, Klemme *et al.*, 2002) or the existence of an amphibole-rich zone in the mantle wedge (Ionov & Hofmann, 1995), and the stability of chlorite-harzburgite with clinohumite during deserpentinization of the subducting slab (Garrido *et al.*, 2005) have been suggested as ways to retain HFSE where arc magmas are generated and/or transported (Saunders *et al.*, 1980, Green & Pearson, 1987, Ryerson & Watson, 1987). Nonetheless, this remains debated as the residence sites of the HFSE is one of the major issues of mantle geochemistry (*e.g.* Haggerty, 1991, Grégoire *et al.*, 2000a, Kalfoun *et al.*, 2002).

Phase relationships during the melting of peridotite imply that high-SiO_2 (mainly for boninites) and high-MgO melts can be extracted only from a relatively shallow (< 2 GPa) mantle source or that these melts reequilibrated at relatively shallow depths (Kushiro & Yoder, 1966, O'Hara, 1968, Green & Ringwood, 1969, Barsdell, 1988). The refractory character of the source inferred above from the abundance of compatible elements thus requires the existence of high temperatures (1150-1350°C) at these shallow depths (*e.g.* Gaetani *et al.*, 2003, Kelemen *et al.*, 2003, Peacock, 2003). This has been the main physical constraint for different tectonic scenarios, mainly aiming to account for the petrogenesis of boninites. These include the initiation of a subduction zone along major transform faults (Cameron *et al.*, 1979, Meijer, 1980, Hickey & Frey, 1982, Hawkins *et al.*, 1984, Hickey-Vargas & Reagan, 1987), diapirs of MORB-source mantle during the earliest stages of back-arc spreading (Crawford *et al.*, 1981, Hickey & Frey, 1982) or the subduction of an active spreading centre (Crawford *et al.*, 1989).

The genesis of boninites in particular has also been envisaged in other environments, unrelated to subduction (*i.e.* continental rifting and ocean-floor spreading) although it implies idealized sequences of events that are probably not common (Crawford *et al.*, 1989).

b. Additional constraints for the genesis of high CaO/Al_2O_3 melts

The high CaO of Cabo Ortegal pyroxenites certainly relates, at least partly, to the segregation and accumulation of abundant cpx but their high CaO/Al_2O_3 (2.2-11.3) is indicative of similarly high CaO/Al_2O_3 in their parental melts. This carries important implications for the melting conditions and imposes additional constraints on the nature of the source region. There is indeed sufficient evidence showing that anhydrous (single-stage) melting of lherzolite cannot produce such high CaO/Al_2O_3 (Falloon *et al.*, 1988, Kushiro, 1996, Green & Falloon, 1998), which requires second-stage melting of refractory lherzolite where cpx remains a residual phase (Schmidt *et al.*, 2004). Maximum CaO/Al_2O_3 in the second-stage melts is reached when cpx is consumed from the residue (*e.g.* Sorbadere *et al.*, 2013), and ideally when earlier (first-stage) melts were derived from a plagioclase lherzolite (Schmidt *et al.*, 2004). This is consistent with the low cpx/opx source inferred for Cabo Ortegal pyroxenites from the modelling of Ti and Zr depletion during batch melting (Gravestock, 1992)

Partial melting of significant proportions of cpx-rich lithologies (olivine clinopyroxenite or wehrlite) can also produce melts with high modal diopside and nepheline-normative compositions similar to those of ultra-calcic picrites (Barsdell, 1988, Della-Pasqua & Varne, 1997) and of melt inclusions found in olivine phenocrysts from arc magmas (Schiano *et al.*, 2000, Médard *et al.*, 2006, Sorbadere *et al.*, 2011). Such melts can either be extracted from their source or produce secondary metasomatic amphibole-bearing veins which could in turn produce melts with nepheline-normative compositions and high Mg# (Pilet *et al.*, 2008, Pilet *et al.*, 2010, Lambart *et al.*, 2012), particularly under anhydrous conditions where solidus difference between peridotite and pyroxenite becomes significant (Sorbadere *et al.*, 2013). Nonetheless, the existence of such pyroxenitic lithologies in the sub-arc mantle may be regarded as an indirect evidence of delamination and is envisaged in the source of the parental melts of Cabo Ortegal pyroxenites.

Alternatively, high CO_2/H_2O ratios have been experimentally demonstrated to shift the melt compositions towards higher normative diopside and thus higher CaO/Al_2O_3 (Della-Pasqua & Varne, 1997, Green *et al.*, 2004). This could suggest that the source region of the parental melts of Cabo Ortegal pyroxenites experienced carbonatite metasomatism prior or during the partial melting episode as it has been suggested for the genesis of boninitic and picritic melts (Falloon & Crawford, 1991, Green & Falloon, 1998). A similar process was envisaged by Gravestock (1992) to account for the paradox of high Ca content *vs* low cpx/opx of Cabo Ortegal pyroxenites. Because the partition coefficient for Nb is higher than for Ta (Green *et al.*, 1992), percolation of carbonatites in the source region of their parental melts could also

account for the high Nb/Ta of Cabo Ortegal pyroxenites [$(Nb/Ta)_{PM}$ = 0.9-3.1]. However, this could be ascribed to the presence of rutile in the source region controlling the amount of Ta entering the melt fraction (Foley *et al.*, 2000, Rapp *et al.*, 2003, Klemme *et al.*, 2005).

c. Isotopic constraints

Assuming the formation of Cabo Ortegal pyroxenites at ~ 390 Ma, which is debated below, we can discuss the implications of their initial isotopic composition in terms of the nature of their source region.

Initial $^{143}Nd/^{144}Nd$ and $^{87}Sr/^{86}Sr$ are fairly homogeneous, mostly ranging between 0.5119 and 0.5122 (ε_{Nd} between 0 and 7.5) and between 0.7037 and 0.7044, respectively. In Sr-Nd space (**Fig. VI. 14**), some of these compositions are located between the depleted MORB mantle (DMM) and the enriched mantle reservoirs (EM I and EM II), which are commonly interpreted as the signature of the subcontinental lithospheric mantle and subducted sediments, respectively (e.g. Salters & White, 1998). An EM I contribution has been previously documented for Cabo Ortegal pyroxenites (Santos et al., 2002). In addition, their relatively high ε_{Nd} compared with the mixing lines between DMM and EM I/II suggest that Cabo Ortegal pyroxenites have experienced a relatively high time-integrated $^{147}Sm/^{144}Nd$. This indicates that the corresponding mantle domain may be older and/or more LREE-depleted than the DMM, which is consis-

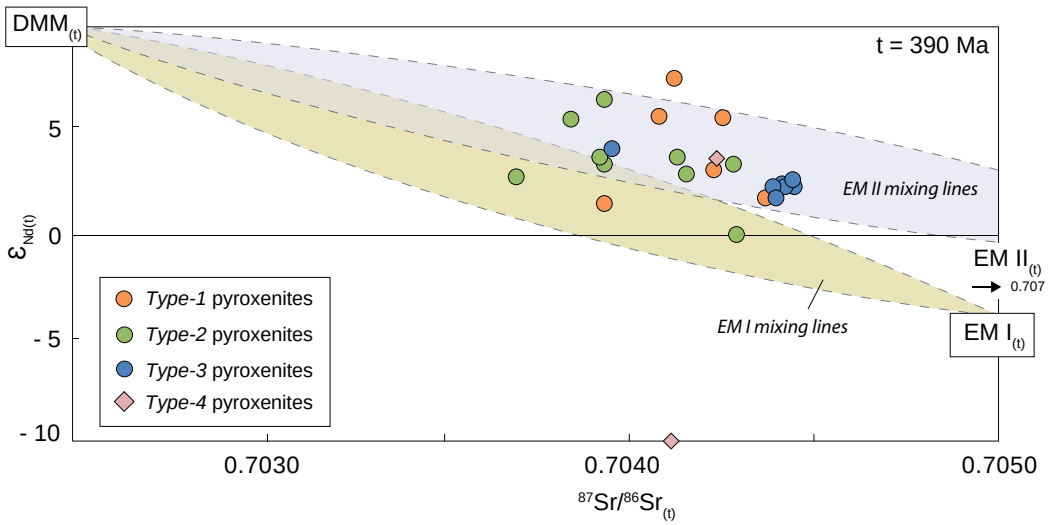

Fig. VI. 14. Initial ε_{Nd} *vs* $^{87}Sr/^{86}Sr$ calculated at 390 Ma for Cabo Ortegal pyroxenites suggesting a potential contribution of either the subcontinental lithospheric mantle (EM I) or subducted sediments (EM II) to the depleted MORB mantle (DMM). Initial compositions of the oceanic reservoirs were calculated at 390 Ma from the compositions of end-member lavas assuming: for EM I, present-day $^{87}Sr/^{86}Sr$ = 0.7052 and ε_{Nd} = -4.5, $^{87}Rb/^{86}Sr$ = 0.037 and $^{147}Sm/^{144}Nd$ = 0.21; for EM II, present-day $^{87}Sr/^{86}Sr$ = 0.7074 and ε_{Nd} = -1.6, $^{87}Rb/^{86}Sr$ = 0.041 and $^{147}Sm/^{144}Nd$ = 0.25 (Hofmann, 2014; and references therein). Mixing lines were calculated with $0.5 < ([Sr]/[Nd])_{EM\,I}/([Sr]/[Nd])_{DMM} < 1.5$ for both EM I and II.

tent with an harzburgitic sub-arc mantle or a sub-continental lithospheric mantle.

Initial $^{176}Hf/^{177}Hf$ ratios are very scattered and reach extremely unradiogenic values (mostly between 0.278 and 0.283; ε_{Hf} between -205 and 18). This may have important implications of particular interest for inferring the characteristics of the source region of the parental melts of Cabo Ortegal pyroxenites. However, they are not straightforward because of the limited reliability of the low initial values, as discussed above. Nonetheless, assuming the qualitative reliability of these data, very unradiogenic initial ε_{Hf} may suggest the implication of a component that had experienced very small time-integrated $^{176}Lu/^{177}Hf$ such as an old and metasomatized mantle domain. This may be consistent with the potential trend towards EM I observed in Sr-Nd space, with the relatively radiogenic initial Nd-isotope compositions and with two-stage model ages calculated from the initial $^{187}Os/^{188}Os$ of the isochrons for sample CO-010 ($\tau_{RD(2)}$ = 1.5-2.5 Ga). Such signature may have been inherited in the source region (e.g. Bizimis et al., 2005) or during the partial replacement of host peridotites as detailed above, and potentially relates to the reworking of a continental margin during the incipient stages of arc magmatism. This is consistent with the shallow depths inferred for the existence of a peritectic reaction during fractional crystallization and with the primitive compositions of the parental melts. In the light of regional geodynamics, we suggest that Cabo Ortegal pyroxenites recorded the building of a volcanic arc on a rifted margin of Gondwana, prior to the opening of the Tethys in Cambro-Ordovician times (e.g. Martínez Catalán et al., 2009)

3. Prograde and retrograde metamorphism

a. Delamination

The occurrence of garnet as relatively undeformed coronas around spinel is indicative of syn- to post-kinematic prograde metamorphism. Previous thermobarometric calculations put the reequilibration of the mineral assemblage at 1.65-1.80 GPa, 800°C (Girardeau & Gil Ibarguchi, 1991) in good agreement with calculations made from the data presented here (1.7 GPa and 780°C). We suggest that this episode is the consequence of the delamination of a pyroxenite-rich domain of sub-arc mantle (arc root), which can be explained by the negative buoyancy of the pyroxenites with respect to surrounding refractory peridotites (Müntener *et al.*, 2001). The Cabo Ortegal Complex may thus represent a unique example of delaminated arc root, a "Herbeira *delaminated* arc root", following on Moreno *et al.* (2001).

b. Syn-subduction exhumation and associated metasomatism

Previous structural studies and kinematic reconstructions have revealed that the ultramaf-

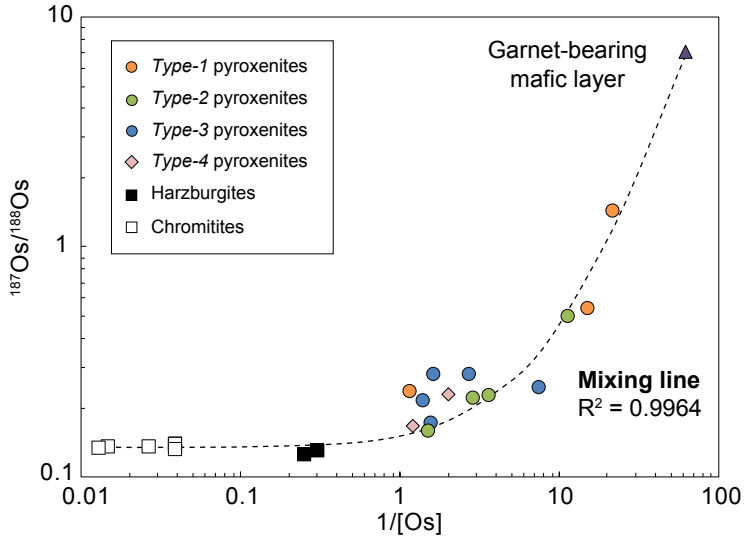

Fig. VI. 15. Measured whole-rock $^{187}Os/^{188}Os$ *vs* 1/Os and potential mixing line between chromitites and harzburgites and the garnet-bearing mafic layer located near the top of the pyroxenite-rich area.

ic massifs of the Cabo Ortegal Complex experienced a HP-HT metamorphic event, and were reorganized and exhumed as a single assemblage together with eclogites, granulites and HP gneisses (Ábalos *et al.*, 2003). The chronology of these tectonothermal events remains controversial and may require exhumation over more than one orogenic cycle (Marcos *et al.*, 2002). However, the combination of subduction-channel processes followed by orogenic deformation remains a reasonable explanation for the retrograde metamorphism (and hydration) of the pyroxenites and of their host peridotites, resulting in amphibolitization and serpentinization. This probably followed the incorporation of the delaminated arc root into a subduction conduit.

Within this scenario, the dominantly interstitial position of base-metal sulfides and their common association with amphibole suggest that addition of S probably accompanied this subduction-related episode and is thus unrelated to the main magmatic/metasomatic episode. Indeed, the abundance of sulfides (up 1 wt %) cannot be accounted for by the low S content of boninitic or picritic melts (*e.g.* Cooper *et al.*, 2010, Ripley & Li, 2013).

Os-isotope systematics supports this late addition of S. Indeed, the increasingly LREE-enriched parts of sample CO-010 have increasingly radiogenic Os. In addition, the wide range of Os-isotope compositions firstly relates to (probably recent) mobility of Re. The correlation between $^{187}Os/^{188}Os$ *vs* 1/Os (**Fig. VI. 15**) implies that this range may arise from the mixing of a non-radiogenic, low-Re/Os component with a highly-radiogenic, high-Re/Os one. Since the

radiogenic end member is represented by the garnet-bearing mafic rocks located near the top of the pyroxenite-rich area, which are dated at ~ 390 Ma (Santos *et al.*, 2002), this mixing event probably relates to the intrusion of the parental melt of these rocks, potentially derived from the continental crust, as suggested by its Os-isotope compositions. In addition, considering that sulfides host most of the budget of platinum-group elements (PGE), and particularly of Re, we can assume that this event also relates to their crystallization, and thus to migration of sulfide melts. From the textural relationships mentioned above, we can infer that amphibolitization and the migration of sulfide melts were coeval and occurred during the subduction-related event at 390 Ma, probably during the early exhumation of the high-pressure units. This requires more investigation and potentially the determination of *in-situ* Os-isotope compositions of sulfides and PGM. However, the preliminary determination of the trace-element content of sulfides yielded very high $^{187}Re/^{188}Os$, preventing the use of LA-MC-ICP-MS for *in-situ* Os-isotope systematics.

4. Implications of the geochronological data

The age of Cabo Ortegal pyroxenites is unclear owing to their complex tectonothermal history. The only (relatively) well-constrained magmatic event has been dated at around 390 Ma (Peucat *et al.*, 1990, Santos Zalduegui *et al.*, 1996, Santos *et al.*, 2002) but it corresponds to the intrusion of the melt from which late garnet pyroxenite dykes crystallized, and probably not the main pyroxenites (*i.e.* those occurring parallel to the tectonic foliation). A cluster of ages around 500 Ma has also been reported but is poorly constrained (Van Calsteren *et al.*, 1979, Santos *et al.*, 2002). Particularly problematic is the fact the some of these external isochrons included not only whole rocks (or cpx and whole rocks) for harzburgites and pyroxenites, but also garnet pyroxenite dykes, which certainly are of different ages (Santos *et al.*, 2002). The significance of these isochrons thus rests only on the fact that they provide ages that are comparable to that of the protoliths of the associated metabasic rocks (Peucat *et al.*, 1990, Ordóñez Casado *et al.*, 2001).

In this study, the consistency between internal Nd isochrons calculated for cpx-amphibole pairs and external isochrons calculated between amphiboles and for cpx, amphibole and whole rocks of the three types of pyroxenite indicates to a certain extent the reliability of the corresponding ages (403-561 Ma). They suggest that Cabo Ortegal pyroxenites formed at around 500 Ma, confirming the previously poorly constrained event dated around that time. This is in good agreement with the external Sr isochron calculated for most *type-1* and -2 pyroxenites

and a harzburgite (491 ± 81 Ma), altough its reliability is uncertain, and with two-stage Nd model ages ranging between 502 and 779 Ma, which overlap within error with an Os isochron calculated for three portions of the increasingly enriched LREE-enriched sample at 801 ± 370 Ma (**Fig. V. 6**) and with a Re-depletion model age (τ_{RD}) at 588 Ma. The relative consistency of these ages also implies that previously reported ages around 390 Ma rather correspond to a metamorphic event. Indeed, if the late magmatic/metasomatic episode responsible for amphibole crystallization and some LREE enrichment had actually occurred around 390 Ma, the addition of an enriched component would be required to account for the apparently old ages, but this is not consistent with the greater sensitivity of low-Nd (*i.e.* high $^{147}Sm/^{144}Nd$) samples to isotopic perturbation (Reisberg & Zindler, 1986).

In addition, Sr isochrons calculated for cpx-amphibole(-whole-rock) aliquots yielded comparatively younger ages (261-326 Ma). The one calculated for a *type-1* pyroxenite is particularly well defined (273 ± 11 Ma), partly owing to the fact that these rocks are essentially a mixture of cpx and amphibole and to the purity of the mineral separates. However, we believe that they might not be geologically meaningful ages because it is very likely that amphibolitization was accompanied by addition of an enriched component, decreasing the slope of the apparent isochrons. This process is illustrated by *type-3* pyroxenites consistently plotting at low $^{87}Rb/^{86}Sr$ and slightly more radiogenic Sr than any other samples with comparable $^{87}Rb/^{86}Sr$. Moreover, the occurence of a magmatic/metasomatic episode around 300-340 Ma is hard to reconcile with the regional tectonic scenario involving the emplacement of the allochthonous units onto the Iberian plate at ~ 360 Ma. This alternative would imply that a significant degree of complexity in the polyphase emplacement of these units has been missed, which is ruled out by the abundance of detailed and consistent studies on that matter, as reviewed above. However, we can envisage that the intrusion of the melt from which garnet pyroxenite dykes crystallized, which clearly postdates that of the parental melt of Cabo Ortegal pyroxenites, as indicated by field relationships, may correspond to the hydration of the pyroxenites during retrograde metamorphism. The late migration of melts (potentially pyroxenite melts) may thus be contemporaneous with this metamorphic episode, and possibly consequent to it.

SUMMARY OF CHAPTER VI

- Only **limited enrichment** of LREE and Li can be directly ascribed to **serpentinization** and is mainly restricted to certain *type-1* pyroxenites. The range **REE patterns** and **enrichment of LILE, U and Th** can instead be explained by **chromatographic** reequilibration during **melt-induced metasomatism.**

- The magmatic *vs* metamorphic **origin of amphibole** is **ambiguous**. Its **post-kinematic** character and **chemical equilibrium** with cpx supports its **secondary origin.** Additional evidence confirms that the **protoliths of *type-1* pyroxenites** were **preferentially deformed** and **hydrated** into ***type-3* pyroxenites**. A **late-magmatic/metasomatism origin** following crystallization of **percolating or trapped residual melts** is nonetheless very likely.

- Mineral and whole-rock chemistry points to **primitive hydrous parental melts** with **high Ca/Al** and **low Al/Si**. **Melt-peridotite interaction** during channeled **porous flows** of **ultra-calcic picrites** produced *type-1* (and the protoliths of *type-3*) pyroxenites. The petrogenesis of *type-2* and *type-4* pyroxenites involves the completion of a **peritectic reaction** and/or **crystal segregation** during the intrusion of high-Ca **boninitic melts** into veins and dykes. These melts may have been **potentially differentiated** from the initially **picritic melts**.

- The genesis of Ca-rich picritic/boninitic melts imposes the existence of **high temperatures** at **low pressures** in a **H_2O-CO_2-fluxed source**, potentially also involving the melting of **delaminated pyroxenites**. The contribution of enriche mantle **EM I and/or EM II component(s)** and the **ancient Hf-isotope signature** may suggest the reworking of a **continental margin** by this primitive arc magmatism and/or the presence of **subducted sediments in the source region**.

- Abundance of **dense pyroxenites** within mantle harzburgites is responsible for the **delamination of an arc root** followed by its **intrusion and exhumation** within a **subduction zone.** This was accompanied by amphibolitization, and potentially by **addition of S and mobilization Re**, as suggested by Os-isotope systematics.

Chapter VII.

General Conclusions

A. PETROGENESIS OF CABO ORTEGAL PYROXENITES

In the Variscan suture of north-western Iberia, the Herbeira massif of the Cabo Ortegal Complex, Spain, presents excellent exposures of unusually abundant pyroxenites occurring interlayered with dunites in a otherwise dominantly harzburgitic domain. The processes responsible for their abundance and geochemical characteristics are not well established, despite the fact that they may represent one of the rare occurrences of sub-arc mantle visible on the Earth's surface. To remedy this, the present thesis has reported new field and petrographic observations complemented by whole-rock and *in-situ* major- and trace-element compositions of pyroxenites, peridotites and chromitites, and Sr-, Nd-, Hf- and Os-isotope systematics.

We have shown that the Cabo Ortegal pyroxenites are distinctive among mantle pyroxenites worldwide for having low Al_2O_3 and TiO_2 and high abundances of compatible elements, reflecting the compositions of their parental melts of picritic to boninitic affinity. Their ubiquitous LILE/HFSE enrichment suggests the generation of primitive hydrous melts by second-stage flux melting of a refractory lherzolite at < 2 GPa, following its percolation by slab-derived fluids and/or carbonatite melts. Particularly high CaO/Al_2O_3 may also relate to the involvement in the source region of olivine- and cpx-rich pyroxenitic lithologies, potentially representing delaminated pyroxenites. These characteristics points towards a mantle wedge source during the building of an island arc, probably on the rifted margin of continental block, with the potential contribution of subducted sediments, as suggested by Hf-isotope systematics and the trend towards EM I /II mantle component(s) in age-corrected Sr-Nd space.

In addition, we have characterized from their field occurrence different subtypes of pyroxenites: olivine clinopyroxenites preserving dunite lenses (*type 1*), massive websterites (*type 2*) and foliated clinopyroxenites (*type 3*), which represent the most deformed and amphibolitized rocks. Subordinate opx-rich websterites (*type 4*) have also been recognised. The consistency between this classification and whole-rock and mineral chemistry has been used to formulate a petrogenetic model that combines magmatic differentiation and melt/peridotite interaction (**Fig. VII. 1**). This model is constrained in terms of regional tectonics by petrographic observations relevant to metamorphism and involves three main stages:

- incipient arc magmatism;
- arc root delamination;
- syn-subduction exhumation.

1. **Incipient arc magmatism (Fig. VII. 1A)**

- A picritic melt intruded and reacted with harzburgites at shallow levels of the sub-arc mantle (< 1.2 GPa). This first produced dunites and chromitites, as evidenced by their high-Cr# spinels. The existence of strongly deformed, thinly layered pyroxenites suggests that this region had previously experienced melt extraction.

- Melt-peridotite interaction occurred at decreasing melt/rock ratio in porous-flows channels partially replacing host dunites. This produced *type-1* (and the protoliths of *type-3*) pyroxenites characterized by primitive compositions (*e.g.* high-Mg#, low Al_2O_3).

- At higher melt/rock ratios, massive (*type-2*) pyroxenites with more evolved compositions were formed following the completion of a peritectic reaction (Fo + Si-rich melt = En) and/or by crystal segregation following the intrusion of boninitic melts into veins and dykes. These Si-rich melts were potentially differentiated from the initially picritic melts, which produced *type-4* pyroxenites with high-Cr# spinels upon interaction with dunites.

- Pyroxenites and host peridotites experienced chromatographic reequilibration with migrating or trapped residual melts. This resulted in a range of spoon-shaped to LREE-enriched patterns and was locally accompanied by late-magmatic crystallization of amphibole.

2. **Arc-root delamination (Fig. VII. 1B)**

- Following this magmatic/metasomatic episode, Cabo Ortegal peridotites and pyroxenites were foliated and isoclinally folded at high temperatures. Sheath folds and, locally, mylonites formed during high-shear strain deformation; the subsequent prograde metamorphism resulted in the development of garnet coronas around spinel. This transition is interpreted as reflecting delamination of the arc root into the mantle wedge and its incorporation into a subduction conduit, driven by gravitational instabilities arising from the existence of dense pyroxenitic lithologies in mantle harzburgites.

3. **Syn-subduction exhumation (Fig. VII. 1C)**

- Amphibolitization of the pyroxenites and serpentinization of their host peridotites occurred as a result of hydration during retrograde metamorphism. Foliated *type-3* pyroxenites were preferentially formed at this stage from the protoliths of *type-1* pyroxenite. This episode was accompanied by addition of S and mobilization of Re, as suggested by Os-isotope systematics and the association of amphibole and abundant base-metal sulfides.

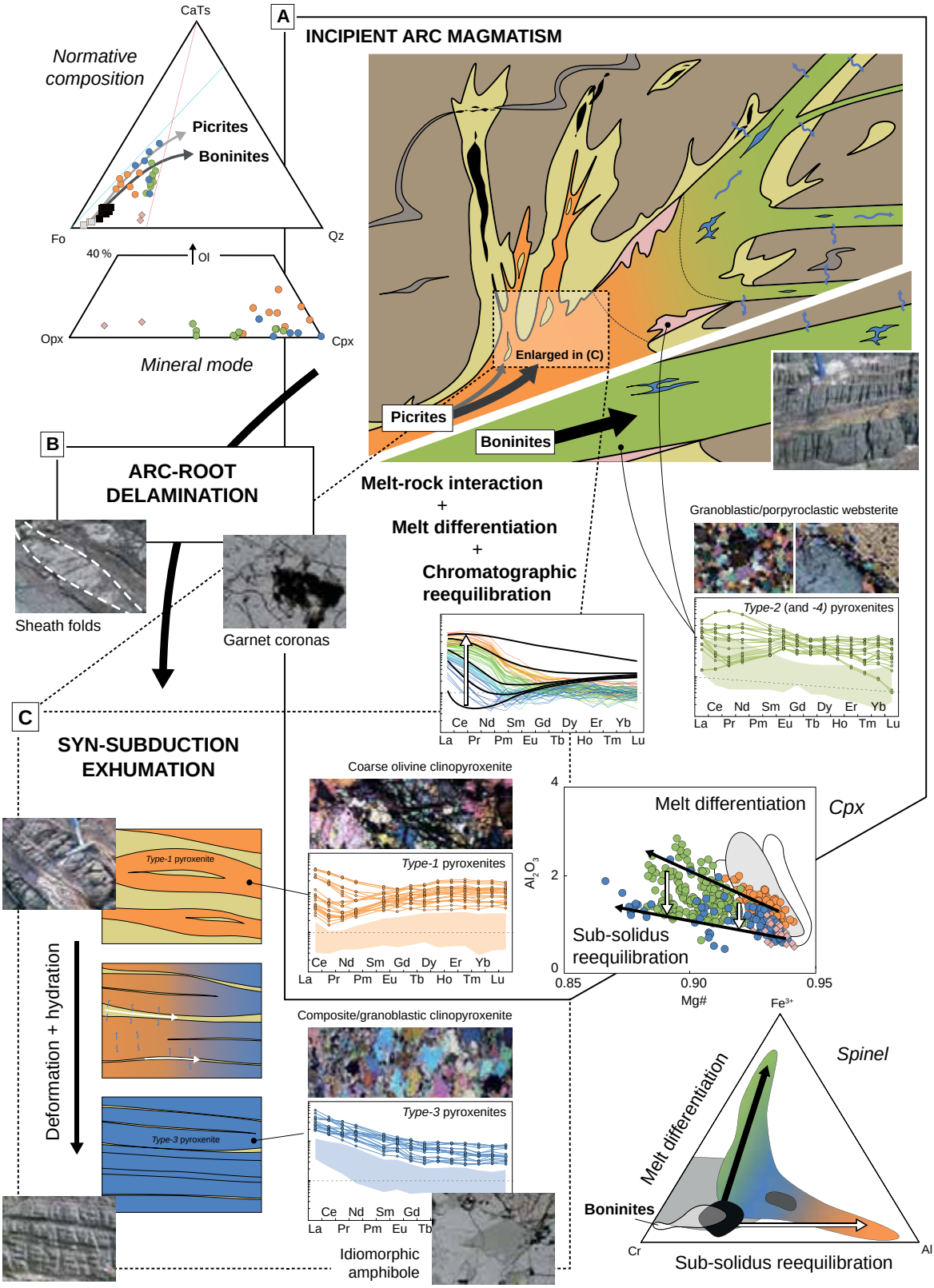

Fig. VII. 1. Summary of the main petrographic and geochemical features associated with **A.** the magmatic/metasomatic episode occurred in an incipient arc root, **B.** deformation and prograde metamorphism during delamination of the arc root and its incorporation into a subduction zone and **C.** retrograde metamorphism and hydration related to syn-subduction exhumation.

B. IMPLICATIONS OF THIS WORK

From the scenario above, we have suggested that the Cabo Ortegal Complex preserves a unique exposure of delaminated arc root: the "**Herbeira *delaminated* arc root**".

Potential implications of this notably relate to the existence of abundant pyroxenites in the upper mantle and to their ability to generate a variety of melt compositions (*e.g.* Yaxley & Green, 1998, Hirschmann *et al.*, 2003, Lambart *et al.*, 2012) whose signature is recognised in most mantle-derived magmas (*e.g.* Hofman, 2003, Sovolev *et al.*, 2005, Herzberg, 2011). Of relevance is also the report of the first Hf-isotope compositions of Cabo Ortegal pyroxenites.

The availability at Earth's surface of exhumed arc cumulates that have experienced delamination provides a natural laboratory for studying this process, which is one of the density-sorting processes invoked to account for the refinement of the continental crust from island and continental arcs (*e.g.* Kelemen *et al.*, 2014, Ducea *et al.*, 2015). This is of a great interest as the existence of a chemically differentiated continental crust, distinct from the oceanic crust, is a unique, but poorly understood, feature of Earth compared to the other terrestrial planets of the Solar System (*e.g.* Rudnick, 1995, Jagoutz & Kelemen, 2015). In this regard, this work contributes to constraining the role of pyroxenite formation during the differentiation of primitive arc magmas at depth. It also documents the well-known transfer of elements from subducted plates to the mantle wedge, whose quantitative contribution to arc magmatism is still debated (*e.g.* Kay, 1980, Kay & Kay, 1985, Plank & Langmuir, 1988, 1993, Hawkesworth *et al.*, 1997).

In addition, we suggest that the Herbeira massif has a great potential for investigations of the role of melt-peridotite interaction in forming podiform chromitites. Despite their economic potential arising from their common association with mineralization of PGE, their petrogenesis is still highly controversial. Proposed models indeed invoke fractional crystallization, melt mixing/hibridization and the contribution of volatile-rich fluids (*e.g.* Page & Barnes, 2009, Gonzalez-Jimenez *et al.*, 2014). We report here the first Os-isotope characterization of Cabo Ortegal pyroxenites and chromitites, thus contributing to the growth of a still limited database.

Finally, this study is another step toward the understanding of a geodynamically complex region of the Variscan belt of Europe, by providing new geochronological data and petrogenetic constraints to the current tectonic scenarios (*e.g.* Martinez Catalan *et al.*, 2009). In particular, it reports preliminary but promising evidence for peri-Gondwanan arc magmatism from the perspective of the mantle domains of the Cabo Ortegal Complex.

REFERENCES

Ábalos, B. (1997). Omphacite fabric variation in the Cabo Ortegal eclogite (NW Spain): relationships with strain symmetry during high-pressure deformation. *Journal of Structural Geology* **19**, 621-637.

Ábalos, B., Azcarraga, J., Gil Ibarguchi, J. I., Mendia, M. S., Santos Zalduegui, J. S. (1996). Flow Stress, strain rate and effective viscosity evaluation in a high-presssure metamorphic nappe (Cabo Ortegal, Spain). *Journal of Metamorphic Geology* **14**, 227-248.

Ábalos, B., Puelles, P., Gil Ibarguchi, J. I. (2003). Structural assemblage of high-pressure mantle and crustal rocks in a subduction channel (Cabo Ortegal, NW Spain). *Tectonics* **22**, 1006-1027.

Abati, J., Dunning, G. R., Arenas, R., Díaz García, F., González Cuadra, P., Martínez Catalán, J. R., Andonaegui, P. (1999). Early Ordovician orogenic event in Galicia (NW Spain): evidence from U–Pb ages in the uppermost unit of the Ordenes Complex. *Earth and Planetary Science Letters* **165**, 213-228.

Abily, B., Ceuleneer, G., Launeau, P. (2011). Synmagmatic normal faulting in the lower oceanic crust: Evidence from the Oman ophiolite. *Geology* **39**, 391-394.

Ackerman, L., Jelínek, E., Medaris Jr, G., Ježek, J., Siebel, W., Strnad, L. (2009). Geochemistry of Fe-rich peridotites and associated pyroxenites from Horní Bory, Bohemian Massif: Insights into subduction-related melt–rock reactions. *Chemical Geology* **259**, 152-167.

Albert, R., Arenas, R., Gerdes, A., Sánchez Martínez, S., Fernández-Suárez, J., Fuenlabrada, J. (2015). Provenance of the Variscan Upper Allochthon (Cabo Ortegal Complex, NW Iberian Massif). *Gondwana Research* **28**, 1434-1448.

Albert, R., Arenas, R., Sánchez Martínez, S., Gerdes, A. (2012). The eclogite facies gneisses of the Cabo Ortegal Complex (NW Iberian Massif): Tectonothermal evolution and exhumation model. *Journal of Iberian Geology* **38**, 389-406.

Allègre, C. J. & Turcotte, D. L. (1986). Implications of a two-component marble-cake mantle. *Nature* **323**, 123-127.

Anonymous. (1972). Penrose field conference on Ophiolites. *Geotimes* **17**, 24-25.

Arai, S. (2013). Conversion of low-pressure chromitites to ultrahigh-pressure chromitites by deep recycling: A good inference. *Earth and Planetary Science Letters* **379**, 81-87.

Arenas, R. (1985). Evolución petrológica y geoquímica de la unidad alóctona inferior del complejo metamórfico básico-ultrabásico de Cabo Ortegal (Unidad de Moeche) y del Silúrico paraautóctono, Cadena Hercínica Ibérica (NW de España). PhD thesis, Universidad Complutense de Madrid, 543.

Arenas, R., Abati, J., Martínez Catalán, J. R., Díaz García, F., Rubio Pascual, F. J. (1997). P-T evolution of eclogites from the Agualada Unit (Ordenes Complex, north-

west Iberian Massif, Spain): Implications for crustal subduction. *Lithos* **40**, 221-242.

Arenas, R., Díez Fernández, R., Sánchez Martínez, S., Gerdes, A., Fernández-Suárez, J., Albert, R. (2014a). Two-stage collision: Exploring the birth of Pangea in the Variscan terranes. *Gondwana Research* **25**, 756-763.

Arenas, R., Gil Ibarguchi, J. I., González Lodeiro, F., Klein, E. M., Martínez Catalán, J. R., Ortega Gironés, E., de Pablo Maciá, J. G., Peinado, M. (1986). Tectonostratigraphic units in the complexes with mafic and related rocks of the NW of the Iberian Massif. *Hercynica* **2**, 87-110.

Arenas, R., Martínez Catalán, J. R., Sánchez Martínez, S., Díaz García, F., Abati, J., Fernández-Suárez, J., Andonaegui, P., Gómez-Barreiro, J. (2007a). Paleozoic ophiolites in the Variscan suture of Galicia (northwest Spain): Distribution, characteristics, and meaning. *Geological Society of America Memoirs* **200**, 425-444.

Arenas, R., Martínez Catalán, J. R., Sánchez Martínez, S., Fernández Suárez, J., Andonaegui, P., Pearce, J. A., Corfu, F. (2007b). The Vila de Cruces Ophiolite: A Remnant of the Early Rheic Ocean in the Variscan Suture of Galicia (Northwest Iberian Massif). *The Journal of geology* **115**, 129-148.

Arenas, R., Rubio Pascual, F. J., Díaz García, F., Martínez Catalán, J. R. (1995). High-pressure micro-inclusions and development of an inverted metamorphic gradient in the Santiago Schists (Ordenes Complex, NW Iberian Massif, Spain): evidence of subduction and syncollisional decompression. *Journal of Metamorphic Geology* **13**, 141-164.

Arenas, R., Sánchez Martínez, S., Castiñeiras, P., Jeffries, T. E., Díez Fernández, R., Andonaegui, P. (2009). The basal tectonic mélange of the Cabo Ortegal Complex (NW Iberian Massif): a key unit in the suture of Pangea. *Journal of Iberian Geology* **35**, 85-125.

Arenas, R., Sánchez Martínez, S., Gerdes, A., Albert, R., Díez Fernández, R., Andonaegui, P. (2014b). Re-interpreting the Devonian ophiolites involved in the Variscan suture: U–Pb and Lu–Hf zircon data of the Moeche Ophiolite (Cabo Ortegal Complex, NW Iberia). *International Journal of Earth Sciences* **103**, 1385-1402.

Arenas, R. S. M., Sonia. (2015). Variscan ophiolites in NW Iberia: Tracking lost Paleozoic oceans and the assembly of Pangea. *Episodes* **38**, 315-333.

Azcárraga, J., Ábalos, B., Gil Ibarguchi, J. I. (2002). On the relationship between kilometer-scale sheath folds, ductile thrusts and minor structures in the basal high-pressure units of the Cabo Ortegal complex (NW Spain). *Journal of Structural Geology* **24**, 1971-1989.

Bai, W.-J., Zhou, M.-F., Robinson, P. T. (1993). Possibly diamond-bearing mantle peridotites and podiform chromitites in the Luobusa and Donqiao ophiolites, Tibet. *Canadian Journal of Earth Sciences* **30**, 1650-1659.

Baker, M. B. & Beckett, J. R. (1999). The origin of abyssal peridotites: a reinterpretation of constraints based on primary bulk compositions. *Earth and Planetary Science*

Letters **171**, 49-61.

Bannister, V., Roeder, P., Poustovetov, A. (1998). Chromite in the Paricutin lava flows (1943–1952). *Journal of Volcanology and Geothermal Research* **87**, 151-171.

Bard, J. P. (1983). Metamorphism of an obducted island arc: Example of the Kohistan sequence (Pakistan) in the Himalayan collided range. *Earth and Planetary Science Letters* **65**, 133-144.

Barnes, S. J. (2000). Chromite in Komatiites, II. Modification during Greenschist to Mid-Amphibolite Facies Metamorphism. *Journal of Petrology* **41**, 387-409.

Barnes, S. J. & Roeder, P. L. (2001). The Range of Spinel Compositions in Terrestrial Mafic and Ultramafic Rocks. *Journal of Petrology* **42**, 2279-2302.

Barrat, J. A., Zanda, B., Moynier, F., Bollinger, C., Liorzou, C., Bayon, G. (2012). Geochemistry of CI chondrites: Major and trace elements, and Cu and Zn Isotopes. *Geochimica et cosmochimica Acta* **83**, 79-92.

Barsdell, M. (1988). Petrology and Petrogenesis of Clinopyroxene-Rich Tholeiitic Lavas, Merelava Volcano, Vanuatu. *Journal of Petrology* **29**, 927-964.

Barsdell, M. & Berry, R. F. (1990). Origin and Evolution of Primitive Island Arc Ankaramites from Western Epi, Vanuatu. *Journal of Petrology* **31**, 747-777.

Barth, M. G., Foley, S. F., Horn, I. (2002). Partial melting in Archean subduction zones: constraints from experimentally determined trace element partition coefficients between eclogitic minerals and tonalitic melts under upper mantle conditions. *Precambrian Research* **113**, 323-340.

Bastida, F., Marcos, A., Marquínez, J., Martínez Catalán, J. R., Pérez-Estaún, A., Pulgar, J. A. (1984). Mapa Geológico de España E. 1: 200.000, Hoja n. º 1 (2-1)(La Coruña) y memoria explicativa, 155 p. Inst. Geol. Min. España.

Batanova, V. G., Suhr, G., Sobolev, A. V. (1998). Origin of Geochemical Heterogeneity in the Mantle Peridotites from the Bay of Islands Ophiolite, Newfoundland, Canada: Ion Probe Study of Clinopyroxenes. *Geochimica et cosmochimica Acta* **62**, 853-866.

Beaumont, C., Ellis, S., Pfiffner, A. (1999). Dynamics of sediment subduction-accretion at convergent margins: Short-term modes, long-term deformation, and tectonic implications. *Journal of Geophysical Research: Solid Earth* **104**, 17573-17601.

Beaumont, C., Jamieson, R. A., Butler, J. P., Warren, C. J. (2009). Crustal structure: A key constraint on the mechanism of ultra-high-pressure rock exhumation. *Earth and Planetary Science Letters* **287**, 116-129.

Bédard, J. H. (1999). Petrogenesis of Boninites from the Betts Cove Ophiolite, Newfoundland, Canada: Identification of Subducted Source Components. *Journal of Petrology* **40**, 1853-1889.

Bédard, J. H. (2006). A catalytic delamination-driven model for coupled genesis

of Archaean crust and sub-continental lithospheric mantle. *Geochimica et cosmochimica Acta* **70**, 1188-1214.

Bédard, J. H. & Hébert, R. (1996). The lower crust of the Bay of Islands ophiolite, Canada: petrology, mineralogy, and the importance of syntexis in magmatic differentiation in ophiolites and at ocean ridges. *Journal of Geophysical Research: Solid Earth* **101**, 25105-25124.

Ben Jamaa, N. (1988). Les péridotites de Bay of Islands (Terre Neuve) et de Cap Ortegal (Espagne): approche pétro-structurale. PhD thesis, Université Paris 7, 245.

Bénard, A. & Ionov, D. A. (2013). Melt– and Fluid–Rock Interaction in Supra-Subduction Lithospheric Mantle: Evidence from Andesite-hosted Veined Peridotite Xenoliths. *Journal of Petrology* **54**, 2339-2378.

Benoit, M., Ceuleneer, G., Polvé, M. (1999). The remelting of hydrothermally altered peridotite at mid-ocean ridges by intruding mantle diapirs. *Nature* **402**, 514-518.

Bernard-Griffiths, J., Peucat, J.-J., Cornichet, J., Ponce de Léon, M. I., Gil Ibarguchi, J. I. (1985). U-Pb, Nd Isotope and REE geochemistry in eclogites from the Cabo Ortegal Complex, Galicia, Spain: An example of REE immobility conserving MORB-like patterns during high-grade metamorphism. *Chemical Geology: Isotope Geoscience section* **52**, 217-225.

Beyer, E. E., Brueckner, H. K., Griffin, W. L., O'Reilly, S. Y., Graham, S. (2004). Archean mantle fragments in Proterozoic crust, Western Gneiss Region, Norway. *Geology* **32**, 609-612.

Beyer, E. E., Griffin, W. L., O'Reilly, S. Y. (2006). Transformation of Archaean Lithospheric Mantle by Refertilization: Evidence from Exposed Peridotites in the Western Gneiss Region, Norway. *Journal of Petrology* **47**, 1611-1636.

Bizimis, M., Griselin, M., Lassiter, J. C., Salters, V. J. M., Sen, G. (2007). Ancient recycled mantle lithosphere in the Hawaiian plume: Osmium–Hafnium isotopic evidence from peridotite mantle xenoliths. *Earth and Planetary Science Letters* **257**, 259-273.

Bizimis, M., Sen, G., Salters, V. J., Keshav, S. (2005). Hf-Nd-Sr isotope systematics of garnet pyroxenites from Salt Lake Crater, Oahu, Hawaii: Evidence for a depleted component in Hawaiian volcanism. *Geochimica et cosmochimica Acta* **69**, 2629-2646.

Blichert-Toft, J. & Albarède, F. (1997). The Lu-Hf isotope geochemistry of chondrites and the evolution of the mantle-crust system. *Earth and Planetary Science Letters* **148**, 243-258.

Blichert-Toft, J., Chauvel, C., Albarède, F. (1997). Separation of Hf and Lu for high-precision isotope analysis of rock samples by magnetic sector-multiple collector ICP-MS. *Contributions to Mineralogy and Petrology* **127**, 248-260.

Bodinier, J.-L., Dupuy, C., Dostal, J. (1988). Geochemistry and petrogenesis of Eastern Pyrenean peridotites. *Geochimica et cosmochimica Acta* **52**, 2893-2907.

Bodinier, J.-L., Garrido, C. J., Chanefo, I., Bruguier, O., Gervilla, F. (2008). Origin of pyroxenite–peridotite veined mantle by refertilization reactions: evidence from the Ronda peridotite (Southern Spain). *Journal of Petrology* **49**, 999-1025.

Bodinier, J.-L. & Godard, M. (2014). Orogenic, Ophiolitic, and Abyssal Peridotites. In: Turekian, K. K. (ed.) *Treatise on Geochemistry* **3** (Second Edition). Oxford: Elsevier, 103-167.

Bodinier, J.-L., Guiraud, M., Fabriés, J., Dostal, J., Dupuy, C. (1987). Petrogenesis of layered pyroxenites from the Lherz, Freychinéde and Prades ultramafic bodies (Ariége, French Pyrénées). *Geochimica et cosmochimica Acta* **51**, 279-290.

Bodinier, J.-L., Menzies, M. A., Thirlwall, M. F. (1991). Continental to Oceanic Mantle Transition—REE and Sr-Nd Isotopic Geochemistry of the Lanzo Lherzolite Massif. *Journal of Petrology* **Special Lherzolites Issue**, 191-210.

Bodinier, J.-L., Merlet, C., Bedini, R. M., Simien, F., Remaidi, M., Garrido, C. J. (1996). Distribution of niobium, tantalum, and other highly incompatible trace elements in the lithospheric mantle: The spinel paradox. *Geochimica et cosmochimica Acta* **60**, 545-550.

Bodinier, J.-L., Vasseur, G., Vernieres, J., Dupuy, C., Fabries, J. (1990). Mechanisms of Mantle Metasomatism: Geochemical Evidence from the Lherz Orogenic Peridotite. *Journal of Petrology* **31**, 597-628.

Bonatti, E. & Michael, P. J. (1989). Mantle peridotites from continental rifts to ocean basins to subduction zones. *Earth and Planetary Science Letters* **91**, 297-311.

Bonatti, E., Ottonello, G., Hamlyn, P. R. (1986). Peridotites from the Island of Zabargad (St. John), Red Sea: Petrology and geochemistry. *Journal of Geophysical Research: Solid Earth* **91**, 599-631.

Borghini, G., Rampone, E., Zanetti, A., Class, C., Cipriani, A., Hofmann, A. W., Goldstein, S. L. (2013). Meter-scale Nd isotopic heterogeneity in pyroxenite-bearing Ligurian peridotites encompasses global-scale upper mantle variability. *Geology* **41**, 1055-1058.

Borghini, G., Rampone, E., Zanetti, A., Class, C., Cipriani, A., Hofmann, A. W., Goldstein, S. L. (2016). Pyroxenite Layers in the Northern Apennines' Upper Mantle (Italy)—Generation by Pyroxenite Melting and Melt Infiltration. *Journal of Petrology,* **57**, 625-653.

Boudier, F. & Nicolas, A. (1985). Harzburgite and lherzolite subtypes in ophiolitic and oceanic environments. *Earth and Planetary Science Letters* **76**, 84-92.

Bouilhol, P., Connolly, J. A. D., Burg, J.-P. (2011). Geological evidence and modeling of melt migration by porosity waves in the sub-arc mantle of Kohistan (Pakistan). *Geology* **39**, 1091-1094.

Bouvier, A., Vervoort, J. D., Patchett, P. J. (2008). The Lu–Hf and Sm–Nd isotopic composition of CHUR: Constraints from unequilibrated chondrites and implications

for the bulk composition of terrestrial planets. *Earth and Planetary Science Letters* **273**, 48-57.

Boyd, O. S., Jones, C. H., Sheehan, A. F. (2004). Foundering Lithosphere Imaged Beneath the Southern Sierra Nevada, California, USA. *Science* **305**, 660-662.

Brey, G. P. & Köhler, T. (1990). Geothermobarometry in Four-phase Lherzolites II. New Thermobarometers, and Practical Assessment of Existing Thermobarometers. *Journal of Petrology* **31**, 1353-1378.

Brey, G. P., Köhler, T., Nickel, K. G. (1990). Geothermobarometry in Four-phase Lherzolites I. Experimental Results from 10 to 60 kb. *Journal of Petrology* **31**, 1313-1352.

Brongniart, A. (1821). Sur le gisement, ou position relative des ophiolites, euphotides, jaspes, etc., dans quelques parties des Apennins: De l'Imprimerie de Madame Huzard (née Vallat la Chapelle), rue de l'Éperon-Saint-André-des Arts, no. 7.

Brooker, R. A., James, R. H., Blundy, J. D. (2004). Trace elements and Li isotope systematics in Zabargad peridotites: evidence of ancient subduction processes in the Red Sea mantle. *Chemical Geology* **212**, 179-204.

Brueckner, H. & Medaris, L. (1998). A tale of two orogens: the contrasting T–P–t history and geochemical evolution of mantle in high-and ultrahigh-pressure metamorphic terranes of the Norwegian Caledonides and the Czech Variscides. *Schweizerische Mineralogische und Petrographische Mitteilungen* **78**, 293-307.

Brueckner, H. K., Elhaddad, M. A., Hamelin, B., Hemming, S., Kröner, A., Reisberg, L., Seyler, M. (1995). A Pan African origin and uplift for the gneisses and peridotites of Zabargad Island, Red Sea: A Nd, Sr, Pb, and Os isotope study. *Journal of Geophysical Research: Solid Earth* **100**, 22283-22297.

Brueckner, H. K. & Medaris, L. G. (2000). A general model for the intrusion and evolution of 'mantle' garnet peridotites in high-pressure and ultra-high-pressure metamorphic terranes. *Journal of Metamorphic Geology* **18**, 123-133.

Burg, J., Bodinier, J.-L., Chaudhry, S., Hussain, S., Dawood, H. (1998). Infra-arc mantle-crust transition and intra-arc mantle diapirs in the Kohistan Complex (Pakistani Himalaya): petro-structural evidence. *Terra Nova* **10**, 74-80.

Byerly, B. L. & Lassiter, J. C. (2014). Isotopically ultradepleted domains in the convecting upper mantle: Implications for MORB petrogenesis. *Geology* **42**, 203-206.

Cameron, W. E. (1985). Petrology and origin of primitive lavas from the Troodos ophiolite, Cyprus. *Contributions to Mineralogy and Petrology* **89**, 239-255.

Cameron, W. E., Nisbet, E. G., Dietrich, V. J. (1979). Boninites, komatiites and ophiolitic basalts. *Nature* **280**, 550-553.

Cann, J. R. (2003). The Troodos Ophiolite and the upper ocean crust; a reciprocal traffic in scientific concepts. *Geological Society of America Special Papers* **373**, 309-321.

Castiñeiras, P. (2005). Origen y evolución tectonotermal de las unidades de O Pino y Cariño (Complejos alóctonos de Galicia): Laboratorio Xeolóxico de Laxe. *Serie Nova Terra* **28**.

Ceuleneer, G. & Le Sueur, E. (2008). The Trinity ophiolite (California): the strange association of fertile mantle peridotite with ultra-depleted crustal cumulates. *Bulletin de la Societe Geologique de France* **179**, 503-518.

Chazot, G., Menzies, M. A., Harte, B. (1996). Determination of partition coefficients between apatite, clinopyroxene, amphibole, and melt in natural spinel lherzolites from Yemen: Implications for wet melting of the lithospheric mantle. *Geochimica et cosmochimica Acta* **60**, 423-437.

Chemenda, A. I., Mattauer, M., Malavieille, J., Bokun, A. N. (1995). A mechanism for syn-collisional rock exhumation and associated normal faulting: Results from physical modelling. *Earth and Planetary Science Letters* **132**, 225-232.

Christensen, N. I. & Mooney, W. D. (1995). Seismic velocity structure and composition of the continental crust: A global view. *Journal of Geophysical Research: Solid Earth* **100**, 9761-9788.

Cipriani, A., Brueckner, H. K., Bonatti, E., Brunelli, D. (2004). Oceanic crust generated by elusive parents: Sr and Nd isotopes in basalt-peridotite pairs from the Mid-Atlantic Ridge. *Geology* **32**, 657-660.

Class, C., Miller, D. M., Goldstein, S. L., Langmuir, C. H. (2000). Distinguishing melt and fluid subduction components in Umnak Volcanics, Aleutian Arc. *Geochemistry, Geophysics, Geosystems* **1**, doi: 10.1029/1999GC000010.

Clénet, H., Ceuleneer, G., Pinet, P., Abily, B., Daydou, Y., Harris, E., Amri, I., Dantas, C. (2010). Thick sections of layered ultramafic cumulates in the Oman ophiolite revealed by an airborne hyperspectral survey: Petrogenesis and relationship to mantle diapirism. *Lithos* **114**, 265-281.

Cohen, A. S. & Waters, F. G. (1996). Separation of osmium from geological materials by solvent extraction for analysis by thermal ionisation mass spectrometry. *Analytica Chimica Acta* **332**, 269-275.

Coish, R. A. (1989). Boninitic lavas in Appalachian ophiolites: a review. Boninites and Related Rocks. Unwin Hyman, London, 264-287.

Coleman, R. G. (1977). *What is an Ophiolite?*: Springer-Verlage.

Coleman, R. G. (1986). Ophiolites and accretion of the North American Cordillera. *Bulletin de la Societe Geologique de France* **8**, 961-968.

Coltorti, M., Downes, H., Grégoire, M., O'Reilly, S. Y. (2010). Petrological evolution of the European lithospheric mantle: introduction. *Geological Society, London, Special Publications* **337**, 1-5.

Condie, K. C., Cox, J., O'Reilly, S. Y., Griffin, W. L., Kerrich, R. (2004). Distribution

of high field strength and rare earth elements in mantle and lower crustal xenoliths from the Southwestern United States: The role of grain-boundary phases. *Geochimica et cosmochimica Acta* **68**, 3919-3942.

Condie, K. C. & Kröner, A. (2013). The building blocks of continental crust: Evidence for a major change in the tectonic setting of continental growth at the end of the Archean. *Gondwana Research* **23**, 394-402.

Conquéré, F. (1977). Pétrologie des pyroxénites litées dans les complexes ultramafiques de l'Ariège (France) et autres gisements de lherzolites à spinelle. *Bull. Soc. Fr. Minér. Cristall.* **100**, 42-80.

Cooper, L. B., Plank, T., Arculus, R. J., Hauri, E. H., Hall, P. S., Parman, S. W. (2010). High-Ca boninites from the active Tonga Arc. *Journal of Geophysical Research: Solid Earth* **115**, B10206.

Crawford, A. J., Beccaluva, L., Serri, G. (1981). Tectono-magmatic evolution of the West Philippine-Mariana region and the origin of boninites. *Earth and Planetary Science Letters* **54**, 346-356.

Crawford, A. J. & Cameron, W. E. (1985). Petrology and geochemistry of Cambrian boninites and low-Ti andesites from Heathcote, Victoria. *Contributions to Mineralogy and Petrology* **91**, 93-104.

Crawford, A. J., Falloon, T. J., Green, D. H. (1989). Classification, petrogenesis and tectonic setting of boninites. In: Crawford, A. J. (ed.) *Boninites and related rocks*. London: Springer, 1-49.

Currie, C. A., Ducea, M. N., DeCelles, P. G., Beaumont, C. (2015). Geodynamic models of Cordilleran orogens: Gravitational instability of magmatic arc roots. *Geological Society of America Memoirs* **212**, 1-22.

Dallmeyer, R. D., Martínez Catalán, J. R., Arenas, R., Gil Ibarguchi, J. I., Farias, P., Bastida, F., Aller, J. (1997). Diachronous Variscan tectonothermal activity in the NW Iberian Massif: Evidence from 40Ar/39Ar dating of regional fabrics. *Tectonophysics* **277**, 307-337.

Davidson, J. P. & Arculus, R. (2006). *The significance of Phanerozoic arc magmatism in generating continental crust*: Cambridge University Press.

Day, J. M. D., Waters, C. L., Schaefer, B. F., Walker, R. J., Turner, S. (2016). Use of Hydrofluoric Acid Desilicification in the Determination of Highly Siderophile Element Abundances and Re-Pt-Os Isotope Systematics in Mafic-Ultramafic Rocks. *Geostandards and Geoanalytical Research* **40**, 49-65.

de Roever, W. P. (1957). Sind die alpinotypen Peridotitmassen vielleicht tektonisch verfrachtete Bruchstücke der Peridotitschale? *Geologische Rundschau* **46**, 137-146.

DeBari, S., Kay, S. M., Kay, R. W. (1987). Ultramafic Xenoliths from Adagdak Volcano, Adak, Aleutian Islands, Alaska: Deformed Igneous Cumulates from the Moho of

an Island Arc. *The Journal of geology* **95**, 329-341.

DeBari, S. M. & Coleman, R. G. (1989). Examination of the deep levels of an island arc: Evidence from the Tonsina Ultramafic-Mafic Assemblage, Tonsina, Alaska. *Journal of Geophysical Research: Solid Earth* **94**, 4373-4391.

DeBari, S. M. & Greene, A. R. (2011). Vertical stratification of composition, density, and inferred magmatic processes in exposed arc crustal sections. *Arc-Continent Collision*: Springer, 121-144.

DeBari, S. M. & Sleep, N. H. (1991). High-Mg, low-Al bulk composition of the Talkeetna island arc, Alaska: Implications for primary magmas and the nature of arc crust. *Geological Society of America Bulletin* **103**, 37-47.

Deer, W. A., Howie, R. A., Zussman, J. (2013). An introduction to rock-forming minerals. *Mineralogical Society*, **444**.

Della-Pasqua, F. N. & Varne, R. (1997). Primitive ankaramitic magmas in volcanic arcs: a melt-inclusion approach. *Oceanographic Literature Review* **12**, 1473.

Dhuime, B., Bosch, D., Bodinier, J. L., Garrido, C. J., Bruguier, O., Hussain, S. S., Dawood, H. (2007). Multistage evolution of the Jijal ultramafic–mafic complex (Kohistan, N Pakistan): Implications for building the roots of island arcs. *Earth and Planetary Science Letters* **261**, 179-200.

Díaz García, F., Arenas, R., Martínez Catalán, J. R., del Tánago, J. G., Dunning, G. R. (1999). Tectonic evolution of the Careón ophiolite (Northwest Spain): a remnant of oceanic lithosphere in the Variscan belt. *The Journal of geology* **107**, 587-605.

Dick, H. J. B., Natland, J. H., Ildefonse, B. (2006). Past and future impact of deep drilling in the oceanic crust and mantle. *Oceanography* **19**, 72-80.

Dickey, J. S. (1969). Partial fusion products in alpine-type peridotites: Serrania de la Ronda and other examples. PhD thesis, Princeton University.

Díez Fernández, R., Foster, D., Gómez Barreiro, J., Alonso-García, M. (2013). Rheological control on the tectonic evolution of a continental suture zone: the Variscan example from NW Iberia (Spain). *International Journal of Earth Sciences* **102**, 1305-1319.

Díez Fernández, R., Martínez Catalán, J. R., Arenas, R., Abati Gómez, J. (2011). Tectonic evolution of a continental subduction-exhumation channel: Variscan structure of the basal allochthonous units in NW Spain. *Tectonics* **30**, doi: 10.1029/2010TC002850.

Dilek, Y. (2003). Ophiolite concept and its evolution. *Geological Society of America Special Papers* **373**, 1-16.

Dilek, Y. & Furnes, H. (2011). Ophiolite genesis and global tectonics: Geochemical and tectonic fingerprinting of ancient oceanic lithosphere. *Geological Society of America Bulletin* **123**, 387-411.

Dilek, Y., Thy, P., Moores, E. M., Grundvig, S. (1990). Late Paleozoic–early Mesozoic

oceanic basement of a Jurassic arc terrane in the northwestern Sierra Nevada, California. *Geological Society of America Special Papers* **255**, 351-370.

Dobrzhinetskaya, L. F., Wirth, R., Yang, J., Hutcheon, I. D., Weber, P. K., Green, H. W. (2009). High-pressure highly reduced nitrides and oxides from chromitite of a Tibetan ophiolite. *Proceedings of the National Academy of Sciences* **106**, 19233-19238.

Doin, M.-P. & Henry, P. (2001). Subduction initiation and continental crust recycling: the roles of rheology and eclogitization. *Tectonophysics* **342**, 163-191.

Downes, H. (2001). Formation and Modification of the Shallow Sub-continental Lithospheric Mantle: a Review of Geochemical Evidence from Ultramafic Xenolith Suites and Tectonically Emplaced Ultramafic Massifs of Western and Central Europe. *Journal of Petrology* **42**, 233-250.

Downes, H. (2007). Origin and significance of spinel and garnet pyroxenites in the shallow lithospheric mantle: Ultramafic massifs in orogenic belts in Western Europe and NW Africa. *Lithos* **99**, 1-24.

Drury, M. R., Van Roermund, H. L. M., Carswell, D. A., De Smet, J. H., Van Den Berg, A. P., Vlaar, N. J. (2001). Emplacement of Deep Upper-Mantle Rocks into Cratonic Lithosphere by Convection and Diapiric Upwelling. *Journal of Petrology* **42**, 131-140.

Drury, S. (1980). The geochemistry of high-pressure gneisses from Cabo Ortegal (NW Spain): residues of deep anatexis. *Geol Mijbouw* **59**, 61-64.

Ducea, M. N. & Barton, M. D. (2007). Igniting flare-up events in Cordilleran arcs. *Geology* **35**, 1047-1050.

Ducea, M. N., Saleeby, J. B., Bergantz, G. (2015). The Architecture, Chemistry, and Evolution of Continental Magmatic Arcs. *Annual Review of Earth and Planetary Sciences* **43**, 10.11-10.33.

Eggins, S. (1993). Origin and differentiation of picritic arc magmas, Ambae (Aoba), Vanuatu. *Contributions to Mineralogy and Petrology* **114**, 79-100.

Elliott, T., Plank, T., Zindler, A., White, W., Bourdon, B. (1997). Element transport from slab to volcanic front at the Mariana arc. Journal of Geophysical Research: Solid Earth 102, 14991-15019.

Fabriès, J., Lorand, J.-P., Bodinier, J.-L., Dupuy, C. (1991). Evolution of the Upper Mantle beneath the Pyrenees: Evidence from Orogenic Spinel Lherzolite Massifs. *Journal of Petrology* **Special Lherzolite Issue**, 55-76.

Falloon, T. J. & Crawford, A. J. (1991). The petrogenesis of high-calcium boninite lavas dredged from the northern Tonga ridge. *Earth and Planetary Science Letters* **102**, 375-394.

Falloon, T. J., Green, D. H., Hatton, C. J., Harris, K. L. (1988). Anhydrous Partial Melting of a Fertile and Depleted Peridotite from 2 to 30 kb and Application to Basalt Petrogenesis. *Journal of Petrology* **29**, 1257-1282.

Fernandez, F. J. (1994). Estructuras desarrolladas en gneises bajo condiciones de alta P y T (Gneises de Chimparra, Cabo Ortegal). PhD thesis, Universidad de Oviedo, 193.

Fernández-Suárez, J., Arenas, R., Abati, J., Martínez Catalán, J. R., Whitehouse, M. J., Jeffries, T. E. (2007). U-Pb chronometry of polymetamorphic high-pressure granulites: An example from the allochthonous terranes of the NW Iberian Variscan belt. In: Hatcher, R. D., Jr, Carlson, M. P., McBride, J. H. & Martínez Catalán, J. R. (eds) Framework of Continental Crust. *Geological Society of America, Memoirs* **200**, 469–488.

Fernández-Suárez, J., Corfu, F., Arenas, R., Marcos, A., Martínez Catalán, J. R., García, F., Abati, J., Fernández, F. J. (2002). U–Pb evidence for a polyorogenic evolution of the HP–HT units of the NW Iberian Massif. *Contributions to Mineralogy and Petrology* **143**, 236-253.

Foley, S. F., Barth, M. G., Jenner, G. A. (2000). Rutile/melt partition coefficients for trace elements and an assessment of the influence of rutile on the trace element characteristics of subduction zone magmas. *Geochimica et cosmochimica Acta* **64**, 933-938.

Frey, F. A. & Prinz, M. (1978). Ultramafic inclusions from San Carlos, Arizona: Petrologic and geochemical data bearing on their petrogenesis. *Earth and Planetary Science Letters* **38**, 129-176.

Frisch, W., Meschede, M., Blakey, R. (2011). Subduction zones, island arcs and active continental margins. *Plate Tectonics*: Springer Berlin Heidelberg, 91-122.

Fuenlabrada, J. M., Arenas, R., Martínez, S. S., García, F. D., Castiñeiras, P. (2010). A peri-Gondwanan arc in NW Iberia: I: Isotopic and geochemical constraints on the origin of the arc—A sedimentary approach. *Gondwana Research* **17**, 338-351.

Gaetani, G. A. & Grove, T. L. (1995). Partitioning of rare earth elements between clinopyroxene and silicate melt Crystal-chemical controls. *Geochimica et cosmochimica Acta* **59**, 1951-1962.

Gaetani, G. A. & Grove, T. L. (1998). The influence of water on melting of mantle peridotite. *Contributions to Mineralogy and Petrology* **131**, 323-346.

Gaetani, G. A., Grove, T. L., Bryan, W. B. (1993). The influence of water on the petrogenesis of subduction-related igneous rocks. *Nature* **365**, 332-334.

Gaetani, G. A., Kent, A. J. R., Grove, T. L., Hutcheon, I. D., Stolper, E. M. (2003). Mineral/melt partitioning of trace elements during hydrous peridotite partial melting. *Contributions to Mineralogy and Petrology* **145**, 391-405.

Galán, G. & Marcos, A. (1997). Geochemical evolution of high-pressure mafic granulites from the Bacariza formation (Cabo Ortegal complex, NW Spain): an example of a heterogeneous lower crust. *Geologische Rundschau* **86**, 539-555.

Galán, G. & Marcos, A. (1998). The high-pressure granulites of the Bacariza Formation: an earlier stage in the exhumation of other eclogites in the Cabo Ortegal Complex (Hercynian belt, NW Spain). *Trabajos de geología* **141**.

Galán, G. & Marcos, A. (2000). The metamorphic evolution of the high pressure mafic granulites of the Bacariza Formation (Cabo Ortegal Complex, Hercynian belt, NW Spain). *Lithos* **54**, 139-171.

García Izquierdo, B., Capote, R., López, R. L. (2011). La fabrica del olivino y las condiciones de la deformacion de las rocas ultramaficas del macizo de Herbeira (Cabo Ortegal, NO del Macizo Ibérico). *Revista de la Sociedad Geológica de España* **24**, 1-2.

Gardien, V., Tegyey, M., Lardeaux, J. M., Misseri, M., Dufour, E. (1990). Crust-mantle relationships in the French Variscan chain: the example of the Southern Monts du Lyonnais unit (eastern French Massif Central). *Journal of Metamorphic Geology* **8**, 477-492.

Garrido, C. J. & Bodinier, J.-L. (1999). Diversity of mafic rocks in the Ronda peridotite: evidence for pervasive melt–rock reaction during heating of subcontinental lithosphere by upwelling asthenosphere. *Journal of Petrology* **40**, 729-754.

Garrido, C. J., Bodinier, J.-L., Burg, J.-P., Zeilinger, G., Hussain, S. S., Dawood, H., Chaudhry, M. N., Gervilla, F. (2006). Petrogenesis of Mafic Garnet Granulite in the Lower Crust of the Kohistan Paleo-arc Complex (Northern Pakistan): Implications for Intra-crustal Differentiation of Island Arcs and Generation of Continental Crust. *Journal of Petrology* **47**, 1873-1914.

Garrido, C. J., Bodinier, J.-L., Dhuime, B., Bosch, D., Chanefo, I., Bruguier, O., Hussain, S. S., Dawood, H., Burg, J.-P. (2007). Origin of the island arc Moho transition zone via melt-rock reaction and its implications for intracrustal differentiation of island arcs: Evidence from the Jijal complex (Kohistan complex, northern Pakistan). *Geology* **35**, 683-686.

Garrido, C. J., López Sánchez-Vizcaíno, V., Gómez-Pugnaire, M. T., Trommsdorff, V., Alard, O., Bodinier, J.-L., Godard, M. (2005). Enrichment of HFSE in chlorite-harzburgite produced by high-pressure dehydration of antigorite-serpentinite: Implications for subduction magmatism. *Geochemistry, Geophysics, Geosystems* **6**, doi:10.1029/2004GC000791.

Gass, I. G., Neary, C. R., Plant, J., Robertson, A. H. F., Simonian, K. O., Smewing, J. D., Spooner, E. T. C., Wilson, R. A. M. (1975). Comments on "the troodos ophiolitic complex was probably formed in an island arc", by A. Miyashiro and subsequent correspondence by A. Hynes and A. Miyashiro. *Earth and Planetary Science Letters* **25**, 236-238.

Gayk, T. & Kleinschrodt, R. (2000). Hot contacts of garnet peridotites in middle/upper crustal levels: new constraints on the nature of the late Variscan high-T/low-P event in the Moldanubian (Central Vosges/NE France). *Journal of Metamorphic Geology* **18**, 293-305.

Gil Ibarguchi, I., Ábalos, B., Campillo, A., Higuero, A., López, B., Pinilla, V., Rodrıguez, C., Rodríguez, R., Urtiaga, K. (1987). Asociaciones con granate-clinopiroxeno en la unidad catazonal superior del complejo de Cabo Ortegal. *Cadernos do Laboratorio*

Xeolóxico de Laxe **12**, 165-181.

Gil Ibarguchi, J. I., Ábalos, B., Azcarraga, J., Puelles, P. (1999). Deformation, high-pressure metamorphism and exhumation of ultramafic rocks in a deep subduction/collision setting (Cabo Ortegal, NW Spain). *Journal of Metamorphic Geology* **17**, 747-764.

Gil Ibarguchi, J. I., Mendia, M., Girardeau, J., Peucat, J.-J. (1990). Petrology of eclogites and clinopyroxene-garnet metabasites from the Cabo Ortegal Complex (northwestern Spain). *Lithos* **25**, 133-162.

Gill, J. B. (1981). The Plate Tectonic Connection. *Orogenic Andesites and Plate Tectonics*: Springer, 13-43.

Gillis, K. M., Snow, J. E., Klaus, A., Abe, N., Adrião, Á. B., Akizawa, N., Ceuleneer, G., Cheadle, M. J., Faak, K., Falloon, T. J. (2013). Primitive layered gabbros from fast-spreading lower oceanic crust. *Nature* **505**, 204-207.

Girardeau, J. & Gil Ibarguchi, J. I. (1991). Pyroxenite-rich peridotites of the Cabo Ortegal complex (Northwestern Spain): evidence for large-scale upper-mantle heterogeneity. *Journal of Petrology* **Special Lherzolites Issue**, 135-154.

Girardeau, J., Gil Ibarguchi, J. I., Ben Jamaa, N. (1989). Evidence for a Heterogeneous Upper Mantle in the Cabo Ortegal Complex, Spain. *Science* **245**, 1231-1233.

Girardeau, J., Gil Ibarguchi, J. I., Ben Jamaa, N. (1990). Les peridotites et pyroxenites du complexe catazonal du Cabo Ortegal. *Cadernos do Laboratorio Xeolóxico de Laxe* **15**, 227-256.

Gómez Barreiro, J., Martínez Catalán, J. R., Arenas, R., Castiñeiras, P., Abati, J., Díaz García, F., Wijbrans, J. R. (2007). Tectonic evolution of the upper allochthon of the Órdenes complex (northwestern Iberian Massif): Structural constraints to a polyorogenic peri-Gondwanan terrane. In: Linnemann, U., Nance, R. D., Kraft, P. & Zulauf, G. (eds) The evolution of the Rheic Ocean: From Avalonian-Cadomian active margin to Alleghenian-Variscan collision. *Geological Society of America, Special Papers* **423**, 315–332.

Gravestock, P. J. (1992). The chemical causes of uppermost mantle heterogeneities. PhD thesis, Open University, 299.

Green, D. H. & Falloon, T. J. (1998). Pyrolite: a Ringwood concept and its current expression. In: Jackson, I. (ed) *The Earth's mantle: composition, structure, and evolution:* Cambridge University Press, 311-378.

Green, D. H. & Ringwood, A. E. (1969). The Origin of Basalt Magmas. *The Earth's Crust and Upper Mantle*: American Geophysical Union, 489-495.

Green, D. H., Schmidt, M. W., Hibberson, W. O. (2004). Island-arc Ankaramites: Primitive Melts from Fluxed Refractory Lherzolitic Mantle. *Journal of Petrology* **45**, 391-403.

Green, T. H., Adam, J., Siel, S. H. (1992). Trace element partitioning between silicate

minerals and carbonatite at 25 kbar and application to mantle metasomatism. *Mineralogy and Petrology* **46**, 179-184.

Green, T. H. & Pearson, N. J. (1987). An experimental study of Nb and Ta partitioning between Ti-rich minerals and silicate liquids at high pressure and temperature. *Geochimica et cosmochimica Acta* **51**, 55-62.

Greene, A., R., DeBari, S. M., Kelemen, P. B., Blusztajn, J., Clift, P. D. (2006). A Detailed Geochemical Study of Island Arc Crust: the Talkeetna Arc Section, South–Central Alaska. *Journal of Petrology* **47**, 1051-1093.

Grégoire, M., Jego, S., Maury, R. C., Polve, M., Payot, B., Tamayo Jr, R. A., Yumul Jr, G. P. (2008). Metasomatic interactions between slab-derived melts and depleted mantle: Insights from xenoliths within Monglo adakite (Luzon arc, Philippines). *Lithos* **103**, 415-430.

Grégoire, M., Lorand, J.-P., O'Reilly, S., Cottin, J.-Y. (2000a). Armalcolite-bearing, Ti-rich metasomatic assemblages in harzburgitic xenoliths from the Kerguelen Islands: implications for the oceanic mantle budget of high-field strength elements. *Geochimica et cosmochimica Acta* **64**, 673-694.

Grégoire, M., McInnes, B. I. A., O'Reilly, S. Y. (2001). Hydrous metasomatism of oceanic sub-arc mantle, Lihir, Papua New Guinea: Part 2. Trace element characteristics of slab-derived fluids. *Lithos* **59**, 91-108.

Grégoire, M., Moine, B. N., O'Reilly, S. Y., Cottin, J.-Y., Giret, A. (2000b). Trace element residence and partitioning in mantle xenoliths metasomatized by highly alkaline, silicate-and carbonate-rich melts (Kerguelen Islands, Indian Ocean). *Journal of Petrology* **41**, 477-509.

Griffin, W. L., Afonso, J. C., Belousova, E. A., Gain, S. E., Gong, X.-H., González-Jiménez, J. M., Howell, D., Huang, J.-X., McGowan, N., Pearson, N. J., Satsukawa, T., Shi, R., Williams, P., Xiong, Q., Yang, J.-S., Zhang, M., O'Reilly, S. Y. (2016). Mantle Recycling: Transition Zone Metamorphism of Tibetan Ophiolitic Peridotites and its Tectonic Implications. *Journal of Petrology* **57**, 655-684.

Griffin, W. L., O'Reilly, S. Y., Abe, N., Aulbach, S., Davies, R. M., Pearson, N. J., Doyle, B. J., Kivi, K. (2003). The origin and evolution of Archean lithospheric mantle. *Precambrian Research* **127**, 19-41.

Griffin, W. L., O'Reilly, S. Y., Afonso, J. C., Begg, G. C. (2009). The Composition and Evolution of Lithospheric Mantle: a Re-evaluation and its Tectonic Implications. *Journal of Petrology* **50**, 1185-1204.

Griffin, W. L., O'Reilly, S. Y., Ryan, C. G. (1999). The composition and origin of sub-continental lithospheric mantle. Mantle Petrology: Field Observations and High Pressure Experimentation: A Tribute to Francis R.(Joe) Boyd. *Geochemical Society, Special Publications* **6**, 13-45.

Griffin, W. L., Powell, W. J., Pearson, N. J., O'Reilly, S. Y. (2008). GLITTER: data re-

duction software for laser ablation ICP-MS. In: Sylvester, P. (ed.) Laser Ablation-ICP-MS in the Earth Sciences. *Mineralogical Association of Canada, Short Course Series* **40**, 204–207.

Griffin, W. L., Wass, S. Y., Hollis, J. D. (1984). Ultramafic Xenoliths from Bullenmerri and Gnotuk Maars, Victoria, Australia: Petrology of a Sub-Continental Crust-Mantle Transition. *Journal of Petrology* **25**, 53-87.

Grove, T. L., Till, C. B., Krawczynski, M. J. (2012). The Role of H_2O in Subduction Zone Magmatism. *Annual Review of Earth and Planetary Sciences* **40**, 413-439.

Gysi, A. P., Jagoutz, O., Schmidt, M. W., Targuisti, K. (2011). Petrogenesis of Pyroxenites and Melt Infiltrations in the Ultramafic Complex of Beni Bousera, Northern Morocco. *Journal of Petrology* **52**, 1679-1735.

Hacker, B. R., Abers, G. A., Peacock, S. M. (2003). Subduction factory 1. Theoretical mineralogy, densities, seismic wave speeds, and H_2O contents. *Journal of Geophysical Research: Solid Earth* **108**, doi: 10.1029/2001JB001127.

Hacker, B. R., Kelemen, P. B., Behn, M. D. (2011). Differentiation of the continental crust by relamination. *Earth and Planetary Science Letters* **307**, 501-516.

Hacker, B. R., Mehl, L., Kelemen, P. B., Rioux, M., Behn, M. D., Luffi, P. (2008). Reconstruction of the Talkeetna intraoceanic arc of Alaska through thermobarometry. *Journal of Geophysical Research: Solid Earth* **113**, doi: 10.1029/2007JB005208.

Hacker, B. R., Mosenfelder, J. L., Gnos, E. (1996). Rapid emplacement of the Oman ophiolite: Thermal and geochronologic constraints. *Tectonics* **15**, 1230-1247.

Haggerty, S. (1989). Upper mantle opaque mineral stratigraphy and the genesis of metasomites and alkali-rich melts. *Kimberlites and related rocks* **2**, 687-699.

Haggerty, S. E. (1991). Oxide mineralogy of the upper mantle. *Reviews in Mineralogy and Geochemistry* **25**, 355-416.

Hamelin, B. & Allègre, C. J. (1985). Large-scale regional units in the depleted upper mantle revealed by an isotope study of the South-West Indian Ridge. *Nature* **315**, 196-199.

Harte, B., Hunter, R., Kinny, P. (1993). Melt geometry, movement and crystallization, in relation to mantle dykes, veins and metasomatism. *Philosophical Transactions of the Royal Society of London A: Mathematical, Physical and Engineering Sciences* **342**, 1-21.

Hauff, F., Hoernle, K., Schmincke, H., Werner, R. (1997). A mid Cretaceous origin for the Galápagos hotspot: Volcanological, petrological and geochemical evidence from Costa Rican oceanic crustal segments. *Geologische Rundschau* **86**, 141-155.

Hawkesworth, C., Gallagher, K., Hergt, J., McDermott, F. (1993). Mantle and slab contribution in arc magmas. *Annual Review of Earth and Planetary Sciences* **21**, 175-204.

Hawkesworth, C. J., Dhuime, B., Pietranik, A. B., Cawood, P. A., Kemp, A. I. S., Storey, C. D. (2010). The generation and evolution of the continental crust. *Journal of the*

Geological Society **167**, 229-248.

Hawkesworth, C. J. & Kemp, A. I. S. (2006). Using hafnium and oxygen isotopes in zircons to unravel the record of crustal evolution. *Chemical Geology* **226**, 144-162.

Hawkins, J. W., Bloomer, S. H., Evans, C. A., Melchior, J. T. (1984). Geodynamics of Back-Arc Regions Evolution of intra-oceanic arc-trench systems. *Tectonophysics* **102**, 175-205.

Hermann, J., Müntener, O., Trommsdorff, V., Hansmann, W., Piccardo, G. B. (1997). Fossil crust-to-mantle transition, Val Malenco (Italian Alps). *Journal of Geophysical Research: Solid Earth* **102**, 20123-20132.

Herrmann, W. & Berry, R. F. (2002). MINSQ−a least squares spreadsheet method for calculating mineral proportions from whole rock major element analyses. *Geochemistry: Exploration, Environment, Analysis* **2**, 361-368.

Hess, H. H. (1955). Serpentines, orogeny, and epeirogeny. *Geological Society of America Special Papers* **62**, 391-408.

Hess, H. H. (1962). History of ocean basins. *Petrologic studies* **4**, 599-620.

Hickey, R. L. & Frey, F. A. (1982). Geochemical characteristics of boninite series volcanics: implications for their source. *Geochimica et cosmochimica Acta* **46**, 2099-2115.

Hickey-Vargas, R. & Reagan, M. K. (1987). Temporal variation of isotope and rare earth element abundances in volcanic rocks from Guam: implications for the evolution of the Mariana Arc. *Contributions to Mineralogy and Petrology* **97**, 497-508.

Hirschmann, M. M. & Stolper, E. M. (1996). A possible role for garnet pyroxenite in the origin of the "garnet signature" in MORB. *Contributions to Mineralogy and Petrology* **124**, 185-208.

Hofmann, A. W. (2014). Sampling mantle heterogeneity through oceanic basalts: isotopes and trace elements. In: Turekian, K. K. (ed.) *Treatise on Geochemistry* (Second Edition). Oxford: Elsevier, **568**, 61-101.

Holbrook, W. S., Lizarralde, D., McGeary, S., Bangs, N., Diebold, J. (1999). Structure and composition of the Aleutian island arc and implications for continental crustal growth. *Geology* **27**, 31-34.

Howell, D., Griffin, W. L., Yang, J., Gain, S., Stern, R. A., Huang, J. X., Jacob, D. E., Xu, X., Stokes, A. J., O'Reilly, S. Y., Pearson, N. J. (2015). Diamonds in ophiolites: Contamination or a new diamond growth environment? *Earth and Planetary Science Letters* **430**, 284-295.

Ionov, D. A., Bodinier, J.-L., Mukasa, S. B., Zanetti, A. (2002). Mechanisms and Sources of Mantle Metasomatism: Major and Trace Element Compositions of Peridotite Xenoliths from Spitsbergen in the Context of Numerical Modelling. *Journal of Petrology* **43**, 2219-2259.

Ionov, D. A., Griffin, W. L., O'Reilly, S. Y. (1997). Volatile-bearing minerals and lithophile trace elements in the upper mantle. *Chemical Geology* **141**, 153-184.

Ionov, D. A. & Hofmann, A. W. (1995). Nb-Ta-rich mantle amphiboles and micas: Implications for subduction-related metasomatic trace element fractionations. *Earth and Planetary Science Letters* **131**, 341-356.

Irvine, T. N. (1965). Chromian Spinel As A Petrogenetic Indicator: Part 1. Theory. Canadian *Journal of Earth Sciences* **2**, 648-672.

Irving, A. J. (1980). Petrology and geochemistry of composite ultramafic xenoliths in alkalic basalts and implications for magmatic processes within the mantle. *American Journal of Science* **280**, 389-426.

Ishiwatari, A. (1985). Alpine ophiolites: product of low-degree mantle melting in a Mesozoic transcurrent rift zone. *Earth and Planetary Science Letters* **76**, 93-108.

Jacobsen, S. B. & Wasserburg, G. J. (1980). Sm-Nd isotopic evolution of chondrites. *Earth and Planetary Science Letters* **50**, 139-155.

Jagoutz, O. & Behn, M. D. (2013). Foundering of lower island-arc crust as an explanation for the origin of the continental Moho. *Nature* **504**, 131-134.

Jagoutz, O. & Kelemen, P. B. (2015). Role of Arc Processes in the Formation of Continental Crust. *Annual Review of Earth and Planetary Sciences* **43**, 363-404.

Jagoutz, O., Müntener, O., Schmidt, M. W., Burg, J.-P. (2011). The roles of flux- and decompression melting and their respective fractionation lines for continental crust formation: Evidence from the Kohistan arc. *Earth and Planetary Science Letters* **303**, 25-36.

Jagoutz, O. & Schmidt, M. W. (2012). The formation and bulk composition of modern juvenile continental crust: The Kohistan arc. *Chemical Geology* **298–299**, 79-96.

Jamtveit, B., Carswell, D. A., Mearns, E. W. (1991). Chronology of the high-pressure metamorphism of Norwegian garnet peridotites/pyroxenites. Journal of Metamorphic *Geology* **9**, 125-139.

Jan, M. Q., Khan, M. A., Windley, B., F. (1992). Exsolution in Al-Cr-Fe^{3+}-rich spinels from the Chilas mafic-ultramafic complex, Pakistan. *American Mineralogist* **77**, 1074-1074.

Jull, M. & Kelemen, P. (2001). On the conditions for lower crustal convective instability. *Journal of Geophysical Research: Solid Earth* **106**, 6423-6446.

Jung, H. & Karato, S.-i. (2001). Water-induced fabric transitions in olivine. *Science* **293**, 1460-1463.

Jweda, J., Bolge, L., Class, C., Goldstein, S. L. (2016). High Precision Sr-Nd-Hf-Pb Isotopic Compositions of USGS Reference Material BCR-2. *Geostandards and Geoanalytical Research* **40**, 101-115.

Kaczmarek, M.-A. & Müntener, O. (2008). Juxtaposition of Melt Impregnation and High-Temperature Shear Zones in the Upper Mantle; Field and Petrological Constraints from the Lanzo Peridotite (Northern Italy). *Journal of Petrology* **49**, 2187-2220.

Kalfoun, F., Ionov, D., Merlet, C. (2002). HFSE residence and Nb/Ta ratios in metasomatised, rutile-bearing mantle peridotites. *Earth and Planetary Science Letters* **199**, 49-65.

Karson, J. A. (1998). Internal structure of oceanic lithosphere: A perspective from tectonic windows. In: Buck, W. R., Delaney, P. T., Karson, J. A., Lagabrielle, Y. (eds) Faulting and Magmatism at Mid-Ocean Ridges. *AGU Geophysical Monograph Series* **106**, 177-218.

Kay, R. W. & Kay, S. M. (1988). Crustal recycling and the Aleutian arc. *Geochimica et cosmochimica Acta* **52**, 1351-1359.

Kay, R. W. & Mahlburg Kay, S. (1993). Plate Tectonic Signatures in the Continental Lithosphere Delamination and delamination magmatism. *Tectonophysics* **219**, 177-189.

Kay, S. M. & Kay, R. W. (1985). Role of crystal cumulates and the oceanic crust in the formation of the lower crust of the Aleutian arc. *Geology* **13**, 461-464.

Kelemen, P. B. (1986). Assimilation of ultramafic rock in subduction-related magmatic arcs. *The Journal of geology* **94**, 829-843.

Kelemen, P. B. (1990). Reaction Between Ultramafic Rock and Fractionating Basaltic Magma I. Phase Relations, the Origin of Calc-alkaline Magma Series, and the Formation of Discordant Dunite. *Journal of Petrology* **31**, 51-98.

Kelemen, P. B. (1995). Genesis of high Mg# andesites and the continental crust. *Contributions to Mineralogy and Petrology* **120**, 1-19.

Kelemen, P. B. & Behn, M. D. (2016). Formation of lower continental crust by relamination of buoyant arc lavas and plutons. *Nature Geoscience* **9**, 197-205.

Kelemen, P. B. & Ghiorso, M. S. (1986). Assimilation of peridotite in zoned calc-alkaline plutonic complexes: evidence from the Big Jim complex, Washington Cascades. *Contributions to Mineralogy and Petrology* **94**, 12-28.

Kelemen, P. B., Hanghøj, K., Greene, A. R. (2014). One View of the Geochemistry of Subduction-Related Magmatic Arcs, with an Emphasis on Primitive Andesite and Lower Crust. In: Turekian, K. K. (ed.) *Treatise on Geochemistry* **3** (Second Edition). Oxford: Elsevier, 749-806.

Kelemen, P. B., Rilling, J. L., Parmentier, E., Mehl, L., Hacker, B. R. (2003). Thermal structure due to solid-state flow in the mantle wedge beneath arcs. In: Eiler, J. (ed) Inside the subduction factory. *AGU Geophysical Monograph Series* **138**, 293-311.

Kelemen, P. B., Shimizu, N., Dunn, T. (1993). Relative depletion of niobium in some arc magmas and the continental crust: partitioning of K, Nb, La and Ce during melt/rock reaction in the upper mantle. *Earth and Planetary Science Letters* **120**, 111-134.

Kerrich, R. & Polat, A. (2006). Archean greenstone-tonalite duality: Thermochemical mantle convection models or plate tectonics in the early Earth global dynamics? *Tectonophysics* **415**, 141-165.

Khan, M. A., Jan, M. Q., Weaver, B. (1993). Evolution of the lower arc crust in Kohistan, N. Pakistan: temporal arc magmatism through early, mature and intra-arc rift stages. *Geological Society, London, Special Publications* **74**, 123-138.

Khan, S. D., Walker, D. J., Hall, S. A., Burke, K. C., Shah, M. T., Stockli, L. (2009). Did the Kohistan-Ladakh island arc collide first with India? *Geological Society of America Bulletin* **121**, 366-384.

Klemme, S., Blundy, J. D., Wood, B. J. (2002). Experimental constraints on major and trace element partitioning during partial melting of eclogite. *Geochimica et cosmochimica Acta* **66**, 3109-3123.

Klemme, S., Prowatke, S., Hametner, K., Günther, D. (2005). Partitioning of trace elements between rutile and silicate melts: Implications for subduction zones. *Geochimica et cosmochimica Acta* **69**, 2361-2371.

Kogiso, T. & Hirschmann, M. (2001). Experimental study of clinopyroxenite partial melting and the origin of ultra-calcic melt inclusions. *Contributions to Mineralogy and Petrology* **142**, 347-360.

Kogiso, T., Hirschmann, M. M., Frost, D. J. (2003). High-pressure partial melting of garnet pyroxenite: possible mafic lithologies in the source of ocean island basalts. *Earth and Planetary Science Letters* **216**, 603-617.

Kornprobst, J. (1969). Le massif ultrabasique des Beni Bouchera (Rif Interne, Maroc): Etude des péridotites de haute température et de haute pression, et des pyroxénolites, à grenat ou sans grenat, qui leur sont associées. *Contributions to Mineralogy and Petrology* **23**, 283-322.

Kornprobst, J., Piboule, M., Roden, M., Tabit, A. (1990). Corundum-bearing Garnet Clinopyroxenites at Beni Bousera (Morocco): Original Plagioclase-rich Gabbros Recrystallized at Depth within the Mantle? *Journal of Petrology* **31**, 717-745.

Kostopoulos, D. & Murton, B. (1992). Origin and distribution of components in boninite genesis: significance of the OIB component. *Geological Society, London, Special Publications* **60**, 133-154.

Kuijper, R. P., Priem, H. N. A., Den Tex, E. (1982). Late Archaean—early proterozoic source ages of zircons in rocks from the Paleozoic orogen of western Galicia, NW Spain. *Precambrian Research* **19**, 1-29.

Kumar, N., Reisberg, L., Zindler, A. (1996). A major and trace element and strontium, neodymium, and osmium isotopic study of a thick pyroxenite layer from the Beni Bousera Ultramafic Complex of northern Morocco. *Geochimica et cosmochimica Acta* **60**, 1429-1444.

Kushiro, I. (1996). Partial Melting of a Fertile Mantle Peridotite at High Pressures: An Experimental Study Using Aggregates of Diamond. *Earth Processes: Reading the Isotopic Code*: American Geophysical Union, 109-122.

Kushiro, I. & Yoder, H. S. (1966). Anorthite—Forsterite and Anorthite—Enstatite Reactions and their bearing on the Basalt—Eclogite Transformation. *Journal of Petrology* **7**, 337-362.

Lambart, S., Laporte, D., Provost, A., Schiano, P. (2012). Fate of pyroxenite-derived melts in the peridotitic mantle: thermodynamic and experimental constraints. *Journal of Petrology* **53**, 451-476.

Lambart, S., Laporte, D., Schiano, P. (2013). Markers of the pyroxenite contribution in the major-element compositions of oceanic basalts: Review of the experimental constraints. *Lithos* **160–161**, 14-36.

Lapierre, H., Brouxel, M., Martin, P., Coulon, C. (1986). The Paleozoic and Mesozoic geodynamic evolution of the Eastern Klamath Mountains (North California) inferred from the geochemical characteristics of its magmatism. *Bulletin de la Société Géologique de France* **2**, 969-980.

Laribi-Halimi, A. (1992). Relations géochimiques dans les péridotites et pyroxénites du Cabo Ortegal (Espagne) : application de l'analyse par activation neutronique. PhD thesis, Université Paris VI, 144.

Le Bas, M. J. (2000). IUGS Reclassification of the High-Mg and Picritic Volcanic Rocks. *Journal of Petrology* **41**, 1467-1470.

Le Roux, V., Bodinier, J.-L., Tommasi, A., Alard, O., Dautria, J.-M., Vauchez, A., Riches, A. (2007). The Lherz spinel lherzolite: refertilized rather than pristine mantle. *Earth and Planetary Science Letters* **259**, 599-612.

Leake, B. E., Woolley, A. R., Arps, C. E., Birch, W. D., Gilbert, M. C., Grice, J. D., Hawthorne, F. C., Kato, A., Kisch, H. J., Krivovichev, V. G. (1997). Report. Nomenclature of Amphiboles: Report of the Subcommittee on Amphiboles of the International Mineralogical Association Commission on New Minerals and Mineral Names. *Mineralogical Magazine* **61**, 295-321.

Leat, P. T. & Larter, R. D. (2003). Intra-oceanic subduction systems: introduction. *Geological Society, London, Special Publications* **219**, 1-17.

Lee, C.-T. A., Cheng, X., Horodyskyj, U. (2006). The development and refinement of continental arcs by primary basaltic magmatism, garnet pyroxenite accumulation, basaltic recharge and delamination: insights from the Sierra Nevada, California. *Contributions to Mineralogy and Petrology* **151**, 222-242.

Lemoine, M., Tricart, P., Boillot, G. (1987). Ultramafic and gabbroic ocean floor of the Ligurian Tethys (Alps, Corsica, Apennines): In search of a genetic imodel. *Geology* **15**, 622-625.

Lenoir, X., Garrido, C. J., Bodinier, J.-L., Dautria, J.-M., Gervilla, F. (2001). The Recrystallization Front of the Ronda Peridotite: Evidence for Melting and Thermal Erosion of Subcontinental Lithospheric Mantle beneath the Alboran Basin. *Journal of Petrology* **42**, 141-158.

Lindsey-Griffin, N. (1977). The Trinity ophiolite, Klamath Mountains, California, North America Ophiolites. *Oreg. Dep. Geol. Min. Ind. Bull.* **95**, 107-120.

Lissenberg, C. J., MacLeod, C. J., Howard, K. A., Godard, M. (2013). Pervasive reactive melt migration through fast-spreading lower oceanic crust (Hess Deep, equatorial Pacific Ocean). *Earth and Planetary Science Letters* **361**, 436-447.

Liu, C.-Z., Snow, J. E., Hellebrand, E., Brügmann, G., von der Handt, A., Büchl, A., Hofmann, A. W. (2008). Ancient, highly heterogeneous mantle beneath Gakkel ridge, Arctic Ocean. *Nature* **452**, 311-316.

Llana-Fúnez, S. & Brown, D. (2012). Contribution of crystallographic preferred orientation to seismic anisotropy across a surface analog of the continental Moho at Cabo Ortegal, Spain. *Geological Society of America Bulletin* **124**, 1495-1513.

Loubet, M. & Allègre, C. J. (1982). Trace elements in orogenic lherzolites reveal the complex history of the upper mantle. *Nature* **298**, 809-814.

Maaskant, P. (1970). Chemical petrology of polymetamorphic ultramafic rocks from Galicia, NW Spain. *Leidse Geol. Meded* **45**, 237-325.

MacLeod, C. J., Johan Lissenberg, C., Bibby, L. E. (2013). "Moist MORB" axial magmatism in the Oman ophiolite: The evidence against a mid-ocean ridge origin. *Geology* **41**, 459-462.

MacLeod, C. J. & Yaouancq, G. (2000). A fossil melt lens in the Oman ophiolite: Implications for magma chamber processes at fast spreading ridges. *Earth and Planetary Science Letters* **176**, 357-373.

Macpherson, C. G., Forrde, E. J., Hall, R., Thirlwall, M. F. (2003). Geochemical evolution of magmatism in an arc-arc collision: the Halmahera and Sangihe arcs, eastern Indonesia. *Geological Society, London, Special Publications* **219**, 207-220.

Malaviarachchi, S. P. K., Makishima, A., Nakamura, E. (2010). Melt–Peridotite Reactions and Fluid Metasomatism in the Upper Mantle, Revealed from the Geochemistry of Peridotite and Gabbro from the Horoman Peridotite Massif, Japan. *Journal of Petrology* **51**, 1417-1445.

Manatschal, G. (2004). New models for evolution of magma-poor rifted margins based on a review of data and concepts from West Iberia and the Alps. *International Journal of Earth Sciences* **93**, 432-466.

Manatschal, G. & Müntener, O. (2009). A type sequence across an ancient magma-poor ocean–continent transition: the example of the western Alpine Tethys ophiolites. *Tectonophysics* **473**, 4-19.

Manning, C. E., MacLeod, C. J., Weston, P. E. (2000). Lower-crustal cracking front at fast-spreading ridges: Evidence from the East Pacific Rise and the Oman Ophiolite. *Geological Society of America Special Papers* **349**, 261-272.

Marchesi, C., Garrido, C. J., Bosch, D., Bodinier, J.-L., Gervilla, F., Hidas, K. (2013). Mantle refertilization by melts of crustal-derived garnet pyroxenite: Evidence from the Ronda peridotite massif, southern Spain. *Earth and Planetary Science Letters* **362**, 66-75.

Marcos, A., Farias, P., Galán, G., Fernández, F. J., Llana-Fúnez, S. (2002). Tectonic framework of the Cabo Ortegal Complex: A slab of lower crust exhumed in the Variscan orogen (northwestern Iberian Peninsula). In: Martínez Catalán, J. R., Hatcher, R. D., Jr, Arenas, R. & Díaz García, F. (eds) Variscan- Appalachian dynamics: The building of the late Paleozoic basement. *Geological Society of America, Special Papers* **364**, 143–162.

Marcos, A., Marquínez, J., Pérez-Estaún, A., Pulgar, J. A., Bastida, F. (1984). Nuevas aportaciones al conocimiento de la evolución tectonometamórfica del Complejo de Cabo Ortegal (NW de España). *Cadernos do Laboratorio Xeolóxico de Laxe* **7**, 125-137.

Martínez Catalán, J. R., Arenas, R., Abati, J., Sánchez Martínez, S., Díaz García, F., Fernández Suárez, J., González Cuadra, P., Castiñeiras, P., Gómez Barreiro, J., Díez Montes, A. (2009). A rootless suture and the loss of the roots of a mountain chain: the Variscan belt of NW Iberia. *Comptes Rendus Géoscience* **341**, 114-126.

Martínez Catalán, J. R., Arenas, R., García, F. D., Rubio Pascual, F. J., Abati, J., Marquínez, J. (1996). Variscan exhumation of a subducted Paleozoic continental margin: The basal units of the Ordenes Complex, Galicia, NW Spain. *Tectonics* **15**, 106-121.

Martínez Catalán, J. R., Díaz García, F., Arenas, R., Abati, J., Castiñeiras, P., González Cuadra, P., Gómez Barreiro, J., Rubio Pascual, F. (2002). Thrust and detachment systems in the Ordenes Complex (northwestern Spain): Implications for the Variscan-Appalachian geodynamics. *Geological Society of America, Special Paper* **364**, 163-182.

Matte, P. (1986). Tectonics and plate tectonics model for the Variscan belt of Europe. *Tectonophysics* **126**, 329-374.

Matte, P. (1991). Accretionary history and crustal evolution of the Variscan belt in Western Europe. *Tectonophysics* **196**, 309-337.

Matte, P. (1998). Continental subduction and exhumation of HP rocks in Paleozoic orogenic belts: Uralides and Variscides. *GFF* **120**, 209-222.

McCaffrey, R. (2009). The tectonic framework of the Sumatran subduction zone. *Annual Review of Earth and Planetary Sciences* **37**, 345-366.

McCarthy, A. & Müntener, O. (2015). Ancient depletion and mantle heterogeneity: Revisiting the Permian-Jurassic paradox of Alpine peridotites. *Geology* **43**, 255-258.

McDonough, W. F. & Sun, S. s. (1995). The composition of the Earth. *Chemical Geology* **120**, 223-253.

McGowan, N. M., Griffin, W. L., González-Jiménez, J. M., Belousova, E., Afonso, J.

C., Shi, R., McCammon, C. A., Pearson, N. J., O'Reilly, S. Y. (2015). Tibetan chromitites: Excavating the slab graveyard. *Geology* **45**.

McGregor, I. (1974). The system MgO–Al_2O_3–SiO_2: solubility of Al_2O_3 in enstatite for spinel and garnet–spinel compositions. *American Mineralogist* **59**, 110-119.

Mckenzie, D. (1984). The Generation and Compaction of Partially Molten Rock. *Journal of Petrology* **25**, 713-765.

Médard, E., Schmidt, M. W., Schiano, P., Ottolini, L. (2006). Melting of Amphibole-bearing Wehrlites: an Experimental Study on the Origin of Ultra-calcic Nepheline-normative Melts. *Journal of Petrology* **47**, 481-504.

Medaris, L. G., Beard, B. L., Jelínek, E. (2006). Mantle-Derived, UHP Garnet Pyroxenite and Eclogite in the Moldanubian Gföhl Nappe, Bohemian Massif: A Geochemical Review, New P-T Determinations, and Tectonic Interpretation. *International Geology Review* **48**, 765-777.

Medaris, L. G., Jr., Beard, B. L., Johnson, C. M., Valley, J. W., Spicuzza, M. J., Jelínek, E., Mísâr, Z. (1995). Garnet pyroxenite and eclogite in the Bohemian Massif: geochemical evidence for Variscan recycling of subducted lithosphere. *Geologische Rundschau* **84**, 489-505.

Medaris, L. G., Wang, H., Jelínek, E., Mihaljevič, M., Jakeš, P. (2005). Characteristics and origins of diverse Variscan peridotites in the Gföhl Nappe, Bohemian Massif, Czech Republic. *Lithos* **82**, 1-23.

Meijer, A. (1980). Primitive arc volcanism and a boninite series: examples from western Pacific island arcs. In: Hayes, D. E. (ed) The tectonic and geologic evolution of Southeast Asian seas and islands. *AGU Geophysical Monograph Series* **23**, 269-282.

Menzies, M., Rogers, N., Tindle, A., Hawkesworth, C. (1987). Metasomatic and enrichment processes in lithospheric peridotites, an effect of asthenosphere-lithosphere interaction. In: Menzies, M. A. & Hawkesworth C. J. (eds) *Mantle metasomatism*, 313-361.

Menzies, M. A. & Dupuy, C. (1991). Orogenic Massifs: Protolith, Process and Provenance. *Journal of Petrology* **Special Lherzolites Issue**, 1-16.

Miller, D. J. & Christensen, N. L. (1994). Seismic signature and geochemistry of an island arc: A multidisciplinary study of the Kohistan accreted terrane, northern Pakistan. *Journal of Geophysical Research: Solid Earth* **99**, 11623-11642.

Miyashiro, A. (1973). The Troodos ophiolitic complex was probably formed in an island arc. *Earth and Planetary Science Letters* **19**, 218-224.

Moine, B. N., Grégoire, M., O'Reilly, S. Y., Delpech, G., Sheppard, S. M. F., Lorand, J. P., Renac, C., Giret, A., Cottin, J. Y. (2004). Carbonatite melt in oceanic upper mantle beneath the Kerguelen Archipelago. *Lithos* **75**, 239-252.

Monterrubio Pérez, S. (1991). Mineralizaciones asociadas a rocas ultrabásicas en el

Hercínico español. PhD thesis, Universidad Complutense de Madrid.

Moores, E. M. & Vine, F. J. (1971). The Troodos Massif, Cyprus and other Ophiolites as Oceanic Crust: Evaluation and Implications. *Philosophical Transactions of the Royal Society of London. Series A, Mathematical and Physical Sciences* **268**, 443-467.

Moreno, T. (1999). Platinum-group elements and chromite mineralization in ultramafic rocks: a case study from the Cabo Ortegal Complex, NW Spain. PhD thesis, Cardiff University, 224.

Moreno, T., Gibbons, W., Prichard, H. M., Lunar, R. (2001). Platiniferous chromitite and the tectonic setting of ultramafic rocks in Cabo Ortegal, NW Spain. *Journal of the Geological Society* **158**, 601-614.

Moreno, T., Prichard, H. M., Lunar, R., Monterrubio, S., Fisher, P. (1999). Formation of a secondary platinum-group mineral assemblage in chromitites from the Herbeira ultramafic massif in Cabo Ortegal, NW Spain. European *Journal of Mineralogy* **11**, 363-378.

Münker, C., Wörner, G., Yogodzinski, G., Churikova, T. (2004). Behaviour of high field strength elements in subduction zones: constraints from Kamchatka–Aleutian arc lavas. *Earth and Planetary Science Letters* **224**, 275-293.

Müntener, O., Hermann, J., Trommsdorff, V. (2000). Cooling History and Exhumation of Lower-Crustal Granulite and Upper Mantle (Malenco, Eastern Central Alps). *Journal of Petrology* **41**, 175-200.

Müntener, O., Kelemen, P. B., Grove, T. L. (2001). The role of H_2O during crystallization of primitive arc magmas under uppermost mantle conditions and genesis of igneous pyroxenites: an experimental study. *Contributions to Mineralogy and Petrology* **141**, 643-658.

Müntener, O. & Ulmer, P. (2006). Experimentally derived high-pressure cumulates from hydrous arc magmas and consequences for the seismic velocity structure of lower arc crust. *Geophysical Research Letters* **33**, doi:10.1029/ 2006GL027629.

Murphy, J. B., Cousens, B. L., Braid, J. A., Strachan, R. A., Dostal, J., Keppie, J. D., Nance, R. D. (2011). Highly depleted oceanic lithosphere in the Rheic Ocean: Implications for Paleozoic plate reconstructions. *Lithos* **123**, 165-175.

Nance, R. D., Gutiérrez-Alonso, G., Keppie, J. D., Linnemann, U., Murphy, J. B., Quesada, C., Strachan, R. A., Woodcock, N. H. (2010). Evolution of the Rheic Ocean. *Gondwana Research* **17**, 194-222.

Navon, O. & Stolper, E. (1987). Geochemical consequences of melt percolation: the upper mantle as a chromatographic column. *The Journal of geology* **95**, 285-307.

Nickel, K. G. & Green, D. H. (1985). Empirical geothermobarometry for garnet peridotites and implications for the nature of the lithosphere, kimberlites and diamonds. *Earth and Planetary Science Letters* **73**, 158-170.

Nicolas, A. (1986). A Melt Extraction Model Based on Structural Studies in Mantle Peridotites. *Journal of Petrology* **27**, 999-1022.

Nicolas, A. (1989). *Structure of ophiolite and dynamics of ocean lithosphere*: Kluwer Academic Publishers, Netherlands.

Nicolas, A. & Boudier, F. (2003). Where ophiolites come from and what they tell us. *Geological Society of America Special Papers* **373**, 137-152.

Nicolas, A., Reuber, I., Benn, K. (1988). A new magma chamber model based on structural studies in the Oman ophiolite. *Tectonophysics* **151**, 87-105.

Nonnotte, P., Ceuleneer, G., Benoit, M. (2005). Genesis of andesitic–boninitic magmas at mid-ocean ridges by melting of hydrated peridotites: Geochemical evidence from DSDP Site 334 gabbronorites. *Earth and Planetary Science Letters* **236**, 632-653.

Novo-Fernández, I., Garcia-Casco, A., Arenas, R., Díez Fernández, R. (2016). The metahyaloclastitic matrix of a unique metavolcanic block reveals subduction in the Somozas Mélange (Cabo Ortegal Complex, NW Iberia): Tectonic implications for the assembly of Pangea. *Journal of Metamorphic Geology*, **34**, 963-985.

O'Hara, M. J. (1968). The bearing of phase equilibria studies in synthetic and natural systems on the origin and evolution of basic and ultrabasic rocks. *Earth-Science Reviews* **4**, 69-133.

O'Reilly, S. Y., Griffin, W. L., Ryan, C. G. (1991). Residence of trace elements in metasomatized spinel lherzolite xenoliths: a proton-microprobe study. *Contributions to Mineralogy and Petrology* **109**, 98-113.

O'Reilly, S. Y. & Griffin, W. L. (1995). Trace-element partitioning between garnet and clinopyroxene in mantle-derived pyroxenites and eclogites: P-T-X controls. *Chemical Geology* **121**, 105-130.

O'Reilly, S. Y. & Griffin, W. L. (2006). Imaging global chemical and thermal heterogeneity in the subcontinental lithospheric mantle with garnets and xenoliths: Geophysical implications. *Tectonophysics* **416**, 289-309.

O'Reilly, S. Y., Griffin, W. L., Poudjom Djomani, Y. H., Morgan, P. (2001). Are lithospheres forever. Tracking changes in subcontinental lithospheric mantle through time: *GSA Today* **11**, 4-10.

O'Hara, M. J. & Yoder, H. S. (1967). Formation and fractionation of basic magmas at high pressures. Scottish *Journal of Geology* **3**, 67-117.

O'Reilly, S. Y. & Griffin, W. L. (2013). Mantle metasomatism. *Metasomatism and the chemical transformation of rock*: Springer, 471-533.

Obata, M. (1980). The Ronda peridotite: Garnet-, spinel-, and plagioclase-lherzolite facies and the P-T trajectories of a high-temperature mantle intrusion. *Journal of Petrology* **21**, 533-572.

Ordóñez Casado, B., Gebauer, D., Schäfer, H. J., Gil Ibarguchi, J. I., Peucat, J.- J. (2001). A single Devonian subduction event for the HP/HT metamorphism of the Cabo Ortegal complex within the Iberian Massif. *Tectonophysics* **332**, 359-385.

Pagé, P. & Barnes, S.-J. (2009). Using trace elements in chromites to constrain the origin of podiform chromitites in the Thetford Mines ophiolite, Québec, Canada. Economic *Geology* **104**, 997-1018.

Pagé, P., Bédard, J. H., Schroetter, J.-M., Tremblay, A. (2008). Mantle petrology and mineralogy of the Thetford Mines ophiolite complex. *Lithos* **100**, 255-292.

Peacock, S. M. (2003). Thermal structure and metamorphic evolution of subducting slabs. In: Eiler, J. (ed) Inside the subduction factory. *AGU Geophysical Monograph Series* **138**, 7-22.

Pearce, J. A. (2008). Geochemical fingerprinting of oceanic basalts with applications to ophiolite classification and the search for Archean oceanic crust. *Lithos* **100**, 14-48.

Pearce, J. A., Lippard, S. J., Roberts, S. (1984). Characteristics and tectonic significance of supra-subduction zone ophiolites. *Geological Society, London, Special Publications* **16**, 77-94.

Pearce, J. A. & Robinson, P. T. (2010). The Troodos ophiolitic complex probably formed in a subduction initiation, slab edge setting. *Gondwana Research* **18**, 60-81.

Pearson, D., Davies, G., Nixon, P. (1995). Orogenic ultramafic rocks of UHP (diamond facies) origin. In: Coleman, R. G., Xiaomin, W. (eds) *Ultrahigh pressure metamorphism*: Cambridge University Press, 456-510.

Pearson, D. G., Davies, G. R., Nixon, P. H. (1993). Geochemical Constraints on the Petrogenesis of Diamond Facies Pyroxenites from the Beni Bousera Peridotite Massif, North Morocco. *Journal of Petrology* **34**, 125-172.

Peate, D. W. & Pearce, J. A. (1998). Causes of spatial compositional variations in Mariana arc lavas: Trace element evidence. *Island Arc* **7**, 479-495.

Pessagno, E. A., Hull, D. M., Hopson, C. A. (2000). Tectonostratigraphic significance of sedimentary strata occurring within and above the Coast Range Ophiolite (California Coast Ranges) and the Josephine Ophiolite (Klamath Mountains), northwestern California. *Geological Society of America Special Papers* **349**, 383-394.

Peucat, J.-J., Bernard-Griffiths, J., Gil Ibarguchi, J. I., Dallmeyer, R. D., Menot, R. P., Cornichet, J., Ponce de Léon, M. I. (1990). Geochemical and geochronological cross section of the deep Variscan crust: The Cabo Ortegal high-pressure nappe (northwestern Spain). *Tectonophysics* **177**, 263-292.

Pilet, S., Baker, M. B., Stolper, E. M. (2008). Metasomatized Lithosphere and the Origin of Alkaline Lavas. *Science* **320**, 916-919.

Pilet, S., Ulmer, P., Villiger, S. (2010). Liquid line of descent of a basanitic liquid at 1.5 Gpa: constraints on the formation of metasomatic veins. *Contributions to Mineralogy*

and Petrology **159**, 621-643.

Pin, C., Ortega Cuesta, L. A., Gil Ibarguchi, J. I. (1992). Mantle-derived, early Paleozoic A-type metagranitoids, from the NW Iberian Massif; Nd isotope and trace-element constraints. *Bulletin de la Société Géologique de France* **163**, 483-494.

Pin, C., Paquette, J. L., Ábalos, B., Santos, F. J., Gil Ibarguchi, J. I. (2006). Composite origin of an early Variscan transported suture: Ophiolitic units of the Morais Nappe Complex (north Portugal). *Tectonics* **25**, TC5001.

Pin, C. & Santos Zalduegui, J. F. (1997). Sequential separation of light rare-earth elements, thorium and uranium by miniaturized extraction chromatography: Application to isotopic analyses of silicate rocks. *Analytica Chimica Acta* **339**, 79-89.

Polat, A. (2012). Growth of Archean continental crust in oceanic island arcs. *Geology* **40**, 383-384.

Polvé, M. & Allègre, C. J. (1980). Orogenic lherzolite complexes studied by ^{87}Rb-^{87}Sr: A clue to understand the mantle convection processes? *Earth and Planetary Science Letters* **51**, 71-93.

Pouchou, J. & Pichoir, F. (1984). A new model for quantitative X-ray microanalysis. Part 1: Application to the analysis of homogeneous samples. *Recherche Aérospatiale* (English Edition) **3**, 13-38.

Powell, W., Zhang, M., O'Reilly, S. Y., Tiepolo, M. (2004). Mantle amphibole trace-element and isotopic signatures trace multiple metasomatic episodes in lithospheric mantle, western Victoria, Australia. *Lithos* **75**, 141-171.

Puelles, P., Ábalos, B., Gil Ibarguchi, J. I. (2005). Metamorphic evolution and thermobaric structure of the subduction-related Bacariza high-pressure granulite formation (Cabo Ortegal Complex, NW Spain). *Lithos* **84**, 125-149.

Puelles, P., Gil Ibarguchi, J. I., Beranoaguirre, A., Ábalos, B. (2012). Mantle wedge deformation recorded by high-temperature peridotite fabric superposition and hydrous retrogression (Limo massif, Cabo Ortegal, NW Spain). *International Journal of Earth Sciences* **101**, 1835-1853.

Python, M. & Ceuleneer, G. (2003). Nature and distribution of dykes and related melt migration structures in the mantle section of the Oman ophiolite. *Geochemistry, Geophysics, Geosystems* **4**, doi:10.1029/2002GC000354.

Rabinowicz, M. & Ceuleneer, G. (2005). The effect of sloped isotherms on melt migration in the shallow mantle: a physical and numerical model based on observations in the Oman ophiolite. *Earth and Planetary Science Letters* **229**, 231-246.

Rampone, E. & Hofmann, A. W. (2012). A global overview of isotopic heterogeneities in the oceanic mantle. *Lithos* **148**, 247-261.

Rampone, E., Hofmann, A. W., Raczek, I. (1998). Isotopic contrasts within the Internal Liguride ophiolite (N. Italy): the lack of a genetic mantle–crust link. *Earth and*

Planetary Science Letters **163**, 175-189.

Rampone, E. & Morten, L. (2001). Records of Crustal Metasomatism in the Garnet Peridotites of the Ulten Zone (Upper Austroalpine, Eastern Alps). *Journal of Petrology* **42**, 207-219.

Rampone, E. & Piccardo, G. B. (2000). The ophiolite-oceanic lithosphere analogue: New insights from the Northern Apennines (Italy). *Geological Society of America Special Papers* **349**, 21-34.

Rapp, R. P., Shimizu, N., Norman, M. D. (2003). Growth of early continental crust by partial melting of eclogite. *Nature* **425**, 605-609.

Rassios, A. & Smith, A. G. (2000). Constraints on the formation and emplacement age of western Greek ophiolites (Vourinos, Pindos, and Othris) inferred from deformation structures in peridotites. *Geological Society of America Special Papers* **349**, 473-483.

Reisberg, L. & Zindler, A. (1986). Extreme isotopic variations in the upper mantle: evidence from Ronda. *Earth and Planetary Science Letters* **81**, 29-45.

Ries, A. C. & Shackleton, R. M. (1971). Catazonal complexes of north-western Spain and north Portugal: Remnants of a Hercynian thrust plate. *Nature, Phys. Sci* **234**, 65-69.

Rioux, M., Hacker, B., Mattinson, J., Kelemen, P., Blusztajn, J., Gehrels, G. (2007). Magmatic development of an intra-oceanic arc: High-precision U-Pb zircon and whole-rock isotopic analyses from the accreted Talkeetna arc, south-central Alaska. *Geological Society of America Bulletin* **119**, 1168-1184.

Rioux, M., Mattinson, J., Hacker, B., Kelemen, P., Blusztajn, J., Hanghøj, K., Gehrels, G. (2010). Intermediate to felsic middle crust in the accreted Talkeetna arc, the Alaska Peninsula and Kodiak Island, Alaska: An analogue for low-velocity middle crust in modern arcs. *Tectonics* **29**, TC3001.

Ripley, E. M. & Li, C. (2013). Sulfide Saturation in Mafic Magmas: Is External Sulfur Required for Magmatic Ni-Cu-(PGE) Ore Genesis? *Economic Geology* **108**, 45-58.

Roberts, N. M. W., Van Kranendonk, M. J., Parman, S., Clift, P. D. (2014). Continent formation through time. *Geological Society, London, Special Publications* **389**.

Robertson, A. (2007). Evidence of continental breakup from the Newfoundland rifted margin (Ocean Drilling Program Leg 210): Lower Cretaceous seafloor formed by exhumation of subcontinental mantle lithosphere and the transition to seafloor spreading. *Proc. ODP, Sci. Results*, 1-69.

Robertson, A. H. F. (2002). Overview of the genesis and emplacement of Mesozoic ophiolites in the Eastern Mediterranean Tethyan region. *Lithos* **65**, 1-67.

Roper, R. A. (2016). The Eclogitic Gneisses of the Cabo Ortegal Complex: provenance and tectonothermal evolution (zircon U-Pb/Lu-Hf methods). PhD thesis, Universidad Complutense de Madrid.

Rudnick, R. L. (1995). Making continental crust. *Nature* **378**, 571-577.

Rudnick, R. L. & Fountain, D. M. (1995). Nature and composition of the continental crust: A lower crustal perspective. *Reviews of Geophysics* **33**, 267-309.

Rudnick, R. L. & Gao, S. (2014). Composition of the continental crust. In: Turekian, K. K. (ed.) *Treatise on Geochemistry* **3** (Second Edition). Oxford: Elsevier, 1-64

Ryan, J., Morris, J., Tera, B., Leeman, B., Tsvetkov, A. (1995). The slab effect as a function of depth: evidence from cross-arc geochemical variations in the Kurile Arc. *Science* **270**, 625-628.

Ryerson, F. J. & Watson, E. B. (1987). Rutile saturation in magmas: implications for Ti-Nb-Ta depletion in island-arc basalts. *Earth and Planetary Science Letters* **86**, 225-239.

Sack, R. & Ghiorso, M. S. (1991). Chromite as a petrogenetic indicator. *Reviews in Mineralogy and Geochemistry* **25**, 323-354.

Salters, V. J. & Dick, H. J. (2002). Mineralogy of the mid-ocean-ridge basalt source from neodymium isotopic composition of abyssal peridotites. *Nature* **418**, 68-72.

Salters, V. J. & White, W. M. (1998). Hf isotope constraints on mantle evolution. *Chemical Geology* **145**, 447-460.

Salters, V. J. M. & Shimizu, N. (1988). World-wide occurrence of HFSE-depleted mantle. *Geochimica et cosmochimica Acta* **52**, 2177-2182.

Sánchez Martínez, S., Arenas, R., Díaz García, F., Martínez Catalán, J. R., Gómez-Barreiro, J., Pearce, J. A. (2007). Careón ophiolite, NW Spain: Suprasubduction zone setting for the youngest Rheic Ocean floor. *Geology* **35**, 53-56.

Sánchez Martínez, S., Arenas, R., Gerdes, A., Castiñeiras, P., Potrel, A., Fernández-Suárez, J. (2011). Isotope geochemistry and revised geochronology of the Purrido Ophiolite (Cabo Ortegal Complex, NW Iberian Massif): Devonian magmatism with mixed sources and involved Mesoproterozoic basement. *Journal of the Geological Society* **168**, 733-750.

Sánchez Martínez, S., Gerdes, A., Arenas, R., Abati, J. (2012). The Bazar Ophiolite of NW Iberia: a relic of the Iapetus–Tornquist Ocean in the Variscan suture. *Terra Nova* **24**, 283-294.

Santos, J. F., Schärer, U., Gil Ibarguchi, J. I., Girardeau, J. (2002). Genesis of pyroxenite-rich peridotite at Cabo Ortegal (NW Spain): geochemical and Pb–Sr–Nd isotope data. *Journal of Petrology* **43**, 17-43.

Santos Zalduegui, J. F., Schärer, U., Gil Ibarguchi, J. I. (1995). Isotope constraints on the age and origin of magmatism and metamorphism in the Malpica-Tuy allochthon, Galicia, NW Spain. *Chemical Geology* **121**, 91-103.

Santos Zalduegui, J. F., Schärer, U., Gil Ibarguchi, J. I., Girardeau, J. (1996). Origin and evolution of the Paleozoic Cabo Ortegal ultramafic-mafic complex (NW Spain):

U-Pb, Rb-Sr and Pb-Pb isotope data. *Chemical Geology* **129**, 281-304.

Satsukawa, T., Piazolo, S., González-Jiménez, J. M., Colás, V., Griffin, W. L., O'Reilly, S. Y., Gervilla, F., Fanlo, I., Kerestedjian, T. N. (2015). Fluid-present deformation aids chemical modification of chromite: Insights from chromites from Golyamo Kamenyane, SE Bulgaria. *Lithos* **228–229**, 78-89.

Saunders, A., Norry, M., Tarney, J. (1991). Fluid influence on the trace element compositions of subduction zone magmas. *Philosophical Transactions of the Royal Society of London A: Mathematical, Physical and Engineering Sciences* **335**, 377-392.

Saunders, A. D., Tarney, J., Kerr, A. C., Kent, R. W. (1996). The formation and fate of large oceanic igneous provinces. *Lithos* **37**, 81-95.

Saunders, A. D., Tarney, J., Weaver, S. D. (1980). Transverse geochemical variations across the Antarctic Peninsula: Implications for the genesis of calc-alkaline magmas. *Earth and Planetary Science Letters* **46**, 344-360.

Scambelluri, M., Hermann, J., Morten, L., Rampone, E. (2006). Melt- *versus* fluid-induced metasomatism in spinel to garnet wedge peridotites (Ulten Zone, Eastern Italian Alps): clues from trace element and Li abundances. *Contributions to Mineralogy and Petrology* **151**, 372-394.

Scherer, E. E., Cameron, K. L., Blichert-Toft, J. (2000). Lu–Hf garnet geochronology: closure temperature relative to the Sm–Nd system and the effects of trace mineral inclusions. *Geochimica et cosmochimica Acta* **64**, 3413-3432.

Schiano, P., Eiler, J. M., Hutcheon, I. D., Stolper, E. M. (2000). Primitive CaO-rich, silica-undersaturated melts in island arcs: Evidence for the involvement of clinopyroxene-rich lithologies in the petrogenesis of arc magmas. *Geochemistry, Geophysics, Geosystems* **1**, doi:10.1029/1999GC000032.

Schmidt, M. W., Green, D. H., Hibberson, W. O. (2004). Ultra-calcic Magmas Generated from Ca-depleted Mantle: an Experimental Study on the Origin of Ankaramites. *Journal of Petrology* **45**, 531-554.

Schneider, M. E. & Eggler, D. H. (1986). Fluids in equilibrium with peridotite minerals: Implications for mantle metasomatism. *Geochimica et cosmochimica Acta* **50**, 711-724.

Shirey, S. B. & Walker, R. J. (1995). Carius Tube Digestion for Low-Blank Rhenium-Osmium Analysis. *Analytical Chemistry* **67**, 2136-2141.

Simon, N. S. C., Carlson, R. W., Pearson, D. G., Davies, G. R. (2007). The Origin and Evolution of the Kaapvaal Cratonic Lithospheric Mantle. *Journal of Petrology* **48**, 589-625.

Sinton, J. M. (1977). Equilibration History of the Basel Alpine-Type Peridotite, Red Mountain, New Zealand. *Journal of Petrology* **18**, 216-246.

Sinton, J. M. & Detrick, R. S. (1992). Mid-ocean ridge magma chambers. *Journal of Geophysical Research: Solid Earth* **97**, 197-216.

Sisson, T. W. & Grove, T. L. (1993). Experimental investigations of the role of H_2O in calc-alkaline differentiation and subduction zone magmatism. *Contributions to Mineralogy and Petrology* **113**, 143-166.

Sobolev, A. V. & Danyushe*vsk*y, L. V. (1994). Petrology and Geochemistry of Boninites from the North Termination of the Tonga Trench: Constraints on the Generation Conditions of Primary High-Ca Boninite Magmas. *Journal of Petrology* **35**, 1183-1211.

Sobolev, A. V., Hofmann, A. W., Sobolev, S. V., Nikogosian, I. K. (2005). An olivine-free mantle source of Hawaiian shield basalts. *Nature* **434**, 590-597.

Sorbadere, F., Médard, E., Laporte, D., Schiano, P. (2013). Experimental melting of hydrous peridotite–pyroxenite mixed sources: Constraints on the genesis of silica-undersaturated magmas beneath volcanic arcs. *Earth and Planetary Science Letters* **384**, 42-56.

Sorbadere, F., Schiano, P., Métrich, N., Garaebiti, E. (2011). Insights into the origin of primitive silica-undersaturated arc magmas of Aoba volcano (Vanuatu arc). *Contributions to Mineralogy and Petrology* **162**, 995-1009.

Steinmann, G. (1927). Die ophiolitischen Zonen in den Mediterranean Zonen. *Compte Rendu, XIVe Congrès géologique International, 1926, Madrid, Graficas Reunidas* **2**, 637-667.

Stern, C. R. & De Wit, M. J. (2003). Rocas Verdes ophiolites, southernmost South America: remnants of progressive stages of development of oceanic-type crust in a continental margin back-arc basin. *Geological Society, London, Special Publications* **218**, 665-683.

Stracke, A., Snow, J. E., Hellebrand, E., von der Handt, A., Bourdon, B., Birbaum, K., Günther, D. (2011). Abyssal peridotite Hf isotopes identify extreme mantle depletion. *Earth and Planetary Science Letters* **308**, 359-368.

Suyehiro, K., Takahashi, N., Ariie, Y., Yokoi, Y., Hino, R., Shinohara, M., Kanazawa, T., Hirata, N., Tokuyama, H., Taira, A. (1996). Continental crust, crustal underplating, and low-Q upper mantle beneath an oceanic island arc. *Science* **272**, 390-392.

Takahashi, N., Kodaira, S., Klemperer, S. L., Tatsumi, Y., Kaneda, Y., Suyehiro, K. (2007). Crustal structure and evolution of the Mariana intra-oceanic island arc. *Geology* **35**, 203-206.

Takazawa, E., Frey, F. A., Shimizu, N., Obata, M., Bodinier, J. L. (1992). Geochemical evidence for melt migration and reaction in the upper mantle. *Nature* **359**, 55-58.

Tatsumi, Y. & Eggins, S. (1995). *Subduction zone magmatism*. Cambridge: Blackwell Science.

Tatsumi, Y., Hamilton, D. L., Nesbitt, R. W. (1986). Chemical characteristics of fluid phase released from a subducted lithosphere and origin of arc magmas: Evidence from high-pressure experiments and natural rocks. *Journal of Volcanology and Geothermal Re-*

search **29**, 293-309.

Tatsumi, Y., Shukuno, H., Tani, K., Takahashi, N., Kodaira, S., Kogiso, T. (2008). Structure and growth of the Izu-Bonin-Mariana arc crust: 2. Role of crust-mantle transformation and the transparent Moho in arc crust evolution. Journal of Geophysical Research: Solid Earth **113**, doi:10.1029/2007JB005121.

Taylor, S. R. & McLennan, S. M. (1985). *The continental crust: its composition and evolution*. Blackwell Scientific Publications.

Taylor, S. R. & McLennan, S. M. (1995). The geochemical evolution of the continental crust. *Reviews of Geophysics* **33**, 241-265.

Thayer, T. P. (1969). Peridotite-Gabbro Complexes as Keys to Petrology of Mid-Oceanic Ridges. *Geological Society of America Bulletin* **80**, 1515-1522.

Trommsdorff, V., Piccardo, G., Montrasio, A. (1993). From magmatism through metamorphism to sea floor emplacement of subcontinental Adria lithosphere during pre-Alpine rifting (Malenco, Italy). *Schweizerische Mineralogische und Petrographische Mitteilungen* **73**, 191-203.

Turner, S. & Hawkesworth, C. (1997). Constraints on flux rates and mantle dynamics beneath island arcs from Tonga–Kermadec lava geochemistry. *Nature* **389**, 568-573.

Turner, S., Hawkesworth, C., van Calsteren, P., Heath, E., Macdonald, R., Black, S. (1996). U-series isotopes and destructive plate margin magma genesis in the Lesser Antilles. *Earth and Planetary Science Letters* **142**, 191-207.

Van Calsteren, P. W. C. (1978). Geochemistry of the polymetamorphic mafic-ultramafic complex at Cabo Ortegal (NW Spain). *Lithos* **11**, 61-72.

Van Calsteren, P. W. C., Boelrijk, N., Hebeda, E., Priem, H., Den Tex, E., Verdurmen, E., Verschure, R. (1979). Isotopic Dating of older elements (including the Cabo Ortegal mafic-ultramafic complex) in the hercynian orogen of NW Spain: manifestations of a presumed early paleozoic mantle-plume. *Chemical Geology* **24**, 35-56.

Van der Wal, D. & Bodinier, J.-L. (1996). Origin of the recrystallisation front in the Ronda peridotite by km-scale pervasive porous melt flow. *Contributions to Mineralogy and Petrology* **122**, 387-405.

Van der Wal, D. & Vissers, R. L. M. (1996). Structural Petrology of the Ronda Peridotite, SW Spain: Deformation History. *Journal of Petrology* **37**, 23-43.

Van Kranendonk, M. J., Hugh Smithies, R., Hickman, A. H., Champion, D. C. (2007). Review: secular tectonic evolution of Archean continental crust: interplay between horizontal and vertical processes in the formation of the Pilbara Craton, Australia. *Terra Nova* **19**, 1-38.

Van Kranendonk, M. J., Smithies, R. H., Griffin, W. L., Huston, D. L., Hickman, A. H., Champion, D. C., Anhaeusser, C. R., Pirajno, F. (2015). Making it thick: a volcanic plateau origin of Palaeoarchean continental lithosphere of the Pilbara and Kaapvaal

cratons. *Geological Society, London, Special Publications* **389**, 83-111.

Vannucci, R., Piccardo, G. B., Rivalenti, G., Zanetti, A., Rampone, E., Ottolini, L., Oberti, R., Mazzucchelli, M., Bottazzi, P. (1995). Origin of LREE-depleted amphiboles in the subcontinental mantle. *Geochimica et cosmochimica Acta* **59**, 1763-1771.

Vasseur, G., Vernières, J., Bodiner, J.-L. (1991). Modelling of Trace Element Transfer between Mantle Melt and Heterogranular Peridotite Matrix. *Journal of Petrology* **Special Lherzolites Issue**, 41-54.

Vissers, R. L. M., Drury, M. R., Strating, E. H. H., Wal, D. v. d. (1991). Shear zones in the upper mantle: A case study in an Alpine Iherzolite massif. *Geology* **19**, 990-993.

Vogel, D. E. (1967). Petrology of an eclogite-and pyrigarnite-bearing polymetamorphic rock Complex at Cabo Ortegal, NW Spain. *Leidse Geol. Meded* **40**, 121-213.

Vuagnat, M. (1964). Remarques sur la Trilogie Serpentinites-Gabbros-Diabases dans le Bassin de la Méditerranée Occidentale. *Geologische Rundschau* **53**, 336-358.

Wallin, T. E. & Metcalf, Rodney V. (1998). Supra-Subduction Zone Ophiolite Formed in an Extensional Forearc: Trinity Terrane, Klamath Mountains, California. *The Journal of geology* **106**, 591-608.

Warren, C. J., Beaumont, C., Jamieson, R. A. (2008). Modelling tectonic styles and ultra-high pressure (UHP) rock exhumation during the transition from oceanic subduction to continental collision. *Earth and Planetary Science Letters* **267**, 129-145.

Warren, J. M., Shimizu, N., Sakaguchi, C., Dick, H. J. B., Nakamura, E. (2009). An assessment of upper mantle heterogeneity based on abyssal peridotite isotopic compositions. *Journal of Geophysical Research: Solid Earth* **114**, doi:10.1029/2008JB006186.

Whitmarsh, R. & Wallace, P. (2001). The rift-to-drift development of the West Iberia non-volcanic continental margin; a review of the contribution of Ocean Drilling Program Leg 173. In: Beslier, M.-O., Whitmarsh, R. B., Wallace, P. J., and Girardeau, J. (eds) *Proceedings of the Ocean Drilling Program, Scientific Results* **173**.

Winchester, J. A., Pharaoh, T. C., Verniers, J. (2002). Palaeozoic amalgamation of Central Europe: an introduction and synthesis of new results from recent geological and geophysical investigations. *Geological Society, London, Special Publications* **201**, 1-18.

Witt, G. & Seck, H. A. (1989). Origin of amphibole in recrystallized and porphyroclastic mantle xenoliths from the Rhenish Massif: implications for the nature of mantle metasomatism. *Earth and Planetary Science Letters* **91**, 327-340.

Witt-Eickschen, G. & Harte, B. (1994). Trace-element Partitioning with Application to Magmatic Processes Distribution of trace elements between amphibole and clinopyroxene from mantle peridotites of the Eifel (western Germany): An ion-microprobe study. *Chemical Geology* **117**, 235-250.

Witt-Eickschen, G. & Seck, H. (1991). Solubility of Ca and Al in orthopyroxene from spinel peridotite: an improved version of an empirical geothermometer. *Contributions*

to Mineralogy and Petrology **106**, 431-439.

Xiong, Q., Zheng, J.-P., Griffin, W. L., O'Reilly, S. Y., Pearson, N. J. (2014). Pyroxenite Dykes in Orogenic Peridotite from North Qaidam (NE Tibet, China) Track Metasomatism and Segregation in the Mantle Wedge. *Journal of Petrology* **55**, 2347-2376.

Xu, X., Yang, J., Robinson, P. T., Xiong, F., Ba, D., Guo, G. (2015). Origin of ultrahigh pressure and highly reduced minerals in podiform chromitites and associated mantle peridotites of the Luobusa ophiolite, Tibet. *Gondwana Research* **27**, 686-700.

Yaxley, G. M. & Green, D. H. (1998). Reactions between eclogite and peridotite: mantle refertilisation by subduction of oceanic crust. Schweiz. *Mineral. Petrogr. Mitt* **78**, 243-255.

Yokoyama, T., Makishima, A., Nakamura, E. (1999). Evaluation of the coprecipitation of incompatible trace elements with fluoride during silicate rock dissolution by acid digestion. *Chemical Geology* **157**, 175-187.

Yoshikawa, M., Kawamoto, T., Shibata, T., Yamamoto, J. (2010). Geochemical and Sr–Nd isotopic characteristics and pressure–temperature estimates of mantle xenoliths from the French Massif Central: evidence for melting and multiple metasomatism by silicate-rich carbonatite and asthenospheric melts. *Geological Society, London, Special Publications* **337**, 153-175.

Yumul, G. P. (2007). Westward younging disposition of Philippine ophiolites and its implication for arc evolution. *Island Arc* **16**, 306-317.

Zandt, G., Gilbert, H., Owens, T. J., Ducea, M., Saleeby, J., Jones, C. H. (2004). Active foundering of a continental arc root beneath the southern Sierra Nevada in California. *Nature* **431**, 41-46.

Zhang, R. Y., Liou, J. G., Yang, J. S., Yui, T.-F. (2000). Petrochemical constraints for dual origin of garnet peridotites from the Dabie-Sulu UHP terrane, eastern-central China. *Journal of Metamorphic Geology* **18**, 149-166.

Zhang, Z. M., Dong, X., Liou, J. G., Liu, F., Wang, W., Yui, F. (2011). Metasomatism of garnet peridotite from Jiangzhuang, southern Sulu UHP belt: constraints on the interactions between crust and mantle rocks during subduction of continental lithosphere. *Journal of Metamorphic Geology* **29**, 917-937.

Zhao, D., Hasegawa, A., Horiuchi, S. (1992). Tomographic imaging of P and S wave velocity structure beneath northeastern Japan. *Journal of Geophysical Research: Solid Earth* **97**, 19909-19928.

Zindler, A. & Hart, S. (1986). Chemical Geodynamics. *Annual Review of Earth and Planetary Sciences* **14**, 493-571.